Remotely measuring the wind using turbine-mounted lidars: Application to power performance testing

Borraccino, Antoine; Courtney, Michael; Wagner, Rozenn

Link to article, DOI:
10.11581/DTU:00000021

Publication date:
2017

Document Version
Publisher's PDF, also known as Version of record

Remotely Measuring The Wind using Turbine-Mounted Lidars: Application to Power Performance Testing

Department of Wind Energy

Antoine Borraccino

DTU Wind Energy PhD-0076(EN)
DOI number: 10.11581/DTU:00000021

May 2017

DTU Wind Energy
Department of Wind Energy

Authors: Antoine Borraccino

Title: Remotely measuring the wind using turbine-mounted lidars: Application to power performance testing.

Department: Wind Energy

2017

Project Period:

June 1st 2014 – May 31st 2017

Education:

PhD

Supervisor:

Senior Researcher Michael Stephen Courtney

Co-supervisors:

Senior Researcher Rozenn Wagner

DTU Wind Energy is a department of the Technical University of Denmark with a unique integration of research, education, innovation and public/private sector consulting in the field of wind energy. Our activities develop new opportunities and technology for the global and Danish exploitation of wind energy. Research focuses on key technical-scientific fields, which are central for the development, innovation and use of wind energy and provides the basis for advanced education.

DTU Wind Energy has a staff of approximately 240 and a further 35 PhD-students, spread across 38 different nationalities. The variety of research, education, innovation, testing and consultancy is reflected in the employment profile which includes faculty with research and teaching responsibilities, researchers and technical academic staff, highly skilled technicians and administrative staff.

Our facilities are situated at DTU Risø Campus and at DTU Lyngby Campus. Furthermore the department is running the national test stations in Høvsøre and Østerild.

Technical University of Denmark
Department of Wind Energy
Frederiksborgvej 399
Building 118
4000 Roskilde
Denmark

www.vindenergi.dtu.dk

DTU Wind Energy
Department of Wind Energy

Ph.D. Thesis

Remotely measuring the wind using turbine-mounted lidars

Application to power performance testing

Antoine Borraccino

Risø campus, Roskilde, 2017

DTU

Technical University of Denmark
DTU Wind Energy
Department of Wind Energy

DTU Risø Campus
Frederiksborgvej 399 Building 125
4000 Roskilde, Denmark
Phone +45 93511124
borr@dtu.dk
www.vindenergi.dtu.dk

Summary

Forward-looking wind lidars mounted on the nacelle of a wind turbines allow to remotely measure the flow upwind. The newest generation of nacelle lidar systems can sense the wind at multiple distances and multiple heights, and consequently has profiling capabilities. Wind lidars are cost-efficient and provide measurements more representative of the wind flow field than conventional meteorology mast. For the purpose of power curve measurement, it is essential that lidars provide traceable measurements and to assess their measurement uncertainty.

A generic calibration methodology was developed, using the so-called white box approach. It consists mainly in calibrating the lidar primary measurements of line-of-sight velocities. The line-of-sight velocity is the projection of the wind vector onto the laser beam propagation path. The calibration is performed in situ, by comparing the lidar velocity measurements to a reference quantity itself traceable to the international standards of units. The uncertainty of the line-of-sight velocity measurements was assessed using a normative methodology (GUM) which is based on the law of propagation of uncertainties. The generic calibration procedure was applied to two commercially developed nacelle lidars systems, the *Avent 5-beam Demonstrator* and the *ZephIR Dual Mode* lidars. Further, the line-of-sight positioning quantities such as inclination angles or beam trajectory were also calibrated and their uncertainties assessed. Calibration results were of high quality, with line-of-sight velocity measurements within 0.9 % of the reference.

In the lidar measurement process, line-of-sight velocities taken in multiple locations (different heights, distances, and directions) are used to reconstruct useful wind characteristics such as wind speed, direction, shear, etc. Wind field reconstruction methods based on model-fitting techniques were developed. The model-fitting wind field reconstruction technique allows to clearly define the wind model – and state its inherent assumptions. Different wind models can be used without changing the general principles of the wind field reconstruction methods. Two wind models were developed in this thesis. The first one employs lidar measurement at a single distance – but several heights –, accounts for shear through a power law profile, and estimates hub height wind speed, direction and the shear exponent. The second model combines the wind model with a simple one-dimensional induction model. The lidar inputs were line-of-sight velocity measurements taken at multiple distances close to the rotor, from 0.5 to 1.25 rotor

diameters. Using the combined wind-induction model, hub height free stream wind characteristics are estimated (speed, direction, shear, induction factor).

With the help of a seven-month full-scale measurement campaign at the Nørrekær Enge wind farm, the model-fitting wind field reconstruction technique and models were demonstrated. The same methods were applied to both the *Avent 5-beam Demonstrator* and *ZephIR Dual-Mode* nacelle lidars. Nacelle lidar estimates of wind characteristics were compared to those measured by instruments mounted on a mast located 2.5 rotor diameters from the turbine on which the lidars were mounted. For wind directions in the 'IEC free sector', the wind speed comparison results showed that lidar-estimates where within 0.7 % from the top-mounted cup anemometer measurements. The secondary wind characteristics (direction, shear, induction factor) were also compared to reference quantities and proved to provide valuable information on the upstream flow field.

The uncertainties of wind field characteristics estimated by the model-fitting reconstruction method were quantified using numerical error propagation techniques called Monte Carlo methods. These numerical methods are particularly relevant to propagate errors trough complex non-linear models, since such models are outside the scope of the GUM methodology. The procedures used to apply Monte Carlo methods to wind field reconstruction codes were detailed. The uncertainty results are provided for a wide-range of wind field characteristics values, and for all the estimated wind characteristics. In particular, the model wind speed uncertainties were shown to be equivalent to the cup anemometer uncertainty that was used to calibrate the lidar line-of-sight velocity.

Finally, the methods were applied to power performance testing, using the experimental data of the Nørrekær Enge campaign. The IEC 61400-12-1 (ed. 2, 2017) standards for *'Power performance measurements of electricity producing wind turbines'* provided the basis to develop procedures applying to nacelle-mounted lidars. The measured power curves using wind speed measurements from the two profiling nacelle lidars and from the mast top-mounted cup anemometer were compared. The power curve uncertainties were also quantified. Further, the annual energy production (AEP) was computed for a range of annual mean wind speeds. At $8\,\mathrm{m\,s^{-1}}$, the lidar-estimated AEP was within 1 % to the one obtained with the cup anemometer.

The combined wind-induction reconstruction technique represents a paradigm shift in power performance testing: it is no longer required to measure far upstream the rotor – between two and four rotor diameters – to approximate the free stream wind speed. Instead, measurements taken close to the turbine rotor by nacelle-mounted profiling lidars can be used to accurately estimate the free stream wind speed. In the future, nacelle lidars are likely to replace meteorological masts for turbine power performance testing.

Dansk sammendrag

Fremadrettede vind-lidarer, monteret på en vindmølles nacelle, gør det muligt at måle den indkommende vind. Den nyeste generation af lidarer monteret på nacellen kan måle vinden i flere afstande og i flere højder og er dermed egnet til at måle vindprofilet. Vind-lidarer er kost-effektive og giver målinger, der er mere repræsentative for vindfeltet end konventionelle meteorologimaster. I forbindelse med effektkurvemålinger er det væsentligt at lidar målinger er sporbare, og at måleusikkerheden bliver estimeret.

Der er udviklet en generel kalibreringsmetode som gør brug af den såkaldte "white box" tilgang. Den består hovedsagelig i kalibrering af lidarens primære "line-of-sight" vindhastigheder. Line-of-sight hastigheden er projektionen af vindvektoren på laserstrålens udbredelsesspor. Kalibreringen udføres på stedet ved sammenligning af lidarens målte hastighed med en reference størrelse som i sig selv er sporbar til de internationale standard enheder. Usikkerheden på den målte line-of-sight hastighed blev undersøgt ved anvendelse af en normativ metode (GUM), som er baseret på princippet om usikkerheders udbredelse. Den generelle kalibreringsmetode blev anvendt på to kommercielt udviklede nacelle lidar systemer, *Avent's 5-stråle Demonstrator* og *ZephIR's Dual Mode* lidar. Endvidere blev line-of-sight positioneringsparametre såsom inklinationsvinkler eller strålebanen også kalibreret og deres usikkerheder blev undersøgt. Kalibreringsresultaterne var af høj kvalitet med line-of-sight hastighedsmålingerne indenfor 0.9 % af deres reference.

I lidar måleprocessen bliver line-of-sight hastighederne målt i multiple positioner (forskellige højder, afstande, og retninger) brugt til at rekonstruere brugbare vind karakteristika, såsom vindhastighed, retning, shear, osv. Et vindfelts rekonstruktion, baseret på model tilpasningsteknikker, blev udviklet. Modeltilpasningsteknikken for rekonstruktion af vindfeltet tillader en klar definition af vindmodellen – og angiver dens iboende antagelser. Forskellige vindmodeller kan anvendes uden at ændre de generelle principper for rekonstruktionsmetoderne for vindfeltets rekonstruktion. To vindmodeller blev udviklet i denne afhandling. Den første anvender lidar målinger fra en enkelt afstand – men i adskillige højder - , og den tager hensyn til shear med et power-law profil, og på den måde estimeres navhøjdevindhastigheden, retningen og shear eksponenten. Den anden model kombinerer vindmodellen med en simpel endimensionel induktionsmodel. Lidar signalerne, der blev anvendt, er line-of-sight hastighedsmålinger målt i multiple

afstande tæt på rotoren, fra 0,5 til 1,25 gange rotor diameteren foran rotoren. Ved anvendelse af den kombinerede vind induktionsmodel blev vindforholdene i navhøjde estimeret (hastighed, retning, shear og induktionsfaktor).

Ved hjælp af en syv måneders fuldskala målekampagne ved Nørrekær Enge vindmøllepark blev rekonstruktionsteknikken til modeltilpasning af vindfeltet demonstreret. De samme metoder blev anvendt på både *Avent's 5-stråle Demonstrator* og *ZephIR's Dual-Mode* nacelle lidar. Estimater på nacelle lidarernes vindkarakteristikker blev sammenlignet med tilsvarende målinger med instrumenter monteret på en mast placeret 2,5 rotordiametre fra vindmøllen som lidarerne var monteret på. For vindretninger i den "IEC frie sektor" viste resultaterne af sammenligningerne på vindhastigheder, at lidar estimaterne var indenfor 0.7 % af målingerne på det top-monterede kopanemometer. De sekundære vindkarakteristikker (retning, shear, induktionsfaktor) blev også sammenlignet med reference målestørrelser og er påvist at give værdifuld information på det indkommende strømningsfelt.

Usikkerhederne på vindfeltets karakteristika, estimeret med rekonstruktionsmetoden til modeltilpasning af vindfeltet, blev kvantificeret ved brug af numeriske fejludbredelsesmodeller kaldt Monte Carlo metoder. Disse numeriske metoder er især relevante for udbredelse af fejl igennem komplekse ikke-lineære modeller fordi sådanne modeller, er uden for anvendelsesområdet af GUM metoden. Procedurerne, der blev brugt for at anvende Monte Carlo metoderne til koderne for rekonstruktion af vindfeltet, blev detaljeret beskrevet. Resultaterne på usikkerhederne er angivet for et stort område af værdierne for vindfeltets karakteristika, og for alle de estimerede vind karakteristika. I særdeleshed viste usikkerhederne på modelvindhastighederne sig at være ækvivalente med kopanemometer usikkerheden, som blev brug til kalibrering af lidar line-of-sight hastigheden.

Endelig blev metoderne anvendt til effektkurve måling ved brug af de eksperimentelle data fra Nørrekær Enge målekampagnen. Standarden IEC 61400-12-1:ed2 "Power performance measurements of electricity producing windturbines" gav grundlag for udvikling af procedurer for anvendelse af nacelle-monterede lidarer. De målte effektkurver med brug af vindhastighedsmålinger fra de to nacelle lidarer til vindprofil målinger og med brug af mastebaseret og top-monteret kopanemometer blev sammenlignet. Usikkerhederne på effektkurverne blev også kvantificeret. Endvidere blev årsenergiproduktionen (AEP) beregnet for et interval af årsmiddelvindhastigheder. Ved $8\,\mathrm{m\,s^{-1}}$ var den lidar estimerede AEP indenfor 1 % af den tilsvarende opnået med kopanemometret.

Den kombinerede rekonstruktionsmetode for vind-induktionen repræsenterer et paradigmeskift i effektkurvemåling: det er ikke længere nødvendigt at tilnærme sig fristrømsvindhastigheden ved at måle langt opstrøms for rotoren – mellem to og fire rotor diametre. I stedet kan målinger taget tæt på vindmøllens rotor med nacelle-monterede lidarer bruges til nøjagtigt at estimere fristrømsvindhastigheden.

I fremtiden er det sandsynligt, at nacelle-lidarer vil overtage meteorologiske master til måling af vindmøllers effektkurver.

Résumé

Les systèmes lidar installés sur la nacelle d'une éolienne permettent de mesurer le vent à distance, par exemple en amont du rotor. Avec la dernière génération de systèmes lidar nacelle, il est possible de sonder le vent à de multiples distances et hauteurs, leur conférant ainsi des capacités profilantes. Le lidar est une technologie fournissant des mesures plus représentatives des écoulements de vent qu'un mât de mesures, et souvent à plus bas coût. Pour l'application mesure de courbes de puissance, il est essentiel d'assurer la traçabilité des mesures lidar et d'évaluer leurs incertitudes de mesure.

Une méthode générique de calibration fondée sur des principes dits de « boîte blanche » et dédiée aux lidars nacelle a été développée. Celle-ci consiste principalement à calibrer la mesure primaire du lidar, la vitesse radiale. La vitesse radiale résulte de la projection du vecteur vent sur le trajet de propagation du faisceau laser. La calibration est effectuée in situ, en comparant les mesures de vitesse radiale du lidar à une quantité de référence, elle-même traçable aux étalons du système international d'unités. L'incertitude de mesure de la vitesse radiale est évaluée en utilisant la norme métrologique (GUM), dont les principes reposent sur la loi de propagation de l'incertitude. La procédure générique de calibration a été appliquée à deux systèmes lidar commerciaux, le *Avent 5-beam Demonstrator* et le *ZephIR Dual Mode*. De plus, les quantités permettant de localiser les mesures de vitesse radiales – telles que les angles d'inclinaison ou liées à la trajectoire des faisceaux – ont elles aussi été calibrées et leurs incertitudes évaluées. Les résultats de calibration se sont révélés être de haute qualité, avec des écarts observés de moins de 0.9 % entre les mesures lidar de vitesse radiale et la quantité de référence.

Le procédé de mesure lidar utilise la mesure de vitesses radiales en de multiples positions (diverses hauteurs, distances et directions) afin de reconstruire des paramètres caractérisant le vent, tels que sa vitesse, sa direction, son profil vertical (cisaillement), etc. Une méthode de reconstruction basée sur l'ajustement de modèles (« fitting ») a été développée. Elle permet de définir clairement le modèle de vent et de présenter les hypothèses inhérentes au modèle. De nombreux modèles de vent peuvent être définis sans modifier les principes de la méthode de reconstruction du vent. Deux modèles de vent ont particulièrement été développés dans cette thèse. Le 1^{er} utilise des mesures lidar à une seule distance – et plusieurs hauteurs –, prend en compte le cisaillement à travers un profil de vent de type loi de puissance, et estime ainsi la vitesse du vent à hauteur du moyeu, sa direction,

et l'exposant de cisaillement. Le $2^{ème}$ modèle combine ce modèle de vent avec un modèle d'induction unidimensionnel. Dans ce cas, les entrées du modèle de reconstruction qui ont été utilisées étaient les vitesses radiales mesurées à de multiples distances situées proches du rotor de l'éolienne – entre 0,5 et 1,5 diamètres. Le modèle combiné vent-induction permet d'estimer la vitesse du vent d'écoulement libre, sa direction, l'exposant de cisaillement ainsi que le facteur d'induction axiale.

La technique de reconstruction du vent par ajustement de modèles a été validée en utilisant les données d'une campagne de mesures à échelle réelle d'une durée de sept mois, au parc éolien de Nørrekær Enge. Les mêmes méthodes ont été appliquées aux deux lidars nacelle, le *Avent 5-beam Demonstrator* et le *ZephIR Dual Mode*. Les valeurs estimées par les lidars nacelle des paramètres de vent ont été comparées à celles mesures par les instruments d'un mât de mesure situé à une distance de l'éolienne de 2,5 diamètres du rotor. Pour les directions de vent hors secteur perturbé, les résultats obtenus sur la vitesse du vent ont fait état d'écart de moins de 0.7 % entre les valeurs estimées par les lidars nacelle et celles mesurées par l'anémomètre à coupelles en tête de mât. Les caractéristiques de vent secondaires (direction, cisaillement, facteur d'induction) ont également été comparées à des quantités de référence et ont démontré leur capacité à fournir des informations utiles sur l'écoulement en amont de l'éolienne.

Par la suite, les incertitudes sur les caractéristiques de vent estimées par la technique de reconstruction par ajustement de modèle ont été quantifies à l'aide de méthodes numériques de propagation des incertitudes, connues sous le nom de méthodes de Monte Carlo. Ces méthodes numériques sont particulièrement appropriées pour la propagation d'erreur pour les modèles non-linéaires et complexes. Ces derniers ne font en effet pas partie du cadre d'application de la méthode GUM. Les procédures utilisées pour appliquer les méthodes de Monte Carlo aux algorithmes de reconstruction de vent ont été décrites, et les résultats d'incertitudes fournis pour un éventail de caractéristiques de vent. En particulier, les incertitudes sur la vitesse du vent se sont révélées être équivalentes à celles de l'anémomètre à coupelles employé pour calibrer la vitesse radiale mesurée par les lidars.

Enfin, les données expérimentales de la campagne de Nørrekær Enge ont été appliquées à la mesure de courbes de puissance. La norme IEC 61400-12-1 (ed. 2, 2017) pour les « mesures de performance de puissance des éoliennes de production d'électricité » a été adaptée afin de développer des procédures applicables aux lidars nacelle. Les courbes de puissance mesurées en utilisant la vitesse du vent provenant des deux lidars nacelle profilant ainsi que provenant de l'anémomètre à coupelles en tête de mât ont été comparées. Les incertitudes de courbe de puissance ont également été calculées. De plus, la production annuelle d'énergie (AEP) a été calculée pour une série de moyennes annuelles de vitesse de vent. À $8\,\mathrm{m\,s^{-1}}$, l'AEP estimée à l'aide des mesures lidars a montré une erreur de moins de 1 % avec l'AEP

obtenue pour l'anémomètre à coupelles.

La technique innovante de reconstruction des caractéristiques de vent utilisant le modèle combiné vent-induction représente une évolution radicale pour les tests de performance de puissance : il n'est plus nécessaire de mesurer le vent suffisamment loin en amont du rotor afin d'approximer la vitesse du vent en écoulement libre. À la place, les mesures prises par un lidar nacelle à proximité du rotor peuvent être utilisées pour estimer la vitesse du vent en écoulement libre avec précision et avec une bonne exactitude. Dans un futur proche, il est fort probable que les lidars nacelle remplaceront les mâts de mesures afin de tester la performance de puissance des éoliennes.

Dedicated to my parents, brother, sister and friends –
for their endless love and support.

Preface

This thesis was prepared at the department of Wind Energy of the Technical University of Denmark in fulfilment of the requirements for acquiring a Ph.D. degree.

The research described in this thesis forms part of the Unified Turbine Testing (UniTTe) project lead by *DTU Wind Energy* and funded by *Innovation Fund Denmark* under grant 1305-00024B. The Ph.D. project focused on the development of calibration methodologies and measurement uncertainty assessment of nacelle-mounted wind lidars, and on the derivation of wind characteristics for wind turbine power performance assessment.

I carried out my Ph.D. project within the 'Test and Measurement' (1.5 years) and 'Meteorology and Remote Sensing' (1.5 years) sections. It was supervised by senior scientist Michael Courtney, and co-supervised by senior scientist Rozenn Wagner. I was engaged in the project from the 1^{st} of June 2014 to the 31^{st} of May 2017.

The ambition of the described research is to contribute in providing the scientific basis for the next generation of wind turbine power performance assessment standards. The Ph.D. project endeavoured to design methods and tools that can be readily employed by the wind energy industry. The work performed in the thesis is largely based on experimental techniques and can thus be classified as applied research in the fields of meteorology, metrology – the science of measurements – and computer sciences.

By reading this thesis, one will gain insights into:

- measurement techniques used in wind energy, with a great emphasis on a remote sensing technology called lidar;
- how to calibrate Doppler wind lidars via a generic methodology;
- how to quantify the uncertainty of lidar measurements;
- state-of-the art wind field reconstruction techniques, allowing to characterise the flow close and far upstream a wind turbine's rotor;
- how to propagate uncertainties through a model using statistical techniques

such as Monte Carlo methods;

- power performance testing procedures: what their current requirements are (in 2017); how nacelle wind lidars can fulfil them and what are the inherent issues to be solved;
- how the use of nacelle lidars benefits power curve measurements;
- what are the uncertainties associated with the measurements of a power curve.

Two peer-reviewed scientific articles are included in my Ph.D. thesis:

- Antoine Borraccino et al. 2016. "Generic Methodology for Field Calibration of Nacelle-Based Wind Lidars". *Remote Sensing* 8 (11): 907. ISSN: 2072-4292. doi:10.3390/rs8110907
- A. Borraccino et al. 2017. "Wind field reconstruction from nacelle-mounted lidar short-range measurements". *Wind Energy Science* 2 (1): 269–283. doi:10.5194/wes-2-269-2017

For both of them, I was the main author and conducted the research work. I am thankful to my co-authors for their contributions, which reside in their extensive guidance and supervision, in their experience for assessing the quality of the results, in their innovative ideas, in advising me to conceive the manuscripts, and last but not least, in using their critical eyes to review them before publishing.

Finally, a note on the use of pronouns in this thesis. "I" is used when I am solely responsible for the decisions or when the text reflects my personal opinion. When the discourse is explanatory, "we" stands for "me and the reader". "we" is also used whenever I write about an insight, or a result which was produced in a collaboration.

To you, the reader, I simply hope you enjoy the read.

Risø campus, Roskilde, June 22, 2017

Antoine Borraccino

PS: credit for the picture on the title page goes to Troels Friis Pedersen.

Acknowledgements

Sometimes, a Ph.D. degree may be viewed as a long and tortuous road. Fortunately, this is certainly not one that I walked through alone. To the persons cited hereafter – and to many others whom I cannot cite here but are very much in my thoughts – I would like to say that, directly or indirectly, you all contributed to making these three years feel much shorter and enjoyable that I could ever have hoped.

I would first like to thank my family. Papa, Maman, you could see in those three years how much I love being home. Copenhagen is not that far from my native Champagne region. Your endless support and love have surely something to do with that – thanks for all the private taxiing between Paris and Troyes, from the french food boxes, many skyping hours, etc. Of course, my thoughts and love also goes towards my sister Léa, my brother Baptiste, his wife and my little niece Alice and my grandparents.

During these three years, I had the luck to be under the supervision of two devoted supervisors, Rozenn Wagner and Michael Courtney. From the start, I realised how different and similar you are, and how much I would learn from such an exceptional combination of characters. You have challenged me, you have advised me, and you have continuously supported me – professionally but also at a personal level in many occasions. I am grateful for these three years working alongside both of you. To Mike specifically, thanks for the "nice people... and Antoine", thanks for being a self-appointed professional pain in the *** (it's actually often helpful!), somehow giving up the leadership of WP2, passing on your critical thinking to me, and teaching me how to write sexy titles. To Rozenn, you formed initially at least half of my french connection at Risø, we have our own frenglish language, you provided me with a cool project to work with, clear guidance, marked me with your highly structured working habits. And, you always listened to me whenever I needed to talk both at and outside work. Many thanks to both of you for all of this.

A special word for my german colleagues and friends from the small but very skilled *Stuttgart Wind Energy* group. My 3-month external stay with you was a turning point in my PhD. To David Schlipf and Florian Haizmann, I would like to express my gratitude for all the time you spent with me, your patience and skills. Working with you made me grow exponentially fast as a scientist, and I enjoyed it very much.

I was fortunate to have my PhD project integrated into a large research project, with a great industry-oriented approach. To the UniTTe consortium and partners, many thanks for all the continuous support and positive feedback, which gave me an extra motivation in the project. In particular, I would like to mention M. Boquet and P. Mazoyer, M. Harris and C. Slinger (thanks for the days at Fairoaks!), I. Antoniou, S. Feeney and R. Rivera Lamata – many thanks for all the valuable reviews and advice.

To my DTU colleagues, many thanks for setting a professional and friendly atmosphere. I was constantly surrounded by a lot of brain power, which helps lifting up our research work. I would like to thank P. Hummelshøj and H.E. Jørgensen for being such accessible leaders during my time in the TEM and MES sections. Thanks to my close colleagues and friends – I am sure you all know why your name is here – Andrea V., Ameya S., Alexander M.F., Nikolay D., Nikola V., Nikolas A., Alfredo P., Troels F.P. Thanks also to all the highly-skilled DTU technicians and engineers, Anders, Per, Kristoffer, Steen, Paula, Paulo, Héctor, Carsten, Ginka, and to my PhD office mates.

I cannot help but write a special paragraph for Guillaume Léa and Stéphanie B.H., and my 'adoptive' nephews Tristan, Soren and Louis. We have spent countless hours together, talking, playing mölkky and tennis, making barbecues in Hulgårds Have, but mostly being there for each others – with sometimes the help of danish beers (other origins were not discriminated). I am very happy to have lived fifty meters away from you during my PhD. All this time together contributed extensively in balancing hard work with many enjoyable hours. I am 100% sure we have many more of these ahead of us. Finally, thanks to all my friends in Denmark and France. Maxime, Guilhem, Claire, Guillaume, Marine, Valentin, Bertille and many others – I have sometimes wished being able to spend more time with you, but the week-ends in Paris or CPH, the Alps or Normandie, allowed to let the steam off and kept me close to you.

Contents

Acronyms

5B-Demo	5-beam Demonstrator
ABL	atmospheric boundary layer
AEP	annual energy production
agl	above ground level
AWTS	Atlantic Wind Test Site
BEM	Blade Element Momentum
BIPM	Bureau International des Poids et Measures (International Bureau of Weights and Measures)
CFD	Computational Fluid Dynamics
CNR	carrier-to-noise ratio
CS	coordinate system
CW	Continuous Wave
DAR	Detection And Ranging
DBS	Doppler Beam Swinging
DTU	Technical University of Denmark
DWL	Doppler Wind Lidar
ECN	Energy research Centre of the Netherlands
FFT	Fast Fourier Transform
GUM	*Guide to the expression of Uncertainty in Measurement*
HWS	Horizontal Wind Speed
IEA	*International Energy Agency*
IEC	*International Electrotechnical Commission*
iid.	independent and identically distributed
IR	infra-red
JCGM	*Joint Committee for Guides in Metrology*
LOS	Line-Of-Sight
LS	Least Squares
MB	Mean Bias
MC	Monte Carlo
MCM	Monte Carlo method

ME Mean Error
MFB Mean Fractional Bias
MFE Mean Fractional Error
MLE Maximum Likelihood Estimator
MSE Mean Squared Error
NKE Nørrekær Enge
NMSE Normalised Mean Squared Error
PCV power curve verification
PDF probability density function
QC Quality Control
REWS rotor equivalent wind speed
RMSE Root Mean Squared Error
RNG Random Number Generator
RSD remote sensing device
RWS Radial Wind Speed
SI International System of units
SSE Sum of Squared Error
TI turbulence intensity
UQ uncertainty quantification
VAD Vertical Azimuth Display
VIM *International Vocabulary of Metrology*
WFC Wind Field Characteristic
WFR Wind Field Reconstruction
ZDM ZephIR Dual Mode

List of Symbols

a_{ind}	axial induction factor
α	half-opening or cone angle
α_{exp}	shear exponent (power law)
C_T	thrust coefficient, constant loaded rotor
$r_{x,y}$	correlation coefficient between x and y, alternatively noted $r\,(x, y)$
$\delta\nu$	Doppler frequency shift
D_{rot}	rotor diameter
E_{kin}	kinetic energy in the wind
ε_y	error on the model output due to its uncertainty
ε_x	error on the model input due to its uncertainty
ε_g	error due to the model uncertainty
ε_a	error due to the model inadequacy
R_0	gas constant of dry air
R_w	gas constant of water vapour
H_{ref}	height above ground level of reference instrument
k	coverage factor
λ	wavelength
μ	mean value
θ_m	model parameters
N_s	number of samples
φ	tilt inclination angle
P_{10min}	10-minute mean net power output
$P_{n,i,j}$	normalised net power output for data point j in bin i
P_i	averaged of normalised net power output in bin i
P_n	normalised net power output
P_{kin}	kinetic power in the wind
P_w	water vapour pressure
B_{10min}	10-minute mean air pressure
$p\,(x)$	probability density function of x
$p\,(y\|x)$	probability density function of y given x

ψ	roll inclination angle
R^2	coefficient of determination
RH_{10min}	10-minute mean relative humidity
ρ_{10min}	10-minute mean air density
ρ_0	reference air density at sea level for the standard atmosphere
ρ_{air}	air density, alternatively simply noted ρ
R_{rot}	rotor radius
$c_{RH,i}$	sensitivity factor for relative humidity in bin i
$c_{B,i}$	sensitivity factor for air pressure in bin i
$c_{T,i}$	sensitivity factor for air temperature in bin i
$c_{V,i}$	sensitivity factor for wind speed in bin i
σ	standard deviation
T_{10min}	10-minute mean air temperature
θ	wind direction
θ_r	relative wind direction or yaw misalignment
θ_{los}	line-of-sight direction
$u_{c,x}$	combined uncertainty of variable x, alternatively noted $u_c(x)$
U_x	expanded uncertainty of variable x, alternatively noted $U(x)$
s_x	standard uncertainty (cat. A) of variable x, alternatively noted $s(x)$
u_x	standard uncertainty (cat. B) of variable x, alternatively noted $u(x)$
V_i	averaged of normalised wind speed in bin i
V_{10min}	10-minute mean wind speed
V_n	normalised wind speed
V_{eq}	energy equivalent wind speed
V_∞	free stream wind speed
V_{hor}	horizontal wind speed
V_H	hub height wind speed
V_{los}	line-of-sight velocity
V_{ref}	reference (line-of-sight) wind speed
u	longitudinal component of wind vector, alternatively noted V_x
v	transversal component of wind vector, alternatively noted V_y
w	vertical component of wind vector, alternatively noted V_z
ξ	non-dimensional distance from the turbine rotor

List of Figures

List of Tables

What do you desire? What makes you itch? What sort of a situation would you like?

[. . .]

Better to have a short life that is full of what you like doing than a long life spent in a miserable way. And after all, if you do really like what you're doing, it doesn't matter what it is. You can eventually turn it, you could eventually become a master of it.

ALAN WATTS

CHAPTER 1

Introduction

Energy supply is one of the top challenges of the 21^{st} century. The transition from the massive use of fossil fuels to sustainable sources is going forth. It is an absolute necessity in order to meet the objective of the Paris Climate Agreement to limit global warming to less than 2 °C compared to pre-industrial levels, which was sealed during the 2015 United Nations Climate Change Conference. Wind energy has played, plays and will play an essential role in the energy mix of our future societies.

Speeding-up the world-wide development of wind power requires large financial investments. Modern wind farm projects are reaching investment scales from a minimum of several millions of euros onshore, to hundreds of millions for a medium -sized farm, and a couple billions or more for the largest offshore projects. These financial investments rely on many parameters – among them are the political and legal environment, wind energy acceptance by the (local) communities, long-term forecasts on electricity prices, the infrastructure, the lifetime of the wind turbines, etc.

In order to ensure the financial viability of a wind farm project, a critical element is the amount of energy that the farm is expected to produce over its lifetime. Due to the stochastic nature of the wind, the industry employs a combination of meteorological models and wind measurements in order to estimate the wind resource at the site of interest. The wind resource alone is insufficient to predict the energy that will be produced. It must be combined with the power performance of the turbines, which answers the question of how much energy a turbine harnesses depending on how much energy is present in the wind, depending on the atmospheric conditions. Power performance testing requires accurate wind measurements.

For the past four decades, power performance testing procedures relied essentially on wind measurements taken by instruments mounted on a meteorological mast. With technological progress in anemometry techniques, new methods have emerged. Instruments allowing to measure the wind remotely – from dozens of meters to several kilometers away – have found their way into the wind energy market. Among these technologies are lidars. Turbine-mounted lidars are attractive instruments for the wind energy industry, in particular for the purpose of power performance testing. They allow to remotely measure the wind directly from

the turbine – for instance its nacelle –, obviating the need for expensive external infrastructures.

The use of nacelle-mounted lidars for power performance testing however does come with technological and scientific challenges, which are the focus of this thesis. The first challenge answered in this thesis is the development of calibration methodologies and the assessment of measurement uncertainty of nacelle-mounted wind lidars. The second challenge to be tackled is how to use the lidar's measurements to provide the best possible wind characteristics for turbine power performance assessment. The last challenge is the demonstration of the suitability of the developed nacelle lidar methods. This was achieved through full-scale measurement campaigns.

In this chapter, after having a short look at the History of anemometry, I introduce Doppler lidars as remote sensing wind measuring instruments, their use in the context of power performance assessment and their basic measurement principles. The research questions this thesis aims at answering and its outline are also detailed.

1.1 A brief History of anemometry

Wind energy science and engineering requires a deep understanding of meteorology. For this purpose, accurate wind observations are needed.

The air in motion, the wind, produces a wide variety of mechanical and physical effects. These effects offer an indirect means to determine the wind velocity (vector quantity). The term of anemometer – derived from the Greek *anemos*, meaning wind or air – describes an apparatus measuring the wind velocity or only its magnitude, the wind speed.

Wind observations have taken place for many centuries (Waldo, 1893; Abbe, 1888). The first anemometer was designed in 1450 by an Italian architect named Leon Battista Alberti. A flat plate was suspended perpendicular to the wind, causing it to swing proportionally to the forces exerted by the wind. Robert Hooke in 1664 described an apparatus using the same principle. In its modern form, the anemometer could orientate itself perpendicular to the wind similarly to wind vanes. Hooke claimed the anemometer could provide wind speed observations within 10 % of the true value. The first rotational anemometer was created by Robinson in 1846. The anemometer featured four cups. The rotation of the cup is induced by the differential pressure the air applies on the cups convex and concave surfaces. The distance the cups travel during a lapse of time is calculated by counting the number of revolutions, which is proportional to the wind speed. Cup anemometers are common instruments for meteorological observations, albeit most modern cup

anemometers have three cups. The 3-cup anemometer was first developed by John Patterson in 1926. The propeller anemometer also relates rotational motion to the wind speed, the main difference being a rotor mounted on a horizontal axis instead of a vertical one – using lift and not drag.

Anemometry can take advantage of non-mechanical effects. Tube anemometers, such as Lind's U-shaped device (1775) or Pitot tubes (1732), convert differential air pressure into speed through the means of a manometer. Heat transfer caused by forced convection is used by hot wires and hot films. Their discovery traces back to the 1900s. Sonic anemometers, developed in the 1950s (Schotland, 1955; Kaimal and Businger, 1963), derive temperature and wind speed along a path defined by a pair of transducers by measuring the time of flight of ultrasonic waves in two opposite directions.

All the aforementioned anemometry techniques are intrusive: the instruments can substantially disturb the flow at the location where they sense the wind. In contrast, Doppler anemometers have the advantage of remotely sensing the wind, i.e. from a distant location. These anemometers, as their name indicates, are based on the Doppler effect. They emit and receive waves of different nature – radio, sound and light respectively for Radars, Sodars and Lidars. The frequency of the emitted radiation is shifted by the presence of scattering particles or targets along the beam path, and employ Detection And Ranging (DAR) techniques. The earliest developments of Doppler wind radars, sodars and lidars were made between the 1950s and 1970s (Lhermitte, 1962; Lawrence et al., 1972; Kaimal and Haugen, 1977).

Technological advances in telecommunication over the past decades – mainly in fibre connected discrete components – have enabled the commercial development of a new generation of Doppler Wind Lidars (DWLs), more efficient, compact and affordable, making them practically usable for wind energy applications (Smith et al., 2006; Cariou et al., 2007). Application examples in wind energy are the measurement of wind profiles, resource and site assessment, measurement of the flow field in the vicinity of a wind turbine or even an entire wind farm, wind turbine control, etc.

1.2 Power performance testing

Turbine performance testing is part of the evaluation procedures of wind energy conversion systems. It aims at relating the electrical (power) and mechanical (loads) behaviour of a wind turbine to atmospheric conditions. Specifically, the power performance of a wind turbine shows how much energy is harnessed as a function of the kinetic energy available in the surrounding wind.

In the development phase of a wind farm, the power curve of a wind turbine is – in association with the assessment of the wind resource – crucial to determining the financial viability of a project. Consequently, the power curve is the object of contractual agreements (guarantee) between a turbine manufacturer and their customer. Turbine manufacturers commonly provide 'sales power curves' in their product brochures as preliminary information. However, the sales and guaranteed power curves are usually different as the manufacturer adapts the turbine and the configuration of its controller to site-specific conditions, terrain complexity, etc.

Additionally, over the lifetime of a wind turbine, verification of its power performance is fundamental to asset management and a critical input to operational assessments. Power curve verification (PCV) is for instance valuable to:

- monitor the blades aerodynamic efficiency. In situations such as icing conditions or erosion, the blade aerodynamics are strongly deteriorated and the power output at a given wind speed drops drastically (Sareen et al., 2014). The added-value of performing blade repairs can be evaluated by measuring the turbine power curve a priori and a posterio of the repairs;
- optimise the turbine controller configuration;
- test the efficiency gains obtained by mounting add-ons on blades such as leading-edge vortex generators or flaps.

In order to aid the development of the wind energy industry, expert group studies were conducted as early as in the 1980s to establish internationally agreed testing procedures to characterize wind turbines. Power performance procedures were first developed by national test stations (Christensen and Dragt, 1987) – such as Risø in Denmark, ECN in the Netherlands, AWTS in Canada, etc – and compiled in recommended practices by the *International Energy Agency* (IEA, 1990).

The *International Electrotechnical Commission* (IEC) publishes the standard for 'Power performance measurements of electricity producing wind turbines', describing how to measure the power curve of a wind turbine. The 1^{st} and 2^{nd} international standards (IEC 61400-12, 1998; IEC 61400-12-1, 2005) demanded the use of meteorological mast-mounted cup anemometers for wind speed measurements. The 3^{rd} standard (IEC 61400-12-1, 2017, edition 2) allows both the use of cup and sonic anemometers, and of ground-based remote sensing devices (RSD) as a complement to mast instrumentation, and vice versa. It however does not allow the use of nacelle-mounted lidars. Standard procedures dedicated to nacelle lidar systems must be developed in order for the next generation of power performance standards to accept them for measuring the wind.

1.3 Why using nacelle lidars in power curve verification?

The usefulness of wind lidars in PCV is twofold: cost-efficiency and representativity of wind measurements.

The continuous and rapid growth of wind turbines' size – from rotor diameters (D_{rot}) of approximately 30 m in 1990, 80 m in 2005, to 164 m (MHI Vestas) and 180 m (Adwen) for the world's largest machines – and the development of wind farms onshore in complex terrain and offshore have challenged the established methods for power performance assessment. Even some of the basic definitions are probably no longer adequate.

Christensen and Dragt (1987) defined the 'virtual' and 'driving' speed, and stated that:

> "The upstream velocity was really chosen as representative of the free-field velocity, that is the velocity in the rotor plane, if the windmill were removed. [...] The wind driving the windmill will then be some suitable average over the rotor area"

For multi-megawatt turbines, measuring the wind speed at one point, e.g. the hub height, is not sufficiently representative of the 'driving' speed and thus questionable. The effects of wind speed and direction variations – called shear and veer respectively – over the rotor swept area on power curves can no longer be neglected (Wagner et al., 2011). It is therefore necessary to have some knowledge of (or measure) the variation of wind speed and direction over the rotor disc.

Light detection and ranging (lidar) is a remote sensing technology addressing this challenge.

Ground-based lidars are used to measure wind profiles (Peña et al., 2009) by simultaneously or successively probing the wind at several heights. They offer a practical and accurate solution for measuring wind over the entire rotor disk, both for resource and power performance assessment.

Whilst ground-based lidars solved this problem onshore, their use is impractical and more costly offshore, and their measurements less reliable in complex terrain. The first generation of turbine-mounted lidars were placed on the nacelle. They had two beams and were performing horizontal wind speed measurements at multiple ranges. Albeit two-beam forward-looking nacelle lidars were unable to estimate the wind shear, they showed promising capabilities to assess power performance (Wagner et al., 2014) and obviate the erection of expensive meteorology masts, especially offshore.

Cutting-edge turbine-mounted lidar systems combine the benefits of both technologies. A wind profiling nacelle lidar probes the wind at multiple heights and distances upstream of a turbine – or downstream for wake measurements – from its nacelle. The commercially available technology comprises rotating-beam (scanning) and multi-beam lidar systems using both Continuous Wave (CW) and pulsed lidar architectures, see Fig. 1.1.

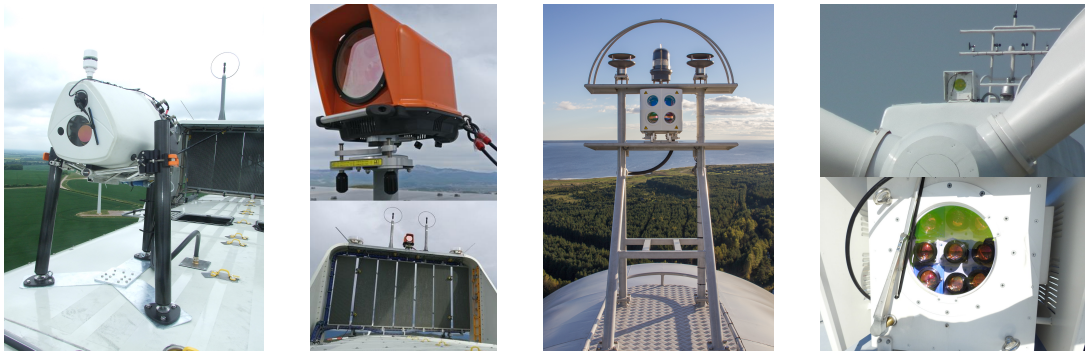

(a) ZephIR Dual Mode (scanning)

(b) Avent Wind Iris (4-beam)

(c) Wind Eye (4-beam)

(d) Diabrezza (9-beam)

Figure 1.1: Profiling nacelle lidars: examples of commercially developed systems. **Source**: **(a)** Chris Slinger, *Zephir Lidar*; **(b)** *Akuo Energy*; **(c)** Dominique Held, *Windar Photonics*; **(d)** *Mitsubishi Electric*, and Kawabata (2016).

1.4 Doppler wind lidar basics

Knowledge of the basic principles of a measuring instrument is key to performing adequate data processing and analysis. I here introduce the measurement chain of Doppler wind lidars.

Doppler anemometers do not measure directly wind characteristics (Hardesty and Weber, 1987). DWLs sense backscattered light from particles moving with the wind (see Fig. 1.2). The return light originates from scatterers contained in a so-called probe volume located along the laser beam propagation path. The contribution of each scatterer is weighted as a function of its distance to the point of focus or centre of the range-gate, respectively for CW and pulsed DWL systems (Angelou et al., 2012; Frehlich, 2013). Next, DWLs transform the time signal into a Doppler power spectrum via Fast Fourier Transforms (applied to a time period). Consequent to the DWL volume averaging property –, each scatterer having its own motion – the derived spectrum corresponds to a distribution or histogram of Doppler frequency shifts.

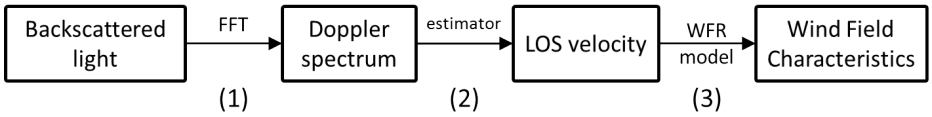

Figure 1.2: Schematic of Doppler wind lidar measurement principles.

In a second step, DWLs infer Line-Of-Sight (LOS) velocities (V_{los}) from Doppler spectra. Examples of commonly used estimators are centroid, median, or Maximum Likelihood (Angelou et al., 2010; Frehlich, 2013).

Wind field characteristics (WFC) – such as speed, direction, shear, etc – are finally estimated by combining multiple LOS velocity measurements obtained by probing the wind in several locations. Except in the cases of co-located synchronised measurements – such as the *WindScanner* (Vasiljevic et al., 2016) or multi-static systems (Magee et al., 1998; Harris et al., 2001) – assumptions about the nature of the wind flow must be made. Making adequate assumptions represent an important challenge due to the complexity of the measured flows and to the large-scales over which the wind is probed by the lidars, and because these assumptions affect the accuracy of the wind characteristics estimated from a DWL's LOS velocity measurements.

1.5 Research questions and outline of the thesis

The thesis' aim is to answer the following research questions:

"What are the uncertainties inherent to the measurements performed using a nacelle-mounted lidar?"
Indeed, traceable measurements are a mandatory requirement in the power and load evaluation of wind turbines. The traceability and uncertainty assessment of the measurements are provided by calibration procedures.

"How can nacelle-mounted lidars provide free-field wind characteristics for power curve measurement?"
A wind lidar only measures the wind velocity component projected on the line-of-sight, i.e. the laser beam propagation path. By combining the measurements along lines-of-sights pointing in different directions, useful information on the wind vector can be obtained. Dedicated methods to reconstruct free-field wind characteristics for power curve measurement have been developed.

The contents of each chapter are briefly described hereafter.

Chapter 1: "Introduction" provides the reader with background knowledge regarding anemometry techniques and power performance testing. The focus is on the use of nacelle lidars for power curve verification.

Chapter 2: "Calibrating Wind Lidars" shows how (turbine-mounted) Doppler wind lidars can be calibrated in a generic manner – via the so-called white-box methodology. The generic procedure was applied to two different commercially developed nacelle lidar systems. The calibration results come with a comprehensive uncertainty budget of the lidar LOS velocity measurements. Further, the question of repeatability of the procedure has been addressed via a verification of the obtained calibration results.

Chapter 3: "Estimating Wind Characteristics" describes the methods of model-fitting wind field reconstruction that were developed in this Ph.D. project and that allow to retrieve various parameters characterising the wind field. The methods are demonstrated using experimental turbine-mounted lidar data acquired during a 7-month full-scale measurement campaign. Two different wind models were presented in the peer-reviewed journal article included in this chapter.

The first one uses lidar measurements taken at a single distance and accounts for the wind shear in order to estimate hub height wind speed, direction and a shear parameter. The second technique consists in measuring at multiple distances close to the rotor and relating the near-rotor inflow to the free-field conditions via a correction of the induction effects. This multi-distance wind field reconstruction technique we developed is a major innovation and allows the estimation of free stream wind speed, direction, shear, and of the so-called induction factor.

Chapter 4: "Uncertainty Quantification Of Lidar-Estimated Wind Characteristics". Monte Carlo methods belong to a family of numerical techniques that can be used to propagate uncertainties through a model. I demonstrate in this chapter how such techniques were applied to the developed wind field reconstruction algorithms in order to assess the uncertainties of the estimated wind characteristics.

Chapter 5: "Application To Power Performance Testing". Two methods for power curve measurement using nacelle-mounted profiling lidars were investigated, based on the two wind field reconstruction models developed in Chapter 3. The procedures to assess power curve uncertainties and to derive the annual energy production are described in detail. The results that were obtained from the two lidar-based methods are compared to the ones obtained with a reference mast-mounted cup anemometer.

Chapter 6: "Conclusions and future work" summarizes and draws the main learnings of the thesis. Research ideas and recommendations for future work are also described.

CHAPTER 2
Calibrating Wind Lidars

This chapter answers the first research question of "What are the uncertainties inherent to nacelle-mounted lidar measurements?".

It consists first of an introduction to metrology – the science of measurements. We also define useful terminology as it is essential to ensure a common understanding of metrological concepts.

Second, a journal article entitled *'Generic methodology for field calibration of nacelle-based wind lidars'* (Borraccino et al., 2016) presents the so-called white box calibration procedure designed to be applicable to any turbine-mounted lidar system. The procedure is demonstrated through the calibration examples and results of two commercially developed nacelle lidars, including a comprehensive assessment of uncertainties. The generic calibration procedure ensures the traceability of the lidar measurements.

Further, the question of repeatability of the generic calibration procedure is investigated with the analysis of a second calibration campaign. Various aspects of the calibration methodology are finally discussed, such as the quality control of lidar raw data, alternative approaches and suggestions for improving the method.

2.1 Metrological concepts

The basic principles of modern metrology lie on the International System of units (SI) (BIPM, 2014). Historically, three base units were defined as a result of international conventions: the metre, kilogram and second respectively for the quantities of length, mass and time. The conventions were first established with the deposition of the platinum standard meter and kilogram after the French Revolution, in 1799; and later in 1875 with the signing of the *Convention du mètre*. Currently, seven base units exist in the SI, which are interdependent.

Moreover, the *Joint Committee for Guides in Metrology* (JCGM) is responsible for the preparation of two major metrological documents: the *International Vocabulary of Metrology* (VIM) (JCGM, 2012) and the *Guide to the expression of Uncertainty in Measurement* (GUM) (JCGM, 2008a). The GUM is internationally recognised as the reference for the evaluation of uncertainty. All the metrological terms employed in this thesis refer to the VIM definitions.

Precision, trueness and accuracy are terms used to qualitatively characterise a measuring instrument. They have a distinct meaning. A precise instrument shows a high level of repeatability, although the measurement value might be biased. Trueness is inversely related to measurement errors. Accuracy combines trueness and precision (see Fig. 2.1).

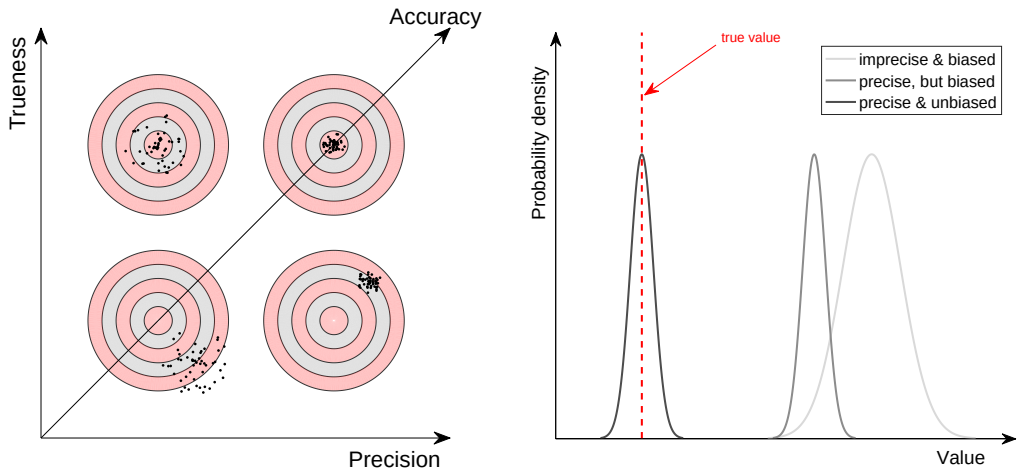

(a) Targets **(b)** Statistical distributions

Figure 2.1: Metrological concepts of precision, trueness and accuracy.

The concept of measurement uncertainty is at the heart of metrology. Measurement values are meaningless if specified without uncertainties. Fundamentally, the true value of a measurand is unknowable. The measurement value is only a best estimate of the measurand. It is consequently obligatory for a measurement result to be followed by a quantitative indication of its reliability.

Measurement uncertainty characterises the dispersion of values attributed to a measurand (random measurement error) under a given set of conditions. For example, a cup anemometer calibration certificate may state: the wind speed standard uncertainty is X m s^{-1} at standard atmospheric temperature and pressure, for a measured value of Y m s^{-1} and turbulence intensity less than Z %. Any systematic measurement error (bias) is not part of the uncertainty, as long as it can be predicted and estimated. If the sensitivity of an instrument to external conditions can be predicted, the measurement must be corrected. Known errors are not uncertainties.

The evaluation of measurement uncertainty can be of two antonymic types: type A uncertainties are evaluated by statistical techniques; type B uncertainties correspond to any other evaluation means, such as from a calibration certificate, classification, or a simple guess based on experience.

Assessing uncertainties and ensuring traceability of a measuring instrument can only be achieved via a calibration. Indeed, according to the VIM, metrological traceability is the

> "property of a measurement result whereby the result can be related to a reference through a documented unbroken chain of calibrations, each contributing to the measurement uncertainty."

A calibrated instrument thus yields measurement values traceable to a reference, which must itself be traceable to the international base quantities. In contrast, 'verification' or 'validation' procedures do not provide traceability. A verification is only a test that e.g. an instrument fulfils a given number of criteria. A validation is a type of verification specific to the intended use of the instrument.

In the case of nacelle lidars, it is strongly desirable for the calibration procedures to be applicable to any existing and upcoming system, i.e. to be generic. Generic procedures allow inter-comparison and the assessment of repeatability of the calibration process.

2.2 Generic methodology for field calibration of nacelle-based wind lidars

remote sensing

MDPI

Article

Generic Methodology for Field Calibration of Nacelle-Based Wind Lidars

Antoine Borraccino *,†, Michael Courtney † and Rozenn Wagner †

DTU Wind Energy, Technical University of Denmark, Kongens Lyngby 2800, Denmark; mike@dtu.dk (M.C.); rozn@dtu.dk (R.W.)

* Correspondence: borr@dtu.dk; Tel.: +45-9351-1124

† Current address: Risø Campus, Frederiksborgvej 399, Roskilde 4000, Denmark.

Academic Editors: Xiaofeng Li and Prasad S. Thenkabail

Received: 28 July 2016; Accepted: 25 October 2016; Published: 2 November 2016

Abstract: Nacelle-based Doppler wind lidars have shown promising capabilities to assess power performance, detect yaw misalignment or perform feed-forward control. The power curve application requires uncertainty assessment. Traceable measurements and uncertainties of nacelle-based wind lidars can be obtained through a methodology applicable to any type of existing and upcoming nacelle lidar technology. The generic methodology consists in calibrating all the inputs of the wind field reconstruction algorithms of a lidar. These inputs are the line-of-sight velocity and the beam position, provided by the geometry of the scanning trajectory and the lidar inclination. The line-of-sight velocity is calibrated in atmospheric conditions by comparing it to a reference quantity based on classic instrumentation such as cup anemometers and wind vanes. The generic methodology was tested on two commercially developed lidars, one continuous wave and one pulsed systems, and provides consistent calibration results: linear regressions show a difference of ∼0.5% between the lidar-measured and reference line-of-sight velocities. A comprehensive uncertainty procedure propagates the reference uncertainty to the lidar measurements. At a coverage factor of two, the estimated line-of-sight velocity uncertainty ranges from 3.2% at 3 $m \cdot s^{-1}$ to 1.9% at 16 $m \cdot s^{-1}$. Most of the line-of-sight velocity uncertainty originates from the reference: the cup anemometer uncertainty accounts for ∼90% of the total uncertainty. The propagation of uncertainties to lidar-reconstructed wind characteristics can use analytical methods in simple cases, which we demonstrate through the example of a two-beam system. The newly developed calibration methodology allows robust evaluation of a nacelle lidar's performance and uncertainties to be established. Calibrated nacelle lidars may consequently be further used for various wind turbine applications in confidence.

Keywords: lidar; calibration; uncertainties; nacelle-mounted; wind turbine; power performance

1. Introduction

1.1. Profiling Lidars for Power Performance

The rapid increase in wind turbines' size has created a need for developing new power performance assessment procedures. The effects of wind speed and direction variations—called shear and veer respectively—over the rotor swept area on power curves can no longer be neglected [1]. Measuring the wind at one point, e.g., hub height, has consequently become insufficient.

Light detection and ranging (lidar) is a remote sensing technology addressing this challenge. Its multiple applications have found their way into the wind energy market. Ground-based lidars are presently being used to measure wind profiles [2]. They offer a practical and accurate solution for measuring wind over the entire rotor disk. Even though two-beam nacelle-based lidars completing

horizontal wind speed measurements are unable to estimate the wind shear, they show promising capabilities to assess power performance [3] and obviate the erection of expensive meteorology masts, especially offshore.

A new generation of commercially developed profiling nacelle lidars combine the benefits of both technologies. A wind profiling nacelle lidar probes the wind at multiple heights and distances upstream of a turbine — or downstream for wake measurements — from its nacelle. The commercially available technology ranges from scanning to multi-beam lidar systems, e.g., the Zephir Dual-Mode (ZDM) and the 5-beam Avent Demonstrator (5B) lidars (Figure 1, see details on the measurement principles of both systems in [4,5]).

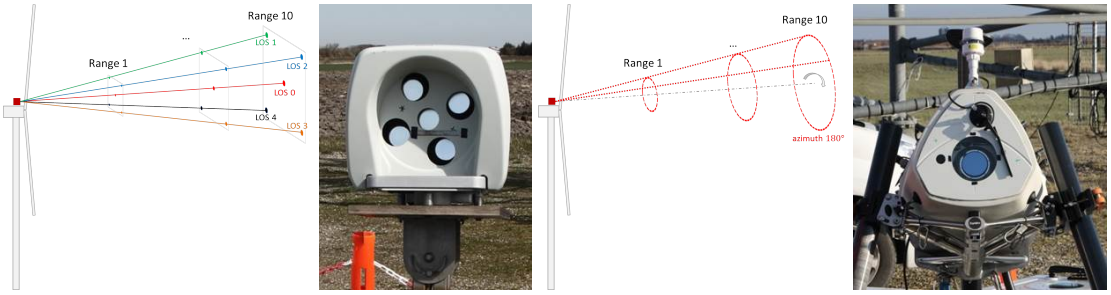

Figure 1. Two wind profiling nacelle lidar examples: 5-beam Avent Demonstrator (**left**) and Zephir Dual-Mode (**right**).

1.2. The Need for Calibration Procedures

Lidars are measuring instruments. As such, their measurements are uncertain and, formally, can only be traced back to international standards via a calibration. In essence, the main role of a calibration is to transfer the traceability of reference instruments and their uncertainties. Developing commercial applications of lidars demands uncertainty quantification, particularly power performance testing. Indeed, the power curve is the primary characteristic of a wind turbine guaranteeing its production. The fundamental reasons for developing calibration procedures is to ensure the measurements are valid and quantify their accuracy—i.e., trueness and precision—by assigning uncertainties to the measurand.

Doppler wind lidars (DWL) do not measure wind characteristics [6,7] directly. They probe the wind by emitting light through a laser beam and at a known wavelength λ. Atmospheric particles following the wind's motion scatter a fraction of the emitted light back to the lidar, at a frequency Doppler-shifted by $\delta\nu$. Scatterers contained in the lidar probe volume yield a histogram of $\delta\nu$ values. The power spectrum is estimated via spectral analysis—i.e., Fourier transforms—of the electrical signal generated by the photodetector. An algorithm, for instance peak, centroid or maximum likelihood, is applied to characterise the Doppler power spectrum and retrieve a single $\delta\nu$ value. $\delta\nu$ is then converted into a Line-Of-Sight (LOS) velocity V_{LOS}, also called radial wind speed (RWS):

$$V_{LOS} = \frac{\delta\nu \cdot \lambda}{2} \tag{1}$$

Wind characteristics are finally estimated by combining multiple V_{LOS} measurements according to an assumed flow model—e.g., horizontally homogeneous for ground-based lidars using Vertical Azimuth Display, see [8,9]. Depending on the employed flow model, profiling nacelle lidars can reconstruct wind speed (WS) and direction (WD), vertical shear, veer, etc.

From first principles (Equation (1)), the LOS velocity is sometimes assumed to be an 'absolute' measurement, in the sense it is derived from well-known physics theory and thus has a negligible uncertainty.

Remote Sens. **2016**, *8*, 907 3 of 24

Most modern Doppler wind lidars operate at a wavelength in the infra-red (IR) region, of ≈1560 nm. The laser wavelength is certified to be within ±1 nm corresponding to a V_{LOS} uncertainty <0.01 $m \cdot s^{-1}$. Yet, spectral broadening due to probe volume effects (aerosol gradients, presence of inhomogeneous wind structures, etc.) [7] and the chosen Doppler frequency shift estimation method create imperfections in lidar V_{LOS} measurements: the shape of Doppler spectra in atmospheric conditions is far from ideal Gaussian or Dirac distributions that are obtained under controlled conditions in a laboratory with a hard target (e.g., moving belt, rotating wheel) or in a wind tunnel. These two arguments contradict the assumption of lidar V_{LOS} being measured 'absolutely'. Unless all the uncertainties of components (optical, mechanical, software) upstream of the V_{LOS} estimation are thoroughly assessed by certified bodies, the only way to quantify the accuracy of V_{LOS} is to compare it to a calibrated reference. In practice, due to the length of the lidar probe, this is only possible through field measurements using for instance calibrated cup anemometers. Then, at the reconstructed wind characteristics level, the flow model inadequacy introduces errors due to e.g., terrain effects, thermal stability, etc. Note that eliminating flow model assumptions and measuring a 3D wind vector is however possible using collocated synchronised V_{LOS} measurements (WindScanner [10] or multi-static systems). For all those reasons, field calibration procedures of lidars are required, at a minimum for power performance applications.

Calibrated measurements are traceable to international standards when they relate to a reference quantity (itself traceable to the SI). The *International Vocabulary of Metrology*, VIM [11], provides definitions of terms in the field of measurements. According to the VIM, a calibration is an:

> *operation that, under specified conditions, in a first step, establishes a relation between the quantity values with measurement uncertainties provided by measurement standards and corresponding indications with associated measurement uncertainties and, in a second step, uses this information to establish a relation for obtaining a measurement result from an indication.*

Additionally, the *Guide to the expression of Uncertainty in Measurement*, GUM [12], suggests analytical methodologies for assessing uncertainties based on the law of propagation of uncertainties.

In this study we attempt to answer the following research questions:

1. Can (nacelle-based) wind lidars be calibrated via a generic procedure, independent of the lidar type or design?
2. How to assess lidar measurement uncertainties?

The use of profiling lidars in power performance and need for calibration procedures were first introduced. In Section 2, two plausible concepts for field calibration of nacelle lidars—so-called 'black' and 'white box' approaches—are discussed. The principles of the generic methodology are detailed in Section 3. Section 4 shortly introduces the calibration of the beam positioning quantities. Section 5 focuses on the calibration and uncertainty quantification of the main input of the lidar reconstruction algorithms: the line-of-sight velocity. Calibration results are illustrated with the examples of the 5-beam Avent Demonstrator and ZephIR Dual-Mode lidar units (Figure 1) that have been calibrated during campaigns in 2014–2015 at DTU's test site for large wind turbines, Høvsøre, Denmark. The propagation of inputs uncertainties to lidar-reconstructed wind characteristics is investigated in Section 6 via the simple case of a two-beam lidar system. Finally, we discuss several aspects of the generic methodology, in particular the prevailing uncertainty sources, the question of repeatability, its limitations and how it could be improved.

2. Two Plausible Calibration Concepts: The White- or the Black-Box

In this section, considering the different levels of measurands in a wind lidar, two different calibration concepts are identified where the lidar is regarded either as a 'black' or a 'white' box. We then argue why the white box methodology presents the highest degree of genericity and further detail its principles and steps.

2.1. Black Box

The 'black box' calibration is a direct comparison of the reconstructed wind characteristics with the corresponding reference quantity. Using this approach, the lidar is seen as a black box, a system where the knowledge of the transfer function between inputs and outputs is not relevant or not necessary (Figure 2).

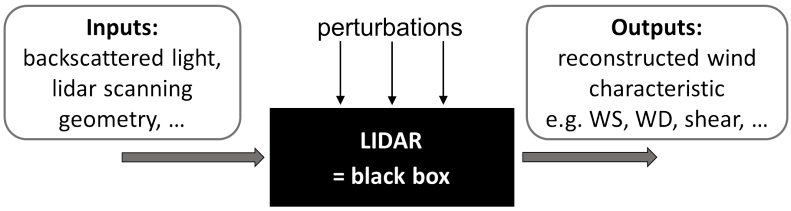

Figure 2. Black box lidar concept.

The wind speed calibration of ground-based lidars is an example of a black box calibration: lidar-estimated horizontal wind speeds (HWS) are compared to reference anemometers placed at multiple heights on a met. mast [13]. For profiling nacelle lidars, the measurement setup of a black box calibration would require:

- **for horizontal wind speed and wind direction:**
  - lidar placed on a platform high enough to allow the beam(s) to not be blocked by the ground in order for the reconstruction algorithm to be available. High stiffness of the tower is required to avoid significant deflections causing the lidar beams to constantly move and sense winds in locations unacceptably far from the reference instruments. This is the reason why we do not recommend calibrating lidars mounted on the nacelle of on an operating wind turbine. The beam perturbations would depend on both the turbine and the actual wind distribution during the testing period. Consequently the repeatability of the calibration would be seriously impaired and the uncertainties increased. For modern wind turbines, the rotor diameter D_{rot} is ∼100 m. Power performance standards (IEC 61400-12-1, [14]) require to measure the free wind at an upstream distance of $2.5D_{rot}$. With a cone or half-opening angle of $\alpha = 15°$, the height of the platform should therefore be $>2.5D_{rot} \tan\alpha \approx 67$ m. In addition, a minimum height should be considered to account for the lidar probe volume and avoid sensing highly inhomogeneous and turbulent winds too close to the ground;
  - a mast with reference instruments (e.g., cup or sonic anemometers, wind vanes) mounted at the location where the lidar-reconstructed wind characteristics are estimated. For a two-beam lidar system, such a location may be at the point directly in between the two beam positions, or formally anywhere between the two beams (see Section 6.2);
  - accurate detection of the lidar beam or centreline, in order to position the reference instruments appropriately. This may be extremely difficult to achieve, particularly if no beam is physically present at the centre of the scanning pattern.
- **for vertical wind shear and veer**: reference wind speed and direction instruments located at several heights ranging between the minimum and maximum measurement heights of the lidar, e.g., from 10 m to 150 m.

In practice, the described example setup makes the black box calibration an unrealistic approach for nacelle-based lidars. Such a setup would be extremely expensive, hard to find or develop, and lidar-specific.

Remote Sens. **2016**, *8*, 907 5 of 24

2.2. White Box

An alternative methodology to the black box consists in calibrating the reconstruction algorithms' inputs. This method will be further referred to as 'white box' calibration. These inputs are V_{LOS} along the different LOS and beam localisation quantities [15]. The white box calibration requires knowledge of the reconstruction algorithms and being able to:

- calibrate the LOS positioning: e.g., by calibrating the lidar's internal inclinometers (if any), by verifying the geometry of the trajectory (opening angle between each LOS and the optical centreline), by verifying the measurement range;
- calibrate the lidar-measured V_{LOS};
- propagate inputs' uncertainties to the lidar-reconstructed wind characteristics.

2.3. Which Concept to Choose?

The black box calibration concept has the advantages of being fast and relatively easy to implement. Its results include the uncertainties related to the adequacy of the wind model used by the reconstruction algorithm. However, the method has also weaknesses:

1. multiple calibrated reference instruments (with certificates) are necessary to calibrate each of the reconstructed wind characteristics—e.g., cup anemometer for wind speed, vane for wind direction;
2. the assumptions formulated in the reconstruction algorithms may not be completely justified and strongly related to the characteristics of the calibration site—e.g., flow homogeneity in complex terrain;
3. the calibration procedure and setup is specific to the scanning trajectory of the lidar system and to each wind characteristic to calibrate (speed, direction, shear, etc.).

The main advantages of the white box are the calibration of physically existing measurands—as opposed to model estimated wind characteristics—and a lower sensitivity to wind field reconstruction assumptions. The uncertainty evaluation of any reconstructed wind characteristics is theoretically permitted by the white box approach, for example propagating uncertainties with the GUM or Monte-Carlo methods [16].

On the negative side, the calibration duration is longer for multi-beam lidars as formally the V_{LOS} along each LOS—i.e., each optical path—should be calibrated. For a scanning lidar system, only one optical path exists and thus only one LOS calibration is required. Combining the calibration of a single beam with an uncertainty assessment due to deviations between beams may also be considered to reduce the calibration duration. Furthermore, to implement calibration procedures for commercial lidar systems, the reconstruction algorithms will need to be provided (as a minimum, to the calibration laboratory). The veracity of the reconstructed wind characteristics must also be addressed. In other words, the underlying physics behind the reconstruction algorithm must be verified once for each parameter and type of lidar.

Irrespective of the technology and design choices—e.g., continuous wave (CW) vs. pulsed systems; single-beam scanning vs. multi-beam step staring; homodyne vs. heterodyne—Doppler wind lidars all have in common that they measure LOS velocities. Thus, **the path towards a generic calibration procedure of nacelle lidars leads to the white box approach**, which we demonstrate hereafter.

3. White Box Calibration: A Generic Methodology

The white box calibration can essentially be divided into seven steps, as represented in Figure 3.

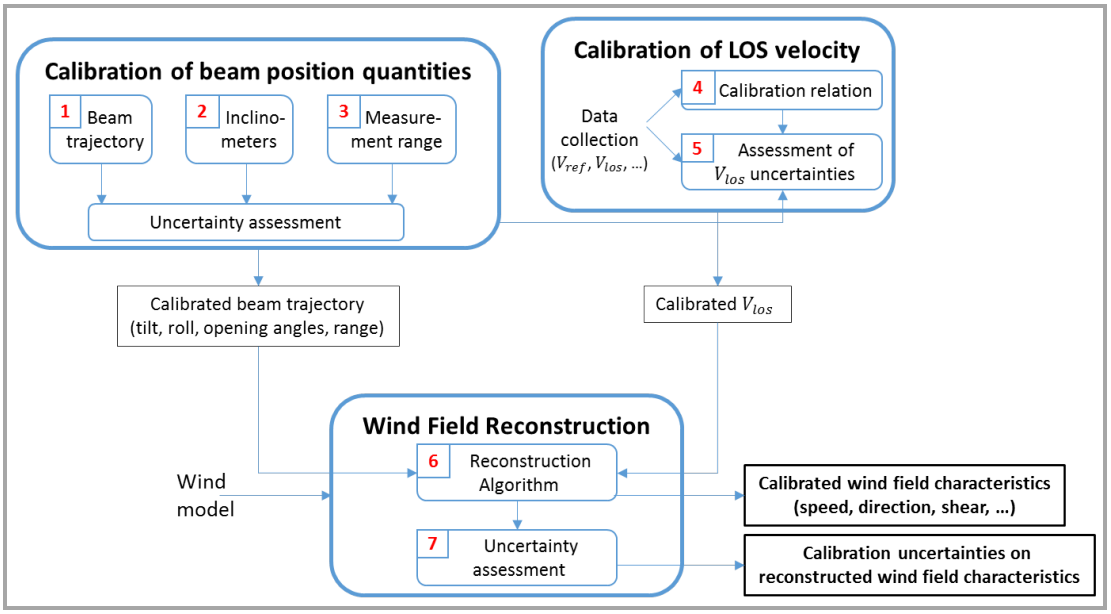

Figure 3. Schematic of the white box calibration concept for wind lidars.

Knowing accurately where the wind is probed is crucial for the estimation of wind characteristics. Hence, the first three steps relate to the beam's position (see Section 4). Step (1) verifies the geometry of the beam(s)' trajectory. The values of the cone or opening angles are measured and compared to the manufacturer's specification. Step (2) is the inclinometers calibration, needed to correct for the lidar-indicated tilt φ_{ind} and roll ψ_{ind} angles, that are involved in the vertical projection of the reference HWS (Equation (2)). The inclinometers calibration allows uncertainty estimations on φ_{ind} and ψ_{ind}. Steps (1) and (2) should be performed prior to the V_{LOS} measurements as they provide information necessary to the range configuration and data analysis. In step (3) the sensing range—obtained either by ranging or variable focus—is verified. As nacelle lidars measure in a flow having vertical and/or longitudinal gradients, a range error will cause biases.

Steps (4) and (5) are the LOS velocity field measurements and uncertainty assessment, where data from the lidar and reference instrument(s) are collected, the calibration relation obtained, and uncertainties propagated to the lidar-measured V_{LOS} (see Section 5). They constitute the most central part of the white box calibration and can generically be applied to any Doppler wind lidar system.

In steps (6) and (7), wind characteristics are estimated according to the reconstruction algorithms and uncertainties on their outputs assessed (see Section 6). For simple wind models assuming horizontal flow homogeneity, wind characteristics may be derived from an analytical expression, in which case the GUM methodology can be applied (see Section 6.2.2).

Essentially, the genericity of the white box approach lies in the V_{LOS} calibration. Indeed, the procedures to complete steps (1)–(3) are specific to the lidar technology (CW, pulsed, scanning or step-staring, etc.). Steps (6) and (7) depends on the reconstruction algorithm, although the framework for uncertainty assessment may be similar.

4. Calibration/Verification of LOS Positioning Input Quantities

By definition (see [11]), a verification simply consists in checking that a quantity lies within a range close to the expected value, while a calibration additionally corrects the quantity value with the calibration relation and assign uncertainties.

The calibration and/or verification of the beam position input quantities may be performed during field testing or in-house—in which case the lidar manufacturer procedures must be audited

Remote Sens. **2016**, *8*, 907 7 of 24

independently. A non-exhaustive list of methodologies to locate the beam includes hard target methods, IR-imaging or the use of IR-sensitive paper.

For the calibration of the 5B and ZDM lidars, the calibration of the inclinometers and verification of the opening or cone angles (steps (1) and (2)) were performed during field testing (Figure 4). As their technology differs, the hard target methods we employed for detecting the beam position were adapted: fixed targets for 5B, moving ones for ZDM. The 3D coordinates of the beam(s)' position were measured with a total station. By placing the lidar in several tilt and roll positions, the inclinometers' readings were compared to the physical tilting and rolling of the beam(s) and a calibration relation was obtained. For 5B, the opening angles can be derived simultaneously to the inclinometers calibration. For ZDM, the geometry parameters are the azimuth position in the scan and the cone angle. The cone angle was derived by fitting the detected beam positions to a circle. To account for potential deviations of the beam trajectory from a circle, an additional uncertainty on the cone angle value may be considered. However, no significant eccentricity was detected during the testing conducted on ZDM. Formally, the accuracy of the azimuth position should also be checked, although we do not expect this to impact significantly the total uncertainties. The detailed procedures and geometrical developments are exemplified in [4,5].

The verification of the sensing range (step (3)) was performed using statistical analysis of the LOS velocity calibration data for 5B, and visual observations of the backscatter levels for ZDM.

Figure 4. Field testing of the 5B (**left**) and ZDM (**right**): inclinometers calibration and beam trajectory verification.

5. LOS Velocity Calibration and Uncertainties

This section provides the methods employed to determine the calibration relation between the lidar-measured V_{LOS} and the reference speed V_{ref} and assess measurement uncertainties. The methods are illustrated through their application to a 5B and a ZDM lidar unit.

For the 5B, the results are presented for LOS0, i.e., the central beam. For ZDM, a 2° wide azimuth sector located at the bottom of the scanning trajectory (centered on an azimuth position of 180°) provides the V_{LOS} measurements to be calibrated. Complete and unit-specific calibration results are reported in [4] for 5B and in [5] for ZDM.

5.1. Reference Quantity

The LOS velocity is calibrated by comparing it to a reference measurand V_{ref} located at the point of focus for a CW lidar and at the centre of the range gate for a pulsed one. V_{ref} is the projection of the wind velocity onto the LOS direction θ_{los}. V_{ref} requires calibrated instruments. A cup and a sonic anemometer—respectively for wind speed and direction—were used to derive V_{ref} as follows:

$$V_{ref} = V_{hor} \cdot \cos\varphi \cdot \cos \underbrace{(\theta - \theta_{los})}_{=\theta_r} \tag{2}$$

where V_{hor} is the HWS, φ is the physical tilt inclination of the lidar beam, θ_r is the relative wind direction, i.e., the difference between the wind and the LOS directions respectively denoted θ and θ_{los}. The definition of V_{ref} is based on time-average measurements of V_{hor}, θ and φ—in this study 10-min periods and vector averages were used. Wind speed and direction variations within the averaging period were therefore assumed to have a negligible impact on instantaneous values of V_{ref}. Equation (2) implicitly neglects the contribution of the vertical component w of the wind vector to the LOS velocity. This approximation is acceptable since for tilt angles $\varphi < 2°$ this contribution is $\sim 3\% \cdot w$ and in flat terrain $w \ll V_{hor}$.

Note that the cup anemometer was preferred for reference wind speed measurements due to the lack of formal uncertainty assessment procedure of sonic-measured wind speed in the current IEC-standards [14].

5.2. Measurement Setup

The measurement setup of a wind lidar field calibration must replicate as closely as possible the conditions in which the lidar measures. Current power performance standards [14] consider 10-min averages of measurements in the 'free stream', typically at 2.5 rotor diameters upstream the turbine. For nacelle lidars, the calibration measurement range should therefore be of the same order, i.e., ∼250 m for modern wind turbines.

Depending on the height of the reference instrument(s), maintaining the beam close to the horizontal may demand installing the lidar on a stiff platform at a similar height. With a relatively small mast, the lidar can be positioned on the ground and its beam tilted up. The tilt angle φ should however be limited to avoid measurement errors due to flow inhomogeneities within the inclined probe volume and caused by vertical shear and veer as well as an eventual sensing range error.

The measurement range D_{conf} is defined as the distance between the lidar and the plane orthogonal to the optical centreline (i.e., the symmetry axis of the lidar trajectory, if it exists). D_{conf} must be configured so that:

$$D_{conf} = D \cdot \cos \alpha \tag{3}$$

where D is the total distance (not the horizontal one) between the lidar and the reference instrument(s), and α the opening angle between the centreline and the LOS to calibrate. D must be accurately measured, for instance using a range-finding theodolite (also called 'total station') or high-resolution GPS.

In the examples of the 5B and ZDM, the calibration was conducted at DTU Wind Energy's test site for large wind turbines, Høvsøre, Denmark. The main site characteristics of Høvsøre are the terrain flatness and a climate featuring high occurrence of strong western winds [17].

V_{ref} was obtained using a cup (type *Thies First Class Advanced*) and a sonic (type *Gill R3*) anemometer—providing calibrated measurements of V_{hor} and θ respectively. They were top-mounted at $H_{ref} = 8.9$ m agl. (above ground level) on two masts separated by 5 m.

The two nacelle lidars were placed on the ground – on its legs for ZDM, on a special structure for 5B. The distance from the masts was ∼260 m. As a result, the physical tilt inclination of the beam from the horizontal was $\varphi \approx 1.6°$—which is different from the reading of the lidar inclinometers. The effective probe lengths at 'half-width half-max' were estimated to 25 m for 5B (constant with the range) and 45 m for ZDM (increase proportionally to the square of the range).

Figure 5 shows the measurement setup in Høvsøre. The beam position was detected using hard target methods and adjusted until its height agl. was the same as the reference instruments. We estimated the standard uncertainty on the beam height to be 10 cm. The lidar beam was positioned close to the reference instrument (Figure 6), with a horizontal separation of ∼1–2 m.

Remote Sens. **2016**, *8*, 907 9 of 24

Figure 5. Calibration measurement setup at DTU Wind Energy's test site, Høvsøre, Denmark. **Left**: Google Earth image; **Right**: the ZDM and 5B lidars.

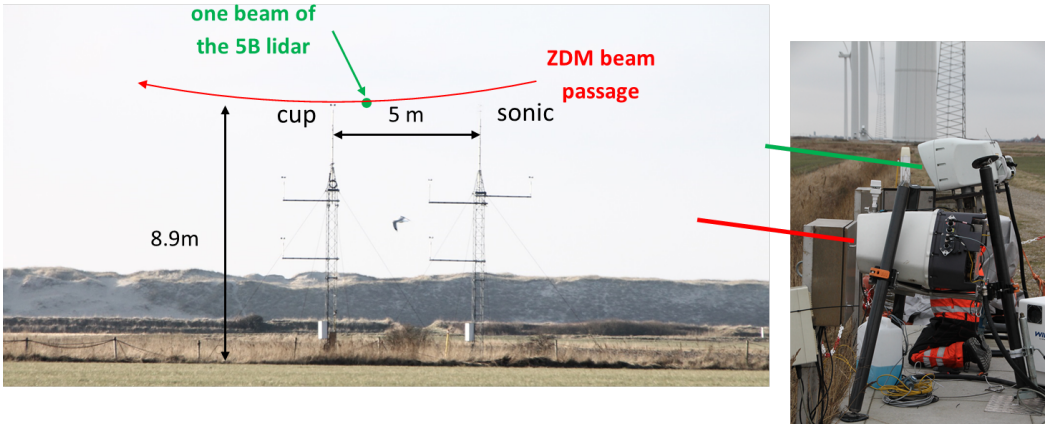

Figure 6. Schematic of the beam positions of the 5B (**green**) and ZDM (**red**) lidars at DTU Wind Energy test site, Høvsøre.

5.3. Data Filtering

For the tested 5B and ZDM lidar units, valid 10-min periods were obtained by filtering datasets as follows:

- **Mast**:
  - Cup wind speed $\in [4, 16]$ m·s^{-1}: corresponding to the range of wind speeds for which the cup anemometer is calibrated, in a wind tunnel;
  - Inflow angle (measured by sonic) $\in [-2°, +2°]$: to limit the contamination of V_{LOS} by the vertical wind speed;
  - wind direction θ measured by sonic anemometer $\in \theta_{los} \pm 40°$: except for the 1st step of the LOS direction evaluation process (see Section 5.4), the direction sector is restricted due to the asymmetric geometry of the employed sonic anemometer that can cause flow distortion. Additionally, this corresponds well to normal operational conditions of nacelle lidars since the wind direction relative to the turbine's yaw position is usually $<< 40°$;
- **5B lidar**: carrier-to-noise ratio >-18 dB and LOS availability $>95\%$. LOS availability is the ratio between successful and total attempts to measure V_{LOS}. These two filters ensure the quality and quantity of data measured by the lidar for each 10-min period;
- **ZDM lidar**: LOS availability $\gtrsim 75\%$. The LOS availability is obtained simultaneously to the averaging of high resolution ($\sim$50 Hz) V_{LOS} measurements contained in a specified azimuth sector, that we chose to be $[179°, 181°]$ (i.e., the bottom of the ZDM scanning trajectory). Details on

the employed averaging process can be found in [5]. Note that the lidar was stable enough to ensure the beam was not hitting the cup anemometer.

The filters are only given as an example of those that can reasonably be applied for the LOS velocity calibration. If different lidar systems, units and measurement setups are employed they should be adapted.

5.4. LOS Direction Evaluation

A two-step statistical analysis of the calibration data allows evaluation of the LOS direction θ_{los}. The advantage of the described method is that θ_{los} values are obtained in the frame of the reference sensor used for wind direction measurement.

5.4.1. Fitting the Lidar Response to Wind Direction

θ_{los} is first approximated by fitting the normalised lidar LOS velocity $V_{LOS,norm}$ to a function of the wind direction θ. In this analysis, all wind directions sectors are valid except for site related specifications (e.g., tower shadowing, presence of obstacles, wakes from neighbouring turbines, etc.). The normalised LOS velocity is:

$$V_{LOS,norm} = \frac{V_{LOS}}{V_{hor} \cos \varphi} \tag{4}$$

The fitting function f_{fit} is:

- a cosine wave for a heterodyne lidar (such as 5B): $f_{fit_1} = A_1 \cdot \cos(\theta - \theta_0) + B_1$;
- a rectified cosine wave for a homodyne lidar (such as ZDM): $f_{fit_2} = A_2 \cdot |\cos(\theta - \theta_0)| + B_2$. Homodyne lidars measure only the magnitude of the Doppler shift – not its sign – which translates into positive LOS velocities for any wind direction θ. In such a case, a rectified cosine must be used. The ambiguity in the fitting due to the two distinct solutions for θ_0 is resolved by choosing the value corresponding to the expected bearing of the LOS, e.g., using GPS coordinates;

The least squares fitting yields gain and offset values ideally equal to 1 and 0 respectively. θ_0 is an approximate estimation of θ_{los}.

Figure 7 shows the fitting results. The gain and offset values are: 0.99 and 0.01° for 5B; 0.97 and 0.03° for ZDM. The coefficients of determination are both >0.98 thus demonstrating the validity of the method. θ_0 values are 286.28° and 288.18° for the 5B and ZDM lidars respectively.

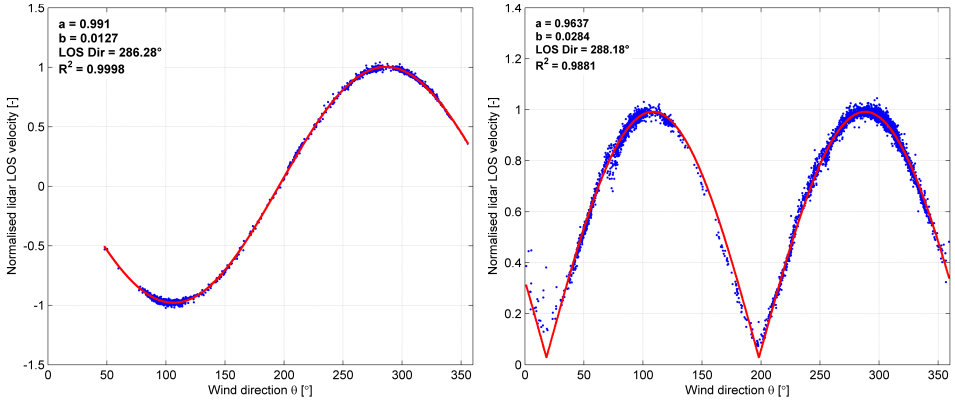

Figure 7. Lidar response to the wind direction. **Left**: 5B, cosine fitting; **Right**: ZDM, rectified cosine fitting.

Remote Sens. **2016**, *8*, 907 11 of 24

5.4.2. Refining the Estimated LOS Direction Using Residuals

A statistical process is further used to refine the estimation of θ_{los}: linear regressions are performed between lidar-measured V_{LOS} and the reference speed V_{hor} projected using angles θ_{proj}—e.g., ∼20 values centered around θ_0 with an increment of 0.1°. Each linear regression yields one Residual Sum of Squares (RSS) value which is then plotted against θ_{proj}. A 2nd order polynomial is fitted to the curve (Figure 8). θ_{los} is taken at the minimum of the parabola. The last step assumes that a minimum of residuals ($\sum \left(V_{LOS} - V_{ref}\right)^2$) is obtained when V_{hor} is projected onto the correct LOS direction. Figure 8 displays the RSS process results.

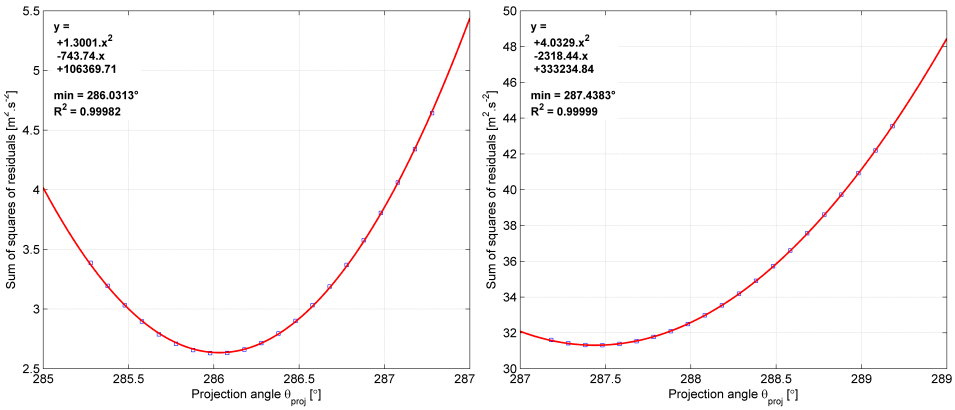

Figure 8. LOS direction evaluation using the RSS process. **Left**: 5B; **Right**: ZDM.

The final estimations of the LOS direction are: $\theta_{los,5B} = 286.03°$ and $\theta_{los,ZDM} = 287.44°$. We typically observed a difference of ∼0.3°–0.7° between the LOS direction θ_{los} provided by the RSS analysis and θ_0 values provided by the cosine fitting. Two plausible explanations affecting the cosine fitting are: lower quality of lidar V_{LOS} measurements for wind directions orthogonal to the LOS; asymmetry of the sonic anemometer's geometry causing biases in measurements outside the preferred direction sector.

The sonic anemometer is aligned to the absolute North, with a mounting uncertainty of ≈2°. Using GPS coordinates, θ_{los} was estimated to ≈285° and ≈286° for 5B and ZDM respectively, which is compatible with the results of the LOS direction evaluation.

5.5. Calibration Relation

The calibration relation is a linear least squares regression performed on the binned V_{LOS} data. A linear regression is first performed on the valid 10-min data in order to visually identify and investigate outliers, if any. The valid data is then binned based on V_{LOS}. The method of bins disregards the quantity of data in each specific bin, and thus allows the fairest comparison between the lidar-measured V_{LOS} and reference speed V_{ref}. A bin width of 0.5 m·s^{-1} was used, similarly to standard power performance testing. A V_{LOS} bin was considered valid if it contains a minimum of three data points. Completion criteria of the data collection may typically be that all V_{LOS} bins between 4 and 12 m·s^{-1} are valid. Indeed, the measurements are performed in uncontrolled conditions. It can thus be time-consuming to fill in the high wind speed bins.

If the tested lidar performs well, the intercept and slope of the unforced regression are expected to be close to 0 and 1 respectively. **The calibration relation we selected is the linear regression forced to a 0 intercept**. However, both types of linear regression results are valid options for the calibration relation.

Figure 9 shows the calibration relation results and the regression coefficients of the forced linear regressions. Each LOS of 5B has successively been calibrated. For ZDM, we calibrated V_{LOS}

measurements contained in a 2°-wide azimuth sector at the bottom of the beam trajectory. A summary of results is provided in Table 1 (see Section 5.7).

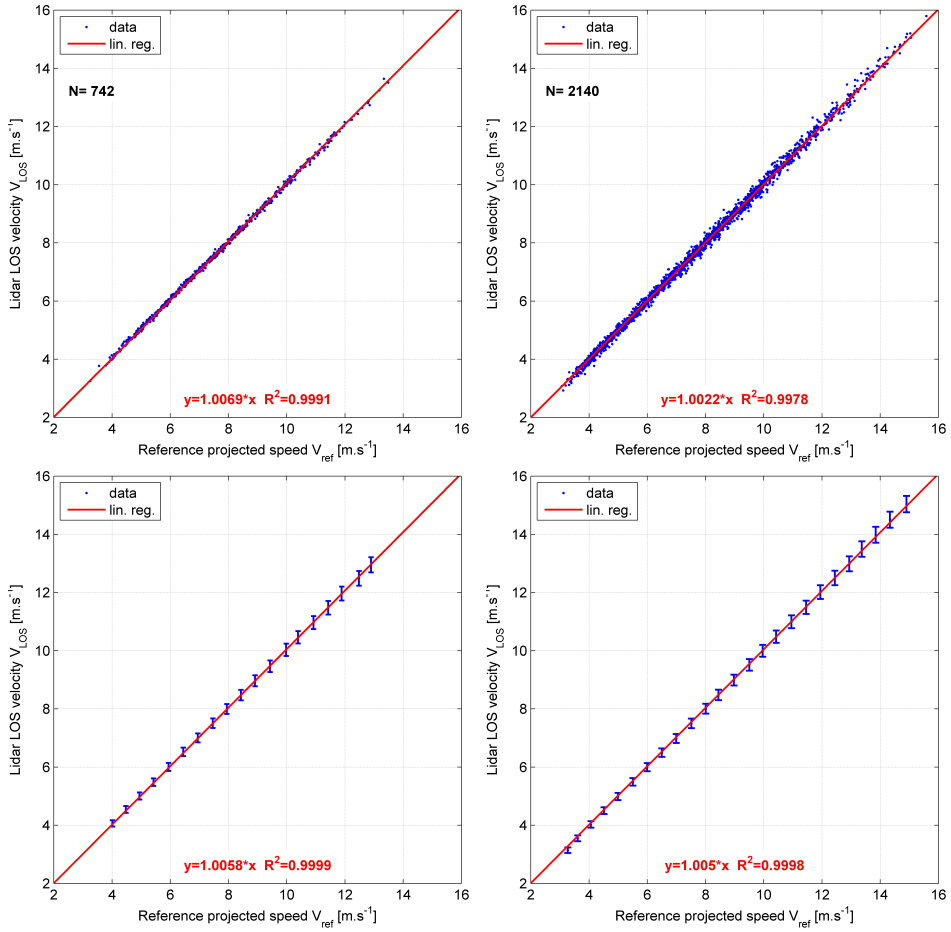

Figure 9. Calibration relation results. **Left column**: 5B; **Right column**: ZDM; **Top row**: 10-min data; **Bottom row**: binned data, including expanded uncertainties in error bars.

The basic filtering applied seems appropriate: no clear outlier is present in the scatter plots of 10-min data. Note that an analysis of the filters significance is provided in the detailed calibration reports of 5B and ZDM (see [4,5]). For both lidars, excellent agreement is obtained between binned V_{LOS} and V_{ref} with consistent gain values showing a difference between 0.5% and 0.9% with the reference (see Table 1). The observed scatter is low: R^2 coefficients are $>$0.9998.

As the LOS velocity calibration is the most important step of the white box concept, the high quality of the results demonstrate the feasibility of the generic methodology to calibrate profiling nacelle lidars.

5.6. Measurement Uncertainties Assessment Procedure

5.6.1. Definition of uncertainty and the GUM methodology

The VIM [11] defines uncertainty as a:

> *non-negative parameter characterizing the dispersion of the quantity values being attributed to a measurand, based on the information used.*

Remote Sens. **2016**, *8*, 907 13 of 24

In essence, the measured quantity value is only an approximation of the unknowable true value, i.e., only a best estimate. The uncertainty of a measured quantity value defines the interval centered on the best estimate and within which the true value lies with a certain probability.

In this paper, V_{LOS} uncertainties are assessed using the GUM methodology [12]. The main steps are summarised hereafter:

1. define the measurement model: $y = f(x_1, \ldots, x_n)$ where y is the best estimate and $x_1, \ldots, x_n$ are the input quantities;
2. list the input quantities and determine their uncertainties $u_{x_1}, \ldots, u_{x_n}$;
3. evaluate covariances between the uncertainties of the input quantities;
4. calculate the measured value y;
5. combine the uncertainties on the input quantities using the law of propagation of uncertainties to obtain $u_{c,y}$;
6. derive and report the expanded uncertainty $U_y = k \cdot u_{c,y}$ where k is the coverage factor (see definition 2.38 in [11]).

Note: the notations employed here for uncertainties of an arbitrary quantity x are: u_x standard uncertainty (i.e., coverage factor $k = 1$); $u_{c,x}$ combined uncertainty; U_x expanded uncertainty.

The GUM methodology relies on the law of propagation of uncertainties (see Section 5.2.2 in [12]) given by :

$$u_{c,y} = \sqrt{\sum_{i=1}^{N} \sum_{j=1}^{N} \frac{\partial f}{\partial x_i} \frac{\partial f}{\partial x_j} u_{x_i} u_{x_j} r_{ij}} \tag{5}$$

where x_i and y are respectively the input quantities and output of the measurement model f, r_{ij} is the correlation coefficient between the uncertainty distributions of x_i and x_j with $i, j \in [1, N]$. Equation (5) is the most general form of the law of propagation of uncertainties. For uncorrelated input quantities, in other words independent variables (see Section 5.1.2 in [12]), $r_{ij} = 0$ when $i \neq j$ and Equation (5) is simplified to:

$$u_{c,y} = \sqrt{\sum_{i=1}^{N} \left(\frac{\partial f}{\partial x_i} \right)^2 u_{x_i}^2} \tag{6}$$

5.6.2. Applying the GUM to the Calibration of $\boldsymbol{V_{LOS}}$

The GUM is applied to the calibration relation between the lidar-measured V_{LOS} and V_{ref}. The measurement model defining the estimated measurand is:

$$y = a \cdot V_{ref} \tag{7}$$

where a is the gain of the forced linear regression on the binned calibration data. Using the law of propagation of uncertainties for uncorrelated input quantities (Equation (6)), we obtain:

$$u_{c,y} = \sqrt{a^2 u_{c,V_{ref}}^2 + V_{ref}^2 u_a^2} \tag{8}$$

The uncertainty u_a is taken as the half-width of the 68% confidence interval (CI) on a (equivalent to a coverage factor $k = 1$ for normally distributed uncertainties). The method to estimate u_a is based on QR-decomposition and T-tests. The order of magnitude of u_a is $10^{-3}[-]$. For LOS 0 of 5B, $u_{a,5B,los_0} = 7.1 \times 10^{-4}$. For ZDM, $u_{a,ZDM} = 1.1 \times 10^{-3}$. Considering this measurement model,

once measuring stand-alone, the best estimate of the lidar-measured V_{LOS} is defined by the reciprocal of the calibration relation:

$$V_{LOS,be} = \frac{V_{LOS}}{a} \tag{9}$$

and its corresponding calibration uncertainty is $u_{c,y}$.

5.6.3. Combined Uncertainty on V_{ref}

In this study, classic anemometry is used to provide V_{ref} (Equation (2)). $u_{c,V_{ref}}$ is derived by combining uncertainties from the reference instruments with the calibration process uncertainties. For the sake of simplicity, and as φ, V_{hor}, θ and θ_{los} are measurements taken by independent systems, their uncertainties can reasonably be assumed uncorrelated. The law of propagation of uncertainties gives:

$$u_{c,V_{ref}} = \sqrt{\left(\frac{\partial V_{ref}}{\partial V_{hor}} \cdot u_{c,V_{hor}}\right)^2 + \left(\frac{\partial V_{ref}}{\partial \varphi} \cdot u_{\varphi}\right)^2 + \left(\frac{\partial V_{ref}}{\partial \theta_r} \cdot u_{c,\theta_r}\right)^2} \tag{10}$$

where $\theta_r = \theta - \theta_{los}$ is the relative wind direction. Based on Equation (2), the partial derivatives are computed for each valid 10-min period:

$$\begin{cases} \frac{\partial V_{ref}}{\partial V_{hor}} = \cos\varphi \cos\theta_r \\ \frac{\partial V_{ref}}{\partial \varphi} = -V_{hor} \sin\varphi \cos\theta_r \\ \frac{\partial V_{ref}}{\partial \theta_r} = -V_{hor} \sin\theta_r \cos\varphi \end{cases} \tag{11}$$

At this stage of the uncertainty assessment procedure, only the values of $u_{c,V_{hor}}$, u_{φ} and u_{c,θ_r} are missing. The uncertainty budget (Section 5.6.4) provides their estimation. Note that angle uncertainties must be expressed in radians when computing the combined uncertainty.

5.6.4. Uncertainty Sources and Budget

The uncertainty evaluation of the cup-measured reference speed V_{hor} follows the IEC-61400-12-1 standard (Annex E in [14]). It should be mentioned that most of the numeric values used in this standard are empirical and somewhat arbitrary. For the LOS velocity calibration procedure, the HWS uncertainty sources are:

(i) **Wind tunnel calibration uncertainty**:

$$u_{cal} = \sqrt{u_{cal,1}^2 + \left(\frac{0.01}{\sqrt{3}} V_{hor}\right)^2} \tag{12}$$

where $u_{cal,1}$ is the uncertainty specified by the calibration certificate for a coverage factor $k = 1$. We used $u_{cal,1} \approx 0.025$ m·s^{-1}. The 2nd term is due to the variability of cup anemometers calibration results for *Measnet* accredited wind tunnels. *Measnet* requires the tunnels to be within $\pm 1\%$ of each other. Hence a 1% uncertainty is added with an assumed rectangular—or uniform—distribution of uncertainty yielding the $1/\sqrt{3}$ factor.

(ii) **Operational—also called classification—uncertainty**:

$$u_{ope} = \frac{k_{class}}{\sqrt{3}} \cdot (0.05 + 0.005 V_{hor}) \tag{13}$$

where k_{class} is the anemometer's classification number characterising the systematic deviations due to environmental conditions, e.g., angular response, turbulence, temperature (influence on

Remote Sens. **2016**, *8*, 907 15 of 24

bearing friction), etc. The cup anemometer used in this study is of type *'Thies First Class Advanced'* which has a class of 0.9A ($k_{class} = 0.9$).

(iii) **Mounting uncertainty**:

$$u_{mast} = 0.5\,\% \cdot V_{hor} \tag{14}$$

related to the mounting of the sensor on the mast. The 0.5 % uncertainty is the default value for top-mounted instruments suggested in the revision of the IEC 61400-12-1.

The only source of **wind direction uncertainty** from the sonic anemometer is the calibration. Indeed, the LOS direction is evaluated in the frame of reference of the wind direction sensor (see Section 5.4). The North mark and boom orientation uncertainties are thus irrelevant. At $k = 1$, the calibration certificates specify a wind direction uncertainty of

$$u_\theta = 0.4^\circ \tag{15}$$

Uncertainty sources in the calibration measurement process are:

(i) LOS direction uncertainty, related to the statistical evaluation of θ_{los} (Section 5.4) and roughly estimated to:

$$u_{\theta_{los}} = 0.1^\circ \tag{16}$$

(ii) Uncertainty of physical inclination angle characterising the uncertainty of the angle used in the vertical projection of the HWS in (Equation (2)) and estimated via the inclinometers' calibration (see [4,5]) to:

$$u_\varphi = 0.05^\circ \tag{17}$$

(iii) Vertical beam positioning uncertainty: characterises how close to the reference instruments height the beam is positioned. Here, modelling the vertical shear profile with the power law, using a shear exponent $\alpha_{exp} = 0.2$, a height uncertainty $u_H = 10\,\text{cm}$ at $H_{ref} = 8.9\,\text{m}$, the wind speed uncertainty due to the height error is:

$$u_{pos} = \alpha_{exp} \cdot \frac{u_H}{H_{ref}} \cdot V_{hor} \approx 0.23\% \cdot V_{hor} \tag{18}$$

(iv) Inclined beam and range uncertainty: practically, the inclined beam implies that the laser light travels, within the probe volume, through a range of heights. The lidar thus senses different wind speeds if there is a wind shear. Additionally, the range uncertainty along the LOS moves the probe volume's center slightly away from the reference instruments' height. A model of this uncertainty can be found in Annex A of [18]. Configuring this model with the 5B and ZDM lidars setup in Høvsøre and a conservative 5 m range uncertainty, we obtained respectively:

$$\begin{cases} u_{inc,5B} = 0.052\% \cdot V_{hor} \\ u_{inc,ZDM} = 0.104\% \cdot V_{hor} \end{cases} \tag{19}$$

(v) Spatial separation uncertainty: the spatial separation between the two reference sensors infers an uncertainty whose magnitude increases with the separation distance. In our case, the two masts are 5 m apart and the terrain is flat. The spatial separation effects can reasonably be neglected.

The combined uncertainty components in Equation (10) are finally computed as follows:

$$\begin{cases} u_{c,V_{hor}} = \sqrt{u_{cal}^2 + u_{ope}^2 + u_{mast}^2 + u_{pos}^2 + u_{inc}^2} \\ u_{c,\theta_r} = \sqrt{u_{\theta}^2 + u_{\theta_{los}}^2} \end{cases} \quad (20)$$

5.6.5. Expanded V_{LOS} Uncertainties

Given a coverage factor k, the expanded LOS velocity uncertainty is:

$$U_{c,y} = k \cdot u_{c,y} \quad (21)$$

Classically, the value of $k = 2$ is chosen in which case $U_{c,y}$ corresponds to the half-width of a 95% CI for a normal probability distribution. If $k = 1$, it corresponds to a 68% CI; if $k = 3$, to a 99% CI.

The combined and expanded uncertainty values depend on the encountered wind conditions (speed, direction, tilting, etc.). Thus, they are computed for each valid 10-min period. They are then averaged in each V_{LOS} bin and may be reported in the form of a table (see [4,5]).

The expanded V_{LOS} measurement uncertainties of 5B and ZDM averaged per bin are displayed in Figure 10. They vary linearly with the LOS velocity ($R^2 > 0.99$). High wind speed bins for the calibration of LOS0 of the 5B lidar do not feature enough data points and are invalid for $V_{LOS} > 13$ m·s^{-1}. However, the linearity of the uncertainties suggests that extrapolation of the uncertainties to the invalid bins is reasonable.

With a coverage factor $k = 2$, the expanded uncertainties vary from ≈3.2% at 3 m·s^{-1} to ≈1.9% at 16 m·s^{-1}, as shown in Figure 10's right axis. The uncertainties results obtained show insignificant deviations between ZDM and all LOS of 5B.

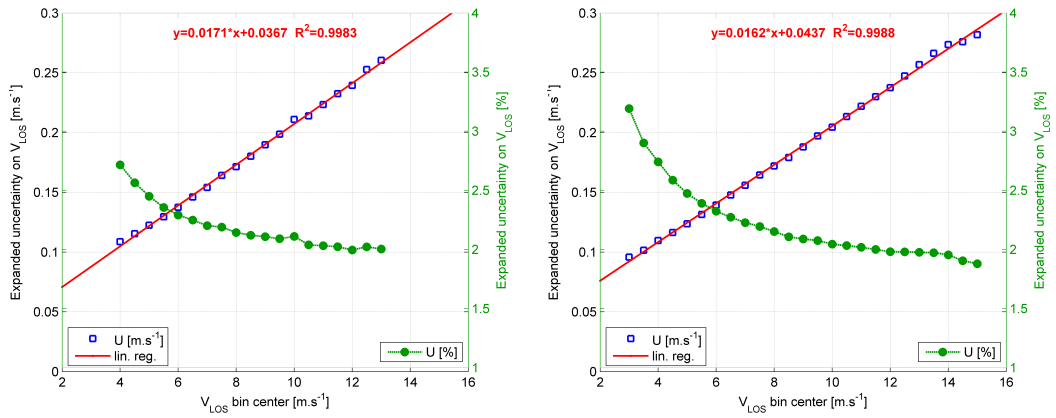

Figure 10. Expanded LOS velocity measurement uncertainties in m·s^{-1} and in % of V_{LOS}. **Left**: 5B; **Right**: ZDM.

5.7. Summary of Calibration Results

The calibration results obtained for the 5B and ZDM lidars are summarised in Table 1.

Remote Sens. **2016**, *8*, 907 17 of 24

Table 1. Summary of LOS velocity calibration results.

Lidar	LOS	Calibration Relation				Expanded Uncertainties ($k = 2$)		
		θ_{los}	a	R^2	$Npts$	U (m·s^{-1})	U at 4 m·s^{-1}	U at 16 m·s^{-1}
5B	LOS 0	286.03°	1.0058	0.9999	742	$0.0171 \cdot V_{LOS} + 0.0367$	2.72%	1.94%
	LOS 1	285.99°	1.0072	0.9999	502	$0.0156 \cdot V_{LOS} + 0.0460$	2.73%	1.84%
	LOS 2	285.99°	1.0084	1.0000	1087	$0.0157 \cdot V_{LOS} + 0.0449$	2.73%	1.85%
	LOS 3	286.06°	1.0090	0.9999	446	$0.0152 \cdot V_{LOS} + 0.0476$	2.73%	1.82%
	LOS 4	285.99°	1.0059	1.0000	1508	$0.0155 \cdot V_{LOS} + 0.0457$	2.68%	1.84%
ZDM	179°–181° azimuth	287.44°	1.0050	0.9998	2140	$0.0162 \cdot V_{LOS} + 0.0437$	2.75%	1.89%

6. Uncertainties of Reconstructed Wind Characteristics

In this section, the reconstruction case of a two-beam nacelle lidar system is used to demonstrate how, as facilitated by the white box methodology, uncertainties on multiple wind characteristics can be estimated. The propagation of calibration uncertainties through the reconstruction algorithm does not account for the flow model inadequacy. The wind model should be validated separately, and the uncertainty due to its inadequacy assessed.

6.1. Wind Field Reconstruction Techniques

To reconstruct wind characteristics from single Doppler wind lidar data, hypotheses on the flow field must be made, i.e., a flow model is assumed.

Examples of spatial assumptions that may be employed in wind field reconstruction (WFR) are: horizontal homogeneity (e.g., VAD techniques classically used by ground-based lidars); two- or three-dimensional wind vector; vertical and/or longitudinal shear profile (linear, power law, log-law, etc.). These assumptions are sufficient for static WFR (see [8], suitable for power performance applications), which disregards the propagation of the wind field over time. In the dynamic case (see [19,20], suitable for turbine control applications) flow models may additionally assume specific velocity and turbulence field structures (coherence) and Taylor's frozen turbulence hypothesis.

Once the flow model is defined, a least squares problem can be formulated: lidar measurements may be fitted to the model by projecting wind characteristics onto multiple LOS, thus minimising errors between 'simulated' and measured LOS velocities.

When the least squares problem is linear (such as in certain cases of flow homogeneity), analytical expressions of wind characteristics can be derived by matrix inversion [8].

The usable methods to propagate uncertainties on V_{LOS} and other inputs to wind characteristics depend on the complexity of the WFR. Numerical techniques such as Monte-Carlo, bootstrap or Polynomial Chaos Expansion may be implemented. Although they might be computationally expensive, they are particularly relevant for non-linear flow models where advanced WFR fitting techniques are employed. The aforementioned uncertainty propagation methods are additionally appropriate to handle correlation between uncertainty distributions. Details on advanced WFR techniques and the corresponding uncertainty propagation methods are outside the scope of this paper.

For the two-beam lidar case hereafter, we chose to apply the GUM methodology as simple analytical expressions of wind characteristics are available.

6.2. Example for a Two-Beam Nacelle Lidar

6.2.1. Reconstruction Algorithm

We here use a simple reconstruction algorithm applied to a two-beam nacelle lidar, see Figure 11. Although the flow model described hereafter is expected to be strongly inadequate for multiple-beam profiling nacelle lidars, the example corresponds to the technique employed by the first generation of

commercial systems—such as the two-beam *Avent Wind Iris* and pair-derived wind characteristics that can be extracted from the *ZephIR Dual Mode* lidar—hence its relevance.

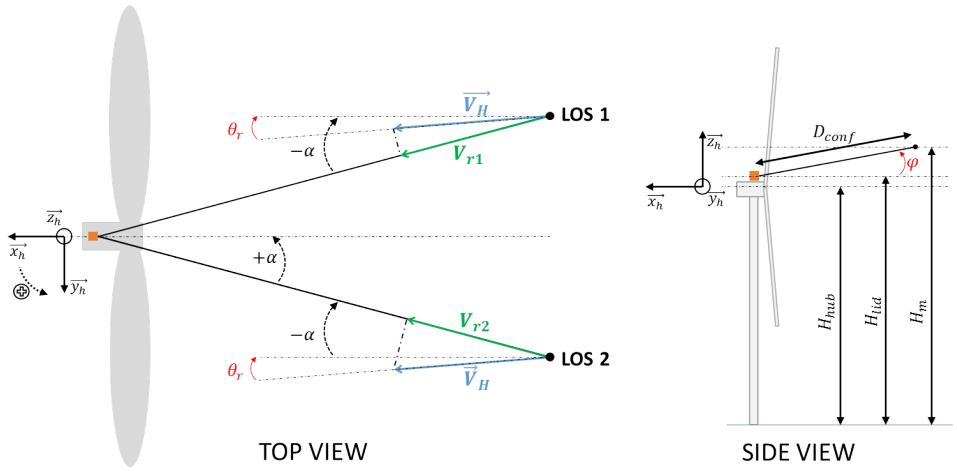

Figure 11. Two-beam nacelle lidar schematics for wind field reconstruction.

At one specific range, the hypotheses of the flow model are:

(1) two-dimensional wind vector: the vertical component V_z is 0, downstream and transverse components are denoted V_x and V_y respectively;
(2) horizontal flow homogeneity: V_x and V_y are independent of the y_h coordinates (see Figure 11) of the beams position;
(3) the probe volume averaging is neglected: time-averaged lidar V_{LOS} are considered as point-like quantities;
(4) the lidar roll inclination is 0°: both beams sense winds at the same height.

The LOS velocities are given by:

$$\begin{cases} V_{r1} = V_H \cos\varphi \cos(\alpha + \theta_r) \\ V_{r2} = V_H \cos\varphi \cos(\alpha - \theta_r) \end{cases} \tag{22}$$

where V_H is the horizontal wind speed, θ_r the wind direction relative to the turbine's yaw position, α the lidar half-opening angle, φ the lidar tilt inclination. The wind vector components are then:

$$\begin{cases} V_x = V_H \cos(\theta_r) \\ V_y = V_H \sin(\theta_r) \end{cases} \equiv \begin{cases} V_x = \frac{V_{r1}+V_{r2}}{2\cos\varphi\cos\alpha} \\ V_y = \frac{-V_{r1}+V_{r2}}{2\cos\varphi\sin\alpha} \end{cases} \tag{23}$$

Finally, the wind speed and relative direction are derived as follows:

$$\begin{cases} V_H = \sqrt{V_x^2 + V_y^2} \\ \theta_r = \text{atan}\left(\frac{V_y}{V_x}\right) \end{cases} \tag{24}$$

In normal operations, the turbine yaws according to the wind direction, θ_r is expected to be close to 0. Hence, for simplicity, we used the arctangent function (atan) instead of its four-quadrant extension (atan2).

u_{θ_r} (Equation (27)) is only the calibration uncertainty of the relative direction. Practically, the alignment of the lidar to the nacelle centreline is an additional source of uncertainty—its magnitude will depend on the mounting procedure – that must be accounted for by quadratically adding it to u_{θ_r}.

Remote Sens. **2016**, *8*, 907 19 of 24

In real-world applications, the lidar tilt will follow closely the nacelle's motion. The two reconstructed wind characteristics are thus valid at the H_m height agl:

$$H_m = H_{lid} + D_{conf} \sin(\varphi) \tag{25}$$

where H_{lid} is the lidar height agl. and D_{conf} the configured measurement range. In the case where the aim is to estimate the wind speed at hub height, as it usually is in power performance testing, a correction of the wind speed reconstructed at H_m should be made, if possible. The issue of nacelle lidars probing the wind at a single height implies an extra uncertainty, characterising the wind speed uncertainty caused by the motion of the turbine's nacelle.

6.2.2. Propagating Uncertainties with the GUM

Applying the law of propagation of uncertainties to the expressions of V_x, V_y (Equation (23)), we obtain:

$$\begin{cases} u_{V_x}^2 = \left(\frac{1}{2\cos\varphi\cos\alpha}\right)^2 \cdot \left(u_1^2 + u_2^2 + 2r_{1,2}u_1u_2\right) + V_x^2\left(\tan^2\varphi \cdot u_\varphi^2 + \tan^2\alpha \cdot u_\alpha^2\right) \\ u_{V_y}^2 = \left(\frac{1}{2\cos\varphi\sin\alpha}\right)^2 \cdot \left(u_1^2 + u_2^2 - 2r_{1,2}u_1u_2\right) + V_y^2\left(\tan^2\varphi \cdot u_\varphi^2 + \frac{u_\alpha^2}{\tan^2\alpha}\right) \end{cases} \tag{26}$$

where $r_{1,2}$ is the correlation coefficient between the uncertainties u_1, u_2 on V_{r1} and V_{r2}. We implicitly assumed that the uncertainties u_φ and u_α are correlated neither with u_1, u_2 nor between each other. Then, the law of propagation is applied to Equation (24) to obtain the wind speed and relative direction uncertainties, respectively denoted u_{V_H} and u_{θ_r}:

$$\begin{cases} u_{V_H}^2 = \frac{1}{V_H^2} \cdot \left(V_x^2u_{V_x}^2 + V_y^2u_{V_y}^2 + 2r_{xy}V_xV_yu_{V_x}u_{V_y}\right) \\ u_{\theta_r}^2 = \frac{1}{V_H^4} \cdot \left(V_y^2u_{V_x}^2 + V_x^2u_{V_y}^2 - 2r_{xy}V_xV_yu_{V_x}u_{V_y}\right) \end{cases} \tag{27}$$

6.2.3. Uncertainty Budget, Results and Scale Analysis

In this paragraph, LOS velocities V_{r1} and V_{r2} are 'simulated' according to Equation (22). All results are obtained with a half-opening angle $\alpha = 15°$—typical of commercial systems—and a tilt $\varphi = -1°$.

At a coverage factor $k = 1$, the uncertainty budget is:

(i) LOS velocity: taking advantage of the previously observed linearity (see Section 5.6.5), the LOS velocity uncertainty of beam i is estimated to $u_i = m \cdot V_{ri} + n$ where $m = 0.008$ and $n = 0.0225$. We here obtained m and n by approximating the gain and offset value of the expanded uncertainty linear relation (see Table 1) and dividing it by the coverage factor;
(ii) Tilt inclination: $u_\varphi = 0.05°$ as prescribed by the inclinometers calibration;
(iii) Opening angle: from the geometry verification, we estimate $u_\alpha = 0.1°$.

In the GUM methodology, the correlation between uncertainty components may have a large impact on the combined uncertainty. The variability of uncertainty results depending on the correlation between u_1 and u_2 is shown in Figure 12. In the full correlation case, both expanded uncertainties U_{V_x} and U_{V_H} are ∼50% higher than in the uncorrelated one. The effect is even more critical for U_{V_y} and U_{θ_r}: the calibration uncertainty is almost zero for $r_{1,2} = 1$. Note that an extra uncertainty quantifying the wind model inadequacy should be added to the calibration uncertainty.

In practice, the LOS velocity calibration will probably be performed for both beams at the same site, with the same reference instruments. Moreover, the reference instruments contribute for >90% to the total V_{LOS} uncertainty (7.1). u_1 and u_2 are most likely highly and positively correlated. In the next paragraphs, we arbitrarily choose $r_{1,2} = 0.9$ and $r_{xy} = 0.2$, later shown to be negligible.

Figure 13 displays expanded uncertainties as a function of wind speed (with $\theta_r = 5°$) and direction (with $V_H = 10\ \mathrm{m{\cdot}s^{-1}}$). U_{V_H} varies linearly with V_H and is approximately of same magnitude as $U_{V_{LOS}}$.

The wind direction uncertainty U_{θ_r} decreases with the wind speed. The relative wind direction has little impact on U_{V_H} and U_{θ_r}, as long as it stays within a reasonable range.

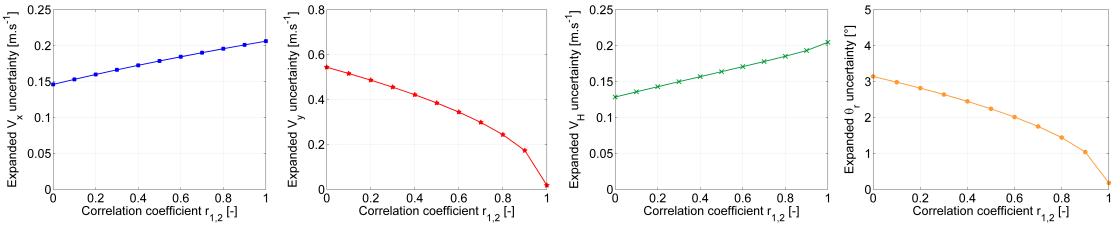

Figure 12. Expanded uncertainties U_{V_x}, U_{V_y}, U_{V_H} and U_{θ_r} as a function of correlation coefficient $r_{1,2}$ ($V_H = 10\,\mathrm{m{\cdot}s^{-1}}$, $\theta_r = 5°$, $r_{xy} = 0.2$).

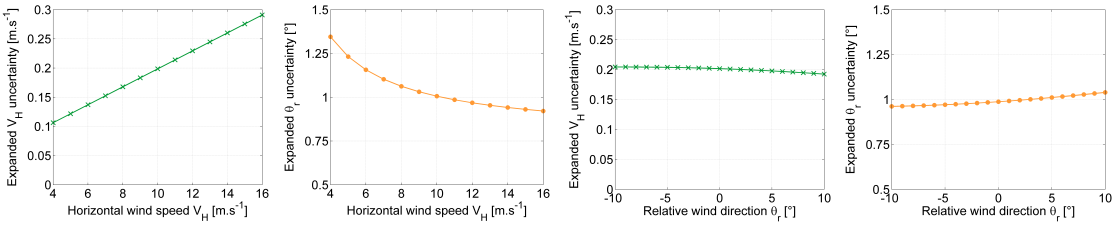

Figure 13. Expanded uncertainties U_{V_H} and U_{θ_r} as a function of V_H and θ_r ($r_{1,2} = 0.9$ and $r_{xy} = 0.2$).

Seeking to identify which terms of Equations (26) and (27) are dominant, a scale analysis is conducted (Table 2) with $V_H \sim 10\,\mathrm{m{\cdot}s^{-1}}$ and $\theta_r \sim 10^{-1}\mathrm{rad} \approx 5°$.

Table 2. Scale analysis of uncertainty components contributing to uncertainties on V_x V_y, V_H and θ_r.

Combined Uncertainty	**Uncertainty Term and Order of Magnitude**				
$u^2_{V_x}$ in $\left[\mathrm{m^2{\cdot}s^{-2}}\right]$	$\frac{u_1^2}{(2\cos\varphi\cos\alpha)^2}$	$\frac{u_2^2}{(2\cos\varphi\cos\alpha)^2}$	$\frac{2r_{1,2}u_1u_2}{(2\cos\varphi\cos\alpha)^2}$	$V_x^2\tan^2\varphi\cdot u_\varphi^2$	$V_x^2\tan^2\alpha\cdot u_\alpha^2$
	10^{-3}	10^{-3}	10^{-3}	10^{-7}	10^{-5}
$u^2_{V_y}$ in $\left[\mathrm{m^2{\cdot}s^{-2}}\right]$	$\frac{u_1^2}{(2\cos\varphi\sin\alpha)^2}$	$\frac{u_2^2}{(2\cos\varphi\sin\alpha)^2}$	$\frac{-2r_{1,2}u_1u_2}{(2\cos\varphi\sin\alpha)^2}$	$V_y^2\tan^2\varphi\cdot u_\varphi^2$	$\frac{V_y^2u_\alpha^2}{\tan^2\alpha}$
	10^{-1}	10^{-1}	-10^{-1}	10^{-9}	10^{-4}
$u^2_{V_H}$ in $\left[\mathrm{m^2{\cdot}s^{-2}}\right]$	$\frac{V_x^2u^2_{V_x}}{V_H^2}$	$\frac{V_y^2u^2_{V_y}}{V_H^2}$	$\frac{2r_{xy}V_xV_yu_{V_x}u_{V_y}}{V_H^2}$		
	10^{-2}	10^{-4}	10^{-3}		
$u^2_{\theta_r}$ in $\left[\mathrm{rad^2}\right]$	$\frac{V_y^2u^2_{V_x}}{V_H^4}$	$\frac{V_x^2u^2_{V_y}}{V_H^4}$	$\frac{-2r_{xy}V_xV_yu_{V_x}u_{V_y}}{V_H^4}$		
	10^{-6}	10^{-4}	10^{-6}		

Concerning u_{V_x} and u_{V_y}, the tilt and opening angle uncertainties are negligible, irrespective of $r_{1,2}$. Uncertainties u_{V_H} and u_{θ_r} are governed respectively by the uncertainty on the downstream and transverse component. The correlation term can be neglected irrespective of the value of r_{xy}. Equations (26) and (27) can thus be approximated by:

$$\begin{cases} u^2_{V_x} \approx \frac{u_1^2+u_2^2+2r_{1,2}u_1u_2}{(2\cos\varphi\cos\alpha)^2} \\ u^2_{V_y} \approx \frac{u_1^2+u_2^2-2r_{1,2}u_1u_2}{(2\cos\varphi\sin\alpha)^2} \end{cases} \quad \text{and} \quad \begin{cases} u^2_{V_H} \approx \frac{V_x^2u^2_{V_x}}{V_H^2} \\ u^2_{\theta_r} \approx \frac{V_x^2u^2_{V_y}}{V_H^4} \end{cases} \tag{28}$$

Remote Sens. **2016**, *8*, 907 21 of 24

7. Discussion

7.1. On Lidar V_{LOS} Uncertainties

An analysis of the measurement uncertainty results is performed in order to identify the prevailing uncertainty sources. Figure 14 illustrates the uncertainty assessment procedure in the form of a tree structure. From bottom to top, the approximate contribution of each uncertainty source to the next level of combined uncertainty is given. For example, the contribution of u_{mast} to $u_{c,V_{hor}}$ is computed as $u_{mast}^2/u_{c,V_{hor}}^2$. This analysis demonstrates that:

(1) the uncertainty of the reference quantity $u_{c,V_{ref}}$ accounts for 99% of the combined LOS velocity uncertainty $u_{c,y}$;
(2) >90% of the reference speed uncertainty $u_{c,V_{ref}}$ is related to the combined reference HWS uncertainty $u_{c,V_{hor}}$;
(3) ~94% of $u_{c,V_{hor}}$ is due to the cup anemometer's calibration, operational and mast uncertainties. The LOS velocity calibration process accounts only for the remaining 6% with u_{inc} and u_{pos}.

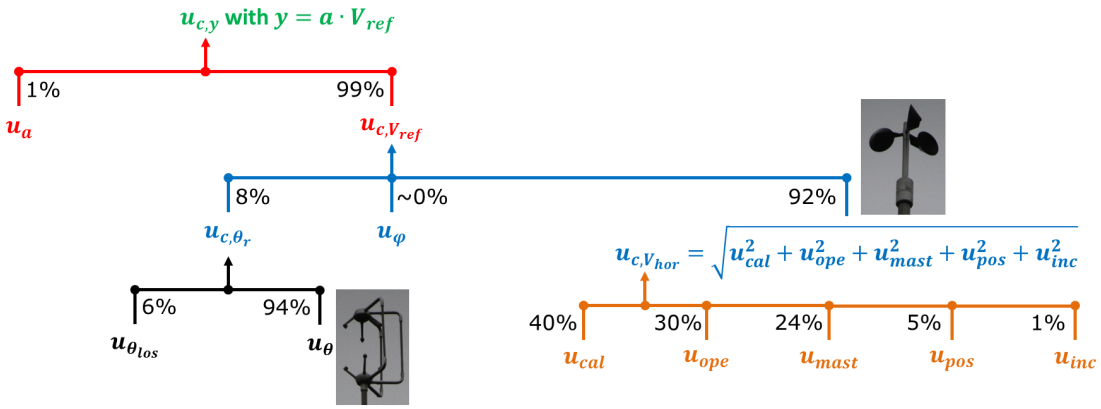

Figure 14. The 'tree' structure of the uncertainty assessment methodology including relative contributions of individual uncertainty sources.

Consequently, a **great majority of the total uncertainty on the LOS velocity is due to the calibration, operational and mast-mounting uncertainty components on the reference quantity**.

This conclusion emphasises the need to improve the cup anemometer uncertainty assessment methodology. In particular, the spread of 1% between *Measnet* accredited wind tunnels is unacceptably large: wind speed measurements from a cup anemometer should not be significantly dependent on the wind tunnel in which it is calibrated. Additionally, measurement errors due to the cup anemometers' sensitivities—to temperature, turbulence intensity, inflow angles, etc.—is incorporated through the classification uncertainty. If such systematic errors can be estimated, they are biases (see definition in VIM, [11]) and should be corrected for instead of considering them as an extra uncertainty.

Currently, improvements in the generic calibration procedure cannot be easily identified since the uncertainty components related to the calibration process account for a negligible proportion of the total LOS velocity uncertainty.

The main goal of this study is to propose and demonstrate a generic calibration procedure in order to make lidar measurements traceable to the International System of Units. Although a single sonic anemometer may conveniently replace the dual-instrument setup, no procedure to assess sonic anemometers' measurement uncertainties is given in the IEC 61400-12-1:2005 norm (but will be in the next revision, see [14]). Thus, the constrain was to use a cup anemometer for the HWS reference instrument. In addition, the wind industry shows a conservative attitude towards wind measurements: for decades, only cup anemometers had been considered.

Alternatively, in the future, lidar-to-lidar calibrations may be performed, using a calibrated lidar as a reference. The principles of the 'white box' calibration will remain valid—replacing V_{ref} by the reference lidar V_{LOS} measurements and directly using uncertainties provided by the calibration certificate. Only slight adjustments of the procedure are anticipated. Lidar-to-lidar calibrations would reduce the calibration duration, however not the uncertainty.

7.2. On Repeatability in Field Measurements

One particularity of field measurements in wind energy is that atmospheric conditions cannot be controlled. Therefore, repeatability does not formally exist. Repeatable conditions could be defined by grouping data according to wind speed, turbulence intensity, temperature, aerosols concentration, thermal stability, etc. Obtaining sufficiently large calibration datasets under repeatable conditions would require years of measurement data and is consequently not reasonably feasible. Thus, LOS velocity measurement uncertainties cannot be assessed using only statistical methods (of 'type A', [11]). Studies of long-term measurement datasets would provide valuable information on the statistical uncertainties of lidar measurements, both at the LOS velocity and reconstructed parameter level. Such studies may even allow to obtain a 'golden' calibrated lidar that could then be used as a reference for other lidars calibration. However, to the author's knowledge, no such studies exist or are ongoing at the time of writing.

7.3. On Limitations of the Application of the White Box

The white box calibration examples demonstrated in this paper feature some limitations—mostly practical—that must be mentioned.

First, the uncertainty components from the reference instruments prevail, emphasizing the need for improving calibration procedures for cup anemometers. Second, the measurement setup is not ideal as measuring at low height above the ground implies high turbulence intensity, which can affect both the reference and lidar measurements, or potential aerosol gradients. On the other hand, a tall mast would require installing the lidar on an expensive stiff platform to avoid extra measurement uncertainties, or significantly tilting up the lidar beam, which would introduce biases.

In the white box calibration, having access to reconstruction algorithms is mandatory. For commercial systems, these algorithms would need to be provided by the lidars' manufacturers to accredited calibration laboratories under confidentiality agreements. The inadequacy and/or uncertainties of the wind field reconstruction algorithms will need to be assessed, for example via Computational Fluid Dynamics and lidar simulator(s).

The presented methodology does not address the volume weighing process inherent to DWL. Further work on this question may thus be required for the white box methodology to achieve an even higher degree of genericity.

A controversial question remains: should the lidar measurements be corrected using the calibration results? Although the VIM provides a clear definition of the calibration and formally requires to apply the calibration relation (i.e., correct the measurements), lidars are currently calibrated in uncontrolled conditions. Indeed, atmospheric field measurements are the most representative of real-world lidar applications. In specific cases where lidars operate in conditions far from those of the calibration, correcting lidar measurements is not always advisable and artificially enlarging the uncertainties may be preferred. This could for instance require adding a classification uncertainty, if available.

8. Conclusions

In the present paper, we developed and demonstrated a generic calibration methodology for wind nacelle lidars. Two different possible calibration concepts were first identified, and their strengths and weaknesses discussed. The retained approach is the so called 'white box' calibration. It consists in calibrating all the inputs of the reconstruction algorithms applied by lidars to estimate wind

Remote Sens. **2016**, *8*, 907 23 of 24

characteristics. In the 'white box' approach, the line-of-sight velocity calibration is central as all Doppler wind lidars first estimate the line-of-sight velocity and then use it for wind field reconstruction. Consequently, the white box calibration concept is generic since applicable to any lidar system with a similar procedure. In opposition, the 'black box' methodology is specific to each reconstructed parameter and requires expensive measurement setups.

The methodology to calibrate and assess the uncertainties of line-of-sight velocity measurements was described and illustrated by the examples of the calibration of two commercially developed lidars: a pulsed multi-beam system developed by *Avent Lidar Technology*; a continuous wave circularly scanning system developed by *ZephIR Lidar*. Calibration results from both lidars have proven to be consistent: the difference between the lidar-measured line-of-sight velocity and reference quantity value lies in the 0.5%–0.9% range. The excellent agreement observed is evidence of the feasibility of the line-of-sight velocity calibration. Uncertainties can be expected to vary between ≈3.5% at 3 $m \cdot s^{-1}$ to ≈2% at 16 $m \cdot s^{-1}$.

Using a simple reconstruction algorithm applied to a two-beam nacelle lidar, inputs uncertainties were propagated to the reconstructed wind speed and relative direction. The assumed degree of correlation between uncertainty components proved to be of critical importance. Results also showed that uncertainties: on wind speed are of same magnitude as line-of-sight velocity uncertainties; on the relative wind direction decrease with the wind speed; are insensitive to the wind direction for normal turbine operational conditions.

Thanks to the generic calibration methodology, traceable lidar-estimated wind characteristics can be obtained and their uncertainties quantified.

Acknowledgments: The calibration procedures were developed within the Unified Turbine Testing (www.UniTTe.dk) project lead by *DTU Wind Energy* and funded by *Innovation Fund Denmark*. The two lidar systems tested and calibrated in this study were kindly provided by the manufacturers, *ZephIR Lidar* and *Avent Lidar Technology*. The authors are thankful for the support, in particular to Matthieu Boquet on Avent's side, and to Michael Harris and Chris Slinger on Zephir's side. This work would not have been possible without the tremendous help of Anders Ramsing Vestergaard at the Høvsøre Test Station, whose skills in lidar field testing were truly appreciated. The authors would also like to thank Per Hansen and Kristoffer Schrøder for their help handling the lidar systems, and Steen Arne Sørensen for collecting and organising the data.

Author Contributions: Antoine Borraccino was in charge of the research work and wrote the paper. Michael Courtney and Rozenn Wagner supervised the research work and the manuscript conception. All co-authors participated to the improvement of the manuscript.

Conflicts of Interest: The authors declare no conflict of interest. The founding sponsors had no role in the design of the study; in the collection, analyses, or interpretation of data; in the writing of the manuscript, and in the decision to publish the results.

References

1. Wagner, R.; Courtney, M.; Gottschall, J.; Lindelöw, P. Accounting for the speed shear in wind turbine power performance measurement. *Wind Energy* **2011**, *14*, 993–1004.
2. Peña, A.; Hasager, C.B.; Gryning, S.E.; Courtney, M.; Antoniou, I.; Mikkelsen, T. Offshore wind profiling using light detection and ranging measurements. *Wind Energy* **2009**, *12*, 105–124.
3. Wagner, R.; Pedersen, T.; Courtney, M.; Antoniou, I.; Davoust, S.; Rivera, R. Power curve measurement with a nacelle mounted lidar. *Wind Energy* **2014**, *17*, 1441–1453.
4. Borraccino, A.; Courtney, M. *Calibration Report for Avent 5-Beam Demonstrator Lidar*; Technical Report; DTU Wind Energy: Roskilde, Denmark, 2016.
5. Borraccino, A.; Courtney, M. *Calibration Report for ZephIR Dual Mode Lidar (Unit 351)*; Technical Report; DTU Wind Energy: Roskilde, Denmark, 2016.
6. Hardesty, R.M.; Weber, B.F. Lidar measurement of turbulence encountered by horizontal-axis wind turbines. *J. Atmos. Ocean. Technol.* **1987**, *4*, 191–203.
7. Lawrence, T.R.; Wilson, D.J.; Craven, C.E.; Jones, I.P.; Huffaker, R.M.; Thomson, J.A.L. A laser velocimeter for remote wind sensing. *Rev. Sci. Instrum.* **1972**, *43*, 512.

8. Schlipf, D.; Rettenmeier, A.; Haizmann, F.; Hofsäß, M.; Courtney, M.; Cheng, P.W. Model based wind vector field reconstruction from lidar data. In Proceedings of the 11th German Wind Energy Conference (DEWEK 2012), Bremen, Germany, 7–8 November 2012.
9. Sathe, A.; Banta, R.; Pauscher, L.; Vogstad, K.; Schlipf, D.; Wylie, S. *Estimating Turbulence Statistics and Parameters from Ground- and Nacelle-Based Lidar Measurements: IEA Wind Expert Report*; Grant No.: 0602-02486B; DTU Wind Energy: Roskilde, Denmark, 2015.
10. Vasiljevic, N. A Time-Space Synchronization of Coherent Doppler Scanning Lidars for 3D Measurements of Wind Fields. Ph.D. Thesis, DTU Wind Energy, Roskilde, Denmark, 2014.
11. Joint Committee for Guides in Metrology. *International Vocabulary of Metrology—Basic and General Concepts and Associated Terms (VIM)*; Technical Report, 200:2012; Bureau International des Poids et Mesures (BIPM): Sèvres, France, 2012.
12. Joint Committee for Guides in Metrology. *Evaluation of Measurement Data—Guide to the Expression of Uncertainty in Measurement*; Technical Report, 100:2008; Bureau International des Poids et Mesures (BIPM): Sèvres, France, 2008.
13. Gottschall, J.; Courtney, M.; Wagner, R.; Jørgensen, H.E.; Antoniou, I. Lidar profilers in the context of wind energy—A verification procedure for traceable measurements. *Wind Energy* **2012**, *15*, 147–159.
14. International Electrotechnical Commission (IEC). *Power Performance Measurements of Electricity Producing Wind Turbines*; IEC 61400-12-1 Ed. 2.0:CCDV; International Electrotechnical Commission: Geneva, Switzerland, 2015.
15. Wagner, R.; Courtney, M.S.; Pedersen, T.F.; Davoust, S. Uncertainty of power curve measurement with a two-beam nacelle-mounted lidar. *Wind Energy* **2016**, 19, 1269–1287.
16. Joint Committee for Guides in Metrology. *Evaluation of Measurement Data—Propagation of Distributions Using Monde Carlo Method*; Technical Report; 101:2008; Bureau International des Poids et Mesures (BIPM): Sèvres, France, 2008.
17. Peña, A.; Floors, R.; Sathe, A.; Gryning, S.E.; Wagner, R.; Courtney, M.S.; Larsén, X.G.; Hahmann, A.N.; Hasager, C.B. Ten years of boundary-layer and wind-power meteorology at Høvsøre, Denmark. *Bound. Layer Meteorol.* **2016**, *158*, 1–26.
18. Borraccino, A.; Courtney, M.; Wagner, R. *Generic Methodology for Calibrating Profiling Nacelle Lidars*; Technical Report; DTU Wind Energy: Roskilde, Denmark, 2015.
19. Raach, S.; Schlipf, D.; Haizmann, F.; Cheng, P.W. Three dimensional dynamic model based wind field reconstruction from lidar data. *J. Phys. Conf. Ser.* **2014**, *524*, 012005.
20. Towers, P.; Jones, B.L. Real-time wind field reconstruction from LiDAR measurements using a dynamic wind model and state estimation. *Wind Energy* **2016**, *19*, 133–150.

2.3 Discussion on alternative approaches for lidar calibration

The black- and the white- box approaches were first presented and discussed during an expert group meeting of the *IEA Wind Task 32* in Glasgow in 2014. The choice between the two different calibration approaches is a rather controversial topic. Among other sources of controversy, the white box approach demonstrated in Section 2.2 may require the provision of sensitive information by lidar manufacturers, such as wind field reconstruction algorithms.

Following the development of the generic methodology and the publication of detailed calibration results (Borraccino and Courtney, 2016b, 2016a) – respectively for the ZDM and 5B-Demo lidars – both approaches were tested on a 2-beam lidar system by Wagenaar et al. (2016) at the Energy research Centre of the Netherlands (ECN) test site. The reference instruments were mounted at 23 m above ground level (agl) and the lidar beams were tilted by approximately 6.5°.

The white box calibration results were of high quality, similar to those obtained for the ZDM and 5B-Demo lidars in Høvsøre. However, results obtained with the black box showed poor agreement between the lidar and the reference wind speed measurements due to the violation at this height of the assumption of flow homogeneity used by the lidar to reconstruct the wind speed. This study demonstrated the inadequacy of the black-box approach for calibrating nacelle lidars. The conclusions by ECN were that "the white box approach from the ground is less sensitive to local conditions and less dependent on the application of the system. This is considered a great advantage".

Alternative techniques for the V_{los} calibration of DWLs involve for instance the use of hard targets moving at calibrated speeds – e.g. a flywheel (cf. *DTU Wind Energy*, TrueWind project), or a moving belt (cf. *ZephIR Lidar*, Antoniou et al. (2007)).

Such calibration methods can be applied indoor and are thus more practical (no field deployment, no dependency on atmospheric conditions, etc). However, their major drawback is the complete lack of representativity. For wind lidars, the Doppler spectra obtained in real-world conditions are more complex (Angelou et al., 2010) than when a lidar beam hits a hard target (see Fig. 2.16). Consequently, the validity and performance of the V_{los} estimator would not be guaranteed in atmospheric conditions, particularly for lidar systems having large probe volumes. Hard target calibration methods may however be relevant for CW DWL systems intended to be used for very short-range measurements (such as the 'lidic') and featuring probe lengths in the order of cm.

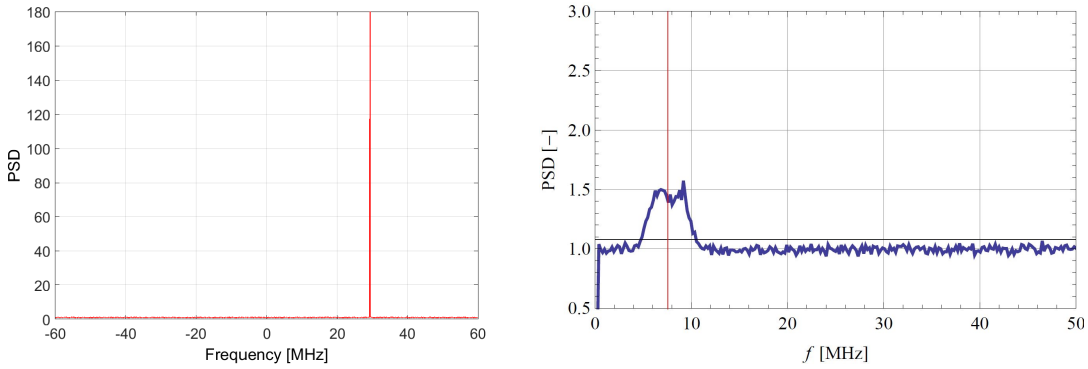

(a) in-lab, using a hard target (Lidic)

(b) atmospheric conditions (Short-Range WindScanner)

Figure 2.16: Doppler frequency Power Spectrum Density examples.
Credit: **(a)** Anders Teigmeier Pedersen; **(b)** Nikolas Angelou.

2.4 Repeatability of the V_{los} calibration

The LOS velocity calibration is a central part of the generic methodology, thus it is important to assess its repeatability. Two plausible sources that can undermine the repeatability are the stability (in time) of the lidar V_{los} measurements and the variability of atmospheric conditions (seasonal effects, wind speed and direction distributions, thermal stability, etc) encountered during the data collection campaigns.

The calibrations of the 5B-Demo and ZDM lidars were conducted prior to a 7-month measurement campaign (see Section 3.2.3). A post-verification campaign was conducted a posteriori, in Høvsøre, between February and May 2016.

During the post-verification campaign of the lidars' V_{los} measurements:

- For 5B-Demo: LOS 0, 2 and 3 were successively tested. No particular operational difficulties were encountered.
- ZDM: both the top and bottom LOS (or 'azimuth sector') were tested. Due to the need to tilt up/down the lidar by an unusually large angle – of approximately 15° – compared to the normal mounting on a turbine, the lidar's position was slightly unstable for the top LOS. As a result, the beam was found to hit the reference cup anemometer regularly. Such events can bias the lidar measurements extensively. Consequently, a data Quality Control (QC) was performed, similarly to the one used when operating on a turbine's nacelle (see Section 2.5).
- the reference cup anemometer unit changed, but was of the same type as

during the first calibration. The reference wind direction instrument (sonic anemometer) was unchanged.

- although the season was the same as for the calibration, the distribution of wind conditions (wind speed, direction, stability, etc) may naturally differ.

Table 2.3 displays the obtained post-verification results. The repeatability of the V_{los} calibration is assessed by comparing them to the (pre-)calibration results (see Table 1, Page 28).

Table 2.3: LOS velocity post-verification results.

Lidar	**LOS**	**Calibration relation**				**Expanded uncertainties** ($k = 2$)		
		θ_{los}	a	R^2	$Npts$	U (m·s^{-1})	U at 4 m·s^{-1}	U at 16 m·s^{-1}
5B-Demo	LOS 0	288.25°	1.0060	0.9999	756	$0.0160 \cdot V_{LOS} + 0.0445$	2.71%	1.88%
	LOS 2	288.53°	1.0055	1.0000	764	$0.0158 \cdot V_{LOS} + 0.0433$	2.67%	1.85%
	LOS 3	288.64°	1.0076	0.9999	435	$0.0154 \cdot V_{LOS} + 0.0475$	2.73%	1.83%
ZDM (with QC)	179°–181° azimuth	289.25°	0.9968	0.9998	758	$0.0157 \cdot V_{LOS} + 0.0456$	2.72%	1.84%
	359°–1° azimuth	287.92°	0.9905	0.9987	894	$0.0162 \cdot V_{LOS} + 0.0471$	2.80%	1.91%

The post-verification results show for 5B-Demo a high level of repeatability. Indeed, for the three tested LOS, the linear regressions' gain values are within 0.2 % of the pre-calibration results. The V_{los} expanded uncertainties are nearly identical – as expected due to the attribution of the prevailing uncertainty sources to the reference cup anemometer. The LOS direction values are consistent between the 3 LOS and their values are $\approx 2°$ higher than during the pre-calibration (consistent with the lidars being positioned $8 - 10$m further South).

For the $179° - 181°$ azimuth sector (bottom LOS) of ZDM, the gain of the linear regression is 0.8 % lower than previously observed. This difference is significant and was thus investigated, although no clear explanation for the deviation could be identified. The $359° - 1°$ azimuth sector (top LOS) results are only presented for indication, as the lidar setup was found to be unstable during this campaign.

Note: the difference of approximately 1 % between 5B-Demo and ZDM are of the same order as the deviations observed during the NKE campaign (see Table 2, Page 56).

2.5 Quality control of the lidar raw data

Once mounted on a wind turbine, nacelle lidars operate in conditions where events that can bias the measurements are frequent. In other words, a thorough QC of the lidar data is necessary in order to discard erroneous measurements. A non-exhaustive list of such events is:

- blade blockage: the laser beam path is regularly occluded by the turbines' blades. For a pulsed lidar, the blades are in the lidar's blind zone (unless pulse durations of less than ≈ 50 ns are used). Thus no backscatter signal is obtained from longer ranges. For a CW lidar, the blades rotational motion can contribute significantly to the Doppler spectrum, albeit the blades are located in the tail of the Lorentzian volume weighting function. Blade blockage occurs approximately $25-40\%$ of the time depending on whether the lidar is positioned at the back of the nacelle or close to the rotor plane. Both full and partial blockage events – returns originating partly from blades and partly from atmospheric scatterers – must be identified;
- hard targets (foreign objects): examples are the turbine's nacelle, a nearby house, a meteorology mast, a neighbouring turbine, birds, etc;
- low quality LOS velocity: the estimator applied to the Doppler spectrum may also provide a quality indicator of the measured V_{los}, e.g. a fitting residual;
- low backscatter signal;
- fog:
  - for CW lidars, fog events cause high backscatter signals for very short ranges, and low signal for longer distances. As a result, the estimated V_{los} does not correspond to the probed measurement location;
  - for pulsed lidars, fog events cause very low backscatter signals, thus reducing the data availability and range capabilities.

A QC algorithm was developed and implemented for the ZDM by processing directly the real-time Doppler spectral data (256 Fast Fourier Transform (FFT) bins recorded at approximately 50 Hz), similar to the one used by *ZephIR Lidar*. The QC process flags events of blade blockage, glints (partial blades) – using moving averages of the quality control flag detecting full blade blockage –, foreign objects, ground returns, and 'low Doppler'. The V_{los} averaging per azimuth sector is then performed accounting only for valid measurements (no flag). The QC process was first implemented for the NKE campaign (Section 3.2), and re-used during the post-verification in Høvsøre (see Fig. 2.17).

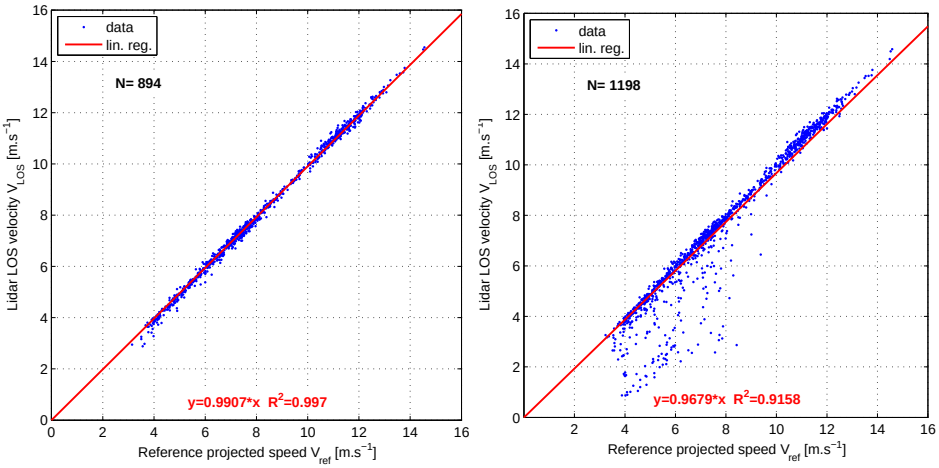

Figure 2.17: Post-verification results of the ZDM top LOS, with (left) and without (right) data quality control.

The 5B-Demo data was provided by the manufacturer with a QC flag of the V_{los} measurement data. Hence, no additional post-processing was required during its calibration.

However, hard target events were identified during the NKE campaign – in that case the lidar beam hit a met. mast – and were not flagged in the lidar data (see LOS 4 in Fig. 2.18(a), Fig. 2.18(b)). A specific filter was implemented to identify such periods (see Sect. 3.4, Page 52).

In the future, pulsed lidar data could also benefit from using dynamic filters and probabilistic methods (Beck and Kühn, 2017). An example of such filters consists firstly in applying a data density function to two-dimensional histograms of carrier-to-noise ratio (CNR) and V_{los} measured over many ranges during a given time period (of e.g. 10 min). Secondly, the dynamic filter identifies data as valid when contained within a trust region (see Fig. 2.18(c), valid data points are within the red polygons). Combined with a minimum CNR threshold value, such a filter ensures both data validity and higher availability at long ranges.

Calibration procedures could include the testing of the quality control of the lidar data as an additional step.

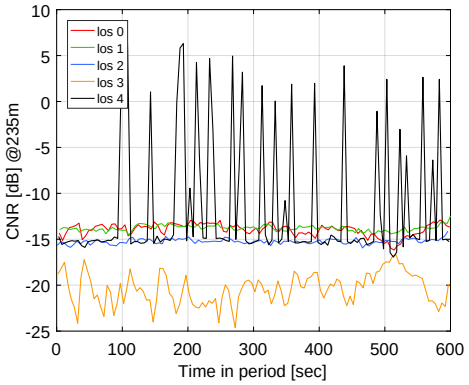

(a) CNR response (timeseries)

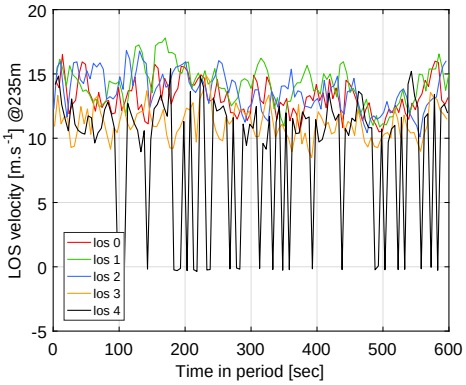

(b) LOS velocity response (timeseries)

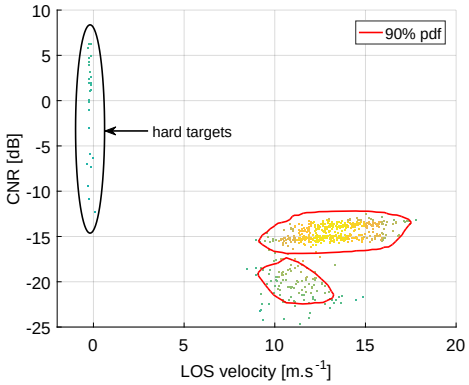

(c) Scatter plot of CNR vs. LOS velocity (all 10 ranges and 5 LOS) colorcoded by data density (low in dark, high in yellow); and 90 % kernel probability density contour (red)

Figure 2.18: Example of hard target events during a 10-minute period (5B-Demo).

2.6 Improvements to the method

In this chapter, we demonstrated the feasibility of the white-box methodology for calibrating nacelle lidars, its applicability to any DWL technology, and its repeatability. Several ways to improve the methods are suggested hereafter.

The calibration of multi-beam lidar systems is time-consuming. The costs associated with the immobilisation of a system for periods of 3 to 6 months constitute the main drawback of the white-box methodology. The possibility of calibrating V_{los} along just a single LOS must be investigated in order to reduce the calibration duration. This requires modelling potential deviations between different LOS in order to establish any extra uncertainty sources. Testing internal components of the lidar system may also be needed in order to answer questions such as: is the

parameterization of the V_{los} estimator – e.g. the Maximum Likelihood Estimator (MLE) – consistent along each optical path? How do backscatter signals compare under similar atmospheric conditions?

Second, although the measurement setup employed in Høvsøre proved to be suitable, it is certainly not ideal due to the low height of the reference mast instrumentation. Indeed, when mounted on a modern wind turbine, a profiling nacelle lidar is likely to sense winds within a range of heights ($\sim 20 - 200$m agl.).

On one hand, it is desirable to calibrate the lidar V_{los} at larger heights since the flow homogeneity within the probe volume is enhanced due to lower absolute wind shear, and the turbulence intensity levels are lower.

On the other hand, if the reference anemometer were top-mounted on a tall mast, the laser beam inclination would be unacceptably large, and thus not representative of operational conditions. The lidar would then need to be lifted on a costly stiff platform. If the platform were not stiff enough, the lidar beam would tilt up or down, adding uncertainties due to sensing height errors. Uncertainties due to sensing height errors are expected to be of the same order of magnitude as those due to the tilted beam of a lidar placed on the ground. For obvious practical reasons, it is preferable to keep the lidar on steady ground.

At a calibration distance of approximately 300 m between the lidar and reference mast, a mast height of $30 - 50$m seems a good compromise.

The contribution of the reference cup anemometer to the total uncertainty was found to prevail (see Section 2.2.7). Reducing the cup anemometer measurement uncertainty is key to many applications in wind energy. This could be achieved by modelling the sensitivity of cup anemometers' measurements to variables such as temperature and turbulence, and correcting the identified measurement biases instead of including them as uncertainty sources (cf. the so-called 'operational' or 'classification' uncertainty). For lidar calibrations, a lower reference speed uncertainty would permit the identification of the main uncertainty sources related to the calibration process and necessary improvements.

Finally, the reference V_{los} measurements may be provided by other instruments, as long as their traceability is ensured. The dual-instrument setup we used in the calibration of the 5B-Demo and ZDM can easily be replaced by:

- a single three-dimensional sonic anemometer;
- very short-range intersecting lidar beams (cf. the *TrueWind* project). Three beams would allow to fully resolve the wind vector (three-dimensional);
- another calibrated lidar ('lidar-to-lidar' calibrations).

CHAPTER 3

Estimating Wind Characteristics

3.1 Introduction

Atmospheric flows are by nature subject to fluctuations, both in space and time. Geostrophic winds characterise large-scale fluctuations. The smaller scales are of importance for wind turbines and farms, since they operate within the atmospheric boundary layer (ABL), i.e. the first few hundred meters from the ground. Those small-scale wind fluctuations are primarily affected by local orography (variation in terrain elevation), surface roughness (land, fields, forests, urban areas) and surrounding obstacles (buildings, wind turbines, etc).

Inherent to the DWLs' measurement process (see Fig. 1.2), assumptions on the flow field must be made to be able to reconstruct useful wind characteristics. The challenge of reconstructing wind characteristics for nacelle-based profiling lidars consists mainly in developing adequate models of ABL winds, while keeping them as simple as possible. In this chapter, we tackle the research question of how wind lidars' primary measurements (V_{los}, trajectory, inclination angles, etc) can be used to estimate various wind parameters, for instance speed, direction or shear. The aim is the estimation of wind characteristics suitable for power performance testing from nacelle-based lidar measurements, which are based on 10-minute mean values.

The chapter includes first a journal article entitled *'Wind field reconstruction from nacelle lidars short range measurements'* (Borraccino et al., 2017), which details the model-fitting approach. The method presents the advantage of clearly defining simple wind models and stating their inherent flow assumptions. Moreover, a simple wind-induction model was developed. Applied to nacelle lidar measurements taken close to the rotor, the combined wind-induction model enables the retrieval of true free-stream wind speed ("V_∞ is found!"). The results presented in the paper concentrate only on the most crucial quantity for PCV, the wind speed.

Several wind field characteristics (WFC) of interest are simultaneously estimated using the model-fitting approach. In a second part, results of the 'secondary' WFC are presented (Section 3.3). Further, the (in-)adequacy of the employed wind models is studied via the statistical analysis of fitting residuals (Section 3.4).

3.2 Wind field reconstruction from nacelle lidars short range measurements

Wind Energ. Sci., 2, 269–283, 2017
www.wind-energ-sci.net/2/269/2017/
doi:10.5194/wes-2-269-2017

eawe european academy of wind energy
Open Access
WIND ENERGY SCIENCE

Wind field reconstruction from nacelle-mounted lidar short-range measurements

Antoine Borraccino[1], David Schlipf[2], Florian Haizmann[2], and Rozenn Wagner[1]

[1]DTU Wind Energy, Roskilde, Denmark
[2]Stuttgart Wind Energy, University of Stuttgart, Stuttgart, Germany

Correspondence to: Antoine Borraccino (borr@dtu.dk)

Received: 21 February 2017 – Discussion started: 6 March 2017
Revised: 25 April 2017 – Accepted: 28 April 2017 – Published: 24 May 2017

Abstract. Profiling nacelle lidars probe the wind at several heights and several distances upstream of the rotor. The development of such lidar systems is relatively recent, and it is still unclear how to condense the lidar raw measurements into useful wind field characteristics such as speed, direction, vertical and longitudinal gradients (wind shear). In this paper, we demonstrate an innovative method to estimate wind field characteristics using nacelle lidar measurements taken within the induction zone. Model-fitting wind field reconstruction techniques are applied to nacelle lidar measurements taken at multiple distances close to the rotor, where a wind model is combined with a simple induction model. The method allows robust determination of free-stream wind characteristics. The method was applied to experimental data obtained with two different types of nacelle lidar (five-beam Demonstrator and ZephIR Dual Mode). The reconstructed wind speed was within 0.5 % of the wind speed measured with a mast-top-mounted cup anemometer at 2.5 rotor diameters upstream of the turbine. The technique described in this paper overcomes measurement range limitations of the currently available nacelle lidar technology.

1 Introduction

In this section, we introduce the measurement principles of Doppler wind lidars, their benefits in the context of power performance verification and the need for new wind field reconstruction (WFR) methods.

1.1 Why using nacelle lidars in power performance testing?

Nacelle-mounted two-beam lidars show promising capabilities to assess power performance (Wagner et al., 2014). Their use obviates the need to erect tall, costly and environmentally invasive meteorology masts, especially offshore. Investigating how to accurately estimate wind characteristics and quantify measurement uncertainties from such instruments is essential in order to consider using nacelle wind lidars in future standards for power performance testing.

The standards (IEC, 2016) require the measurement of hub height wind speed in order to measure a turbine's power curve. This is typically achieved by mounting cup anemometers on a mast. The recommenced distance from the turbine to the mast is 2.5 rotor diameters (D_{rot}). At this distance, the measured wind speed is considered a sufficient approximation of free-stream wind speed. For testing a turbine's performance using nacelle lidars, measurements are commonly taken at the same distance. However, for large wind turbines ($D_{\mathrm{rot}} \gtrsim 150$ m), the currently available nacelle lidar technology features insufficient range capabilities of 300–400 m. Additionally, at $2.5 D_{\mathrm{rot}}$ the wind experiences a speed deficit up to 0.7 % due to the turbine's induction and thus is not in the "free stream" (also true when the turbine is closely aligned with the mast direction) – note the 0.7 % value is calculated using Eq. (10) and a canonical axial induction factor value of $1/3$. Consequently, a reliable method to estimate free-stream wind characteristics from nacelle lidar short-range measurements is necessary.

1.2 Wind measurements with Doppler lidars

Doppler wind lidars (DWLs) do not measure directly wind characteristics (Hardesty and Weber, 1987). They primarily sense backscattered light from particles moving with the wind. The return light originates from scatterers contained in a so-called probe volume located along the lidar beam. Wind field characteristics (WFCs) – such as wind speed at hub height or vertical shear – are estimated combining velocity measurements taken over different lines of sight (LOS). Except in the cases of co-located synchronised measurements (e.g. WindScanner (Vasiljevic et al., 2016) or multi-static systems), the different LOS velocities result from probing the wind in several locations; therefore, assumptions on the wind flow must be made.

A wind lidar is usually provided with or without embedded reconstruction algorithms. In the first case, the lidar manufacturer implements its own methods to estimate WFCs. Using embedded reconstruction algorithms, the lidar may be seen as a "black box". In the second case, the user himself condenses raw lidar data into useful information.

We chose the second approach to ensure transparency and flexibility. The model-fitting technique (Schlipf et al., 2012), initially developed for nacelle lidar systems to assist wind turbine control, was adapted to other nacelle lidar systems and applications (Schlipf, 2016). In this method, the LOS velocity (V_{los}) and beam positions measurement data can be used to reconstruct wind characteristics using a model-fitting approach, where a wind model is defined by assuming horizontal homogeneity, vertical shear profiles, two- or three-dimensional wind vectors, etc. Knowing the DWL beam's location, one can simulate V_{los} by projecting the modelled wind vector onto the LOS. A least squares problem is formulated: the reconstruction algorithm minimises the error between lidar-measured and model-estimated V_{los}. As a result, the model WFCs are obtained.

Commercial nacelle lidar systems may employ alternative methodologies, for example:

- The "four-beam Wind Iris" developed by *Avent Lidar Technology* assumes horizontal homogeneity at two different heights independently, which yields simple analytical expressions to estimate horizontal wind speed and relative direction (Mazoyer, 2016). Wind shear and veer profiles are then calculated by the lidar in realtime, and hub height wind speed and direction are interpolated rather than directly measured. The former "Wind Iris" (two-beam system) also assumed horizontal homogeneity to estimate wind speed and direction at the sensed height.

- In the "Dual Mode" system developed by *ZephIR lidar*, several reconstruction algorithms are implemented. One of them fits the raw measurements based on assumptions of horizontal wind flow, wind yaw misalignment and power law vertical shear. Another one employs pairs of beams to estimate wind speed and direction similarly as a two-beam lidar, but at several heights below and above the hub (Medley et al., 2014). This latter algorithm allows vertical shear profiles to be measured, as well as estimations of wind veer and rotor equivalent wind speed.

1.3 Motivations and research questions

From V_{los} and other raw lidar measurements, the WFR relies on hypotheses on the wind field. The (in)adequacy of these hypotheses plays a crucial role in condensing lidar raw measurements into information useful for various atmospheric and wind energy science applications, and affects the quality of the estimated WFCs. Consequently, WFR techniques must be carefully described, and the underlying flow hypotheses clearly stated.

In this study we investigated the following research questions:

1. Can free-stream wind characteristics be estimated using lidar measurements in the near flow of the turbine's rotor?

2. How do those lidar-estimated wind field characteristics compare to measurements from mast-mounted instrumentation?

Section 2 describes the model-fitting wind field reconstruction approach. We considered one "static" wind model, and its underlying physical assumptions are provided. Further, a combined wind-induction model is proposed, based on a simple induction model, allowing the retrieval of free-stream wind characteristics from V_{los} measured close to the turbine's rotor. Section 3 details the Nørrekær Enge measurement campaign, providing the real-world testing environment of the newly developed wind field reconstruction technique. In Sect. 4, results are presented through comparisons between lidar-estimated and reference mast measurements of wind speed. WFCs have been reconstructed at several distances and heights above ground level (a.g.l.). Finally, we discuss in Sect. 5 potential improvements to the WFR methods, as well as several questions related to their application to nacelle lidars for power performance testing.

2 Wind field reconstruction

In this section, we define the concept of "wind field reconstruction" and describe the so-called model-fitting WFR technique used in this study, starting with the description of the necessary inputs, coordinate systems, lidar model and minimisation problem. Next, several wind model examples are presented as well as a combined wind-induction model.

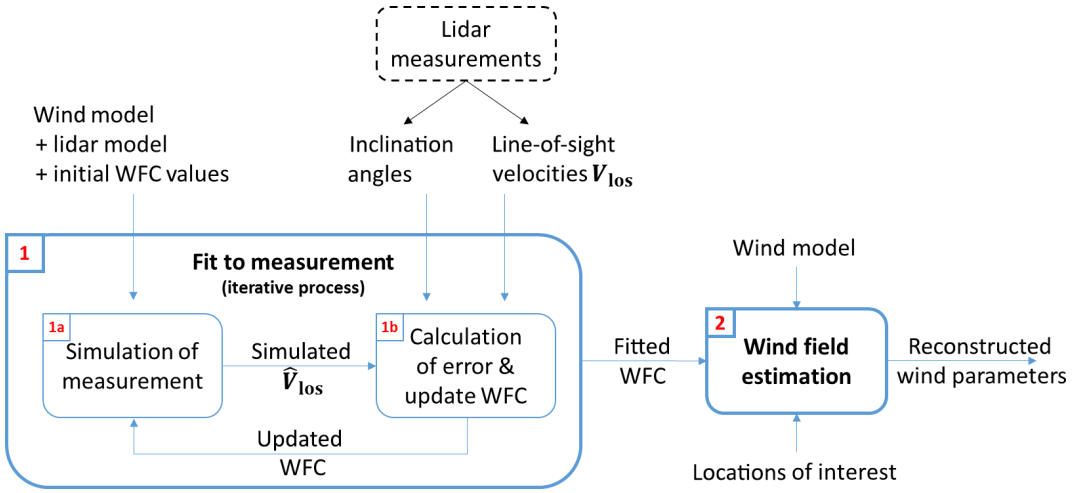

Figure 1. Flow chart of the model-fitting Wind Field Reconstruction methodology.

2.1 Methodology

Wind Field Reconstruction is the process of combining data containing information on wind vectors (e.g. V_{los}) in multiple locations in order to retrieve wind field characteristics relevant to the application. WFCs can, for instance, be wind speed, direction, horizontal and vertical gradient – called shear and veer respectively for speed and direction – turbulence (intensity, length scales, etc.).

With a Doppler wind system (lidar, sodar, radar, etc), performing WFR necessitates hypotheses on the spatial and temporal variations of the wind field. The reconstruction hypotheses and the WFCs define a wind model. Whenever possible, flow assumptions should rely on physical laws governing atmospheric flows.

Depending on the needs and applications, WFR techniques can employ two types of wind models:

- "Static" models: the time dependency of the wind field variations is disregarded – i.e. stationarity is assumed. Typically, time-averaged measurement data provide the inputs to the reconstruction algorithms. Spatial flow assumptions are made, for example on the number of components of the wind vector (one, two or three), on horizontal homogeneity or on the vertical shear profile.

- "Dynamic" models: both the time and spatial variations are accounted for. Flow models may be based on Navier–Stokes equations or Taylor's frozen turbulence hypothesis.

Dynamic WFR is suitable for turbine control applications (Raach et al., 2014; Towers and Jones, 2016) or evaluation of turbulence. For power performance assessment, requiring estimation of 10 min statistics of wind characteristics, static WFR is adequate. This paper thus focuses on static wind models. We additionally chose to use the model-fitting WFR technique, further detailed in the rest of this section.

The flow chart in Fig. 1 describes the model-fitting WFR methodology. The inputs to the process are as follows:

- The wind model: the flow assumptions define the wind vector dimension (2-D or 3-D) and the WFCs.

- The WFC initial values: in order to initialise the fitting process. Initial values have no influence on the fitted WFC values (output) if the solution of the minimisation problem is unique, and can for example be all set to 0.

- The lidar model: measurement trajectory and range configuration, point-like or volume-averaged V_{los} quantities.

- Lidar raw measurement data: 10 min average V_{los} and inclination angles (tilt and roll).

- For lidar systems with large motions (e.g. installed on floating wind turbines or platforms), additional sensors may be helpful (Schlipf et al., 2015).

In step (1), the lidar measurements are fitted to the wind model via an iterative optimisation process. At each iteration, the error between lidar-measured and model-simulated V_{los} is calculated. The fitting process minimises the V_{los} error and outputs the fitted WFC values. In step (2), the wind field is estimated at the locations of interest applying the wind model to the WFC values, thus yielding reconstructed wind parameters – for example, horizontal wind speed at $2.5D_{\mathrm{rot}}$ upstream and hub height.

2.2 Formulation and solving of the minimisation problem

In order to fit WFCs to the lidar measurements (step (1) in Fig. 1), a least squares (LS) problem is formulated. The objective is to minimise the error between lidar-measured $\boldsymbol{V}_{\mathrm{los}}$

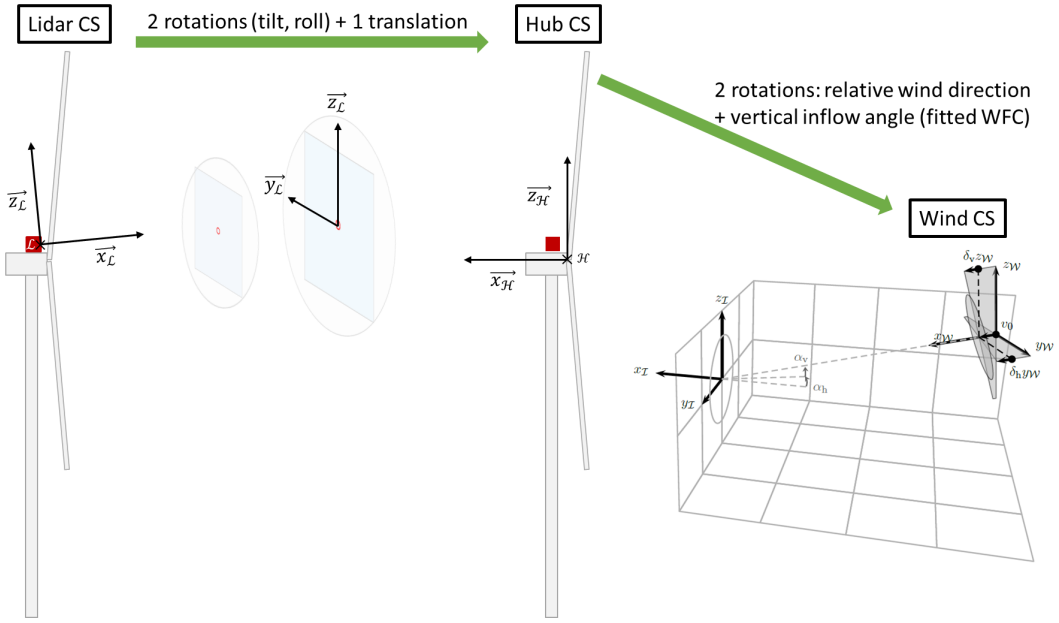

Figure 2. Schematic and relation between used lidar, hub and wind coordinate systems.

and model-simulated $\widehat{\boldsymbol{V}}_{\mathrm{los}}$ where the error is defined as

$$\left\| \boldsymbol{V}_{\mathrm{los}} - \widehat{\boldsymbol{V}}_{\mathrm{los}} \right\|_2 = \sqrt{\sum_{i=1}^{N_{\mathrm{los}}} \left(V_{\mathrm{los},i} - \widehat{V}_{\mathrm{los},i} \right)^2}. \tag{1}$$

Note that $\boldsymbol{V}_{\mathrm{los}}$ and $\widehat{\boldsymbol{V}}_{\mathrm{los}}$ are vectors of length corresponding to the number N_{los} of V_{los} measurements .

For linear wind models, such as when flow homogeneity is assumed, the solution of the LS problem can be obtained by matrix inversion (Schlipf et al., 2012). More complex flow models are usually non-linear (see Sect. 2.4). To solve a non-linear LS problem, optimisation algorithms may be utilised. In this paper, we selected the Levenberg–Marquardt algorithm (Marquardt, 1963), also called the damped least-squares – an optimal gradient-based minimisation method – to solve the non-linear LS problem (Eq. 1).

The convexity of the cost function of such a non-linear LS problem ensures the uniqueness of the optimal solution, i.e. any found local extremum is also a global one. The convexity of a multi-dimensional function can be formally proved by deriving or numerically approximating the Hessian matrix of the cost function, and determining whether it is definite positive. In this work, the uniqueness of the solution was tested by forcing initial WFCs (see Fig. 1) to a wide range of values. With this approach, the optimisation starts from several distant points of the multi-dimensional space. WFC results were found to be identical.

Moreover, several parameters of the Levenberg–Marquardt algorithm can be tuned, such as tolerances on residuals and the damping parameter. We employed the default values of the Matlab®-integrated Levenberg–Marquardt algorithm. Tuning the damping parameter mainly affects the convergence speed, which was satisfactorily fast with a computational time of the order of $1/100\,\mathrm{s}$ for each measurement period. A range of low tolerance values was also tested, showing no impact on the fitted WFCs compared to the default case.

2.3 Lidar model

2.3.1 Coordinate systems

When performing WFR, the locations at which the lidar measures V_{los} in relation to the lidar position on the nacelle play a crucial role in accurately simulating the measurements (see step (1a) in Fig. 1). Coordinate systems (CSs) must therefore be carefully defined. Moreover, the mathematical definition of the wind model may be simpler in one CS or another. Adequately selecting the CS allows an easier and more robust fitting of the lidar measurements to the wind model.

The developed WFR method employs several CSs. We here define the lidar, hub and wind CS (Fig. 2).

The lidar CS $\left(\mathcal{L}, \boldsymbol{x}_{\mathcal{L}}, \boldsymbol{y}_{\mathcal{L}}, \boldsymbol{z}_{\mathcal{L}}\right)$ is a right-handed Cartesian orthonormal system with its origin at the point where the lidar emits its beam and the x axis defined by the lidar optical centreline, pointing upwind for the power curve application. The location of measurement point j in the lidar CS is denoted $(x_{j,\mathcal{L}}, y_{j,\mathcal{L}}, z_{j,\mathcal{L}})$ and derived directly from the measurement ranges and lidar geometry (e.g. opening angles).

The hub CS $\left(\mathcal{H}, \boldsymbol{x}_{\mathcal{H}}, \boldsymbol{y}_{\mathcal{H}}, \boldsymbol{z}_{\mathcal{H}}\right)$ origin is at the centre of the rotor plane. The hub CS is obtained by transforming

the lidar CS with two rotations (tilt around $\boldsymbol{y}_{\mathcal{L}}$ and roll around $\boldsymbol{x}_{\mathcal{L}}$) and one translation corresponding to the lidar position in the hub CS $\left(x_{L,\mathcal{H}}, y_{L,\mathcal{H}}, z_{L,\mathcal{H}}\right)$. The x axis of the hub CS points downwind. $\left(\boldsymbol{x}_{\mathcal{H}}, \boldsymbol{y}_{\mathcal{H}}\right)$ defines a horizontal plane.

The wind CS $\left(\mathcal{H}, \boldsymbol{x}_{\mathcal{W}}, \boldsymbol{y}_{\mathcal{W}}, \boldsymbol{z}_{\mathcal{W}}\right)$ shares the origin of the hub CS (no translation) and its x axis is aligned with the mean wind vector – in other words it is obtained by using the fitted relative wind direction and vertical flow angle and applying two rotations.

Since the lidar follows the turbine's motion, the three aforementioned CSs are independent of the turbine's yaw position.

2.3.2 Measurement simulation

Simulating the lidar consists in computing the LOS velocities. To do so, the beam coordinates are expressed in the same CS as the one used for defining the wind model. First, in the lidar CS, the coordinates $(x_{j,\mathcal{L}}, y_{j,\mathcal{L}}, z_{j,\mathcal{L}})$ of measurement point j are directly derived from the lidar trajectory and measurement range. The trajectory may be defined for example by the lidar cone or half-opening angles. Then, in the hub CS, the normalised vector $\boldsymbol{n}_{j,\mathcal{H}}$ towards measurement point j is given by

$$\boldsymbol{n}_{j,\mathcal{H}} = \begin{bmatrix} x_{n,j,\mathcal{H}} \\ y_{n,j,\mathcal{H}} \\ z_{n,j,\mathcal{H}} \end{bmatrix} = \frac{1}{\sqrt{\left(x_{j,\mathcal{L}}^2 + y_{j,\mathcal{L}}^2 + z_{j,\mathcal{L}}^2\right)}} \left(\begin{bmatrix} x_{L,\mathcal{H}} \\ y_{L,\mathcal{H}} \\ z_{L,\mathcal{H}} \end{bmatrix} - \begin{bmatrix} x_{j,\mathcal{H}} \\ y_{j,\mathcal{H}} \\ z_{j,\mathcal{H}} \end{bmatrix} \right). \tag{2}$$

The lidar LOS velocities can be modelled either as point-like or volume-averaged quantities. If the volume-averaged lidar model is used, the simulation of the measurements requires the integration of the probe volume weighting function (Sathe et al., 2011; Angelou et al., 2012). For static WFR, the difference between volume-averaged and point-like LOS velocities is only significant if the mean wind field along the beam path features large non-linearities. For the sake of simplicity, we only considered the point-like model. Hence, the simulation of the lidar measurements is the projection of the local wind vector $\boldsymbol{U}_j$ onto LOS_j, mathematically obtained by

$$\widehat{V}_{\mathrm{los},j} = \boldsymbol{n}_{j,\mathcal{H}} \cdot \boldsymbol{U}_j, \tag{3}$$

where $\cdot$ is the scalar product.

2.4 Wind and induction models

In this paragraph, we propose, describe and mathematically define the two static flow models employed in this analysis:

1. a wind model assuming horizontal flow, vertical shear and veer profiles;
2. the previous wind model combined with a simple induction model.

Let $[u, v, w]$ be the three components of the wind vector $\boldsymbol{U}$. A static wind model is defined by the function f as follows:

$$\boldsymbol{U}(x, y, z) = f(x, y, z, p_1, \ldots, p_N), \tag{4}$$

where x, y, z are the field coordinates in an arbitrary CS, and $p_1, \ldots, p_N$ are the WFCs. In the general case, the wind vector is three-dimensional (3-D). In flat terrain or offshore, the vertical component w of the wind vector can reasonably be neglected. The flow is assumed horizontal, and thus the wind vector is two-dimensional (2-D): $\boldsymbol{U} = [u, v, 0]$.

2.4.1 Wind model

The wind model hypotheses are horizontal homogeneity, wind speed varying with height according to a chosen shear profile, and homogeneous relative wind direction (no veer). V_0 denoting the horizontal wind speed at hub height H_{hub}, θ_{r} the relative direction, and p_{shear} a shear parameter, the wind model in the hub CS is given by

$$\boldsymbol{U}(x_{\mathcal{H}}, y_{\mathcal{H}}, z_{\mathcal{H}}) = \boldsymbol{U}(z_{\mathcal{H}}) = f(z_{\mathcal{H}}, V_0, \theta_{\mathrm{r}}, p_{\mathrm{shear}}). \tag{5}$$

Vertical shear profiles depend mainly on atmospheric stability, terrain elevation and roughness. The following are examples of shear profiles:

i. Logarithmic law:

$$V(z_{\mathcal{H}}) = \frac{v_*}{\kappa} \log\left(\frac{z_{\mathcal{H}} + H_{\mathrm{hub}}}{z_0}\right), \tag{6}$$

where v_* is the friction velocity, κ the Von Kármán constant, and z_0 the roughness length.

ii. Power law:

$$V(z_{\mathcal{H}}) = V_0 \left(\frac{z_{\mathcal{H}} + H_{\mathrm{hub}}}{H_{\mathrm{hub}}}\right)^{\alpha}, \tag{7}$$

where α is the shear exponent.

iii. Linear:

$$V(z_{\mathcal{H}}) = V_0 \delta_v z_{\mathcal{H}}, \tag{8}$$

where δ_v is the linear vertical shear gradient.

The logarithmic law is only valid for neutral stratification. For buoyancy driven (BD) wind profiles, Högström (1988) proposed empirical formulas to account for stability and correct the log law. BD profile corrections were fitted to measurements and are not valid for very stable stratification. The determination of stability classes – usually based on the Obukhov length or on the bulk Richardson number – is sensitive to the employed methods (Holtslag et al., 2014). Moreover, a DWL cannot determine the stability class on its own and external instruments would be required. Therefore, the logarithmic profile was not considered in this study.

In wind engineering applications, the power law is often used. When measurements are taken in a narrow heights range – such as nacelle lidars measuring within the rotor area – the power law is a simple and accurate enough approximation of the wind profile if no further information is available. In addition, the IEC (2016) norm suggests its use to characterise shear profiles.

The linear profile is an even simpler approximation of the wind profile. The largest non-linearities in the log- or power-law profiles are located close to the ground. In situations where measurements are taken at heights sufficiently far from the ground – we propose above ≈ 30 m as a rule of thumb – a linear profile may be considered. Contrary to the log and power laws requiring knowledge of the measurement height a.g.l., no site-specific information is necessary. However, the linear profile does not physically characterise wind profiles. Further, we only consider the power-law wind profile.

2.4.2 Combined wind-induction model

By harnessing energy from the wind, an operating turbine creates an induction zone upstream of its rotor (Sørensen, 2016; Simley et al., 2016): the closer to the turbine, the lower the wind speed. Adequately modelling wind speed variations in the induction zone constitutes the main challenge of the WFR for nacelle lidar measurements taken, for example, within 0.5 to 2 rotor diameters upstream of the turbine. Computational fluid dynamics simulations (Troldborg and Meyer Forsting, 2017) have shown that, at upstream distances larger than $0.5D_{\mathrm{rot}}$, the induction becomes insensitive to the blades' aero-elastic properties or to the turbine's control strategy. Except in the direct proximity of the rotor plane, the induction zone of a wind turbine is self-similar (see Sect. 5.1 for discussion). The "intensity" of the induction, however, depends on the thrust generation capabilities of the turbine, which may be quantified via an induction factor.

The vortex cylinder model applied to the actuator disk concept yields a simple expression characterising the induction (Branlard and Gaunaa, 2015; Medici et al., 2011) that can be integrated into a WFR model. This simple induction model is one-dimensional. It only is a function of the streamwise distance to the turbine. If both vertical shear (with a power law profile) and induction effects are accounted for, the combined wind-induction model takes the following form:

$$\boldsymbol{U}(x_{\mathcal{H}}, y_{\mathcal{H}}, z_{\mathcal{H}}) = \boldsymbol{U}(x_{\mathcal{H}}, z_{\mathcal{H}}) = f(x_{\mathcal{H}}, z_{\mathcal{H}}, V_0, \theta_{\mathrm{r}}, \alpha, a), \quad (9)$$

where a is the induction factor. With $\boldsymbol{U} = [u, v, 0]$ defined in the hub CS, the cross-stream wind component negligibly contributes to the generation of thrust by the turbine. The analytical induction function thus applies to the streamwise component of the wind vector and is given by

$$\frac{u(x_{\mathcal{H}}, z_{\mathcal{H}} = 0)}{u_\infty} = 1 - a\left[1 + \frac{\xi}{\sqrt{1+\xi^2}}\right], \quad (10)$$

where u_∞ is the streamwise component of the free-stream wind speed V_∞ at hub height, $\xi = x_{\mathcal{H}}/R_{\mathrm{rot}}$ is the non-dimensional longitudinal coordinate in the hub CS. Combining Eq. (10) with the power-law shear profile in Eq. (7), the wind-induction model is given by

$$V(x_{\mathcal{H}}, z_{\mathcal{H}}) = \sqrt{u^2(x_{\mathcal{H}}, z_{\mathcal{H}}) + v^2(z_{\mathcal{H}})} \quad (11)$$
$$= \left(\frac{z_{\mathcal{H}} + H_{\mathrm{hub}}}{H_{\mathrm{hub}}}\right)^{\alpha} \sqrt{u_\infty^2\left(1 - a\left[1 + \frac{\xi}{\sqrt{1+\xi^2}}\right]\right)^2 + v_\infty^2},$$

with $u_\infty = V_\infty cos(\theta_{\mathrm{r}})$ and $v_\infty = V_\infty \sin(\theta_{\mathrm{r}})$.

The wind-induction model yields four WFCs: the hub height free-stream wind speed V_∞ and relative direction θ_{r}, the shear exponent α and the induction factor a.

3 Testing environment: the Nørrekær Enge measurement campaign

The Unified Turbine Testing (http://www.unitte.dk/) research project aims at establishing turbine performance testing procedures applicable in any type of terrain, i.e. for onshore simple or complex sites as well as offshore. Within UniTTe, a 7-month measurement campaign was conducted in Nørrekær Enge (NKE), between June 2015 and January 2016.

This section provides details on the site, wind farm layout, mast instrumentation and nacelle lidar setup.

3.1 Terrain, climate and wind farm

The NKE wind farm is located in northern Jutland, Denmark, and owned by Vattenfall[1]. The park comprises one row of 13 Siemens 2.3 MW turbines with a rotor diameter D_{rot} of 93 m and a hub height H_{hub} of 80 m a.g.l. The orientation of the turbines' row is 75–255°. The site is mainly characterised by open crop fields and flat terrain. In the vicinity of turbine number 4 (T04), except for the turbines' foundations, variations in elevation of ± 1 m are observed (see Fig. 3). The prevailing wind direction is west. In Jutland, such western winds often feature high speeds (Peña et al., 2016).

3.2 Meteorological mast and turbine instrumentation

A meteorological mast was installed 232 m from T04 approximately in the 103° direction (see Fig. 3). The mast instrumentation complies with the requirements of the standards for power performance measurement (IEC61400-12-1, 2005):

[1]Find more information at https://corporate.vattenfall.dk/vores-vindmoller-i-danmark/vindmolleparker/norrekar-enge-vindmollepark/

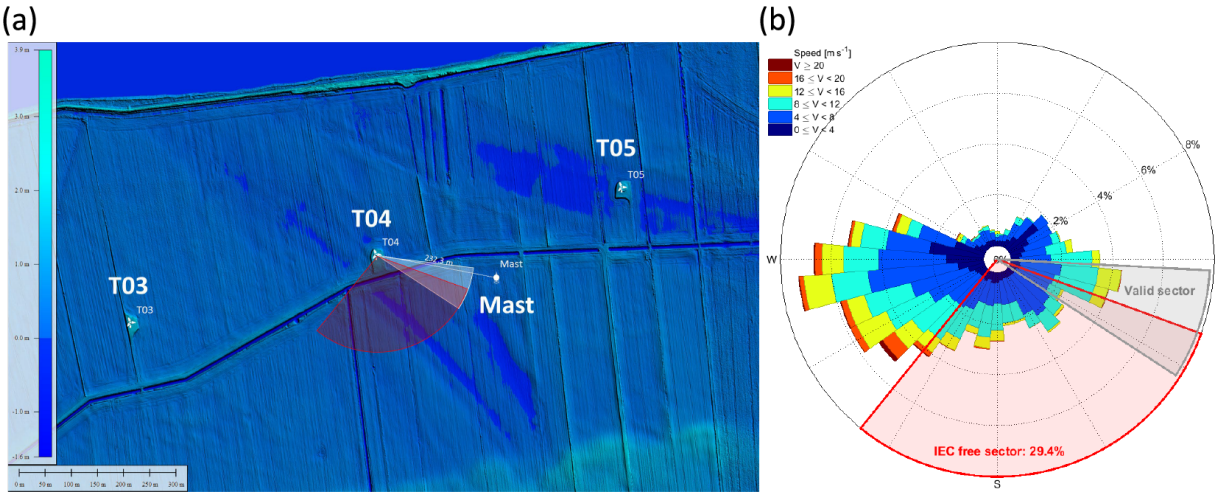

Figure 3. **(a)** Elevation map in the vicinity of T04, Nørrekær Enge wind farm. Map: DHM/terrain (0.4 m grid). Source: Styrelsen for Dataforsyning og Effektivisering. **(b)** Wind rose during the NKE campaign, measured by the top-mounted cup anemometer and wind vane.

- one top-mounted cup anemometer at 80 m a.g.l.;
- three cup anemometers and wind vanes at 33.5, 57.5 and 78 m a.g.l.;
- one sonic anemometer at 76 m a.g.l.;
- other sensors: air temperature at 2 and 78 m, relative humidity at 78 m, atmospheric pressure at 77 m, and precipitation at 20 m a.g.l.

More details about the measurement system of the NKE experiment can be found in Vignaroli and Kock (2016).

3.3 Nacelle-mounted lidars: measurement characteristics and configuration

Two commercially developed profiling nacelle lidar systems were mounted on the nacelle of T04 (see Fig. 4): a five-beam Avent Demonstrator (5B-Demo) and a ZephIR Dual Mode (ZDM).

The five-beam Demonstrator is, like the other *Avent* lidars, a pulsed system measuring V_{los} at several distances simultaneously along each LOS by range gating. The five LOS form a square trajectory (four corners and centre). They are measured successively at 1 Hz; thus, a complete cycle takes 5 s. Being a pulsed system, the turbine's blades are in the lidar's "blind zone" and cannot contaminate V_{los}; the only effect of blade blockage is a reduced LOS availability.

The ZephIR Dual Mode is a continuous wave (CW) system featuring a variable focus to interrogate multiple distances successively. Each distance is conically scanned. ZDM samples V_{los} at high frequency ($\approx$ 50 Hz). For each V_{los} measurement, the azimuthal position is recorded as the centre of the probed circle arc. An algorithm averaging raw high-frequency V_{los} measured in separate azimuthal sectors and yielding a pseudo "48-beam lidar" was developed. When a lidar beam hits a blade, V_{los} can be significantly contaminated by the presence of the blade. Consequently, the data were quality-controlled using recordings of Doppler spectra in order to remove invalid V_{los} measurements such as in the event of full or partial blade blockage and low Doppler signals (due to, for example, moving grass close to the ground).

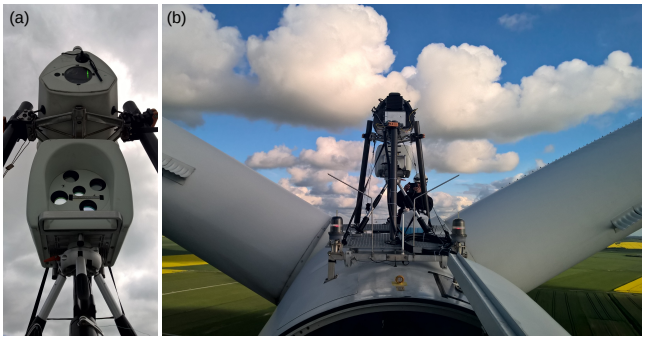

Figure 4. Measurement campaign in Nørrekær Enge (Denmark): the five-beam Avent Demonstrator and ZephIR Dual Mode lidars mounted on a Siemens 2.3 MW turbine. The five-beam Demonstrator is below the ZephIR Dual Mode. **(a)** From the front; **(b)** from the back

Prior to the NKE campaign, the 5B-Demo and ZDM lidars were calibrated at DTU's test section for large wind turbines, Høvsøre, Denmark. The calibration ensures traceability of the lidar measurements to international systems of units and provide estimates of the V_{los} measurement uncertainty. The calibration methodology employed the so-called "white-box" approach (Borraccino et al., 2016). Calibration reports and more details on the lidars' measurement principles can be found in Borraccino and Courtney (2016a) and Borraccino and Courtney (2016b).

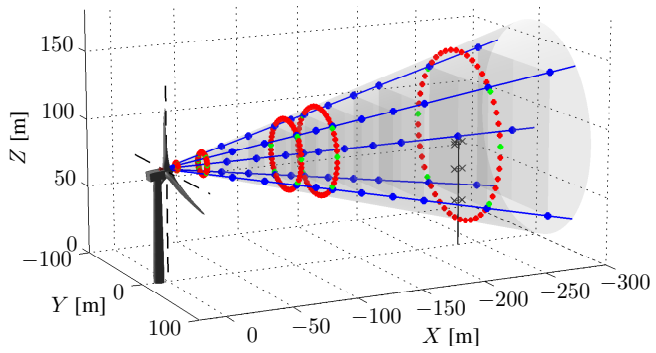

Figure 5. Lidar measurement trajectories in NKE. In blue: five-beam Avent Demonstrator. In red and green: ZephIR Dual Mode, the 48 azimuth-averaged LOS (red), including the 6 LOS (green) considered in the reconstruction cases of this paper.

The lidars were aligned with T04's axis via their internal alignment systems (visible laser lights) and measured to $\lesssim 0.5°$. Their position $(x_{L,\mathcal{H}}, y_{L,\mathcal{H}}, z_{L,\mathcal{H}})$ in the hub coordinate system (see Sect. 2.3.1) was measured with a total station: for both lidars, the distance from the rotor plane is $x_{L,\mathcal{H}} \approx 2.5$ m.

Table 1 provides the range configuration of the 5B-Demo and ZDM lidars in NKE, and the time spent at each distance during one cycle for ZDM. The corresponding measurement trajectories are visualised in Fig. 5.

3.4 Data filtering

Following the procedure for assessing free sectors in Annex A of (IEC, 2016), no significant obstacle exists in the vicinity of T04 in NKE other than neighbouring turbines causing wakes. The disturbed sectors were calculated for the meteorology mast and for the nacelle lidars using the IEC formula for wakes adapted to nacelle lidars (Wagner and Davoust, 2013). The resulting undisturbed sectors are 110–219° and 318–22°. Note that this procedure is conservative.

Practically, wake sectors were observed approximately for wind directions $\in [28°, 84°] \cup [240°, 300°]$, based on turbulence intensity measured by the mast top-mounted anemometer. Additionally, the error between the lidar-reconstructed (with the wind model from Sect. 2.4) and mast-measured wind speed is analysed prior to filtering (Fig. 6). Large errors due to wakes are observed in consistent sectors.

In order to compare the lidar and the mast measurements, we selected a sector of $[93°, 123°]$, close to the turbine-mast direction of 103°.

Valid 10 min measurement periods are obtained by filtering datasets as follows:

- Mast: wind direction measured by the wind vane at 78 m a.g.l. $\in [93°, 123°]$.
- Turbine:
  - connected to the grid without disruption;
  - operating without disruption;
  - moderate yaw misalignment – also called relative wind direction. Only periods where the yaw misalignment measured by the spinner sonic anemometer $\in [-10°, +10°]$ are considered.
- 5B-Demo lidar:
  - LOS availability $> 30\,\%$. Note that, due to the blades roots thickness, the bottom beams encounter blockage more frequently than the central or top beams. Thus, the LOS availability threshold is set to a relatively low value.
  - Carrier-to-noise ratio (CNR) > -20 dB for all five LOS, using the realtime data. Additionally, the presence of the mast may bias the 10 min average V_{los} towards 0 when one of the lidar's beam hits the mast frame. Such 10 min periods were removed from the analysis by thresholding the difference between the observed maximum and mean CNR. The threshold was set to an arbitrary value of 15 dB;
  - Tilt and roll measured by the lidar's internal inclinometers are real numbers.
  - All of the five LOS must pass the filtering for the period to be valid.
- ZDM lidar:
  - LOS availability $> 30\,\%$ independently of the azimuth sector considered. This criterion is more often met when the beam points upwards than downwards for the same reasons as for 5B-Demo.
  - LOS count > 50. The count is the number of times ZDM attempts to measure V_{los} in a 10 min period. Combined with the $> 30\,\%$ minimum availability, this filter ensures a minimum quantity of data points to compute the average V_{los} in the considered azimuth sectors.
  - Tilt and roll measured by the lidar's internal inclinometers are real numbers.
  - Fog filtering: periods where fog is detected are rejected. Fog biases lidar measurements, particularly for a CW system. Abnormally strong backscatter returns from short ranges are observed. When the focus is at longer distances, these short-range returns are in the tail of the lidar Lorentzian weighting function. As a result, the measured V_{los} does not correspond to the LOS velocity at the expected measurement distance, due to the lidar volume-averaging properties. Fog events were detected by thresholding both the mean backscatter at 10 m and its ratio with the backscatter at the range of interest.

Table 1. Configuration of lidar measurement distances during the Nørrekær Enge campaign.

Lidar	Configured measurement distances (m)											
5B-Demo	–	–	49	72	95	109	121	142	165	188	235	281
ZDM	10 (5 s)	30 (10 s)	–	–	95 (10 s)	–	120 (10 s)	–	–	–	235 (15 s)	–
Lidar	**Distances in hub CS adimensionned by $D_{rot}(-)$**											
5B-Demo	–	–	0.5	0.75	0.99	1.14	1.27	1.5	1.75	1.99	2.5	2.99
ZDM	0.08	0.30	–	–	0.99	–	1.26	–	–	–	2.5	–

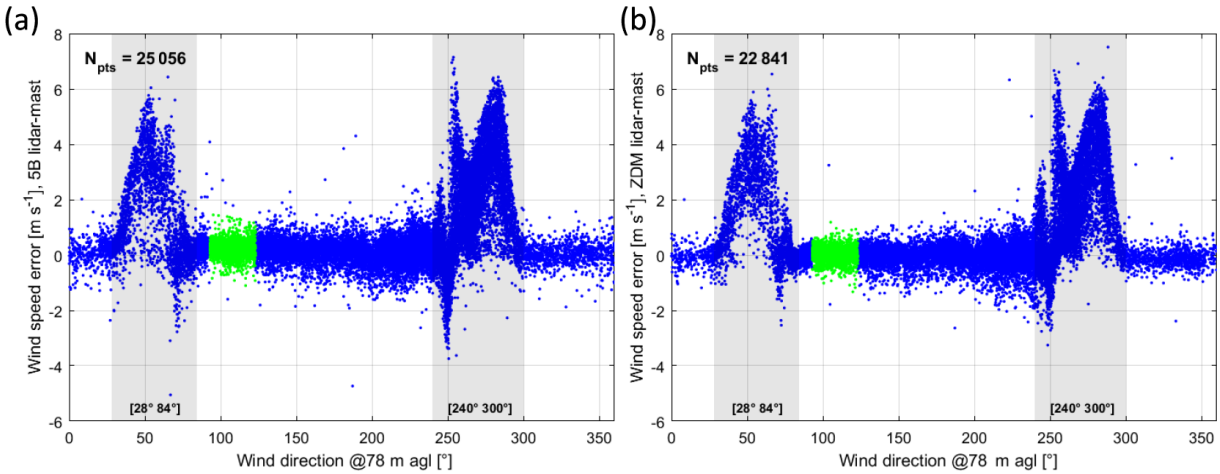

Figure 6. Analysis of horizontal wind speed error (lidar-reconstructed at 235 m minus mast-measured). Grey shaded areas show wind directions with wakes. Data in green are in the selected sector. **(a)** 5B-Demo lidar. **(b)** ZDM lidar.

– In the employed reconstruction case, six LOS are used (see green dots in Fig. 5). Each LOS must pass the filtering for the period to be valid.

4 Results

In this section, the results obtained with the WFR methods are presented through comparisons between the lidar-estimated (reconstructed) and mast-measured horizontal wind speeds.

The data analysis is performed on joint datasets. A valid period is consequently obtained when the mast, turbine, and both lidars have successfully passed the filters detailed in Sect. 3.4. Joint datasets allow for the results of various reconstruction cases to be compared, as the variability in the wind conditions cannot be source of deviations. On the negative side, the number of data points is significantly reduced.

4.1 Reconstruction with wind model

The flow is here assumed to be horizontal (no vertical component). The wind model assuming a power law shear profile (see Sect. 2.4) is applied to the lidars V_{los} measurements taken:

– For ZDM, at 235 m. This corresponds to the mast-turbine distance ($2.5D_{rot}$).

– For 5B-Demo, at 188 m. Due to operational issues during the campaign (dust and salts accumulating on the optical head's window), using the 235 m range requires stricter quality filtering, leading to very small datasets (fewer than 200 data points). The considered 188 m distance ($2.0D_{rot}$) is the shortest one accepted for power performance testing by the IEC (2016) norm.

Figure 7 displays scatter plots of the horizontal wind speeds – denoted V_{hor} – measured by the top-mounted cup anemometer, and estimated at 80 m a.g.l. from the lidars' measurements. Unforced (red) and forced (black) linear regressions results are also displayed. Compared to the mast measurements, both lidars overestimate the wind speed by 1–1.5 % (forced regression), with consistent coefficients of determination $R^2 > 0.993$.

In the considered wind model, a shear exponent is fitted to the lidar measurements, thus allowing wind speed estimations at any desired height. The selected height should, however, remain within the probed lidar heights, approximately

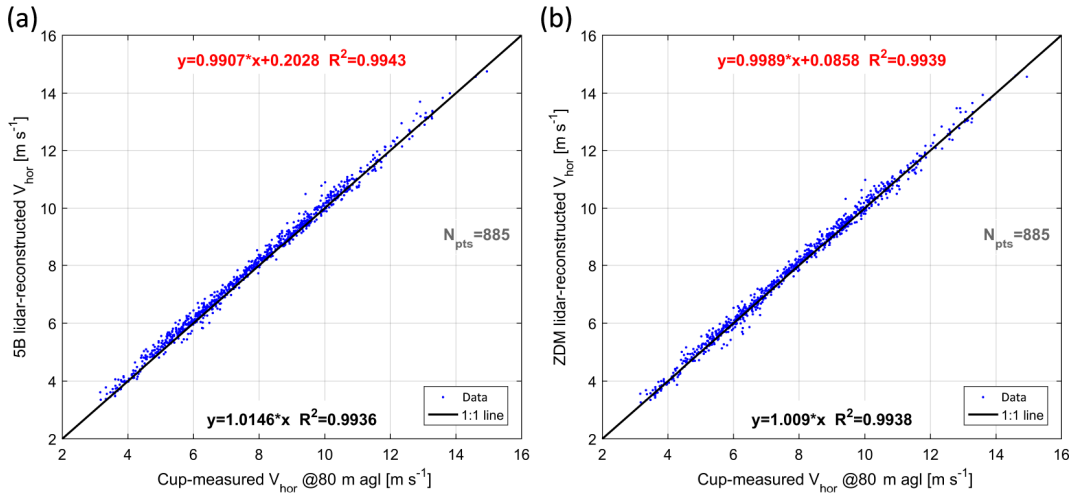

Figure 7. Comparison between mast-measured and lidar-estimated horizontal wind speed at 80 m height a.g.l. **(a)** 5B-Demo lidar, using five LOS, at $2.0D_{\mathrm{rot}}$. **(b)** ZDM lidar, using six LOS, at $2.5D_{\mathrm{rot}}$.

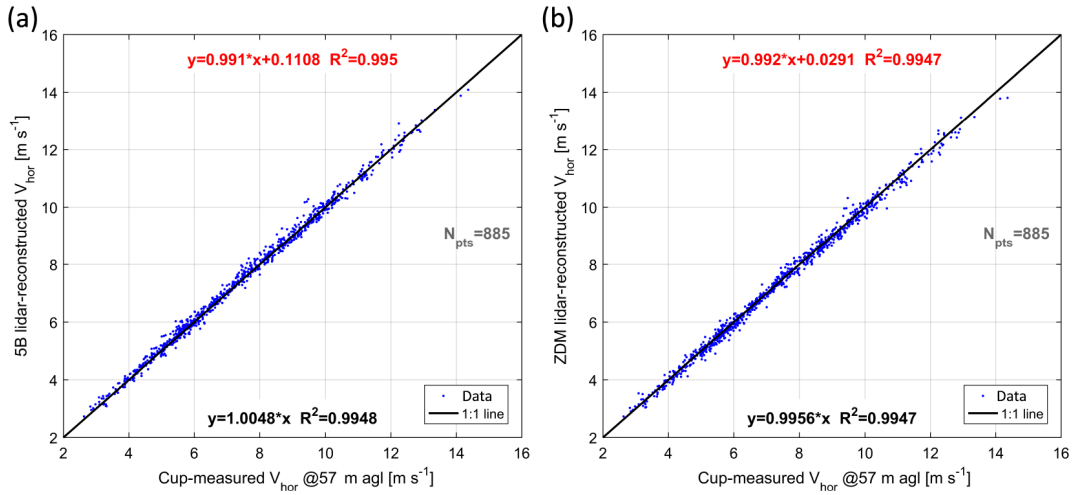

Figure 8. Comparison between mast-measured and lidar-estimated horizontal wind speed at 57.5 m height a.g.l. **(a)** 5B-Demo lidar, using five LOS, at $2.0D_{\mathrm{rot}}$. **(b)** ZDM lidar, using six LOS, at $2.5D_{\mathrm{rot}}$.

40–120 m a.g.l. in NKE. This is illustrated by Fig. 8, where the wind speed is estimated by the lidar at 57.5 m a.g.l. for comparison with a side-mounted cup anemometer. Although no V_{los} measurement is taken at this particular height, a high level of agreement between the lidar estimates and mast measurements of V_{hor} is obtained, thus demonstrating a satisfactory level of the adequacy of the fitted shear profile.

4.2 Reconstruction with combined wind-induction model

In this paragraph, the combined wind-induction model is used to perform WFR on the lidars' short-range measurements. Multiple distances sufficiently separated from one another are required to fit the simple induction model (Eq. 11).

Only V_{los} measurements taken close to the rotor, thus experiencing a significant wind speed deficit, were selected as inputs to the reconstruction. We chose the first four ranges, from 0.5 to $1.15D_{\mathrm{rot}}$ for the 5B-Demo lidar, and the three distances from 0.3 to $1.25D_{\mathrm{rot}}$ for ZDM. These distances are the closest to the turbine's rotor for which the induction may be considered self-similar. Hence, the 10 m range measured by ZDM was discarded. In addition, the wind field experiences larger longitudinal gradients close to the turbine. The fitting of the induction factor is thus facilitated and more robust. Finally, proving the concept of WFR using lidar short-range measurements can only be achieved if the free-stream measurements are discarded from the inputs of the WFR algorithms. Although the V_{los} measurements are taken close to the rotor, lidar estimates of wind speed can be reconstructed from the fitted WFCs at any distance upstream and any height.

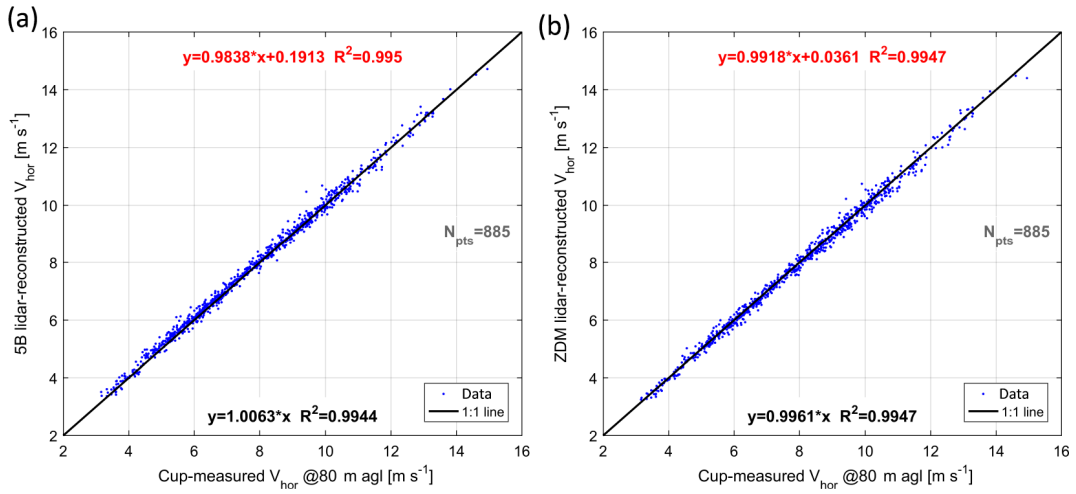

Figure 9. Comparison between mast-measured and lidar-estimated horizontal wind speed at hub height and $2.5D_{\mathrm{rot}}$ using short-range measurements. **(a)** 5B-Demo lidar, using five LOS and four ranges. **(b)** ZDM lidar, using six LOS and three ranges.

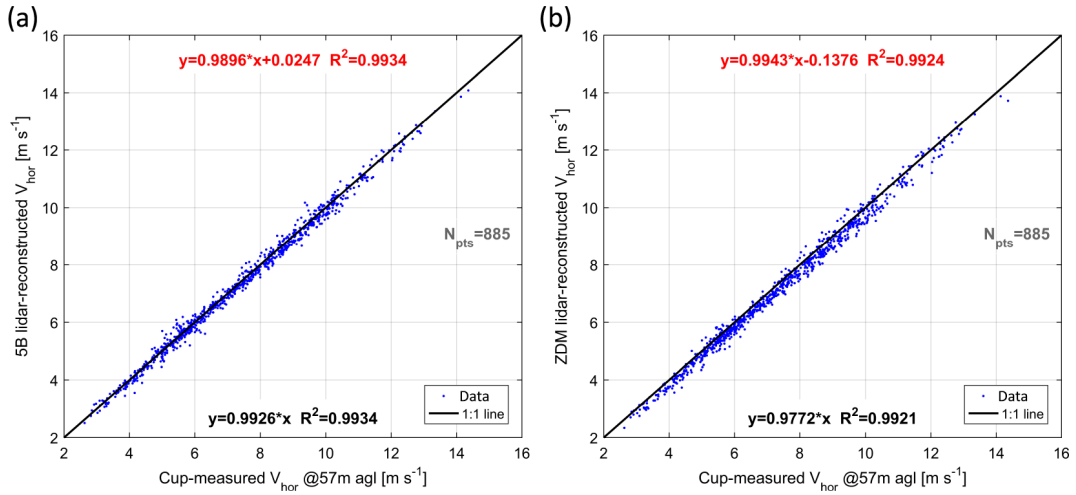

Figure 10. Comparison between mast-measured and lidar-estimated horizontal wind speed at 57.5 m height a.g.l and $2.5D_{\mathrm{rot}}$ using short-range measurements. **(a)** 5B-Demo lidar, using five LOS and four ranges. **(b)** ZDM lidar, using six LOS and three ranges.

In Fig. 9, V_{hor} is estimated at $2.5D_{\mathrm{rot}}$ upstream (i.e. $\xi = -5$; see Eq. 9) and hub height – by using the fitted free-stream wind speed V_{∞}, induction factor a, and shear exponent α. The comparisons between the lidar-estimated and mast-measured wind speed show an excellent level of agreement with gain errors of $+0.6$ and $-0.4\,\%$ for 5B-Demo and ZDM respectively. The scatter is slightly reduced in comparison to Fig. 7, with R^2 values > 0.994. Note also that the mast dataset is exactly the same in both Figs. 7 and 9.

Wind speed comparisons at 57.5 m a.g.l. are displayed in Fig. 10. Although the fitted WFCs are the same as in the hub height comparison (Fig. 9), the lidar estimates deviate from the cup measurements by $2\,\%$ for ZDM and $0.7\,\%$, for 5B-Demo. Using short-range V_{los} measurements, the lidar trajectories cover a narrower range of heights (in this case, ~ 60–100 m a.g.l.). The comparison height is outside this range, which may explain the larger deviations observed here in the lidar estimates of wind speed. Another plausible source of deviation at this height could be mast shadowing effects affecting the side-mounted cup anemometer's measurements, although in the chosen wind direction sector the boom is outside the wake of the mast.

4.3 Summary of WFR results

A summary of all results is given in Table 2. Four cases of data filtering are analysed:

1. Joint datasets for the restricted wind sector $[93°, 123°]$ (displayed in Figs. 7 and 9).

Table 2. Summary of comparison results between lidar-estimated and mast-measured horizontal wind speed, at hub height.

Data filtering		Reconstruction case		Forced linear regressions results			
Case	Direction sector	Dataset	Lidar	Input measurement ranges	Gain	R^2	Number of periods
1	$[93°, 123°]$	Joint	5B-Demo, 5 LOS	2.0 D_{rot}	1.0146	0.9936	885
			ZDM, 6 LOS	2.5 D_{rot}	1.0090	0.9938	
			5B-Demo, 5 LOS	from 0.5 to 1.15 D_{rot}	1.0063	0.9944	
			ZDM, 6 LOS	from 0.3 to 1.25 D_{rot}	0.9961	0.9947	
2	$[93°, 123°]$	Disjoint	5B-Demo, 5 LOS	2.0 D_{rot}	1.0133	0.9953	1476
			ZDM, 6 LOS	2.5 D_{rot}	1.0080	0.9942	2143
			5B-Demo, 5 LOS	from 0.5 to 1.15 D_{rot}	1.0057	0.9961	1123
			ZDM, 6 LOS	from 0.3 to 1.25 D_{rot}	0.9965	0.9962	2659
3	$[120°, 219°]$ (IEC free sector)	Joint	5B-Demo, 5 LOS	2.0 D_{rot}	1.0059	0.9848	2815
			ZDM, 6 LOS	2.5 D_{rot}	1.0028	0.9841	
			5B-Demo, 5 LOS	from 0.5 to 1.15 D_{rot}	0.9997	0.9877	
			ZDM, 6 LOS	from 0.3 to 1.25 D_{rot}	0.9923	0.9885	
4	$[120°, 219°]$ (IEC free sector)	Disjoint	5B-Demo, 5 LOS	2.0 D_{rot}	1.0041	0.9840	4588
			ZDM, 6 LOS	2.5 D_{rot}	1.0038	0.9860	5615
			5B-Demo, 5 LOS	from 0.5 to 1.15 D_{rot}	0.9988	0.9888	4099
			ZDM, 6 LOS	from 0.3 to 1.25 D_{rot}	0.9935	0.9897	6199

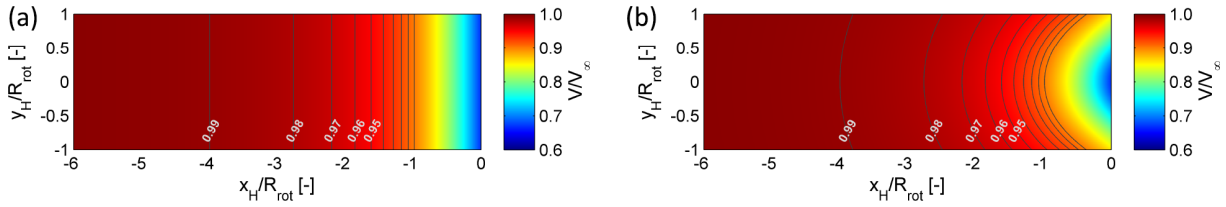

Figure 11. Analytical flow field in the induction zone of a wind turbine, at hub height and with an induction factor $a = 0.334$. **(a)** One-dimensional model (Eq. 10). **(b)** Two-dimensional model.

2. Disjoint datasets for the restricted wind sector $[93°, 123°]$.

3. Joint datasets for the "IEC" undisturbed sector $[120°, 219°]$.

4. Disjoint datasets for the "IEC" undisturbed sector $[120°, 219°]$.

In the disjoint case, filters are applied independently to each lidar and reconstruction cases, and then combined with the mast and turbines' filters. In the joint case, all filters are combined.

Cases (1) and (2) show an overestimation of 1–1.5 % between the lidar estimates and mast measurements using the wind model and a single lidar measurement range. In the undisturbed sector (cases 3 and 4), the overestimation is only of 0.5 %, which may be attributed to the mast being most of the time outside the turbine's induction. Moreover, the coefficients of determination values drop significantly, to approximately 0.9850. A plausible explanation is the larger separation between the lidar measurement points and the mast location causing decorrelation between the wind speed signals.

Multi-distance reconstruction cases including the simple induction model provide robust estimates of wind speed at hub height, with observed gain errors within 0.5 %. Retrieving accurate estimates of free-stream wind characteristics based on nacelle lidar near flow measurements thus proves to be feasible. However, the wind speed comparison results are not as consistent at the 57 m height a.g.l. Using the short-range measurements, the covered range of heights is more narrow and the quality of fit of the shear characteristic may be impaired.

In all of the four cases, 5B-Demo overestimates the wind speed by 0.5–1.0 % compared to ZDM. Comparisons in V_{los} between the two lidars were performed for closely located measurement points. The difference in reconstructed speed is consistent with the difference observed in V_{los} comparisons. Correcting the lidars V_{los} measurements according to the calibration relations would bring the speed estimates from both systems closer, but cannot fully explain the difference. In cases (2) and (4), the valid number of data points is lower for 5B-Demo than for ZDM. This is due to dust and salts accumulating on the 5B-Demo windows during summer, causing lower power levels in the emitted and backscattered signals,

and to the lack of an automatic cleaning system for this prototype lidar. The issue is more significant at ranges further from the 5B-Demo lidar's focus point: for example, the valid periods are twice as numerous when applying the wind model at the $1.0D_{\mathrm{rot}}$ rather than the $2.0D_{\mathrm{rot}}$ measurement range.

Plausible explanations for biases between the two WFR models are as follows:

- signal extinction at long ranges can yield lower-quality V_{los} measurements;
- lower coherence at long ranges: due to increased spatial separation between V_{los} measurement locations;
- lidar volume averaging effects: at large distance, and for LOS oriented downwards, the lidars probe heights where strong non-linear wind shear occurs.

5 Discussions

5.1 On modelling improvements in lidar WFR

The induction model used in this paper is one-dimensional. It accounts only for the streamwise variation of the flow and neglects any radial dependency of the induction. The induction model therefore assumes constant loading of the rotor. In reality, the thrust generation varies with the radial coordinate due to the blades aerodynamic profile.

Within the UniTTe project, Reynolds-averaged Navier–Stokes simulations were carried out for a variety of turbine sizes and rotor designs (Troldborg and Meyer Forsting, 2017). The turbine-induced flow field proves to be self-similar. A two-dimensional engineering model of the induction was also proposed, by adjusting Eq. (10). Figure 11 displays analytical induction flow fields respectively generated with the one- (Fig. 11a) or two-dimensional models (Fig. 11b). Although the radial evolution of the induction seems to be only significant at distances lower than 2 rotor radii, such a more advanced description of the flow field may be implemented as part of the WFR and improve the wind-induction model adequacy.

Regarding lidar modelling, in this paper we performed point-like simulations of V_{los} measurements. The lidar model could be enhanced by integrating the lidar probe volume weighting function. The simulation of the V_{los} measurement would then be carried out by choosing a discrete number of points along the lidar beam path and associating weights with each point.

5.2 On free-stream wind in power performance testing

In the power performance norms (IEC 61400-12-1 and IEC 61400-12-2), free-stream wind speed is defined as "the horizontal component of free stream wind that would exist at the position of the centre of the turbine's rotor if the turbine were not present". It is therefore impossible to measure free-stream wind directly.

The wind speed measured by a cup anemometer top-mounted on a met mast typically located $2.5D_{\mathrm{rot}}$ from the turbine is only an approximation of V_{∞}. When the turbine is closely aligned with the mast and operates at a high thrust coefficient (below rated speed), the $2.5D_{\mathrm{rot}}$ wind already experiences a deficit in speed of the order of 0.5 % or more. In opposition, the combined wind-induction model estimates the true free-stream wind speed, the V_{∞} characteristic.

5.3 Advantages and limitations of measuring with a mast or nacelle-based lidars

The mast-based power performance procedures were originally designed for turbines of much smaller size than modern megawatt ones. For large modern turbines, these procedures have the following limitations:

- The uneconomical cost of tall masts, particularly offshore.
- The decorrelation between power and wind speed signals: for a 120 m rotor diameter turbine, the mast must be placed 300–500 m from the turbine. Over such large distances, significant decorrelation phenomena occur.
- Reduced undisturbed wind sector: e.g. when the mast is in the wake of neighbouring turbines.

Mast-based measurements rely on well-established anemometry techniques (cup or sonic anemometers). This constitutes the main strength of current power performance procedures.

In contrast, WFR from lidars requires hypotheses on the flow inherent to their measurement principles. These hypotheses may be questionable. However, we demonstrated in this paper that model-fitting WFR from nacelle-based lidar short-range measurements takes advantage of the enhanced spatial information – the wind being probed at multiple heights and upstream distances – and provides robust estimates of true free-stream wind.

Lidar short-range measurements techniques overcome both the current technological range limitation of nacelle-based systems and the aforementioned signal decorrelation issues. Additionally, close to the turbine, induction effects are anticipated to prevail over terrain ones (Forsting et al., 2016). Short-range nacelle lidar measurements might also open the path towards free-stream wind estimations in situations where it cannot be measured, such as in complex terrain or perhaps in an offshore array (due to wake interaction).

6 Conclusions

In this paper we presented a wind field reconstruction technique applicable to nacelle-based profiling lidars and providing wind speed estimations designed to be suitable for power performance verification. The method fits 10 min averaged lidar measurements to an assumed wind model by minimising

the error between lidar-measured and wind model-estimated line-of-sight velocities.

Experimental data from a 7-month measurement campaign conducted in Nørrekær Enge, Denmark, was used to compare wind field characteristics estimates obtained with nacelle lidars and an IEC-compliant meteorology mast. Identical wind field reconstruction algorithms were applied independently to two commercially developed nacelle lidars.

The profiling capabilities of the five-beam Avent Demonstrator and of the ZephIR Dual Mode lidar systems allowed for defining flow models yielding estimates of wind speed, direction and vertical shear. Such a wind model was applied to measurements taken first at a single distance far upstream of the turbine. The model proved its ability to provide consistent wind speed estimations at several heights: lidar-estimated and mast-measured wind speeds agreed with an error of approximately 1–1.5 %.

Next, the turbine's induction was accounted for by integrating a simple induction model – derived from the vortex sheet and the actuator disk theories – into the reconstruction algorithms. Utilising the combined wind-induction model, free-stream wind characteristics were estimated by fitting lidar measurements taken at several distances close to the rotor. This innovative method provides robust estimates of the free-stream wind speed. Wind speeds reconstructed at the mast distance and hub height were within 0.5 % of cup anemometer measurements.

The reconstruction algorithm developed here can be applied to any type of nacelle-based wind lidar system and any type of wind turbine rotor.

Data availability. The research work presented in this article is part of a project where strict confidentiality agreements were made with several industrial partners (lidar manufacturers, turbine manufacturer, wind farm owner). Consequently, the data cannot be publicly accessed.

Author contributions. Antoine Borraccino conducted the research work and wrote the paper. David Schlipf and Florian Haizmann extensively contributed to the development of the wind field reconstruction method. Rozenn Wagner supervised the research work and contributed to the structure of the paper. All co-authors participated in the conception of the manuscript.

Competing interests. The authors declare that they have no conflict of interest.

Acknowledgements. The research work carried out and reported in this paper was performed under the Unified Turbine Testing (www.UniTTe.dk) project lead by DTU Wind Energy and funded by Innovation Fund Denmark. The two lidar systems providing the measurement data used in the study were kindly provided by the manufacturers, ZephIR Lidar and Avent Lidar Technology. The authors are thankful for the support, in particular that of Matthieu Boquet and Paul Mazoyer on Avent's side and Michael Harris and Chris Slinger on ZephIR's side. Thanks to Vattenfall and Siemens Wind Power for providing the site and turbine to conduct the measurement campaign. Thanks also to Andrea Vignaroli, Carsten Weber Kock and DTU Wind Energy's Test and Measurement section, whose work ensured the acquisition of high-quality datasets, and to Rozenn Wagner for all the valuable advice. We would also like to acknowledge the contributions of Alexander Meyer Forsting and Niels Troldborg, whose expertise in flow modelling provided confidence in the use of simple induction models.

Finally, special thanks to Stuttgart Wind Energy's group for welcoming Antoine Borraccino during a 3-month stay. This work would not have been possible, and certainly not as productive, without the support and contributions of David Schlipf and Florian Haizmann.

Edited by: S. Aubrun
Reviewed by: S. Feeney and D. Di Domenico

References

Angelou, N., Mann, J., Sjöholm, M., and Courtney, M.: Direct measurement of the spectral transfer function of a laser based anemometer, Rev. Sci. Instrum., 83, 033111, doi:10.1063/1.3697728, 2012.

Borraccino, A. and Courtney, M.: Calibration report for ZephIR Dual Mode lidar (unit 351), Tech. Rep., DTU Wind Energy, Denmark, http://orbit.dtu.dk/files/123699869/Calibration_report_for_ZephIR.pdf, 2016a.

Borraccino, A. and Courtney, M.: Calibration report for Avent 5-beam Demonstrator lidar, Tech. Rep., DTU Wind Energy, Denmark, http://orbit.dtu.dk/files/123699807/Calibration_report_for_Avent.pdf, 2016b.

Borraccino, A., Courtney, M., and Wagner, R.: Generic Methodology for Field Calibration of Nacelle-Based Wind Lidars, Remote Sens., 8, 907 pp., doi:10.3390/rs8110907, 2016.

Branlard, E. and Gaunaa, M.: Cylindrical vortex wake model: right cylinder, Wind Energy, 18, 1973–1987, doi:10.1002/we.1800, 2015.

Forsting, A. R. M., Bechmann, A., and Troldborg, N.: A numerical study on the flow upstream of a wind turbine in complex terrain, J. Phys. Conf. Ser., 753, 032041, doi:10.1088/1742-6596/753/3/032041, 2016.

Hardesty, R. M. and Weber, B. F.: Lidar Measurement of Turbulence Encountered by Horizontal-Axis Wind Turbines, J. Atmos. Ocean. Tech., 4, 191–203, doi:10.1175/1520-0426(1987)004<0191:lmoteb>2.0.co;2, 1987.

Högström, U.: Non-dimensional wind and temperature profiles in the atmospheric surface layer: A re-evaluation, Bound.-Lay. Meteorol., 42, 55–78, doi:10.1007/BF00119875, 1988.

Holtslag, M. C., Bierbooms, W. A. A. M., and van Bussel, G. J. W.: Estimating atmospheric stability from observations and correcting wind shear models accordingly, J. Phys. Conf. Ser., 555, 012052, doi:10.1088/1742-6596/555/1/012052, 2014.

IEC: IEC 61400-12-1 FDIS, Power performance measurements of electricity producing wind turbines, IEC, 2016.

Marquardt, D. W.: An Algorithm for Least-Squares Estimation of Nonlinear Parameters, J. Soc. Ind. Appl. Math., 11, 431–441, doi:10.1137/0111030, 1963.

Mazoyer P., B. M.: Retrieving wind speed at constant height above ground level in complex terrain with a Wind Iris 4-beam nacelle Lidar, in: Wind Europe Summit 2016, https://windeurope.org/summit2016/conference/allposters/PO263.pdf, 2016.

Medici, D., Ivanell, S., Dahlberg, J., and Alfredsson, P. H.: The upstream flow of a wind turbine: blockage effect, Wind Energy, 14, 691–697, doi:10.1002/we.451, 2011.

Medley, J., Barker, W., Harris, M., Pitter, M., Slinger, C., Mikkelsen, T., and Sjöholm, M.: Evaluation of wind flow with a nacelle-mounted, continuous wave wind lidar, in: EWEA 2014 conference, http://www.zephirlidar.com/wp-content/uploads/2014/09/PO162_Full_Paper_Submitted.pdf, 2014.

Peña, A., Floors, R., Sathe, A., Gryning, S.-E., Wagner, R., Courtney, M. S., Larsén, X. G., Hahmann, A. N., and Hasager, C. B.: Ten Years of Boundary-Layer and Wind-Power Meteorology at Høvsøre, Denmark, Bound.-Lay. Meteorol., 158, 1–26, doi:10.1007/s10546-015-0079-8, 2016.

Raach, S., Schlipf, D., Haizmann, F., and Cheng, P. W.: Three Dimensional Dynamic Model Based Wind Field Reconstruction from Lidar Data, J. Phys. Conf. Ser., 524, 012005, doi:10.1088/1742-6596/524/1/012005, 2014.

Sathe, A., Mann, J., Gottschall, J., and Courtney, M. S.: Can Wind Lidars Measure Turbulence?, J. Atmos. Ocean. Tech., 28, 853–868, doi:10.1175/JTECH-D-10-05004.1, 2011.

Schlipf, D.: Lidar-assisted control concepts for wind turbines, Ph.D. thesis, Institute of Aircraft Design, University of Stuttgart, doi:10.18419/opus-8796, 2016.

Schlipf, D., Rettenmeier, A., Haizmann, F., Hofsäß, M., Courtney, M., and Cheng, P. W.: Model Based Wind Vector Field Reconstruction from Lidar Data, in: Proceedings of the German Wind Energy Conference DEWEK, Bremen, Germany, 2012.

Schlipf, D., Simley, E., Lemmer, F., Pao, L., and Cheng, P. W.: Collective Pitch Feedforward Control of Floating Wind Turbines Using Lidar, Journal of Ocean and Wind Energy, 2, 223–230, doi:10.17736/jowe.2015.arr04, 2015.

Simley, E., Angelou, N., Mikkelsen, T., Sjöholm, M., Mann, J., and Pao, L. Y.: Characterization of wind velocities in the upstream induction zone of a wind turbine using scanning continuous-wave lidars, J. Renewable Sustainable Energy, 8, 013301, doi:10.1063/1.4940025, 2016.

Sørensen, J. N.: General Momentum Theory for Horizontal Axis Wind Turbines, vol. 4 of Research Topics in Wind Energy, Springer International Publishing, SSN: 2196-7806, doi:10.1007/978-3-319-22114-4, 2016.

Towers, P. and Jones, B. L.: Real-time wind field reconstruction from LiDAR measurements using a dynamic wind model and state estimation, Wind Energy, 19, 133–150, doi:10.1002/we.1824, 2016.

Troldborg, N. and Meyer Forsting, A.: Simulations of wind turbine induction in uniform inflow, Wind Energy, submitted, 2017.

Vasiljevic, N., Lea, G., Courtney, M., Cariou, J.-P., Mann, J., and Mikkelsen, T.: Long-Range WindScanner System, Remote Sens., 8, 896, doi:10.3390/rs8110896, 2016.

Vignaroli, A. and Kock, C.: UniTTe MC2 Nårrekær Enge Measurement System & Calibration report, DTU Wind Energy, Denmark, 2016.

Wagner, R. and Davoust, S.: Nacelle lidar for power curve measurement – Avedøre campaign, Tech. rep., DTU Wind Energy, Denmark, http://findit.dtu.dk/en/catalog/2185764001, projektno.: EUDP: Nacelle lidar for power performance measurement (journal no. 64009-0273), 2013.

Wagner, R., Pedersen, T., Courtney, M., Antoniou, I., Davoust, S., and Rivera, R.: Power curve measurement with a nacelle mounted lidar, Wind Energy, 17, 1441–1453, doi:10.1002/we.1643, 2014.

3.3 Results for secondary wind characteristics

In this section, results obtained on secondary WFC such as yaw misalignment θ_r, shear exponent α_exp and axial induction factor a_ind are presented.

The results correspond to the datasets of case (3) (see Table 2, Page 56). Similarly to the wind speed results in the journal article, the following reconstruction cases are considered:

- WFR using the 'wind' model, and lidar measurements at:
  - $2D_\mathrm{rot}$ for 5B-Demo;
  - $2.5D_\mathrm{rot}$ for ZDM;
- using the combined 'wind-induction' model, and lidar measurements close to the rotor at:
  - four distances between 0.5 and $1.2D_\mathrm{rot}$ for 5B-Demo;
  - three distances between 0.3 and $1.2D_\mathrm{rot}$ for ZDM (see Table 1, Page 53).

3.3.1 Yaw misalignment

The yaw misalignment is of interest for several wind turbine applications. It is for instance an input to the turbine controller used to determine when to activate the yaw motor in order to move the turbine towards the wind. Nacelle lidars' measurements are being more and more often considered to correct the wind direction sensor measurements – typically a nacelle-mounted vane or a 3D sonic anemometer. In the case where the vane measurements are biased due to mounting issues or disturbed by the turbine's operation, identifying and correcting measurement biases of yaw direction allow to extract more power.

Fig. 3.12 and Fig. 3.13 display scatter plots of the relative wind direction θ_r estimated by the 5B-Demo (b), ZDM (c), and by the spinner anemometer (a) (Pedersen et al., 2014), as a function of the wind speed by the mast top-mounted cup anemometer. The spinner sonic anemometer is considered hereafter as the reference sensor since it was calibrated on site.

In Fig. 3.12, the wind model (see Sect. 2.4.1, Page 49) is applied to the lidar measurements at $2.0D_\mathrm{rot}$ and $2.5D_\mathrm{rot}$ respectively for 5B-Demo and ZDM. The reconstructed θ_r values are similar for both lidars and significantly more scattered than the spinner sonic anemometer estimates. At low wind speed, the scatter is increased, due to higher inhomogeneities in the flow. Above $6\,\mathrm{m\,s^{-1}}$, the bin-average trends are consistent for the three measurement systems, although a bias is observed: the yaw misalignment is within $[-2°, 0°]$ for the two lidars and approximately $-3°$ for the spinner sonic anemometer.

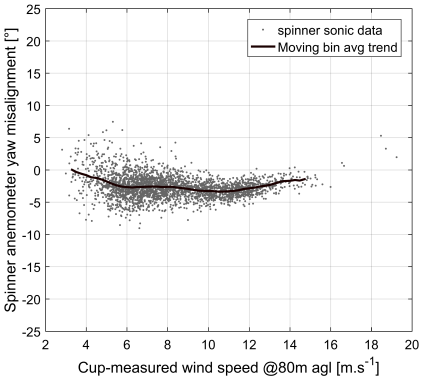

(a) spinner anemometer

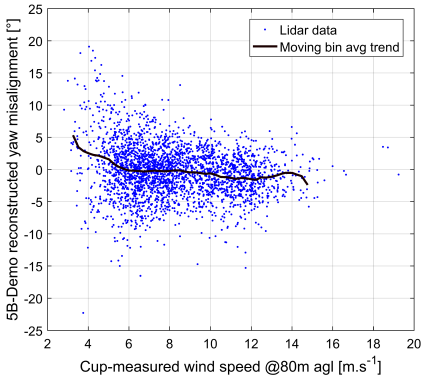

(b) 5B-Demo

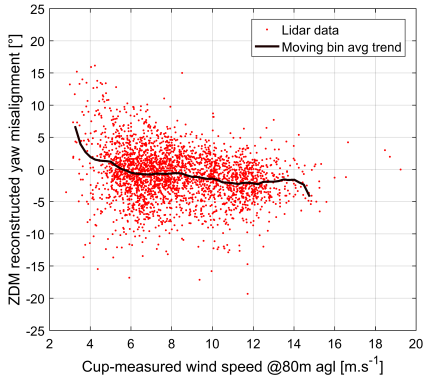

(c) ZDM

Figure 3.12: Yaw misalignment measurements as a function of cup-measured hub height wind speed, Nørrekær Enge campaign. Lidar WFR performed using the 'wind' model and measurements close to the mast distance.

In Fig. 3.13, the short-range measurement technique is used by applying the combined wind-induction model (see Sect. 2.4.2, Page 50) to the lidar measurements at multiple distances close to the rotor. Compared to Fig. 3.12, the main difference is a clear scatter reduction in the lidar estimates of θ_r. This is due to the lower physical separation between the lidar probed measurement points than when using long measurement ranges. Additionally, the three systems' bin-average θ_r values show good agreement.

The yaw misalignment results indicate a satisfactory alignment of the lidar systems to the turbine's centerline during their installation on the nacelle. And, no significant disturbance of the turbine yaw alignment was observed due the presence of the two nacelle lidars on the nacelle – this was checked pre- and post-installation. Note also that by adding the yaw misalignment to the turbine yaw position angle, the wind direction can be retrieved – understood here in its conventional

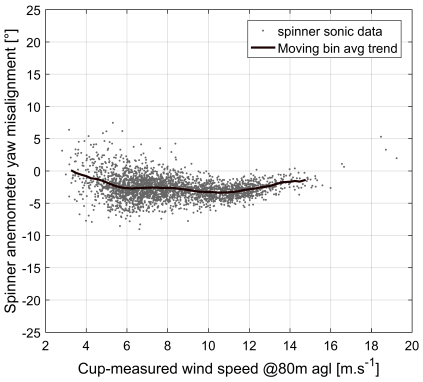

(a) spinner anemometer

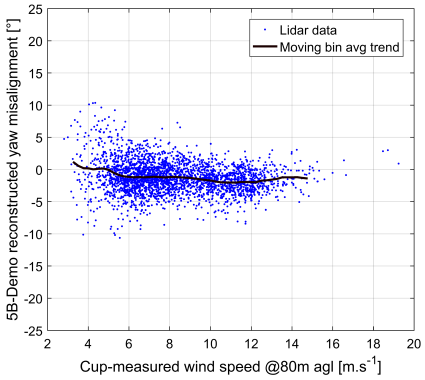

(b) 5B-Demo

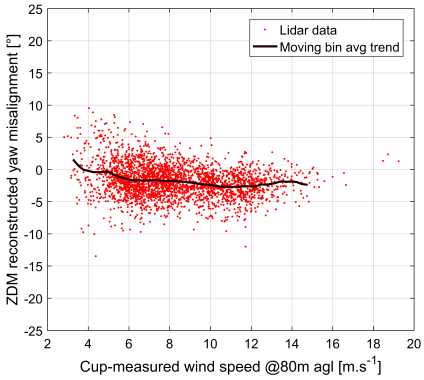

(c) ZDM

Figure 3.13: Yaw misalignment measurements as a function of cup-measured hub height wind speed, Nørrekær Enge campaign. Lidar WFR performed using the 'wind-induction' model and measurements close to the turbine rotor.

meteorological definition (0° for Northern winds, positive in the clockwise direction).

For the existing and upcoming very large turbines ($D_{\text{rot}} > 150\,\text{m}$), measuring at long distances for yaw misalignment studies is most likely not best. At long ranges, the lidar measurement points are indeed separated by large distances of approximately 100 m (assuming half-opening or cone angle of 15°). Reducing the opening or cone angle of the nacelle lidar trajectory would not necessarily be a beneficial solution to this issue as the lidar's various LOSs would be close to co-linear, and the cross-stream wind speed contamination insufficient to accurately reconstruct θ_{r}.

Albeit the wind-induction model seem to provide better estimates of yaw misalignment, one may question how representative the θ_{r} WFC is of the hub height

free stream wind vector. Computational Fluid Dynamics (CFD) studies have shown that the wind turns outwards when approaching the turbine rotor. Fig. 3.14 shows that the relative wind direction varies as a function of the distance from the turbine. In case of perfect alignment to the free stream wind direction (Fig. 3.14(a)), we can observe that on the edge of the rotor swept area the wind direction has changed by over 1° at $1D_{\mathrm{rot}}$. In Fig. 3.14(b), this turning $\Delta\theta_{\mathrm{r}}$ of the wind when approaching the rotor is shown to depend on the turbine alignment to the free stream wind direction.

In the developed WFR algorithms, the simple induction model was applied only to the wind vector's axial component u, while the cross-stream component v remained constant. Consequently, a turning of the wind is obtained in the induction zone. The combined wind-induction model is consistent with the CFD results.

Consequently, the short-range measurements technique is the most adequate of the two described methods to estimate yaw misalignment using nacelle lidars.

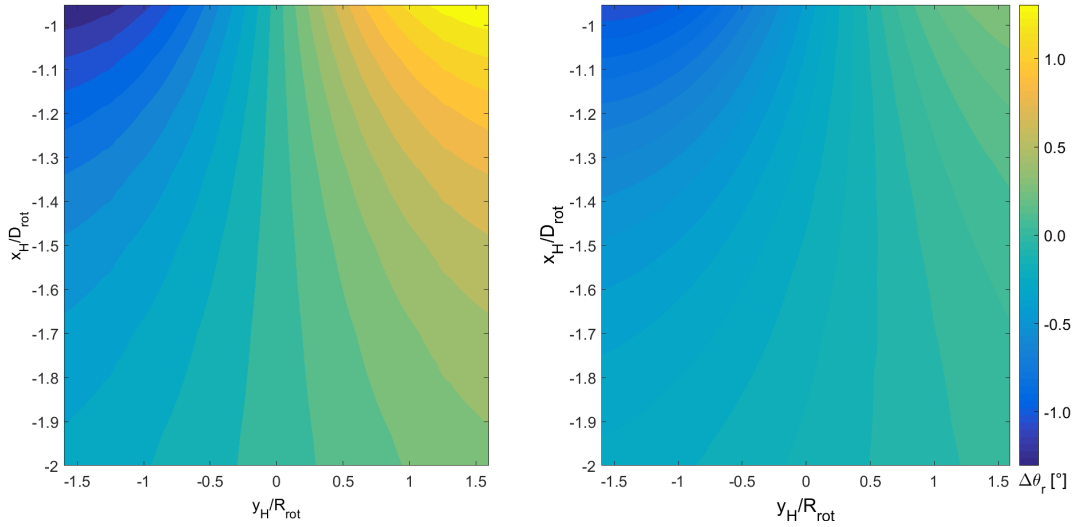

(a) For $\theta_r = 0°$ (in free stream)

(b) For $\theta_r = 30°$ (in free stream)

Figure 3.14: Evolution of wind direction in the induction zone of a wind turbine, simulated with CFD, at high thrust ($C_{\mathrm{T}} = 1.0$). $(x_{\mathrm{H}}, y_{\mathrm{H}})$ are coordinates expressed in the hub system (see Table 2, Page 46).
Credit: Alexander Meyer-Forsting (*DTU Wind Energy*).

3.3.2 Shear exponent

The lidar-estimated shear exponent α_{exp} is compared to a reference value derived from the mast top-mounted cup anemometer wind speed measurements at 80 m and 57.5 m agl, see Fig. 3.15 and Fig. 3.16.

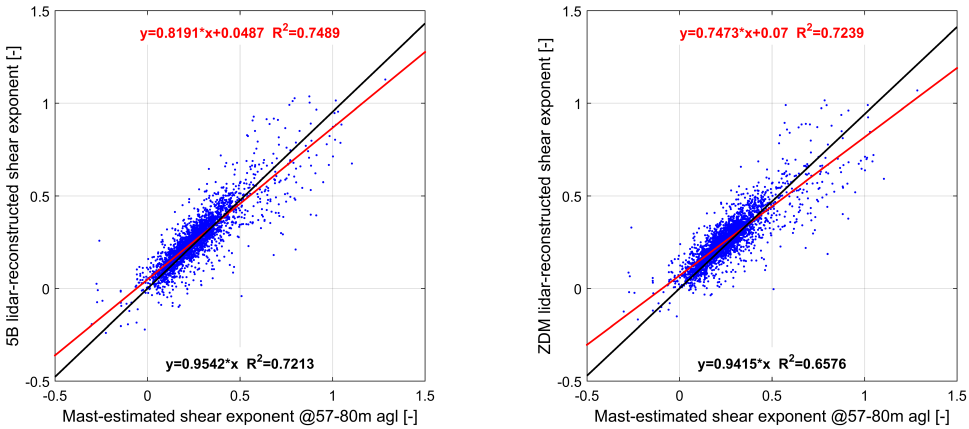

(a) 5B-Demo **(b)** ZDM

Figure 3.15: Comparison between mast-derived and lidar-estimated shear exponent. Lidar WFR performed using the 'wind' model and measurements close to the mast distance.

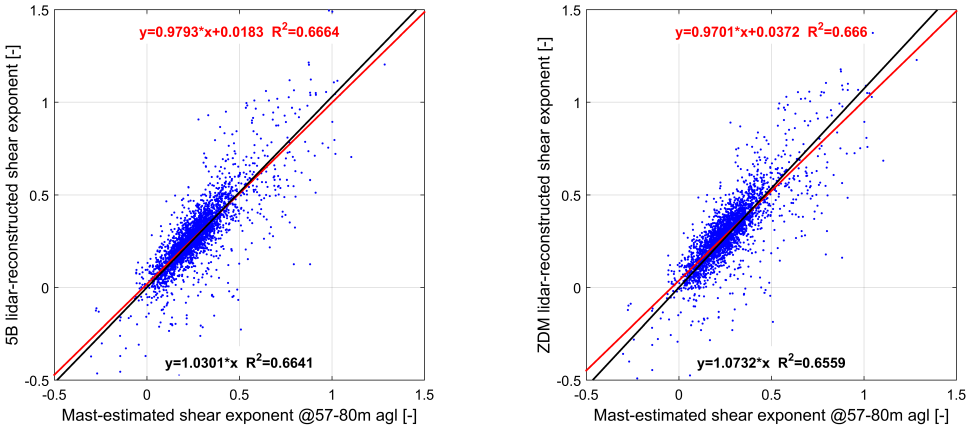

(a) 5B-Demo **(b)** ZDM

Figure 3.16: Comparison between mast-derived and lidar-estimated shear exponent. Lidar WFR performed using the 'wind-induction' model and measurements close to the turbine rotor.

A large majority of the estimated α_{exp} values fall within a $[0, 0.5]$ range , which is compatible with expectations of power-law shear profiles in the ABL.

The forced linear regressions' gain values indicate an agreement within 5 % between the lidar- and mast-based estimates of α_{exp}. Although a clear linear correlation is observed, the scatter is high ($R^2 \approx 0.65$). Results are comparable for both systems independently of the two considered WFR models. Using short-range lidar measurements and the combined 'wind-induction' model (Fig. 3.16), the shear exponent is overestimated compared to the case where the 'wind' model is used. This may be attributed to the different probed measurement heights – approximately $[60\,\text{m}, 100\,\text{m}]$ agl. and $[35\,\text{m}, 125\,\text{m}]$ agl. respectively for the short-range measurements and the ones close to the mast. To some extent, the difficulty for the WFR optimisation algorithm to separate the shear from the induction effects may also explain the observed differences.

Considering the mast wind speed measurements are taken only at and below hub height – whilst the lidars also probe the wind above H_{hub} –, the lidar-estimated α_{exp} is likely more representative of the wind shear profile driving the wind turbine than the one derived from the mast.

3.3.3 Induction factor

3.3.3.1 Testing of the induction model

The axial induction factor a_{ind} is one of the four WFC of the combined wind-induction model. Therefore, I only consider here the reconstruction case using lidar measurements close to the rotor. In essence, a_{ind} quantifies the longitudinal variation of wind speed upstream of the turbine's rotor. The axial induction factor can be defined as the non-dimensional (streamwise) speed deficit at the rotor plane ($x_{\text{H}} = 0$), mathematically given by

$$a_{\text{ind}} = \frac{V_\infty - V\,(x_{\text{H}} = 0)}{V_\infty}\ . \tag{3.1}$$

The above mathematical definition is valid when the turbine yaw is perfectly aligned with the wind direction. In a yawed case, the V symbols must simply be replaced by u as the turbine generates thrust almost entirely from the streamwise component. In the combined wind-induction reconstruction model, the induction model was effectively applied to the u component of the wind vector.

Furthermore, the induction model defines the variation of the wind speed upstream of the turbine rotor as follows:

$$\frac{V\left(x_{\mathrm{H}}=0\right)}{V_{\infty}}=1-a_{\mathrm{ind}}\left(1+\frac{\xi}{\sqrt{1+\xi^{2}}}\right)\ , \tag{3.2}$$

where $\xi = x_{\mathrm{H}}/R_{\mathrm{rot}}$ is the non-dimensional distance from the rotor, and takes negative values upstream.

The validity of this simple induction model is demonstrated in Fig. 3.17. For these graphs, the hub height wind speed V_{H} was estimated for 5B-Demo and ZDM using the wind model, and applied successively to each measurement distance (see Table 1, Page 53). Therefore, Fig. 3.17(a) and Fig. 3.17(b) plot a total of 2815 data points at each distance. V_{H} was made non-dimensional by dividing it by the free stream wind speed V_{∞} estimated from the wind-induction model and lidar measurements close to the rotor. Additionally, the induction model of Eq. (3.2) is plotted for reference induction factors $a_{\mathrm{ind}} \in [0.1, 0.5]$.

We can observe in the two scatter plot figures that the evolution of the wind speed is close to what is predicted by the wind-induction model. However, it is highly scattered, which suggests that a_{ind} values depend on other parameters – at the very least a_{ind} is known to be wind speed dependent.

Consequently, the 10 min non-dimensional speed $V_{\mathrm{H}}/V_{\infty}$ was averaged per V_{∞} wind speed bins, with a width chosen to $0.5\,\mathrm{m\,s^{-1}}$. The results are displayed in Fig. 3.17(c) and Fig. 3.17(d). In these plots, we can already see that the combined wind-induction model fits well the evolution of the wind speed upstream the turbine's rotor. It can also be anticipated that the induction factors reconstructed values were higher for 5B-Demo than for ZDM (see Fig. 3.18).

The fitting of the induction factor by the optimiser – in our case the Levenberg-Marquardt algorithm – during wind field reconstruction is facilitated when using measurement distances close to the rotor plane, for instance below one rotor diameter. The local gradients - slopes of tangent to the reference curves – are orders of magnitude higher close to the rotor than farther, and thus the fitting of a_{ind} is less sensitive to LOS velocity measurement errors due either to measurement uncertainty or flow inhomogeneities.

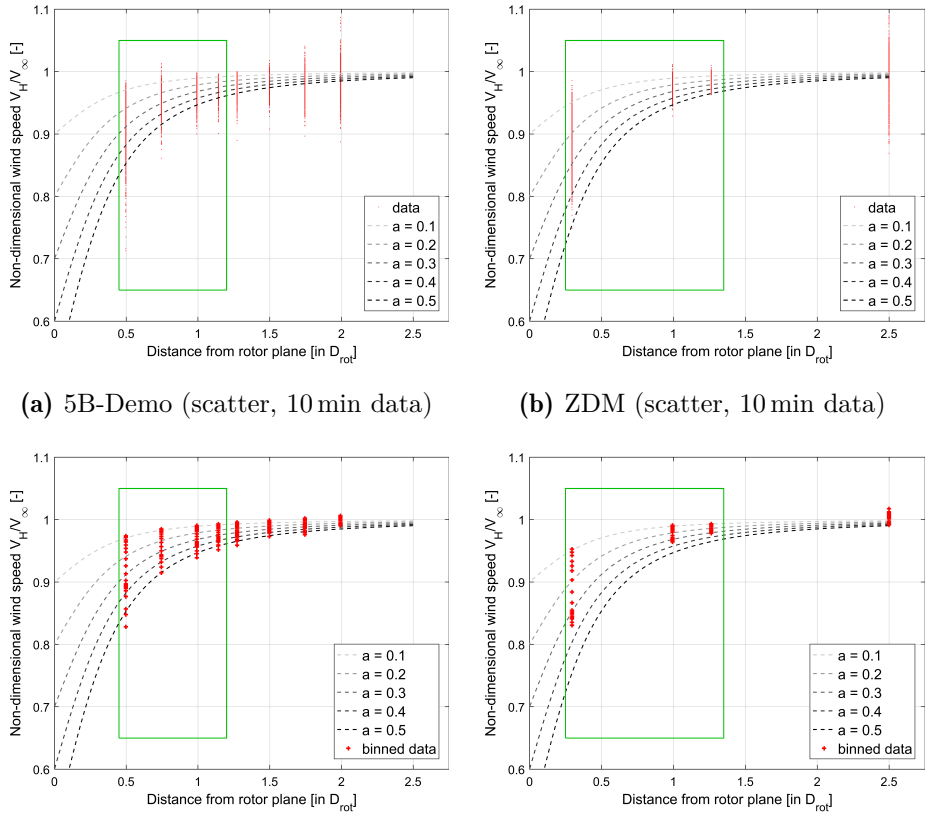

(a) 5B-Demo (scatter, 10 min data)

(b) ZDM (scatter, 10 min data)

(c) 5B-Demo (binned data)

(d) ZDM (binned data)

Figure 3.17: Lidar-reconstructed wind speed as a function of the upstream distance to the rotor plane. The green rectangles show which measurement distances where used to estimated V_∞ from the lidar V_{los} measurements in the combined wind-induction reconstruction case.

3.3.3.2 Induction factor curve

Fig. 3.18 displays the reconstructed a_{ind} as a function of the lidar-estimated free stream wind speed V_∞. Simulations were also conducted for a number of wind speeds using the *HAWC2* aero-servo-elastic code and the Siemens 2.3 MW turbine model of the NKE farm (credit: N. Dimitrov, *DTU Wind Energy*).

The *HAWC2* curve of a_{ind} is reasonably well reproduced by the nacelle lidar experimental data. The spread is reduced at wind speeds $V_\infty > 8\,\text{m}\,\text{s}^{-1}$. This may be caused by the increased turbulence at low speeds and the turbine's response to rapidly varying upstream flow conditions. At $V_\infty < 5\,\text{m}\,\text{s}^{-1}$, abnormally high (up to 0.8) and low values (down to 0.1) are observed. The developed WFR models assume stationarity, which is particularly violated at low speeds where the turbine

is likely to operate at different regimes within a 10-minute period.

Below $8\,\mathrm{m\,s^{-1}}$, a_{ind} bin-averaged values are within $[0.35, 0.37]$ and $[0.30, 0.33]$ respectively for 5B-Demo and ZDM. Both lidar show an overestimation of a_{ind} compared to the *HAWC2* simulation results. The clear differences observed between the two lidar systems may be due to the different number and separation between the used distances, and possibly also to the different measurement trajectories (no central beam in ZDM).

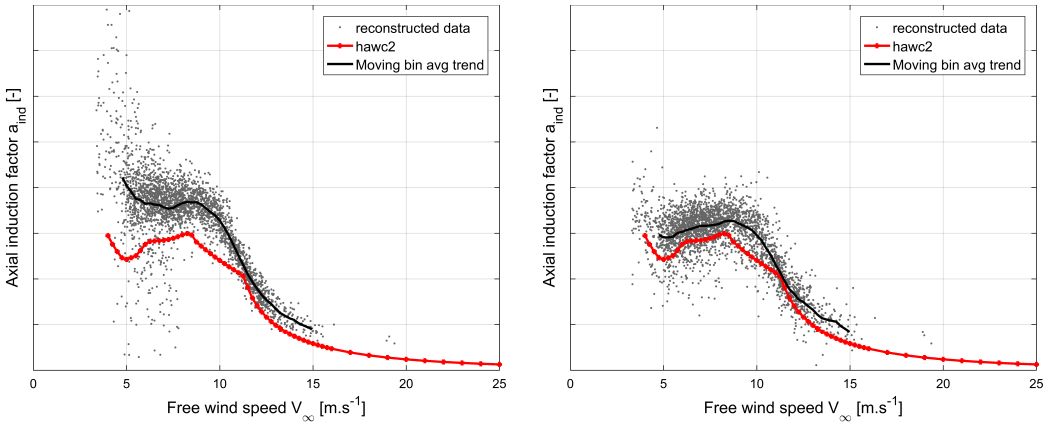

(a) 5B-Demo **(b)** ZDM

Figure 3.18: Lidar-reconstructed axial induction factor as a function of free stream wind speed. Lidar WFR performed using the 'wind-induction' model and measurements close to the turbine rotor. Y-scale removed to ensure confidentiality.

3.3.3.3 Thrust coefficient curve

A wind turbine rotor design is partly characterised by its thrust coefficient curve. The thrust coefficient is particularly important for steady loads analysis and for wake modelling (Nygaard and Hansen, 2016). The induction factor obtained using the combined wind-induction model provides a means to estimate the thrust coefficient – denoted C_{T} – of a wind turbine rotor solely from nacelle lidar measurements. To do so, a relation between C_{T} and a_{ind} must be assumed.

The simplest relation is provided by the one-dimensional momentum theory, which is however invalid at high rotor loadings. This situation is known as the turbulent-wake rotor state. The breakdown of the momentum theory at high loading is typically accounted for in Blade Element Momentum (BEM) codes by applying a tip-loss correction for induction factors above a critical value a_{c} (see summary in Sect. 10.2.2 of Branlard, 2017a). A variety of tip-loss corrections have

been proposed, yielding different relation between C_T (constant loaded rotor) and a_ind. The following relations were here considered:

- using the 1D-momentum theory (no tip-loss correction) (Hansen, 2008):

$$C_\mathrm{T} = 4a_\mathrm{ind}\left(1 - a_\mathrm{ind}\right). \tag{3.3}$$

- a third order polynomial relation (proposed by Madsen et al., 2010):

$$a_\mathrm{ind} = k_3 C_\mathrm{T}^3 + k_2 C_\mathrm{T}^2 + k_1 C_\mathrm{T}, \tag{3.4}$$

  where $k_1 = 0.25116$, $k_2 = 0.05450$, $k_3 = 0.08921$ – based on Glauert's empirical correction and actuator disk CFD simulations. The solving of the 3^{rd} order polynomial was performed numerically. It yielded three real/complex roots, and the real root was chosen as the correct C_T value.

- using a simple correction of the uniformly loaded rotor C_T accounting to some extent for the variability of local thrust coefficients in the radial direction (proposed by Troldborg and Meyer Forsting, 2016):

$$C_\mathrm{T} = \frac{4a_\mathrm{ind}\left(1 - a_\mathrm{ind}\right)}{\gamma}, \tag{3.5}$$

  where $\gamma = 1.1$.

These three $C_\mathrm{T} = f\left(a_\mathrm{ind}\right)$ relations can be visualised in Fig. 3.19. It is clearly visible that significantly different C_T will be obtained for a_ind above the canonical 1/3 value. The 'Troldborg' curve is below the one from the momentum theory and follows the same shape, since it simply scales the momentum theory relation. The 'Madsen' curve is significantly different from the two others approximately for $a_\mathrm{ind} > 0.35$ as this methods attempts at better modelling the turbulent-wake rotor state (high loadings situations).

For the NKE campaign, the turbine on which the nacelle lidars were mounted had been fully instrumented with strain gauges (bending moments at tower top and bottom, blade flap- and edge-wise moments, shaft torque, etc) for the purpose of loads verification. The measurements of tower bottom bending moments can be used to estimate the thrust forces acting on the turbine rotor (Réthoré, 2006; Vignaroli and Kock, 2016). For each 10-minute period, the loads- and mast-based thrust coefficient is then obtained by:

$$C_\mathrm{T} = \frac{T}{\frac{1}{2}\rho_\mathrm{air}\pi R_\mathrm{rot}^2 V_\mathrm{hor}^2}, \tag{3.6}$$

where T is the thrust; V_hor is the wind speed at hub height measured by the top-mounted cup anemometer; ρ_air is the air density derived from pressure, temperature and relative humidity measurements (IEC 61400-12-1, 2017). Note that

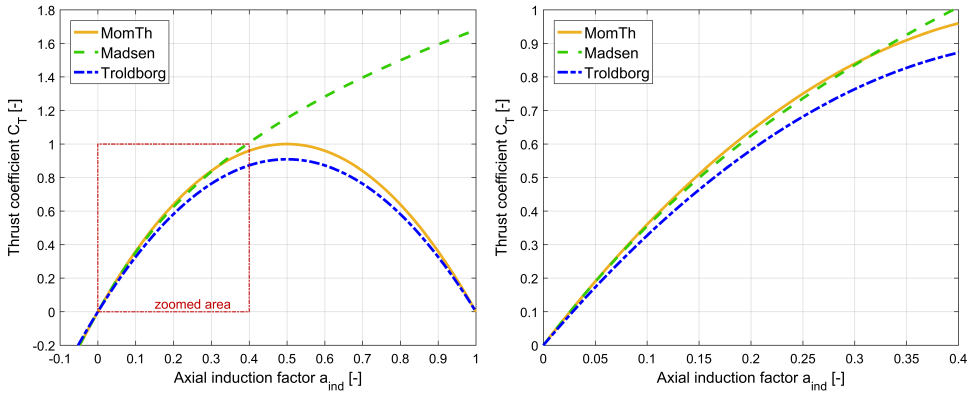

Figure 3.19: The relation between thrust coefficient C_T and axial induction factor a_ind according to several models. The graph on the right is a zoom on the red rectangle.

Réthoré estimated the standard uncertainty on C_T to $4-8\,\%$. The C_T value derived using the loads measurements is only an estimate, and not necessarily the true value.

The estimated C_T were averaged per wind speed bins of $0.5\,\mathrm{m\,s^{-1}}$ width. In Fig. 3.20, the loads- and mast-based C_T curve matches the *HAWC2* values closely at high wind speeds. At low speeds, a clear bias and a large scatter are observed, although the trends are visually similar.

For 5B-Demo and ZDM, the C_T curves are estimated by converting a_ind using the three aforementioned methods. The three methods provide C_T values close to each other at high speeds, and differ significantly at low speeds (high loading) – as expected due to the different theoretical basis between them.

Using the momentum theory method (in yellow) seems to provides the best agreement with the load- and mast-based curve. The 'Troldborg' method (in blue) matches best the *HAWC2* curve, proving its ability to map reasonably well the thrust forces exerting on the rotor to a more theoretical constant loaded case – C_T derived using the thrust resulting from the *HAWC2* simulations of airfoil data and the simulated free stream hub height wind speed. Significant differences between the momentum theory and 'Madsen' methods are only identified at low speeds and for 5B-Demo, due to the abnormally high values of a_ind previously identified in Fig. 3.18(a) and that the two methods are nearly the same except for $a_\mathrm{ind} < 0.35$.

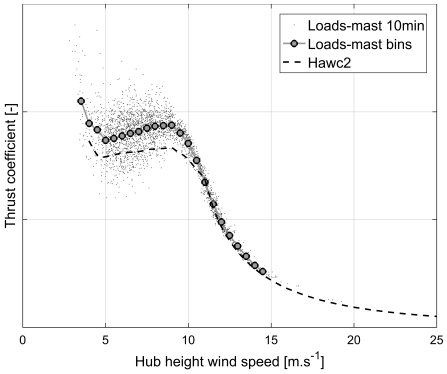

(a) loads- and mast-based measurements

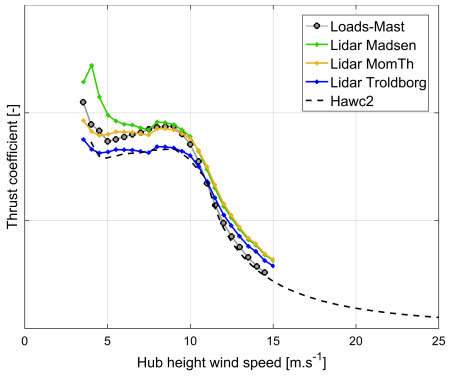

(b) 5B-Demo

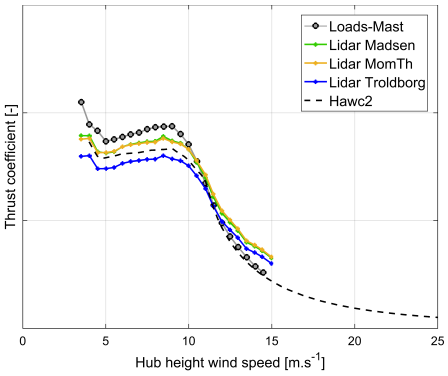

(c) ZDM

Figure 3.20: Thrust coefficient as a function of cup-measured hub height wind speed, Nørrekær Enge campaign. Y-scale removed to ensure confidentiality.

3.4 Wind model adequacy

In this section, the adequacy of the wind- and combined wind-induction models is assessed. To do so, I defined and analysed several model performance indicators – statistical metrics of LOS velocity residuals.

By definition, the behaviour of any physical system – here the wind – is only partially described by a model. Model adequacy – sometimes also called discrepancy – can be defined and assessed through statistical methods (Reggiani and Marchetti, 1975; Goldstein et al., 2013). In essence, a model is adequate for an intended task when it provides unbiased predictions of the physical system's characteristics. Assessing the adequacy of a model allows us to gain confidence in its predictions and requires the quantification of errors.

Note: the question of model adequacy is different from its correct implementation – unless the implementation of the model is itself subject to approximation such as for instance a CFD model for which results can depend on discretisation techniques, grid resolution, etc.

In WFR from lidar measurements, the wind model adequacy is key to retrieving accurate estimates of the WFC. The wind model assumptions yield a simplified representation of the flow field. For instance, it is trivial that a wind model assuming zero wind shear would be inadequate when applied to DWL V_{los} measurements taken at several heights in the ABL. Another example is the situation where a ground-based lidar measures the wind – e.g. using Vertical Azimuth Display (VAD) or Doppler Beam Swinging (DBS) techniques – in complex terrain: the horizontal homogeneity assumption is often violated, therefore yielding large errors (Bingöl et al., 2009; Klaas et al., 2015) and requiring more complex WFR models.

The developed model-fitting WFR methods are based on the minimisation of the vectorial distance between lidar-measured (observations) and model-simulated (predictions) LOS velocities, denoted $\boldsymbol{V}_{\text{los}}$ and $\widehat{\boldsymbol{V}}_{\text{los}}$ respectively. For each measurement period, the residual metrics defined in Table 3.3 are computed. For more details on their meaning, see Yu et al., 2006.

Table 3.3: Metrics used for evaluation of model performance based on residuals between observations and model predictions.

Metrics	**Acronym**	**Mathematical expression***
mean bias	MB	$\frac{1}{N}\sum_{i=1}^{N}\widehat{x}_i - x_i$
mean error	ME	$\frac{1}{N}\sum_{i=1}^{N}\lvert\widehat{x}_i - x_i\rvert$
mean fractional bias	MFB	$\frac{1}{N}\sum_{i=1}^{N}2\frac{\widehat{x}_i - x_i}{\widehat{x}_i + x_i}$
mean fractional error	MFE	$\frac{1}{N}\sum_{i=1}^{N}2\frac{\lvert\widehat{x}_i - x_i\rvert}{\widehat{x}_i + x_i}$
sum of squared error	SSE	$\sum_{i=1}^{N}(\widehat{x}_i - x_i)^2$
mean squared error	MSE	$\frac{\text{SSE}}{N}$
root mean squared error	RMSE	$\sqrt{\text{MSE}}$
normalised mean squared error	NMSE	$\frac{\frac{\text{MSE}}{N}}{\frac{1}{N}\sum_{i=1}^{N}x_i^2}$

*$\boldsymbol{x}$: observations; $\widehat{\boldsymbol{x}}$: model predictions (vectors of length N).

For the V_{los} residuals, we have $x_i = V_{\text{los},i}$ with i from 1 to N_{los} and:

- for the wind model reconstruction cases, $N_{\text{los}} = 5$ for 5B-Demo, $N_{\text{los}} = 5$ for ZDM;
- for the wind-induction model reconstruction cases, $N_{\text{los}} = 4 \times 5$ for 5B-Demo, $N_{\text{los}} = 3 \times 6$ for ZDM.

In the following analysis of V_{los} residuals, only the Mean Bias (MB) and Root Mean Squared Error (RMSE) are considered. Fig. 3.21 and Fig. 3.22 display histograms of MB and RMSE for both nacelle lidars and both WFR models.

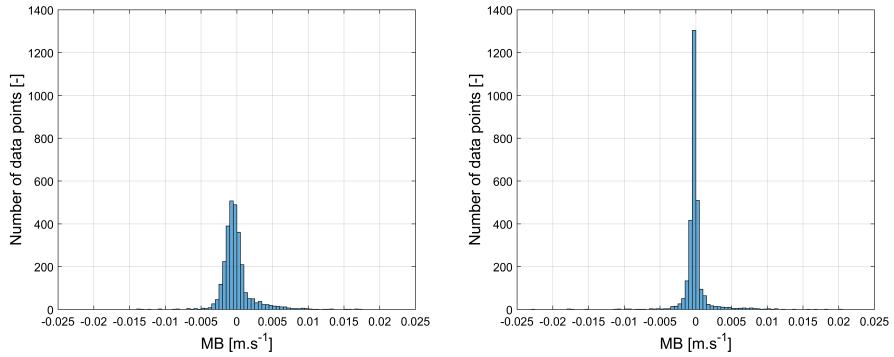

(a) 5B-Demo **(b)** ZDM

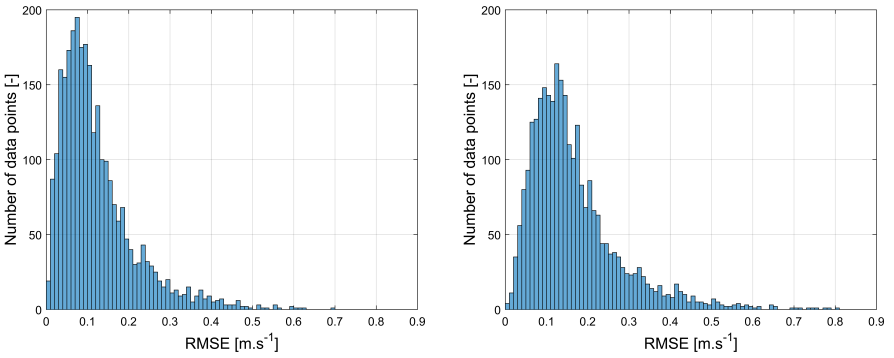

(c) 5B-Demo **(d)** ZDM

Figure 3.21: Histograms of mean bias (MB) and root mean squared error (RMSE). Lidar WFR performed using the 'wind' model and measurements close to the mast distance.

For all four cases, the MB follows closely a bell-shaped distribution. MB values are of the order of $10^{-3}\,\mathrm{m\,s^{-1}}$. Cases using the 'wind-induction' model applied to short-range measurements yields MB values lower than the 'wind' model applied to measurements at a longer distance. Observed MB values are lower for ZDM than 5B-Demo. Both WFR models are unbiased since the MB histograms are close to be centered on 0 (Table 3.4). Additionally, the standard deviations are low.

Table 3.4: Summary of mean bias (MB) results in NKE: average μ and standard deviation σ values in $\mathrm{m\,s^{-1}}$.

Lidar	WFR model			
	'wind'		'wind-induction'	
	$\mu\,(MB)$	$\sigma\,(MB)$	$\mu\,(MB)$	$\sigma\,(MB)$
5B-Demo	-1.2×10^{-4}	$+22 \times 10^{-4}$	-0.16×10^{-4}	$+5.4 \times 10^{-4}$
ZDM	-0.81×10^{-4}	$+19 \times 10^{-4}$	$+0.28 \times 10^{-4}$	$+1.3 \times 10^{-4}$

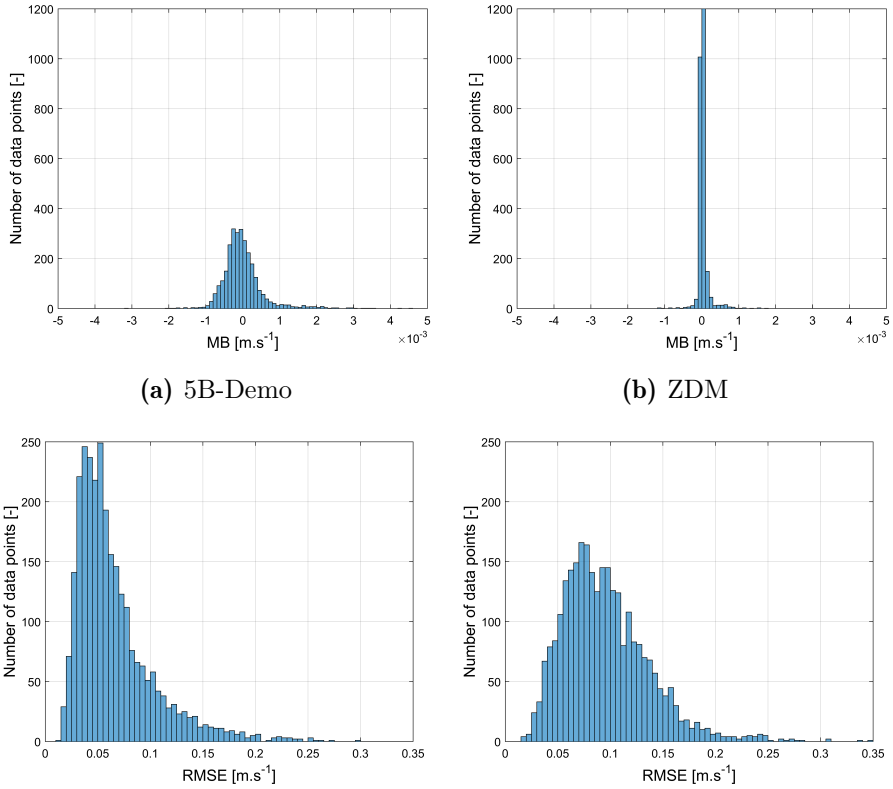

(a) 5B-Demo **(b)** ZDM

(c) 5B-Demo **(d)** ZDM

Figure 3.22: Histograms of mean bias (MB) and root mean squared error (RMSE). Lidar WFR performed using the 'wind-induction' model and measurements close to the turbine rotor.

The RMSE is a quantitative measure of the V_{los} error made for each 10-minute period due the WFR model inadequacy. Most of the RMSE values are within a range of approximately $[0.03, 0.20]\,\mathrm{m\,s^{-1}}$. The RMSE appears to follow a Weibull distribution. Table 3.5 provides statistics obtained from the histograms.

Table 3.5: Summary of root mean squared error (RMSE) results in NKE: average μ and standard deviation σ values in $\mathrm{m\,s^{-1}}$.

Lidar	WFR model			
	'wind'		'wind-induction'	
	$\mu\,(RMSE)$	$\sigma\,(RMSE)$	$\mu\,(RMSE)$	$\sigma\,(RMSE)$
5B-Demo	0.123	0.093	0.066	0.038
ZDM	0.166	0.109	0.095	0.041

The observed values are slightly higher for ZDM than for 5B-Demo. For the 'wind' model case, this can possibly be attributed to the absence of a central beam, to a significantly larger probe length at such a measurement distance, and/or to averaging process employed for ZDM – LOS velocites are averaged per azimuthal sectors (see Sect. 3.3, Page 51). For the 'wind-induction' model, ZDM's larger RMSE may be caused by the inclusion of the 30 m measurement distance ($0.3D_{\mathrm{rot}}$). Indeed, according to CFD simulations (Troldborg and Meyer Forsting, 2016), simple induction flow models are less adequate at distances very close to the rotor plane (below $0.5D_{\mathrm{rot}}$). Note that the 30 m could not be left out as the two other ranges ($1D_{\mathrm{rot}}$ and $1.2D_{\mathrm{rot}}$) were likely too close to each other for the fitting of the induction factor to be of sufficient quality.

3.5 Discussions and further work

In this chapter, the research question of how to estimate wind parameters from nacelle lidar measurements was answered. Possible improvements to the model-fitting WFR methods are here discussed, as well as further research and development topics permitted by this novel approach.

3.5.1 Enhancing model-fitting WFR methods

Three key elements of the model-fitting WFR methods can be improved upon future studies: the wind model, the lidar model, and the optimisation algorithm.

The wind model employed to estimate WFC must be carefully selected based on campaign specific information such as terrain complexity, turbine sizes, measurement configuration, etc. For the purpose of demonstration, only two models were considered (see Pages 49 to 50). The analysis of the NKE campaign experimental data guided the development of many different wind models. It is for instance possible to:

- reconstruct veer: the vertical wind direction variation may at first be assumed linear (one extra WFC);
- replace the 1D induction model in order to account for the flow field variability in the radial direction. Such an engineering '2D induction model' (Troldborg and Meyer Forsting, 2016) was tested (no extra WFC). The obtained wind speed results were negligibly different for this campaign. Alternatively, more advanced numerical codes could be integrated, such as vorticity-based methods (Branlard, 2017b). Vorticity-based codes provide a remarkable compromise between accuracy (vs. full CFD) and a low computing time;
- reconstruct a full 3D wind vector, e.g. by assuming a constant vertical inflow angle (one extra WFC). This can be particularly relevant in sites with a significant terrain slope. Reconstructing the inflow angle may however prove difficult as the vertical wind speed w is likely to contaminate insufficiently the lidar V_{los} measurement, unless the lidar beam is significantly tilted (up or down).

The lidar model can be enhanced by integrating a weighting function distributed along the lidar beam(s) and representative of the volume averaging inherent to DWL measurement principles – although numerical studies have shown that these effects are minor for measurements in the induction zone of a turbine. This integration only modifies how $\widehat{\boldsymbol{V}}_{\text{los}}$ is simulated upon each iteration of the 'fit to measurement' step (see Fig. 3.1).

The algorithm minimising the cost function of $\left\|\boldsymbol{V}_{\text{los}} - \widehat{\boldsymbol{V}}_{\text{los}}\right\|_2$ also has potential for improvements. The Levenberg-Marquardt algorithm demonstrated its ability to provide robust solutions to the defined non-linear Least Squares (LS) problem with a low computing time – typically of the order of hundredths of a second. Its tuning parameters may be adapted to further increase computing efficiency (see Sect. 2.2, Page 47). Other suitable algorithms may also be considered in the future.

The strength of the developed WFR models reside in their ability to characterise the flow field and lidar measurements using only few parameters. Increasing the complexity of the model(s) may challenge the robustness of the solutions provided by the optimisation algorithm. Simpler models are preferable over unnecessary complex ones.

Finally, I would like to open the question of wind farm effects on the induction, e.g. offshore. Is the simple induction function still valid for wind farms comprising multiple rows of turbines (see also Meyer Forsting et al., 2016)?

The extent of the induction zone upstream a turbine – and of the wake downstream – does not depend only on the energy extracted by the turbine of interest,

but also of the operation of neighbouring turbines. As long as the turbine from which the forward-looking nacelle lidars measure is in the first row of the wind farm, the induction is likely to be still usable, although the reconstructed induction factors will certainly higher values than for a single turbine or a single-row wind farm.

3.5.2 Benchmarking WFR codes

To increase the acceptance and the use of nacelle-based lidar systems in wind energy industrial applications, WFR codes should be benchmarked.

In the present study, the same model-fitting WFR codes (MatLab®-based) were applied independently to two different lidar systems. The implementation of the WFR codes was validated by testing them against CFD simulations results. This exercise was performed using a wide variety of wind profiles and conditions. A basic point-like lidar simulator corresponding to the systems of the NKE campaign was used. With this method, the wind characteristics are known at the boundary of the simulated domain, thus allowing to compare reconstructed WFC to CFD-based ones, and to validate the implementation of the WFR codes.

The independent evaluation of WFR codes will require both their testing using simulated lidar data and full-scale measurement campaigns. One way to compare the performance of different WFR codes is to quantify the model adequacy trough comparisons of V_{los} residuals under identical conditions.

3.5.3 A 'smart' lidar

The residual metrics defined in Table 3.3 can be used to create a 'smart' lidar (idea credit: A. Meyer Forsting).

Instead of somewhat arbitrarily selecting the same wind model for each measurement period, a 'smart' lidar could apply several different wind models to the same input measurement data. The wind models could for instance assume different shear (power law, log-law, linear, multi-linear, etc) or veer profiles.

In a second step, the lidar would select the most adequate wind model (cf. decision theory), i.e. the model that is likely to best characterise the flow field during a specific measurement period. Such a method would be particularly valuable to identify various atmospheric stability conditions.

3.5.4 Optimisation of trajectory and optimal lidar design

The locations where the lidar measures V_{los} – in a given order and at a given frequency – defines the lidar trajectory. The lidar trajectory is primarily defined in the lidar coordinate system (CS).

Except for complex scanning systems, the lidar trajectory results from a limited number of parameters such as:

- for 5B-Demo: number of LOSs, vertical and horizontal half-opening angles, configured range gates, accumulation time per LOS;
- for ZDM: number of LOSs (or 'azimuth sectors'), cone angle, azimuthal position, configured focus distances; re-focusing time sequence.

Optimising the lidar design and trajectory consists in identifying the combination of parameters that provides the best WFC estimates, given a number of constrains.

Let us consider the example of nacelle-based profiling lidars employing the combined wind-induction model to estimate free stream hub height wind speed from short-range measurements. From the end-user point of view, trajectory optimisation would answer the questions of

- how many measurement ranges and LOS should be used?
- how far from the rotor plane must the measurement ranges be?
- how separated from one another do they need to be?

See also Fig. 3.17 in order to visually sense the importance of these questions. The constrains of the optimisation can for instance be a minimum number of points sampled over a 10-minute period, a range of distances where the WFR model is valid, a maximum measurement range due to the lidar capabilities or to site- and turbine- specific issues. The optimisation may be single- or multi-objective: minimisation of V_{los} residuals, maximisation of data availability, etc.

On the lidar manufacturers' side, formal optimisation techniques may be valuable in order to design their product. Currently, trajectory parameters such as opening or cone angles and the number of LOS are fixed. The best nacelle lidar design certainly differs significantly depending on whether it shall be used for PCV, turbine control, or (re-)calibration of the nacelle wind direction sensor (e.g. wind vane or sonic anemometer). The constrains and objectives differ too. Note however that the considerations made hereafter discard industrial constrains such as components availability, standardisation of the production process and overall costs.

A nacelle lidar system for feed forward turbine control will probably be optimised

with the objectives of reducing extreme and fatigue loads, or maximising the electrical power output. Feed forward control benefits from high rotor coverage (multiple beams) and high sampling rate. An important constrain is the near-perfect operational availability of the lidar measurements, to ensure the safe operation of the turbine.

For power performance testing, availability is less critical. The design optimisation will aim at providing the most adequate description of the upstream flow field over averaging time periods. Added-value would certainly be present in a flexible lidar design, giving the possibility to choose for example within a range of opening- or cone angles so that the lidar trajectory can be adapted to a wide range of turbine sizes.

For the calibration of the nacelle wind direction sensor – e.g. during turbine commissioning – a wider opening angle is likely advantageous, whilst multi- and long-range lidar measurement capabilities may not be necessary.

CHAPTER 4

Uncertainty Quantification Of Lidar-Estimated Wind Characteristics

In Chapter 3, the model-fitting wind field reconstruction technique was developed. Two different types of models were applied to nacelle lidar experimental data from a full-scale measurement campaign – a wind model accounting for shear, and a combined wind-induction model – and designed to be suitable for power performance testing. With the developed reconstruction techniques, wind field characteristics (WFC) such as speed, direction, shear or the axial induction factor were estimated. The results obtained during the Nørrekær Enge measurement campaign proved to agree well with the measurements from mast-mounted instruments. However, measurements or estimates of the wind characteristics lack meaning if their uncertainty is not specified. The quantification of measurement uncertainties is a requirement of the power performance standards (IEC 61400-12-1, 2017).

The two lidars used during the NKE measurement campaign had been previously calibrated according to the generic methodology described in Chapter 2 – using the so-called white-box approach. As part of these calibration procedures, uncertainties on the lidar measurements of LOS velocities (see Sect. 5, Page 18) and on LOS positioning quantities (e.g. the inclinometers) were assessed. Those quantities are the inputs required to reconstruct wind characteristics.

This chapter shows how numerical techniques such as Monte Carlo methods (MCM) can be used to propagate lidar measurements uncertainties through a wind field reconstruction (WFR) model. It provides uncertainty results for lidar-estimated wind characteristics. A framework for uncertainty quantification related to the use of models is firstly presented. The reader is then introduced to the principles of Monte Carlo methods (MCM). Further, I detail the methodology developed in order to propagate uncertainties on the lidar LOS velocities and other inputs through three WFR models, and used to quantify the model uncertainties on wind characteristics. Results are presented for a two-beam nacelle lidar, and the 5B-Demo and ZDM lidars matching the configuration of the NKE campaign. Finally, I propose to quantify the combined uncertainty on lidar-based wind speed estimates by accounting for the model inadequacy through fitting residuals.

4.1 Framework for the quantification of model uncertainty

Assuming the existence of true inputs $\boldsymbol{x}$, true outputs $\boldsymbol{y}$ (vector quantities), a model is a simplistic representation of the true process – e.g. a system or phenomenon – relating $\boldsymbol{y}$ to $\boldsymbol{x}$.

No perfect model exists. Due to our incomplete knowledge of the process or limitations in the effects that can reasonably be accounted for, a model is essentially wrong, to a certain extent. Fig. 4.1 schematizes a framework for uncertainty quantification in models. In this framework, the starting point is the true inputs,

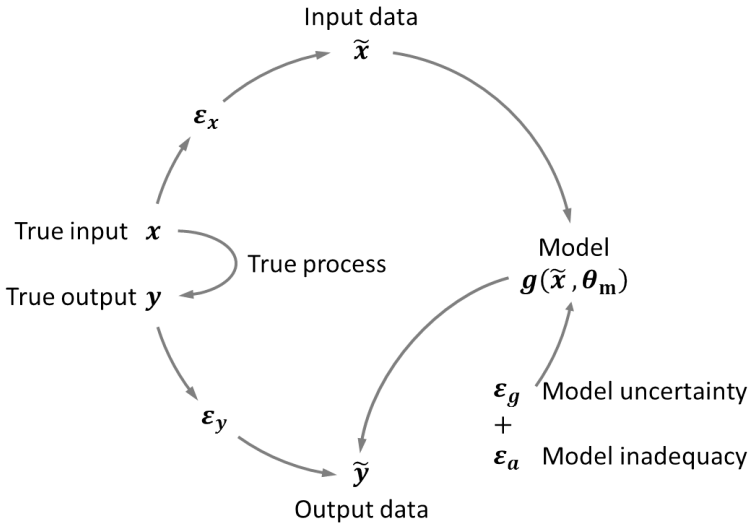

Figure 4.1: A framework for models with uncertainty. Adapted from Huard and Mailhot, 2006.

necessarily unknowable. Practically, the model inputs may be measurement data $\tilde{\boldsymbol{x}}$. Analogously, the model outputs $\tilde{\boldsymbol{y}}$ are only estimates of $\boldsymbol{y}$. Therefore, error terms $\boldsymbol{\varepsilon_x}$ and $\boldsymbol{\varepsilon_y}$ are introduced:

$$\begin{aligned} \tilde{\boldsymbol{x}} &= \boldsymbol{x} + \boldsymbol{\varepsilon_x}, \\ \tilde{\boldsymbol{y}} &= \boldsymbol{y} + \boldsymbol{\varepsilon_y}. \end{aligned} \tag{4.1}$$

The model is denoted $g(\boldsymbol{x}, \boldsymbol{\theta}_{\mathrm{m}})$, where $\boldsymbol{\theta}_{\mathrm{m}}$ are the model parameters, if any are required. The structural error on the model is split in two terms $\boldsymbol{\varepsilon_g}$ and $\boldsymbol{\varepsilon_a}$. $\boldsymbol{\varepsilon_g}$ is the random error due to the model uncertainty. $\boldsymbol{\varepsilon_a}$ characterises the error due to the model inadequacy (see Section 3.4 for definitions).

The output error model is finally expressed as follows:

$$\boldsymbol{y} + \boldsymbol{\varepsilon_y} = g(\boldsymbol{x} + \boldsymbol{\varepsilon_x}, \boldsymbol{\theta}_{\mathrm{m}}) + \boldsymbol{\varepsilon_g} + \boldsymbol{\varepsilon_a}. \tag{4.2}$$

Taking a Bayesian approach, the framework allows the quantification of uncertainties in relation to the use of models (Huard and Mailhot, 2006). The aim is to assess the probability density functions (PDFs) $p(\boldsymbol{\varepsilon_y})$ of output errors – and to characterise it via an uncertainty parameter (or confidence interval) – by propagating the input uncertainties $p(\boldsymbol{\varepsilon_x})$ through the model.

Model errors most often depend on the input variables. In the general case, the distribution of model errors due to the model uncertainty is written

$$p(\boldsymbol{\varepsilon_g}) \equiv p(\boldsymbol{y}|\boldsymbol{x}, \boldsymbol{\theta}_{\mathrm{m}}, g, \boldsymbol{\varepsilon_x}) . \tag{4.3}$$

In the following sections of this chapter, the focus is on the estimation of the model uncertainty. A variety of statistical techniques exist in order to propagate uncertainties (or errors) through a model. We can for instance mention bootstrapping, MCM, and techniques employing model surrogates such as polynomial chaos expansion. In this chapter, only MCM were investigated for quantifying the uncertainty related to wind field reconstruction models since this numerical technique is subject to little approximation in contrast to the other methods. On the negative side, MCM have a high computational cost.

4.2 Introduction to Monte Carlo methods

Monte Carlo methods date from the early 1940s. The original development of MCM is attributed to E. Fermi, S. Ulam, J. Von Neumann and N. Metropolis (Metropolis and Ulam, 1949; Metropolis, 1987) as part of USA's efforts to develop nuclear weapons during World War II.

MCM are a class of statistical techniques often used to computationally solve physical or mathematical problems. They rely on large-scale random sampling of the model inputs, and on the evaluation of the model outputs for each of the samples. Application examples are numerical integration, optimisation, sensitivity or reliability analysis, and uncertainty quantification (UQ).

For the evaluation of uncertainty in measurements, the valid application of the GUM methodology is limited since it essentially relies on the central limit theorem, and Gaussian-distributed inputs x_i and output(s) y_i of an analytical linearised measurement model (Cox and Siebert, 2006). The JCGM details the conditions for the valid application of the MCM (see Sect. 5.10 in JCGM, 2008b). In the context of uncertainty quantification, MCM allow for instance to:

- simulate systems with many degrees of freedom;

- consider arbitrary distributions of errors (uncertainty);
- propagate uncertainties through both explicit and implicit models – where the model output cannot be directly expressed as a function of the inputs.

When its application is valid, the GUM provides exact results. In contrast, the domain of validity of MCM is nearly unlimited, but it only yield approximate solutions of the distribution of model output errors – the approximation errors converge towards 0 when the number of MC samples N_s increases ($\rightarrow \infty$).

Fig. 4.2 illustrates the principles of MCM. In this example, a parametric model having three input and two output variables was used.

The basic steps of MCM are:

- step 1: definition of the parametric model;
- step 2: generation of a set of inputs (of size N_s);
- step 3: model evaluation. The outputs $\boldsymbol{y_i} = g\left(\boldsymbol{x_i}, \boldsymbol{\theta}_m\right)$ are computed, for $i = 1$ to N_s;
- step 4: analysis of the results. The output distributions are characterised for example via histograms, correlation, confidence intervals, summary statistics, etc.

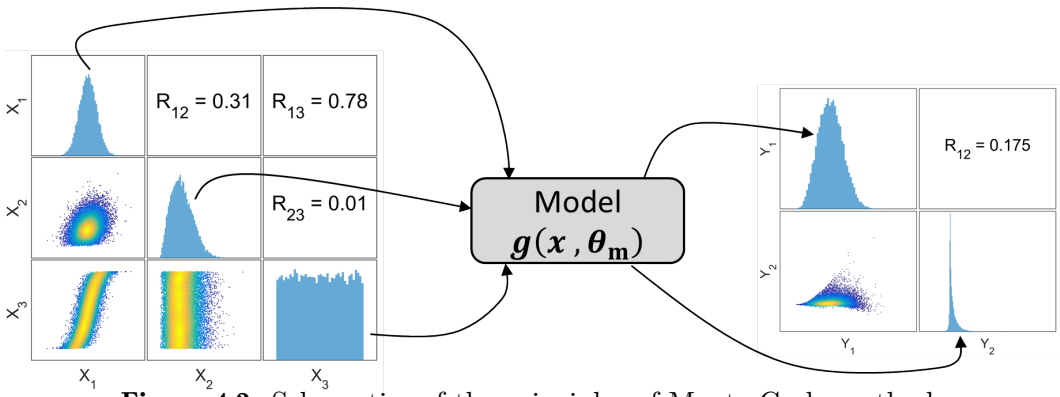

Figure 4.2: Schematics of the principles of Monte Carlo methods.

The MC simulation consists mainly of steps 2 and 3, while steps 1 and 4 can be considered pre- and post-processing steps.

In step 2, the inputs are sampled according to their multivariate probability distribution. The multivariate probability distribution is composed of both the marginal distributions (histograms on the diagonal of the plot matrix) and the joint distributions (scatter plots in lower triangle) as the input variables may be correlated. The sampling process is performed by combining a Random Number Generator (RNG) with isoprobabilistic transforms (e.g. Rosenblatt (Rosenblatt,

1952), generalised Nataf (Lebrun and Dutfoy, 2009), Cholesky decomposition). Such a process allows to map arbitrarily distributed inputs to standard space – i.e. where variables are independent and identically distributed (iid.). In practice, the RNG is first applied to generate the standard iid. variables. The transformation is then used to convert the iid. variables into the desired inputs $\boldsymbol{x}$ (correlated and arbitrarily distributed).

4.3 Monte Carlo methods and uncertainty propagation in wind field reconstruction models

This section provides the methods that were used to propagate the uncertainty in the inputs of a WFR flow model to its outputs, the wind field characteristics. In the next sections, these methods are applied to a homogeneous flow model (Section 4.4), to the wind model accounting for shear (Section 4.5), and to the combined wind-induction model (Section 4.6). A working example employing the simple case of a two-beam lidar and the homogeneous illustrate those methods.

4.3.1 Methods

The inputs of a lidar static WFR model subject to uncertainty are the LOS velocities $\boldsymbol{V}_{\text{los}}$ (of size N_{los}) and the quantities providing the position of the measurement points – tilt and roll inclination angles, measurement distance, cone or half-opening angles, etc.

Practically, I chose to perform one MC simulation for study cases defining different sets of WFC. The methods that were used to perform each MC simulation and the inherent assumptions are given hereafter.

Inputs' uncertainties and distributions of errors

All input error distributions are assumed Gaussian – with mean and standard deviation denoted μ and σ respectively.

For $j = 1$ to N_{los}, the mean $\mu\left(V_{\text{los},j}\right)$ is computed by projecting the local wind vector $\overrightarrow{U}_j = [u_j, v_j, w_j]$ onto the different LOS (see Eq. 2-3, Page 48), where $\overrightarrow{U}_j$ is obtained from the flow model and the set of WFC. Similarly to Sect. 6.2.3. (Page 30), the standard uncertainty $\sigma_{V_{\text{los},j}}$ is calculated by taking advantage of the observed linear relation between the mean V_{los} and its expanded uncertainty (see Table 1, Page 28, with $k = 2$). With a coverage factor $k = 1$, we approximated this linear relation to

$$\sigma_{V_{\text{los},j}} = 0.008 \cdot \mu\left(V_{\text{los},j}\right) + 0.0225\text{m}\,\text{s}^{-1}. \tag{4.4}$$

Table 4.1 provides the used parameter values for the distributions of errors of the tilt φ and roll ψ inclination angles, and cone- or half-opening angle α. The standard deviation (uncertainty)s were obtained from the inclinometers calibration and geometry verification results (Borraccino and Courtney, 2016b, 2016a). The joint distributions between LOS velocities are assumed partially correlated with a coefficient of $r_{i,j} = 0.9$, where $i, j \in [1, N_{\text{los}}], i \neq j$. The reason for such a high level of correlation between V_{los} uncertainties is that most of the calibration uncertainty sources are common to all the LOS. Other random variables are assumed uncorrelated.

Table 4.1: Parameters of input distributions used for uncertainty quantification in WFR models.

Input variable	**Mean value μ**	**Standard uncertainty σ ($k = 1$)**
Tilt* φ	0°	0.05°
Roll ψ	0°	0.05°
Opening or cone angle α	15°	0.1°
LOS velocities	$V_{\text{los},j}$ m s^{-1}	$0.008 \cdot \mu(V_{\text{los},j}) + 0.0225$ m s^{-1}

*for the two-beam lidar case, $\mu(\varphi) = -1^\circ$

Generation of a set of inputs

The generation of the input samples was performed via *UQLab* – an open-source software for the general purpose of uncertainty quantification which supports MatLab®-based modelling tools (Marelli and Sudret, 2014). The 'input' module of *UQLab* employs the generalised Nataf iso-probabilistic transform to map between variables in standard normal and physical spaces (Lataniotis et al., 2015a).

Model evaluation

The WFR model is evaluated for each of the N_{s} input samples. The 'model' module of *UQLab* (Lataniotis et al., 2015b) was used, for practical reasons (efficient module for vectorised variables). With a simple code, the model evaluation can simply be seen as a for-loop on the number of samples.

Analysis of output distributions

Since the model inputs are assumed to be normally distributed, the marginals of the model outputs are also Gaussian. Hence, the outputs distributions can simply be characterised by the mean and standard deviation statistics – the later being the standard uncertainty. In addition, the correlation between the output distributions of errors is computed.

4.3.2 Working example

As an example, we consider the simple case of a two-beam nacelle lidar measuring at a single distance, with its beams at same height agl (see Fig. 11, Page 29). The WFR model assumes horizontal flow homogeneity and yields two analytical expressions for the wind speed and relative direction, respectively denoted V_{H} and θ_{r}. The parametric model is now defined (step 1).

The study case is: $V_{\mathrm{H}} = 10\,\mathrm{m\,s^{-1}}$ and $\theta_{\mathrm{r}} = 5°$. $V_{\mathrm{los},1}$ and $V_{\mathrm{los},2}$ are computed according to the wind model (see Eq. 22, Page 29). Standard input uncertainties are derived as in Table 4.1. Note that the roll inclination is here discarded from the uncertain inputs in order to match the case where the GUM was applied (see Sect. 6, Page 28).

$N_s = 2 \times 10^4$ input samples are generated. Fig. 4.3 shows the obtained inputs' marginal and joint distributions. The joint distributions' scatter plots are color-coded to represent the data density (low density in blue, high density in yellow). Correlation coefficients r_{13} and r_{23} between LOS velocites and the tilt angle are not exactly equal to zero due to numerical errors (limited number of samples).

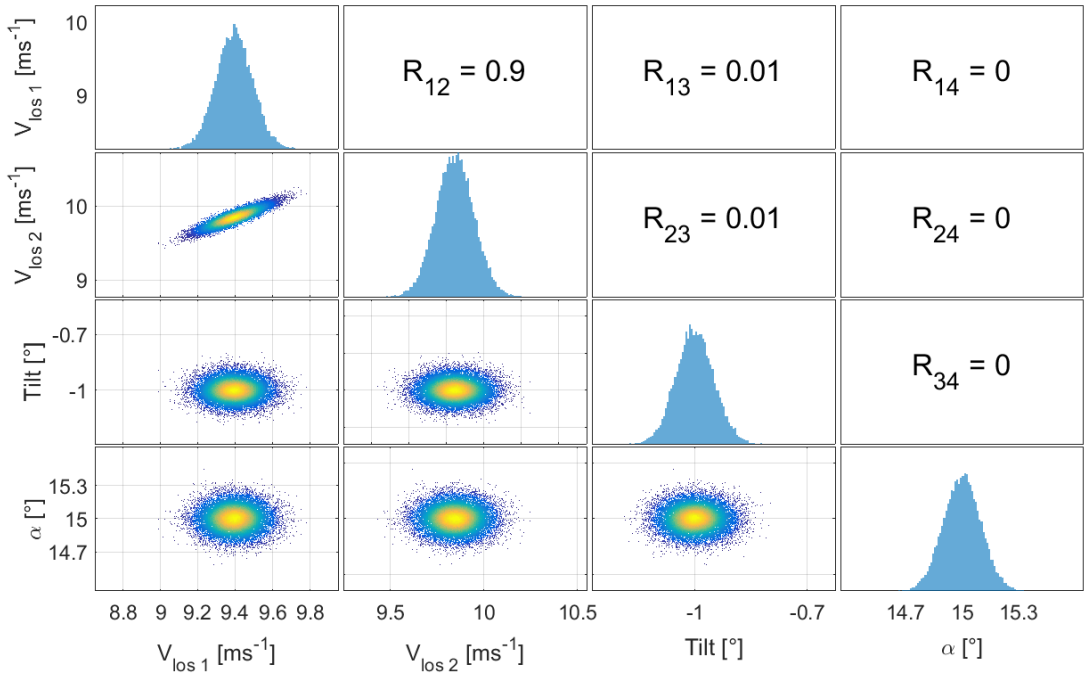

Figure 4.3: MC simulation working example for a two-beam nacelle lidar: input distributions.

Next, the WFC V_{H} and θ_{r} are computed (see Eq. 23 and Eq. 24, Page 29). Fig. 4.4 displays histograms of V_{H} and θ_{r}. The mean values match the WFC of

the study case, as expected. However, a small error is observed due to the finite number of samples. The standard deviations σ are the standard uncertainties on V_{H} and θ_{r}. The correlation coefficient between the two output distributions is in this example of $r_{V_{\mathrm{H}},\theta_{\mathrm{r}}} = 0.045$, i.e. the V_{H} and θ_{r} uncertainties are not correlated.

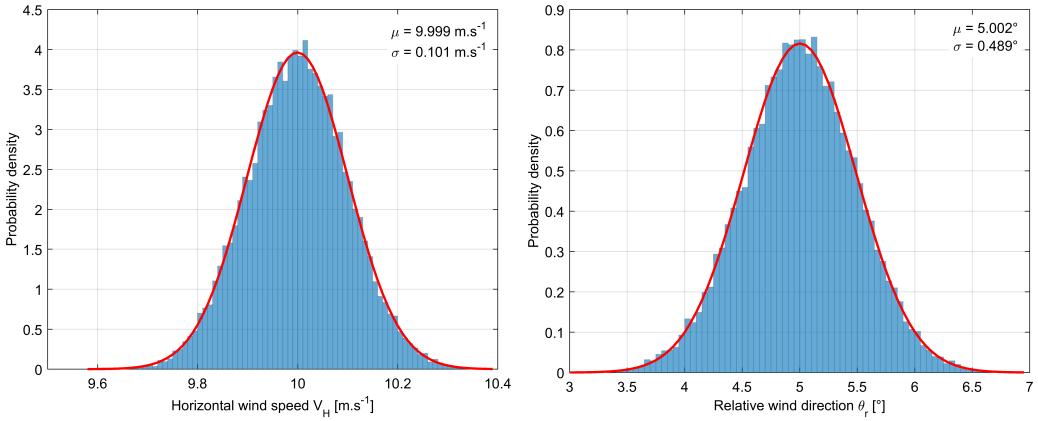

Figure 4.4: MC simulation working example for a two-beam nacelle lidar: outputs histograms.

4.4 Uncertainty of a horizontally homogeneous wind model: applied to a two-beam nacelle lidar

This section demonstrates the ability of MCM methods to provide valid results for the purpose of uncertainty assessment in WFR models. In order to do so, the simple case of a two-beam nacelle lidar is used. Results can be compared to the ones obtained using the GUM methodology (see Fig. 13, Page 31).

4.4.1 Study cases

The following study cases are selected:

- wind speed: $V_{\mathrm{H}} \in [4, 16]\,\mathrm{m\,s^{-1}}$, with a step of $0.5\,\mathrm{m\,s^{-1}}$;
- relative wind direction: $\theta_{\mathrm{r}} \in [-10°, 10°]$, with a step of $1°$.

The half-opening angle of the lidar pair of beams is $\alpha = 15°$. The tilt angle is $\varphi = -1°$. The wind model assumes horizontal homogeneity (see analytical expressions in Eq. 23 and Eq. 24, Page 29). The correlation between the two LOS velocities is assumed to $r_{1,2} = 0.9$.

4.4.2 Wind field characteristics uncertainty results

Fig. 4.5 displays the expanded (coverage factor $k = 2$) model uncertainties on V_{H} and θ_{r}. The results prove to be almost identical to the ones obtained with the GUM.

The only notable difference concerns the variability of uncertainties as a function of θ_{r}: while the GUM methodology predicted a slight decrease of $U_{V_{\mathrm{H}}}$ and increase of $U_{\theta_{\mathrm{r}}}$, MCM show strictly no dependency of $U_{V_{\mathrm{H}}}$ to the relative direction, and a wide parabolic trend for $U_{\theta_{\mathrm{r}}}$ with a maximum for $\theta_{\mathrm{r}} = 0°$.

The cause of this deviation is the correlation r_{V_x,V_y} – between error distributions on the streamwise and transverse wind speeds (V_x, V_y) – arbitrarily assumed to 0.2 as part of the GUM's two-step uncertainty assessment process. This assumption made for simplifying calculations is incorrect. Indeed, r_{V_x,V_y} is directly linked to the correlation coefficient $r_{1,2}$ between LOS velocities. In contrast, no such assumption was required for the MC simulations.

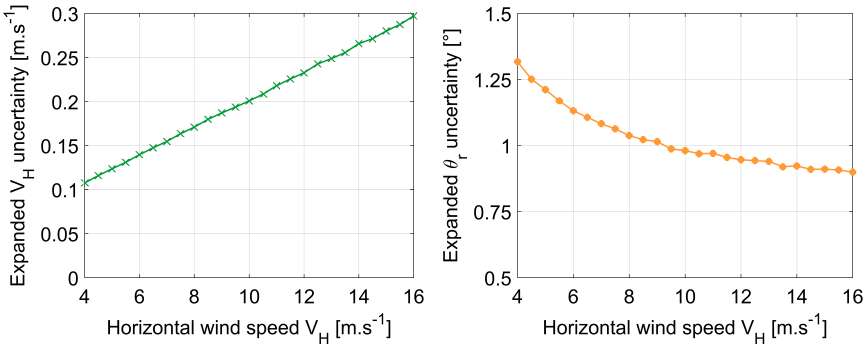

(a) vs. V_{H}, for $\theta_{\mathrm{r}} = 5°$

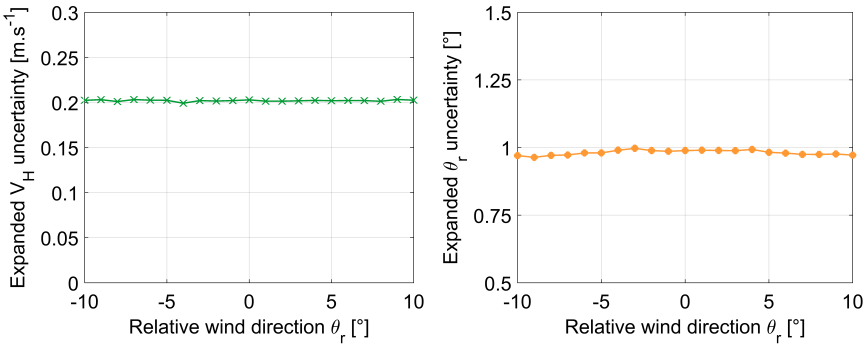

(b) vs. θ_{r}, for $V_{\mathrm{H}} = 10\,\mathrm{m\,s^{-1}}$

Figure 4.5: Two-beam lidar MC results: expanded uncertainties U_{V_H} and U_{θ_r} as a function of V_{H} and θ_{r} ($r_{1,2} = 0.9$).

Although the uncertainty deviations between the two methods are negligible, it is valuable to identify how far from reality the assumed value of r_{V_x,V_y} was. In order to do so, V_x and V_y were added to the model outputs. MC simulations were performed for the study case of $V_\mathrm{H} = 10\,\mathrm{m\,s^{-1}}$ and $\theta_\mathrm{r} = 5°$ and a range of different $r_{1,2}$ values; r_{V_x,V_y} is calculated for each of the MC simulation. Fig. 4.6 shows that $r_{V_x,V_y} < 0.2$ except when $r_{1,2}$ is close to 1. In particular for $r_{1,2} = 0.9$, we have $r_{V_x,V_y} \approx 0.1$.

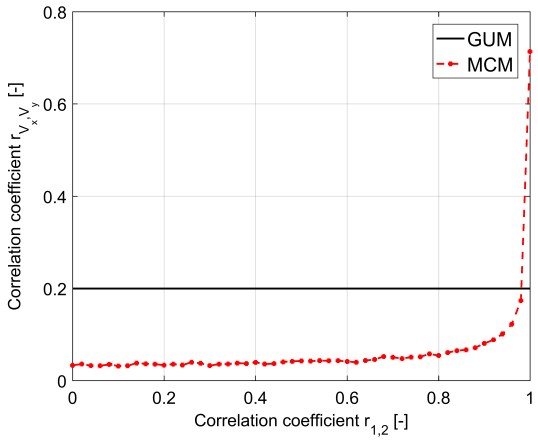

Figure 4.6: Two-beam lidar MC results: r_{V_x,V_y} vs. $r_{1,2}$, for $V_\mathrm{H} = 10\,\mathrm{m\,s^{-1}}$ and $\theta_\mathrm{r} = 5°$.

The correlation coefficient $r\,(V_\mathrm{H}, \theta_\mathrm{r})$ results are presented in Fig. 4.7. The observed $r\,(V_\mathrm{H}, \theta_\mathrm{r})$ values show no dependency to the wind speed, and a linear increase with the relative direction. Within the range of typical operational θ_r values, U_{V_H} and U_{θ_r} can be considered uncorrelated since $r\,(V_\mathrm{H}, \theta_\mathrm{r})$ remains small.

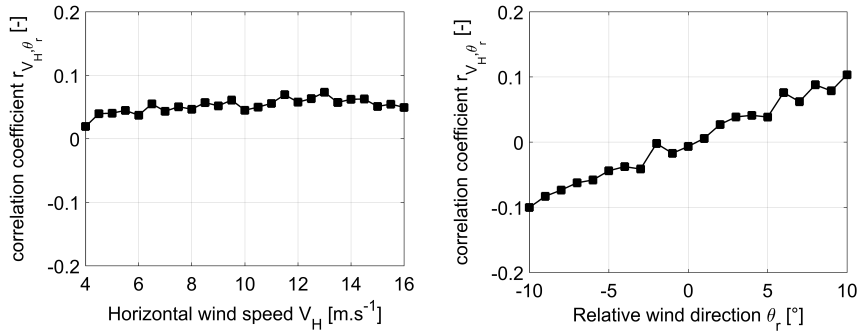

(a) vs. V_H, for $\theta_\mathrm{r} = 5°$ **(b)** vs. θ_r, for $V_\mathrm{H} = 10\,\mathrm{m\,s^{-1}}$

Figure 4.7: Two-beam lidar MC results: correlation between V_H and θ_r distributions of errors.

4.5 Uncertainty of a wind model accounting for shear: applied to profiling nacelle lidars

4.5.1 Study cases

In this section, the parametric model considered is the WFR model assuming horizontal wind speed homogeneity and accounting for vertical shear via a power law (see Sect. 2.4.1, Page 49).

The model-fitting WFR approach is used both to simulate the V_{los} mean values of the distributions of errors and to reconstruct the hub height wind speed V_{H}, relative direction θ_{r} and shear exponent α_{exp} for each MC sample.

MC simulations are conducted for two profiling lidar systems – the 5B-Demo and ZDM – with measurement trajectories that correspond to the configuration of the NKE measurement campaign (see Fig. 5, Page 52). Only the $2.5D_{\mathrm{rot}}$ measurement distance is considered here for model UQ.

The following study cases are selected:

- wind speed: $V_{\mathrm{H}} \in [4, 16]\,\mathrm{m\,s^{-1}}$, with a step of $0.5\,\mathrm{m\,s^{-1}}$;
- relative wind direction: $\theta_{\mathrm{r}} \in [-10°, -4°, -2°, 0°, 2°, 4°, 10°]$;
- shear exponent: $\alpha_{\mathrm{exp}} \in [-0.1, 0.5]$, with a step of 0.1.

The tilt and roll angles are respectively $\varphi = 0°$ and $\psi = 0°$. In total, $25{\times}7{\times}7 = 1225$ MC simulations were performed for each lidar, with a sample size of $N_{\mathrm{s}} = 5 \times 10^3$.

4.5.2 Wind field characteristics uncertainty results

Fig. 4.8 displays the expanded (coverage $k = 2$) model uncertainties on V_{H}, θ_{r} and α_{exp} as a function of speed, direction and shear.

For both 5B-Demo and ZDM, the wind speed uncertainty $U_{V_{\mathrm{H}}}$ values are imperceptibly different from the results of the two-beam lidar case (see Fig. 4.5). $U_{V_{\mathrm{H}}}$ linearly increases with the wind speed, and depends neither on θ_{r} nor α_{exp}.

The relative direction and shear exponent uncertainties $U_{\theta_{\mathrm{r}}}$ and $U_{\alpha_{\mathrm{exp}}}$ decrease with V_{H} – following an hyperbolic shape – similarly to the two-beam lidar case. $U_{\theta_{\mathrm{r}}}$ is significantly higher for 5B-Demo than ZDM. This is likely due to the different measurement trajectories: 5B-Demo's central beam is more sensitive to the relative direction as no other V_{los} measurement is taken at the same height.

$U_{\theta_{\mathrm{r}}}$ is independent of both θ_{r} and α_{exp}. $U_{\alpha_{\mathrm{exp}}}$ varies significantly only with α_{exp}. The observed values are of the order of 1×10^{-2} or less. 5B-Demo values of $U_{\alpha_{\mathrm{exp}}}$ are marginally smaller than for ZDM.

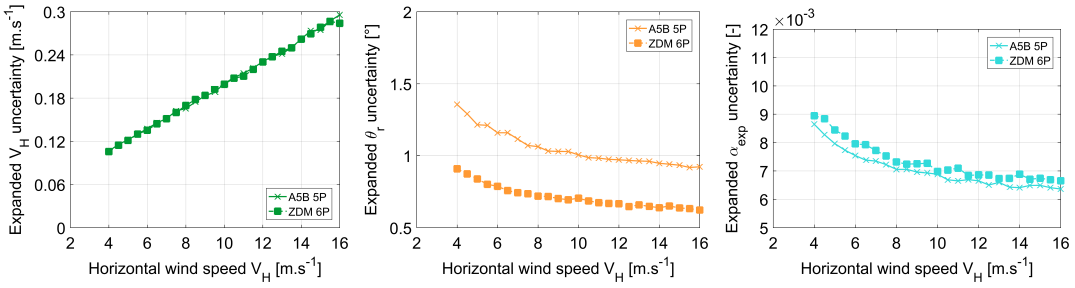

(a) vs. V_{H}, for $\theta_{\mathrm{r}} = 4°$, $\alpha_{\mathrm{exp}} = 0.2$

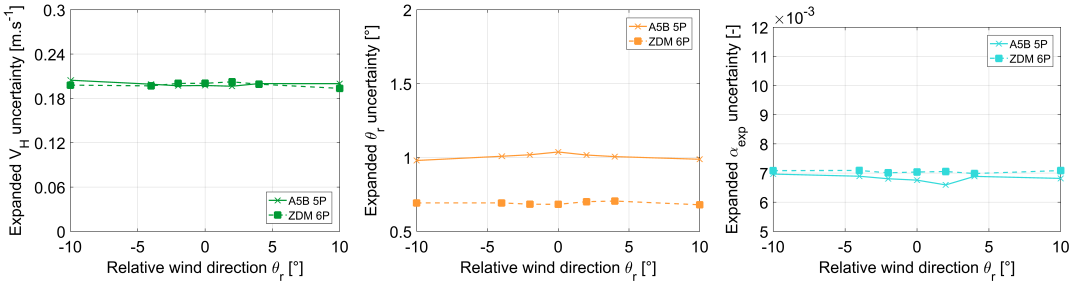

(b) vs. θ_{r}, for $V_{\mathrm{H}} = 10\,\mathrm{m\,s^{-1}}$, $\alpha_{\mathrm{exp}} = 0.2$

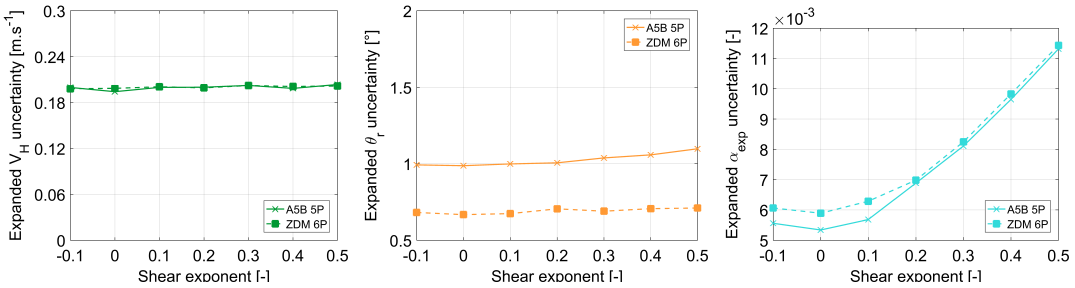

(c) vs. α_{exp}, for $V_{\mathrm{H}} = 10\,\mathrm{m\,s^{-1}}$, $\theta_{\mathrm{r}} = 4°$

Figure 4.8: Profiling nacelle lidars MC results: expanded uncertainties $U_{V_{\mathrm{H}}}$, $U_{\theta_{\mathrm{r}}}$, $U_{\alpha\mathrm{exp}}$ as a function of V_{H}, θ_{r} and α_{exp}.

The correlation coefficients $r\,(V_{\mathrm{H}}, \theta_{\mathrm{r}})$, $r\,(V_{\mathrm{H}}, \alpha_{\mathrm{exp}})$, $r\,(\theta_{\mathrm{r}}, \alpha_{\mathrm{exp}})$ between the model output distributions of errors are displayed in Fig. 4.9. We can observe that:

- the three correlation coefficients have a similar trend and magnitudes for both lidar systems;
- $r\,(V_{\mathrm{H}}, \theta_{\mathrm{r}})$ values are almost identical to the two-beam lidar case – where there was no reconstruction of shear;
- $U_{V_{\mathrm{H}}}$ and $U_{\alpha\mathrm{exp}}$ are negatively correlated for positive shear exponents – the most common case in the ABL. The magnitude of $r\,(V_{\mathrm{H}}, \alpha_{\mathrm{exp}})$ decreases with

the wind speed – from -0.3 at $4\,\mathrm{m\,s^{-1}}$ to -0.15 at $16\,\mathrm{m\,s^{-1}}$ – and increases with the shear.

When using the 'wind' model to perform WFR from profiling nacelle lidars, the combined wind speed uncertainty shall consequently account at least for the correlation between U_{V_H} and U_{α_exp}. Indeed strong wind speeds are often observed under neutral conditions (significant α_exp). In such a situation, neglecting $r\,(V_\mathrm{H}, \alpha_\mathrm{exp})$ may give rise to significant combined uncertainty errors.

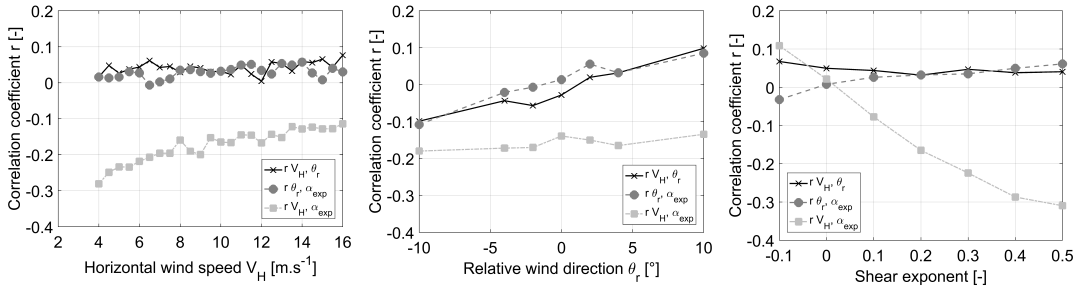

(a) for 5B-Demo

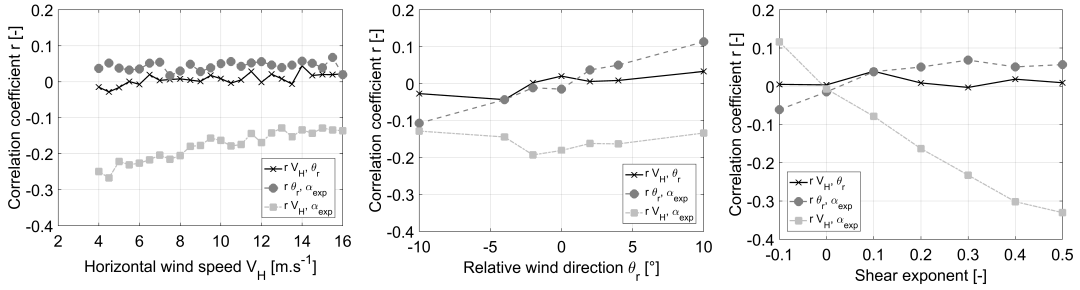

(b) for ZDM

Figure 4.9: Profiling nacelle lidars MC results: correlation between V_H, θ_r and α_exp distributions of errors.

4.6 Uncertainty of a combined wind-induction model: applied to profiling nacelle lidars

4.6.1 Study cases

In this section, the parametric model considered is the combined wind-induction model. The model accounts for vertical shear via a power law, and wind speed deficits in the turbine induction are modelled by a simple one-dimensional function (see Sect. 2.4.2, Page 50).

The model-fitting WFR approach is used both to simulate the V_{los} mean values of the distributions of errors and to reconstruct the free stream hub height wind speed V_∞, relative direction θ_{r}, shear exponent α_{exp} and induction factor a_{ind} for each MC sample.

MC simulations are conducted for the 5B-Demo and ZDM and using the measurement trajectories of the NKE measurement campaign (see Fig. 5, Page 52). The used lidar measurement distances are close to the turbine rotor, and identical to the cases of Sect. 4.2, Page 54:

- for 5B-Demo: four distances from 0.5 to $1.15D_{\text{rot}}$;
- for ZDM: three distances from 0.3 to $1.25D_{\text{rot}}$.

The following study cases are selected:

- wind speed: $V_{\text{H}} \in [4, 16]\,\text{m}\,\text{s}^{-1}$, with a step of $0.5\,\text{m}\,\text{s}^{-1}$;
- relative wind direction: $\theta_{\text{r}} \in [-10°, 0°, 10°]$;
- shear exponent: $\alpha_{\text{exp}} \in [-0.1, 0.5]$, with a step of 0.1;
- induction factor a_{ind}: 9 values are selected for each wind speed (see Fig. 4.10). These values are calculated based on the average C_T curve of several pitch-regulated wind turbines, and using $a_{\text{ind}} = \frac{1}{2}\left(1 - \sqrt{1 - \gamma C_T}\right)$ to convert C_T into a_{ind} (see Eq. (3.5) in Section 3.3.3), with $\gamma = 1.1$.

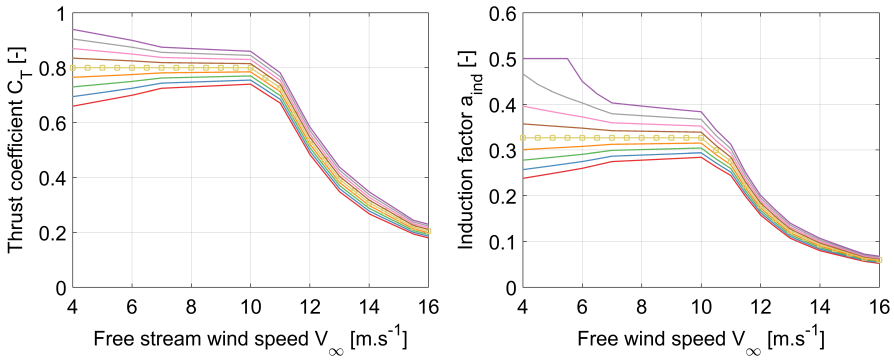

Figure 4.10: Thrust coefficient (left) and induction factor (right) curves used to generate the study cases of MC simulation for uncertainty quantification of the combined wind-induction model. The curve with markers is considered as 'nominal'.

The tilt and roll angles are respectively $\varphi = 0°$ and $\psi = 0°$. In total, $25 \times 3 \times 7 \times 9 = 4725$ MC simulations were performed for each lidar, with a sample size of $N_{\text{s}} = 5 \times 10^3$.

4.6.2 Wind field characteristics uncertainty results

Fig. 4.11 displays the expanded (coverage $k = 2$) model uncertainties on V_∞, θ_r, α_exp and U_{a_ind} as a function of speed, direction, shear and induction factor.

The combined wind-induction model uncertainty results are consistent with the ones obtained with the wind model. The observations on values and trends of speed, direction and shear uncertainties are identical. In particular, the remarkable observation of U_{V_∞} increasing linearly with V_∞ remains unchanged.

It is interesting to note that using the combined wind-induction model U_{θ_r} is lower by 0.4° to 0.8° than previously observed (see Fig. 4.9). A plausible explanation is that since multiple ranges are used, the optimisation problem – of the model-fitting WFR method and solved for each MC sample – is highly over-constrained. In other words, the WFR algorithm has many more inputs than required to fit the WFC to the V_los measurements.

U_{α_exp} values have slightly increased in comparison to the 'wind' model uncertainties, but remain small.

All four expanded uncertainties are shown to be independent of the induction factor values (bottom row of plots). U_{a_ind} is moreover independent of θ_r, α_exp and U_{a_ind} values.

Finally, U_{a_ind} decreases with increasing wind speed, following an hyperbolic trend. U_{a_ind} values obtained for ZDM are about half of the ones observed for 5B-Demo, although ZDM uses three measurement distances instead of four for 5B-Demo – the three ZDM distances are however distributed on a greater range of distances.

The cross-correlation coefficients between the model output distributions of errors are displayed in Fig. 4.12. As the correlation matrix is of dimension 4, there are 6 coefficients (lower triangle) to analyse. The observations made in Section 4.5.2 are still valid with the combined wind-induction model. Additionally, we can observe that:

- all correlation coefficients are independent of a_ind;
- U_{V_∞}, U_{α_exp} and U_{θ_r} can be considered uncorrelated to U_{a_ind} since the three corresponding correlation coefficients are within $[-0.1, 0.1]$.

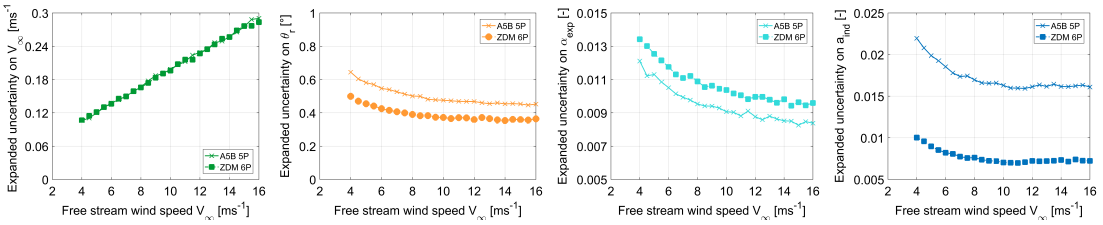

(a) vs. V_∞, for $\theta_\mathrm{r} = 0°$, $\alpha_\mathrm{exp} = 0.2$, $a_\mathrm{ind} = f\,(V_\infty)$

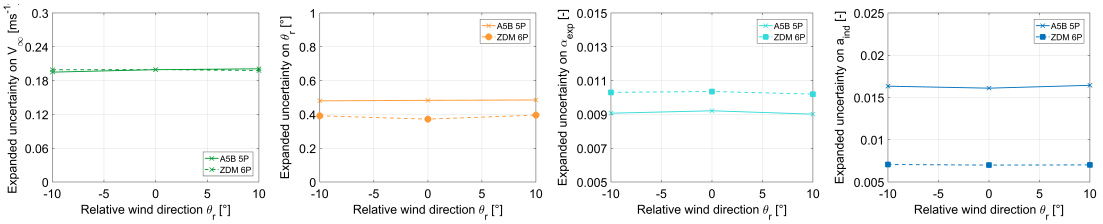

(b) vs. θ_r, for $V_\infty = 10\,\mathrm{m\,s^{-1}}$, $\alpha_\mathrm{exp} = 0.2$, $a_\mathrm{ind} = f\,(V_\infty)$

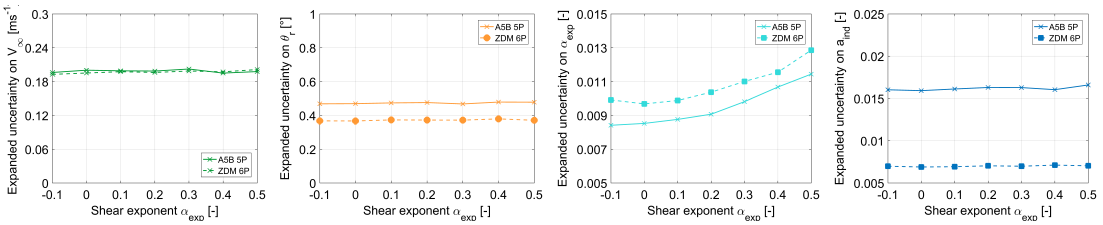

(c) vs. α_exp, for $V_\infty = 10\,\mathrm{m\,s^{-1}}$, $\theta_\mathrm{r} = 0°$, $a_\mathrm{ind} = f\,(V_\infty)$

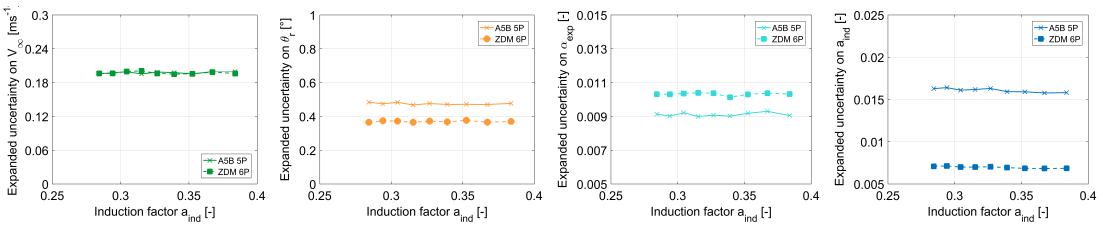

(d) vs. a_ind, for $V_\infty = 10\,\mathrm{m\,s^{-1}}$, $\theta_\mathrm{r} = 0°$, $\alpha_\mathrm{exp} = 0.2$

Figure 4.11: Profiling nacelle lidars MC results: expanded uncertainties U_{V_H}, U_{θ_r}, U_{α_exp}, U_{a_ind} as a function of V_H, θ_r, α_exp and a_ind.

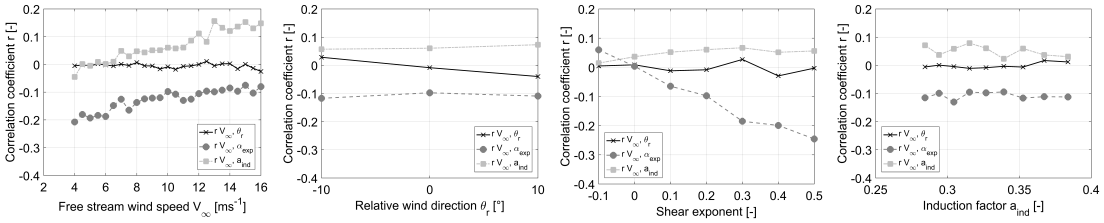

(a) for 5B-Demo: $r\left(V_{\infty}, \theta_{\mathrm{r}}\right)$, $r\left(V_{\infty}, \alpha_{\mathrm{exp}}\right)$, $r\left(V_{\infty}, a_{\mathrm{ind}}\right)$

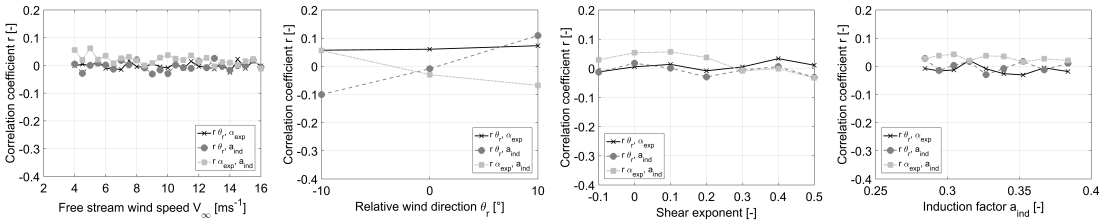

(b) for 5B-Demo: $r\left(\theta_{\mathrm{r}}, \alpha_{\mathrm{exp}}\right)$, $r\left(\theta_{\mathrm{r}}, a_{\mathrm{ind}}\right)$, $r\left(\alpha_{\mathrm{exp}}, a_{\mathrm{ind}}\right)$

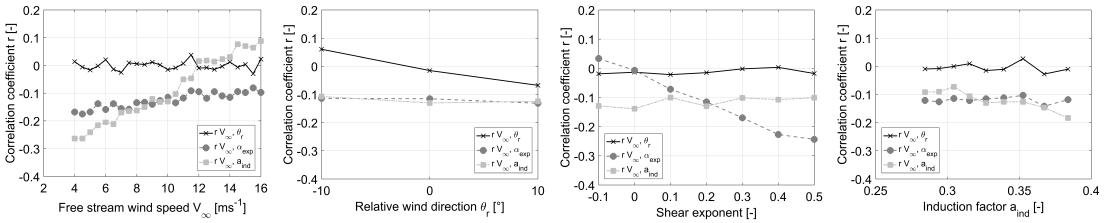

(c) for ZDM: $r\left(V_{\infty}, \theta_{\mathrm{r}}\right)$, $r\left(V_{\infty}, \alpha_{\mathrm{exp}}\right)$, $r\left(V_{\infty}, a_{\mathrm{ind}}\right)$

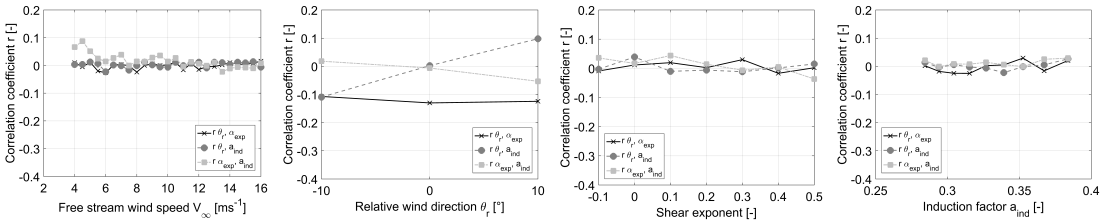

(d) for ZDM: $r\left(\theta_{\mathrm{r}}, \alpha_{\mathrm{exp}}\right)$, $r\left(\theta_{\mathrm{r}}, a_{\mathrm{ind}}\right)$, $r\left(\alpha_{\mathrm{exp}}, a_{\mathrm{ind}}\right)$

Figure 4.12: Profiling nacelle lidars MC results: correlation between V_{∞}, θ_{r}, α_{exp} and a_{ind} distributions of errors.

4.7 Combining model uncertainties and line-of-sight velocity residuals

In the previous sections, the uncertainties related to several WFR models were assessed (see $\boldsymbol{\varepsilon_g}$ in Fig. 4.1). The model uncertainty quantification was performed using simulated inputs obtained by inversion of the model. Consequently, the model was perfectly adequate (unbiased) and $\boldsymbol{\varepsilon_a} = \mathbf{0}$.

In practical applications, nacelle lidar experimental data provide the inputs to the WFR model. The model inadequacy shall be integrated into the uncertainty assessment of the model-estimated WFC.

In this purpose, we propose to combine the obtained model uncertainties with V_{los} residuals, using the RMSE statistics (see Section 3.4). For each 10 min period of experimental lidar data, the following process is used:

1) lidar-measured LOS velocities and inclinations angles are used to estimate the WFC according to the chosen model;
2) the RMSE between measured and model-estimated LOS velocities is computed (see Table 3.3);
3) model uncertainties on WFC are extracted from look-up tables. The look-up tables contain the results of the MC simulations, for multiple sets of WFC. The estimated WFC are used to find the closest corresponding set in the look-up tables, and read the model uncertainties and correlation coefficients between distributions of errors of the WFC from the tables;
4) values of the model uncertainties and RMSE are combined assuming they are uncorrelated – since the model uncertainties are considered independent from the physical uncertainties – yielding the total uncertainty on the considered WFC.

The method to combine model uncertainties and RMSE statistics is provided hereafter. The resulting uncertainties denoted $u_{c,V_{\text{H}}}$ and u_{c,V_∞} – respectively for the 'wind' and 'combined wind-induction' models – are the combined hub height wind speed uncertainties from the lidar measurements and can be used for the assessment of power curve uncertainty (see Chapter 5).

4.7.1 For the wind model accounting for shear

We here consider the WFR case using the wind model accounting for shear. The model uncertainty $u_{V_{\text{H}}}$ – extracted from the MC uncertainty look-up tables – is

combined with the $RMSE$ to compute u_{c,V_H} as follows:

$$u_{c,V_\mathrm{H}} = \sqrt{u_{V_\mathrm{H}}^2 + RMSE^2}. \tag{4.5}$$

Note that the law of propagation of uncertainties was here used assuming uncorrelated uncertainty components.

Furthermore, the combined uncertainty on the wind speed $V\left(z_\mathcal{H}\right)$ can be computed for any height $z_\mathcal{H}$ (see Fig. 2, Page 48). The GUM methodology is applied to the following model f_1 (see also Eq. 7, Page 49):

$$f_1 = V\left(z_\mathcal{H}, V_\mathrm{H}, \theta_\mathrm{r}, \alpha_\mathrm{exp}\right) = V_\mathrm{H}\left(\frac{z_\mathcal{H} + H_\mathrm{hub}}{H_\mathrm{hub}}\right)^{\alpha_\mathrm{exp}}, \tag{4.6}$$

yielding the following expression for $u_{c,V(z_\mathcal{H})}$

$$\begin{aligned} u_{c,V(z_\mathcal{H})}^2 = &\left(\frac{\partial f_1}{\partial V_\mathrm{H}}\right)^2 {u_{c,V_\mathrm{H}}}^2 + \left(\frac{\partial f_1}{\partial \theta_\mathrm{r}}\right)^2 u_{\theta_\mathrm{r}}^2 + \left(\frac{\partial f_1}{\partial \alpha_\mathrm{exp}}\right)^2 u_{\alpha_\mathrm{exp}}^2 \\ &+ 2r\left(V_\mathrm{H}, \theta_\mathrm{r}\right)\left(\frac{\partial f_1}{\partial V_\mathrm{H}}\right)\left(\frac{\partial f_1}{\partial \theta_\mathrm{r}}\right) u_{c,V_\mathrm{H}} u_{\theta_\mathrm{r}} \\ &+ 2r\left(V_\mathrm{H}, \alpha_\mathrm{exp}\right)\left(\frac{\partial f_1}{\partial V_\mathrm{H}}\right)\left(\frac{\partial f_1}{\partial \alpha_\mathrm{exp}}\right) u_{c,V_\mathrm{H}} u_{\alpha_\mathrm{exp}} \\ &+ 2r\left(\theta_\mathrm{r}, \alpha_\mathrm{exp}\right)\left(\frac{\partial f_1}{\partial \theta_\mathrm{r}}\right)\left(\frac{\partial f_1}{\partial \alpha_\mathrm{exp}}\right) u_{\theta_\mathrm{r}} u_{\alpha_\mathrm{exp}}\ , \end{aligned} \tag{4.7}$$

where u_{θ_r}, u_{α_exp}, and the three correlation coefficients are extracted from the MC uncertainty look-up tables. The expressions of the partial derivatives are given in Appendix A. One can show that at hub height ($z_\mathcal{H} = 0$), the partial derivatives equal 0, except the one in respect to V_H which is unity. Thus, we obtain the consistent result that: $u_{c,V(z_\mathcal{H}=0)} = u_{c,V_\mathrm{H}}$.

4.7.2 For the wind-induction model

The considered WFR case is now using the combined wind-induction model.

The model uncertainty u_{V_∞} – extracted from the MC uncertainty look-up tables – is combined with the $RMSE$ to compute u_{c,V_∞} as follows:

$$u_{c,V_\infty} = \sqrt{u_{V_\infty}^2 + RMSE^2}. \tag{4.8}$$

Additionally the combined uncertainty on the wind speed $V\left(x_{\mathcal{H}}, z_{\mathcal{H}}\right)$ can be derived for any upstream position $x_{\mathcal{H}}$ and height $z_{\mathcal{H}}$ (see Fig. 2, Page 48). The GUM methodology is applied to the following model f_2 (see also Eq. 11, Page 50):

$$\begin{aligned} f_2 &= V\left(x_{\mathcal{H}}, z_{\mathcal{H}}, V_{\mathrm{H}}, \theta_{\mathrm{r}}, \alpha_{\mathrm{exp}}, a_{\mathrm{ind}}\right) \\ &= V_{\infty}\left(\frac{z_{\mathcal{H}}+H_{\mathrm{hub}}}{H_{\mathrm{hub}}}\right)^{\alpha_{\mathrm{exp}}} \sqrt{\cos^2\theta_{\mathrm{r}}\left(1-a_{\mathrm{ind}}\left[1+\frac{\xi}{\sqrt{1+\xi^2}}\right]\right)^2+\sin^2\theta_{\mathrm{r}}}, \end{aligned} \tag{4.9}$$

where $\xi = \frac{x_{\mathcal{H}}}{R_{\mathrm{rot}}}$. The combined uncertainty $u_{c,V(x_{\mathcal{H}},z_{\mathcal{H}})}$ is then given by

$$\begin{aligned} u^2_{c,V(x_{\mathcal{H}},z_{\mathcal{H}})} = &\left(\frac{\partial f_2}{\partial V_{\infty}}\right)^2 {u_{c,V_{\infty}}}^2 + \left(\frac{\partial f_2}{\partial \theta_{\mathrm{r}}}\right)^2 u^2_{\theta_{\mathrm{r}}} + \left(\frac{\partial f_2}{\partial \alpha_{\mathrm{exp}}}\right)^2 u^2_{\alpha_{\mathrm{exp}}} + \left(\frac{\partial f_2}{\partial a_{\mathrm{ind}}}\right)^2 u^2_{a_{\mathrm{ind}}} \\ &+ 2r\left(V_{\infty}, \theta_{\mathrm{r}}\right)\left(\frac{\partial f_2}{\partial V_{\infty}}\right)\left(\frac{\partial f_2}{\partial \theta_{\mathrm{r}}}\right) u_{c,V_{\infty}} u_{\theta_{\mathrm{r}}} \\ &+ 2r\left(V_{\infty}, \alpha_{\mathrm{exp}}\right)\left(\frac{\partial f_2}{\partial V_{\infty}}\right)\left(\frac{\partial f_2}{\partial \alpha_{\mathrm{exp}}}\right) u_{c,V_{\infty}} u_{\alpha_{\mathrm{exp}}} \\ &+ 2r\left(V_{\infty}, a_{\mathrm{ind}}\right)\left(\frac{\partial f_2}{\partial V_{\infty}}\right)\left(\frac{\partial f_2}{\partial a_{\mathrm{ind}}}\right) u_{c,V_{\infty}} u_{a_{\mathrm{ind}}} \\ &+ 2r\left(\theta_{\mathrm{r}}, \alpha_{\mathrm{exp}}\right)\left(\frac{\partial f_2}{\partial \theta_{\mathrm{r}}}\right)\left(\frac{\partial f_2}{\partial \alpha_{\mathrm{exp}}}\right) u_{\theta_{\mathrm{r}}} u_{\alpha_{\mathrm{exp}}} \\ &+ 2r\left(\theta_{\mathrm{r}}, a_{\mathrm{ind}}\right)\left(\frac{\partial f_2}{\partial \theta_{\mathrm{r}}}\right)\left(\frac{\partial f_2}{\partial a_{\mathrm{ind}}}\right) u_{\theta_{\mathrm{r}}} u_{a_{\mathrm{ind}}} \\ &+ 2r\left(\alpha_{\mathrm{exp}}, a_{\mathrm{ind}}\right)\left(\frac{\partial f_2}{\partial \alpha_{\mathrm{exp}}}\right)\left(\frac{\partial f_2}{\partial a_{\mathrm{ind}}}\right) u_{\alpha_{\mathrm{exp}}} u_{a_{\mathrm{ind}}}\ , \end{aligned} \tag{4.10}$$

where standard WFC uncertainties and the correlation coefficients are extracted from the MC uncertainty look-up tables. The expressions of the partial derivatives are given in Appendix A. It can be demonstrated that at hub height ($z_{\mathcal{H}} = 0$) and in the free stream ($\xi \to -\infty$), the partial derivatives converge to 0, except the one in respect to V_{∞} which is unity. This confirms that we have: $u_{c,V(x_{\mathcal{H}}\to-\infty,z_{\mathcal{H}}=0)} = u_{c,V_{\infty}}$.

4.8 Discussions

In this chapter, we used Monte Carlo Methods to quantify the uncertainties of lidar-estimated WFC. Several WFR models were considered. The methods we used to propagate the uncertainties on the inputs of the WFR models were built around a framework for the quantification of model uncertainty.

Hereafter, we discuss the assumptions made to perform MC simulations, the effect of finite number of samples on the uncertainty results, the absence of lidar classification uncertainty, and how these methods could be used in the context of power performance standards.

4.8.1 On the inputs distributions

MC simulations were performed for a number of study cases (sets of WFC) and several wind models.

For each MC simulation, samples were drawn from inputs' distributions of errors assumed to be Gaussian. These inputs are multiple V_{los} and lidar trajectory parameters (tilt, roll, opening angles, etc). All the uncertainty parameters used to characterise the Gaussian distributions of inputs originated from calibration procedures and/or verification tests (see Chapter 2) where care was taken to correct for any potential non-random errors (biases).

Nonetheless, the lidar V_{los} measurements were calibrated using cup anemometers as the main reference instrument. Cup anemometers are known to be sensitive to external parameters such as turbulence, temperature and inflow angles. These sensitivities are included into the uncertainty assessment of the cup anemometers' wind speed measurements (Fig. 2.10) instead of correcting them, through the so-called operational uncertainty. The cup's operational uncertainty contributed significantly to the lidar V_{los} combined uncertainties. However, the effect of including the cup's operational uncertainty in the V_{los} uncertainty assessment procedure is only an over-estimation of the lidar V_{los} uncertainties – not the inclusion of a measurement bias.

Consequently, the assumption of Gaussian-distributed input samples is reasonable.

4.8.2 On the convergence of Monte Carlo simulations

The GUM provides exact uncertainty results under several conditions for its application to be valid – such as linearised analytical measurement models, Gaussian-equivalent inputs distributions (the uncertainty parameters are converted into a Gaussian-equivalent width) and Gaussian-distributed outputs, etc.

The WFR models using the model-fitting approach are not analytical, non-linear, and have many inputs. The GUM conditions of valid application are therefore far from being met. Hence, we chose to use statistical techniques instead, particularly MCM as they are valid for any model (see clause 5.4.3 in JCGM, 2008b).

The uncertainty quantification results using MC simulations are however imperfect – only approximations of the exact results – since it is impossible to simulate an infinite number of samples. The convergence of the MC simulation results was tested for both the 'wind' and 'combined wind-induction' WFR models. Fig. 4.13 shows the relative errors (in %) on the WFC uncertainties obtained with $N_\mathrm{s} = 10^3, N_\mathrm{s} = 5 \times 10^3, N_\mathrm{s} = 2 \times 10^4$ samples. The reference uncertainty values used to calculate the relative error were obtained with $N_\mathrm{s} = 10^5$. We can observe that for all four WFC, the relative errors oscillate around 0 and their magnitudes tend to decrease with a higher number of samples.

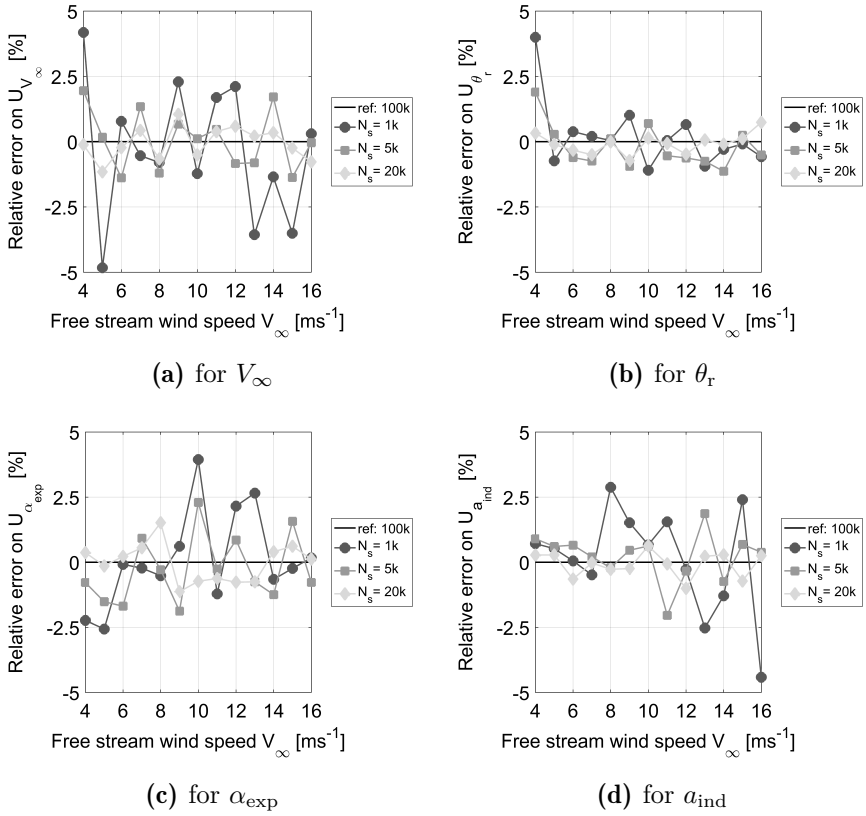

(a) for V_∞ **(b)** for θ_r

(c) for α_exp **(d)** for a_ind

Figure 4.13: Effect of sample size on MC simulation results: relative errors on the WFC uncertainties as a function of wind speed, using the combined wind-induction model. Case where $\theta_\mathrm{r} = 4°$, $\alpha_\mathrm{exp} = 0.2$, a_ind takes its 'nominal' value.

MCM are in general computationally expensive. In the previous sections, we used $N_\mathrm{s} = 5 \times 10^3$ samples. This number of samples was found to be a good compromise between the convergence of the uncertainty results – with relative errors within 2 % – and computation time.

Regarding computation time – using a single CPU (Intel i7-4600) – each MC simulation of 5×10^3 samples takes:

- for the wind model, $\approx 35\,\mathrm{s}$. In total, the simulation of the 1225 study cases lasted ≈ 12 hours for each lidar case;
- for the combined wind-induction model, $\approx 90\,\mathrm{s}$. In total, the simulation of the 4725 study cases took ≈ 5 days for each lidar case.

In the future, using calibrated surrogate models – obtained using e.g. polynomial chaos expansion techniques (Sudret, 2008; Foti et al., 2016) – for predicting the uncertainty instead of full Monte Carlo simulations might be possible. Employing surrogate models would speed-up calculations by several orders of magnitude.

4.8.3 On the application of MCM to wind field reconstruction codes of commercial nacelle lidars

Power performance standards demand the quantification of uncertainties of the wind measuring instrument. In this chapter, using MCM for quantifying uncertainties on the lidar-reconstructed wind characteristics was facilitated by the easy access to the WFR codes – as those were developed within this Ph. D. project.

Commercial WFR codes embedded into nacelle lidar systems are likely to be considered proprietary and confidential. In such a case, applying MCM for quantifying the uncertainty of the outputs of the WFR codes could prove more difficult.

However, extensive knowledge and open-access to the WFR code is not required in order to perform MC simulations. For nacelle lidars to be considered in the next generation of power performance standards, we suggest to tackle the aforementioned issue simply by requiring the provision of the following information:

- a list of the WFR model inputs;
- an encoded program (executable) of the WFR code;
- a list of the WFR model outputs.

In so doing, the test laboratory performing the ‘white-box’ calibration of a commercial nacelle lidar would be able to assess the model uncertainty of the lidar-reconstructed wind characteristics and provide the results in the calibration report.

CHAPTER 5
Application To Power Performance Testing

Power performance testing aims at relating the net power output of a wind turbine to the free flow wind conditions. The end result is the measured power curve, which is obtained by averaging power, wind speed and several other variables per wind speed bins. Furthermore, the power curve uncertainty shall be assessed.

The procedures for the measurement of a turbine's power curve are detailed in the IEC 61400-12-1, 2017 standards. One key element is the wind speed measuring instrument. In the latest standards (2017), it is allowed to use either mast-mounted cup or sonic anemometers, a ground-based 'remote sensing device' (usually a lidar or sodar), or a combination of both.

Similar methods could be applied to nacelle lidar wind measurements, albeit they must be developed and tested. The methods and results of the previous chapters provide all the elements necessary to test the power performance of a wind turbine using nacelle lidars.

With the model-fitting wind field reconstruction techniques (Chapter 3), wind characteristics – speed, direction, shear, etc – are estimated from the lidars' primary measurements (of LOS velocities and measurement position quantities). In order to quantify the uncertainties of the lidar-reconstructed wind characteristics, the inputs of the WFR models were calibrated and their uncertainties assessed (Chapter 2). The inputs' uncertainties were then propagated through the WFR models using Monte Carlo methods and combined with the model inadequacy uncertainty (Chapter 4).

I demonstrate in this chapter how nacelle-based profiling lidar systems can be used for measuring a power curve and assess its uncertainty. First, the methodologies employed to derive power curve results and assess their uncertainties are provided in detail. The power curve results are obtained using the experimental data from the NKE campaign (see Section 3.2.3). For the nacelle lidars, three wind speed estimation methods are investigated. The results obtained with two different nacelle lidar systems – the 5B-Demo and ZDM – are compared to the ones with the reference mast-mounted cup anemometer.

Further, the annual energy production annual energy production (AEP) is analysed following the standards' methodology.

Note: whenever possible, the notations in this chapter correspond to the ones in IEC 61400-12-1, 2017.

5.1 Methods for power curve measurement

The methods for measuring the power curve of a wind turbine are based on the so-called 'method of bins'. It consists of collecting measurement data over a sufficiently long time period – usually several months –, and binning them according to the 10-minute mean normalised wind speed.

5.1.1 Wind speed definitions: hub height and energy equivalent quantities

A wind turbine extracts its energy from the kinetic energy E_{kin} present in the wind. In terms of power, the available power P_{kin} in the wind can simply be expressed as

$$P_{\text{kin}} = \frac{\mathrm{d}E_{kin}}{\mathrm{d}t} = \frac{1}{2}\rho A V^3 \ , \tag{5.1}$$

where t is the time, ρ is the air density, V the wind speed, and A an area through which the wind flows – e.g. the rotor swept area. Both ρ and V vary across the rotor area. In its most general form, the kinetic energy flux through A is given by:

$$P_{\text{kin}} = \int_A \frac{1}{2}\rho\,(\mathrm{d}A)\cdot V^3\,(\mathrm{d}A)\,\mathrm{d}A \ , \tag{5.2}$$

While the former standards (IEC 61400-12-1, 2005) utilized the measurement of hub height wind speed – i.e. Eq. (5.1) effectively applies with A being the rotor swept area –, the standards are now in 2017 based on the estimation of a rotor-averaged quantity, the so-called rotor equivalent wind speed (REWS). Assuming that ρ is constant over A, the energy equivalent speed V_{eq} is computed as follows:

$$V_{\text{eq}} = \left(\frac{P_{\text{kin}}}{\frac{1}{2}\rho A}\right)^{1/3} \ . \tag{5.3}$$

Albeit V_{eq} is more representative of P_{kin} than the hub height wind speed V_{hub}, the difference between the two quantities is practically only significant for large wind turbines operating in conditions where the wind experiences strongly non-linear variations with height.

The standards additionally integrate wind veer – the variation of the wind direction with height – into the calculation of P_{kin} and thus of V_{eq}.

In this chapter, only the hub height wind speed was considered for conducting the power performance tests. This allows simpler comparisons between mast- and nacelle lidar-based power curve measurements. Consequently, no shear, REWS or veer correction was applied to the measurement data.

For the mast-based power curve, the cup anemometer top-mounted at hub height H_{hub} was used (case 0). The IEC correction for 'mast flow distortion' only applies to side-mounted instruments and is here irrelevant (see Annex S in IEC 61400-12-1, 2017).

For the power curves based on the nacelle lidars' measurements, the model-fitting WFR method was employed. The hub height wind speed is estimated according to the following cases:

- case 1: using the 'wind' model and lidar V_{los} measurements (see Sect. 4.1, Page 53) taken:
  - (a) for 5B-Demo, at $2D_{\text{rot}}$ upstream of the rotor plane;
  - (b) for ZDM, at $2.5D_{\text{rot}}$ upstream of the rotor plane.
- case 2: using the 'combined wind-induction' model and lidar V_{los} measurements taken close to the turbine rotor (see Sect. 4.2, Page 54)
  - (a) for 5B-Demo, the wind speed is estimated at $2.5D_{\text{rot}}$;
  - (b) for ZDM, the wind speed is estimated at $2.5D_{\text{rot}}$;
  - (c) for 5B-Demo, the fitted free stream wind speed V_{∞} is used;
  - (d) for ZDM, the fitted free stream wind speed V_{∞} is used.

The filters applied to the measurement datasets are detailed in Sect. 3.4 (Page 52), except that the valid wind direction sector is replaced by the 'IEC free sector' (see Annex A in IEC 61400-12-1, 2017) – $[110°, 219°]$ for turbine 04 in NKE. The datasets are joined between the different measuring instruments (mast, lidars, etc) in order to obtain datasets of the same size and containing the same time periods. For the wind speed comparison results, see 'case (3)' in Table 2, Page 56.

Finally, the terrain in the NKE wind farm vicinity is flat (see Fig. 3(a), Page 51), as per the definition of Annex B of IEC 61400-12-1, 2017. Consequently, the power performance test was conducted without a site calibration.

5.1.2 Power curve normalisation

The standard power curve of a wind turbine must be normalised. The purpose of normalising the data is to improve the accuracy of the results by formulating variables in a concrete manner, and to allow the comparison of power curve results from different data sets – such as the power curve of the same turbine measured at a different times of the year.

The normalisation is primarily performed according to air density. For a given wind speed, a turbine extracts more energy at high than low air density. For stall-regulated wind turbines, the air density normalisation is applied to the 10-minute mean of the net power output ($P_{10\,\mathrm{min}}$). For pitch-regulated turbines – this is the case of the SWT-2.3-93 turbine in NKE – it applies to the 10-minute mean wind speed $V_{10\,\mathrm{min}}$, and the normalised wind speed V_{n} is computed as:

$$V_{\mathrm{n}} = V_{10\,\mathrm{min}} \left(\frac{\rho_0}{\rho_{10\,\mathrm{min}}} \right)^{1/3} , \tag{5.4}$$

where ρ_0 is the reference air density , and $\rho_{10\,\mathrm{min}}$ is the 10-minute mean air density, derived using measurements of air temperature ($T_{10\,\mathrm{min}}$), hub height pressure ($B_{10\,\mathrm{min}}$), and relative humidity ($RH_{10\,\mathrm{min}}$).

The reference air density value here used is $\rho_0 = 1.225\,\mathrm{kg/m^3}$, corresponding to the international standard atmosphere at sea level, where $T_0 = 15\,^{\circ}\mathrm{C}$, $B_0 = 1013.25\,\mathrm{hPa}$, $RH_0 = 0\,\%$.

The formula to determine $\rho_{10\,\mathrm{min}}$ is:

$$\rho_{10\,\mathrm{min}} = \frac{1}{T_{10\,\mathrm{min}}} \left(\frac{B_{10\,\mathrm{min}}}{R_0} - RH_{10\,\mathrm{min}} \cdot P_{\mathrm{w}} \left[\frac{1}{R_0} - \frac{1}{R_{\mathrm{w}}} \right] \right) , \tag{5.5}$$

where $R_0 = 287.05\,\mathrm{J\,kg^{-1}\,K}$ and $R_{\mathrm{w}} = 461.5\,\mathrm{J\,kg^{-1}\,K}$ are the gas constants of respectively dry air and water vapour, and

$$P_{\mathrm{w}} = 0.0000205 \cdot \exp(0.0631846 \cdot T_{10\,\mathrm{min}})\,[\mathrm{Pa}]$$

is the water vapour pressure.

Additionally, the standards recommend to normalise the power curve data to a reference turbulence intensity value. The turbulence intensity normalisation is not mandatory. In the derived results of this chapter, no turbulence intensity normalisation was applied to the data.

5.2 Measured power curve results

The measured power curves are presented both in scatter plots of 10 min normalised power and speed, and of bin-averaged data. Note that in these graphs, the axes are normalised by the rated power and rated wind speed to ensure confidentiality.

5.2.1 Based on 10-minute data

Fig. 5.1 shows the scatter plots of the measured power curves. The reference power curve ('ref') was provided by the turbine manufacturer and corresponds to the site-specific power curve.

In Fig. 5.1, the first observation is an obvious reduction of the scatter when the wind speed is estimated using the nacelle lidars in comparison to the mast-based power curve. This scatter reduction can be attributed to the higher correlation between the wind driving the turbine and the wind sensed by the nacelle lidars since they always measure directly upwind. In contrast, there is a significant signal decorrelation between the mast-measured wind speed and power output when the turbine is not closely aligned to the mast. The low scatter in the power curve measured by the nacelle lidars is desirable and will reduce the category A uncertainty on the power output (denoted $s_{\mathrm{P},i}$, see Sect. Section 5.3).

Visually, all five measured power curves seem to agree well with the reference power curve. We can however identify a small shift to the right for the lidar cases using the 'wind' model rather than the combined 'wind-induction' model. This observation is consistent with the overestimation of wind speed when using the 'wind' model applied to lidar measurements close to the mast distance, in comparison to the mast top-mounted cup anemometer measurements (see Table 2, Page 56).

At low wind speeds, the measured power curves appear to be below the reference power curve – obtained for a standard 10 % turbulence intensity (TI). This is likely related to the lack of TI normalisation of the wind speed. In order to verify this, the turbulence intensity measured by the mast top-mounted cup anemometer is plotted against the normalised wind speed, see Fig. 5.2. The dataset corresponds exactly to the one used for power curve measurements. One can observe that for normalised speeds between 0.4 and 0.8, the bin-averaged TI is 1 % to 2 % lower than the standard 10 % value. This result is consistent with the effect that TI normalisation would have here on the measured power curves: at low speeds, the normalisation would reduce the normalised speed values (shift to the left, i.e. enhancement from the power curve perspective); close to rated speed, the power output is affected negatively by the wind speed fluctuations (shift to the right).

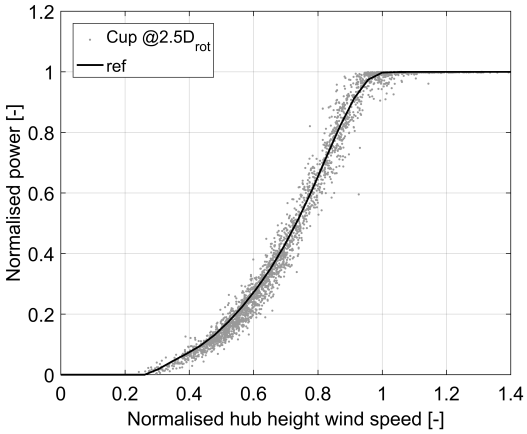

(a) Mast top-mounted cup anemometer

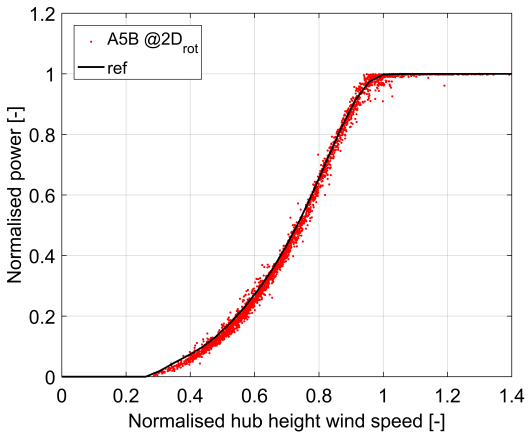

(b) 5B-Demo, V_{H} from the 'wind' model

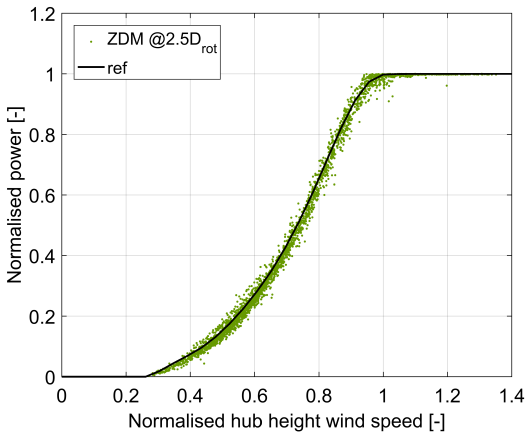

(c) ZDM, V_{H} from the 'wind' model

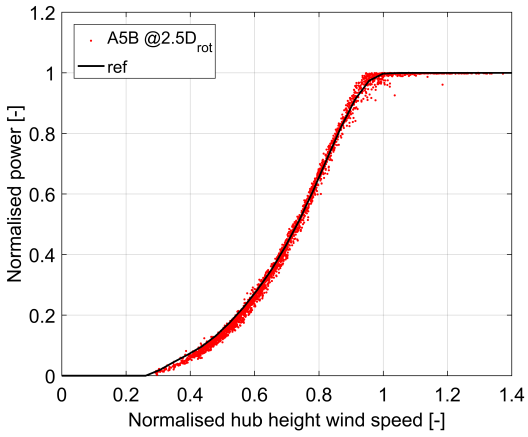

(d) 5B-Demo, with 'wind-induction' model

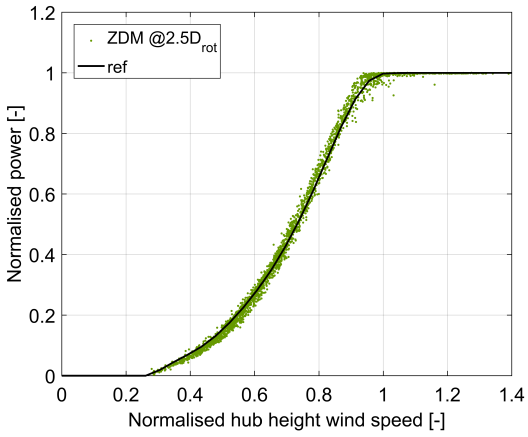

(e) ZDM, with 'wind-induction' model

Figure 5.1: Measured power curves of turbine 04 during the NKE campaign, in the form of scatter plots of 10 min normalised power and speed. The hub height wind speed estimates are obtained from the mast top-mounted cup anemometer, and from the 5B-Demo and ZDM nacelle lidars using two different wind field reconstruction models.

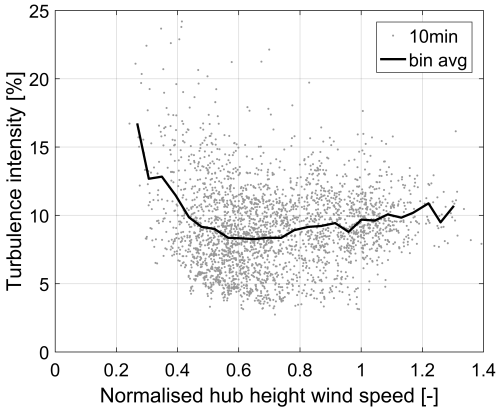

Figure 5.2: Turbulence intensity vs. cup-measured wind speed (normalised) used for power curve measurements.

For the lidar cases where only measurements at multiple distances close to the turbine rotor (from 0.5 to 1.2 D_{rot}) are used together with the combined wind-induction model, the measured power curves using directly the V_∞ wind characteristic were not presented as the scatter plots differ negligibly from Fig. 5.1(d) and Fig. 5.1(e).

Instead, the relative difference $\left(V_\infty - V_{\text{H},2.5D_{\text{rot}}}\right)/V_\infty$ is analysed as a function of wind speed in Fig. 5.3. This relative difference basically quantifies the error made on the wind speed by assuming that the free stream wind speed can be approximated by the wind speed at $2.5D_{\text{rot}}$. We can observe that below rated wind speed the relative difference is most of the time within 0.5 % to 1 % as previously discussed (see Sect.5.1, Page 57). As expected, the observed trends – obtained by smoothing the bin averaged data – in the relative speed difference match entirely the induction factor curves (Fig. 3.18).

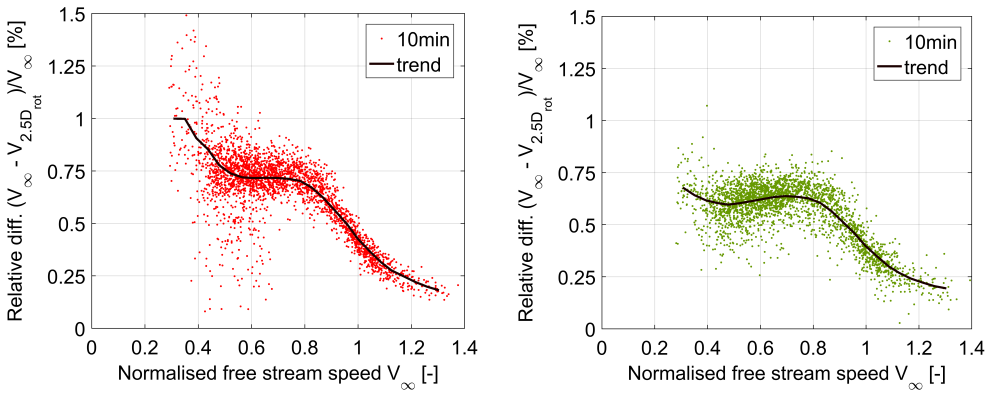

(a) for 5B-Demo **(b)** for ZDM

Figure 5.3: Relative difference between the free stream wind speed V_∞ and the speed estimated at $2.5D_{\text{rot}}$; obtained using the combined wind-induction model.

5.2.2 Bin-averaged measured power curves

Fig. 5.4 shows the measured power curves obtained via the method of bins. The power curves from the three wind measuring instruments – the mast-mounted cup anemometer, the 5B-Demo and the ZDM lidars – are extremely close from each other and a high level of agreement is obtained with the reference power curve. This proves that profiling nacelle lidars can provide valid measurements for power performance testing.

The only noticeable differences are:

- at low wind speed, a higher speed than the reference power curve for all three systems (Fig. 5.4(a)). As previously suggested, the cause is the lack of TI normalisation of the wind speed (see Fig. 5.2).
- when using the wind-induction model and wind speed estimates at $2.5D_{\text{rot}}$ (Fig. 5.4(b)), ZDM seems to under-estimate the speed, except at low wind speeds;
- the power curves measured using the V_∞ characteristic of the wind-induction model are slightly shifted to the right.

The impact of the free stream wind speed approximation on the measured power curves is further analysed in Fig. 5.5 by looking at the relative difference $\Delta P_{i,\text{rel}}$ in the bin-averaged normalised power, expressed as follows:

$$\Delta P_{i,\text{rel}} = \frac{P_i\left(V_{\text{H},2.5D_{\text{rot}}}\right) - P_i\left(V_\infty\right)}{P_i\left(V_\infty\right)}. \tag{5.6}$$

At low wind speed, the results are very sensitive to the number of measurement periods in the bins and thus not meaningful. For normalised wind speeds $\in [0.4, 0.8]$, when using the wind speed estimated at $2.5D_{\text{rot}}$, the bin-averaged power is over-estimated by 2 % to 3 %. Above 0.8, $\Delta P_{i,\text{rel}}$ decreases rapidly and reaches values close to zero above rated wind speed. This is directly related to the rapidly decreasing magnitude of the thrust coefficient for wind speeds close to rated speed. Indeed, the relative wind speed deficit at a given distance upstream the turbine rotor is greater at low than high wind speeds.

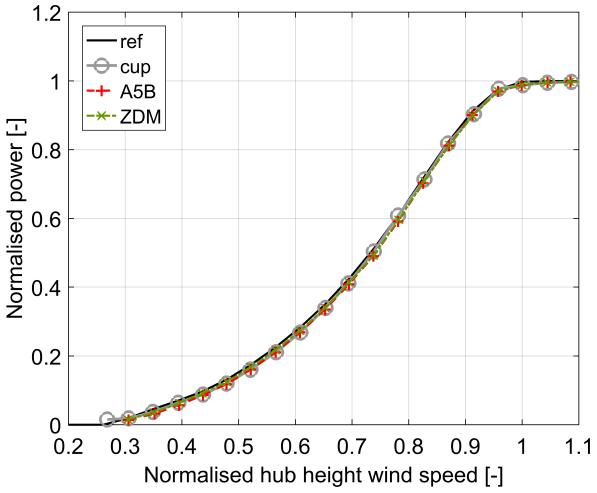

(a) Mast-based; 5B-Demo and ZDM using the 'wind' model.

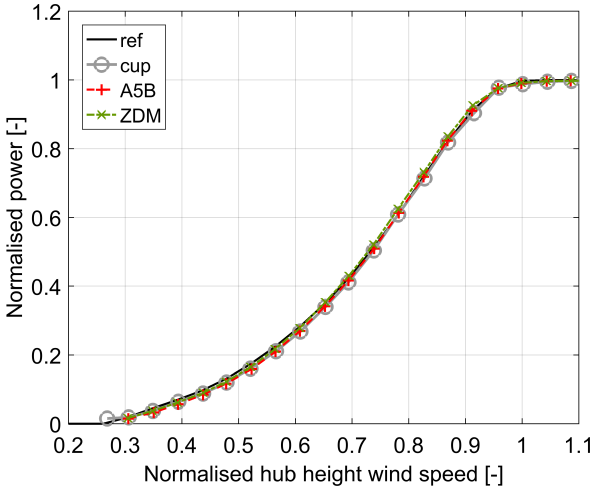

(b) Mast-based; 5B-Demo and ZDM, using the 'wind-induction' model and wind speed estimated at $2.5D_{\text{rot}}$.

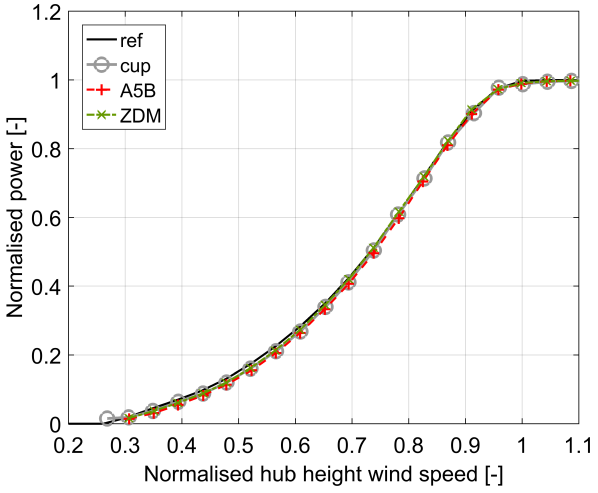

(c) Mast-based; 5B-Demo and ZDM, using the 'wind-induction' model and the V_∞ characteristic.

Figure 5.4: Bin-averaged measured power curves of turbine 04 during the NKE campaign.

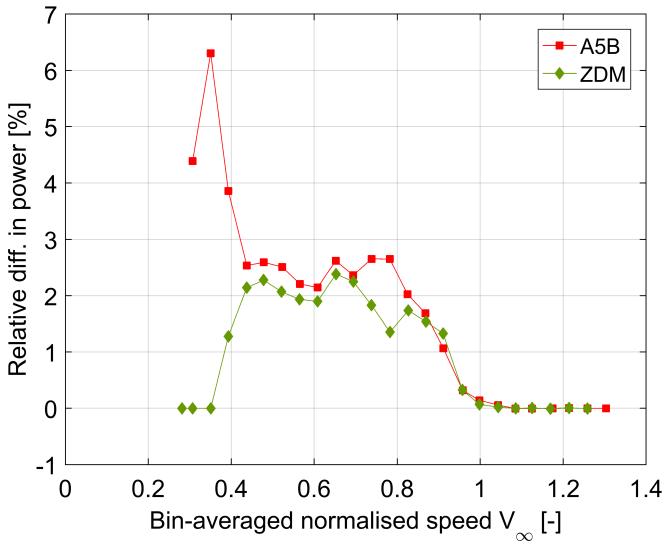

Figure 5.5: Relative difference in the bin-averaged output power between the lidar cases where the free stream wind speed V_∞ and the speed estimated at $2.5D_{\text{rot}}$ are obtained using the combined wind-induction model.

5.3 Power curve uncertainties

The power curve uncertainty is the combined uncertainty on the power (in [kW]), per wind speed bin. The IEC 61400-12-1, 2017 requires the reporting of the category A, category B, and combined standard uncertainties. In particular, the category B uncertainty combines a large number of uncertainty sub-components from different sources.

This section describes the uncertainty assessment procedure that was used for the NKE measurement campaign. It follows closely the procedure in the standards, which is itself based on the GUM methodology. When occurring, deviations from the requirements of the standards are clearly stated and their reason is explained. Secondly, the power curve uncertainty results are provided.

5.3.1 Uncertainty assessment procedure, sources and budget

Utilizing the notation of the IEC 61400-12-1, 2017, the standard uncertainty on the electric power $u_{c,\mathrm{P},i}$ in wind speed bin i is given by:

$$u^2_{c,\mathrm{P},i} = \underbrace{s^2_{\mathrm{P},i} + u^2_{\mathrm{P},i}}_{\text{on power } \mathrm{P}_i} + \underbrace{c^2_{\mathrm{T},i}u^2_{\mathrm{T},i} + c^2_{\mathrm{B},i}u^2_{\mathrm{B},i} + c^2_{\mathrm{RH},i}u^2_{\mathrm{RH},i}}_{\text{on air density } \rho_i} + \underbrace{c^2_{\mathrm{V},i}u^2_{\mathrm{V},i} + c^2_{\mathrm{V},i}s^2_{\mathrm{SC},i} + c^2_{\mathrm{V},i}u^2_{\mathrm{M},i}}_{\text{on wind speed } \mathrm{V}_i}, \tag{5.7}$$

where the terms are defined in Table 5.1 below. Cross-references to the relevant sections or equations are also provided. Note that the quadratic sum in Eq. (5.7) implicitly assumes that the uncertainty components are uncorrelated.

No site calibration was conducted for the NKE measurement campaign. Consequently, we have $s_{\mathrm{SC},i} = 0$.

The 'method' uncertainty aims at assessing uncertainties of corrections for shear, veer, vertical flow angle and turbulence intensity made to the wind speed measurements – either at hub height, or of the REWS, or at several heights covering partly the rotor.

The 'method' uncertainty is here discarded from the power curve uncertainty analysis by setting $u_{\mathrm{M},i}$ to zero. Since the purpose in this chapter is to compare the power curve uncertainty results on hub height wind speed measured or estimated from different measuring systems (mast-mounted cup anemometer, nacelle lidars), this uncertainty component would take the same values for all the used wind speed measuring instruments. Moreover, the procedure to assess $u_{\mathrm{M},i}$ described in the

Table 5.1: Components and terms of the combined uncertainty $u_{c,\mathrm{P},i}$ on electric power in bin i.

Term	Symbol	Category	Unit	cf.
Standard uncertainty on				
power	$s_{\mathrm{P},i}$	A	kW	Eq. (5.8)
	$u_{\mathrm{P},i}$	B	kW	Eq. (5.9)
air temperature	$u_{\mathrm{T},i}$	B	K	Eq. (5.10)
air pressure	$u_{\mathrm{B},i}$	B	Pa	Eq. (5.11)
relative humidity	$u_{\mathrm{RH},i}$	B	-	Eq. (5.13)
wind speed	$u_{\mathrm{V},i}$	B	$\mathrm{m\,s^{-1}}$	Section 5.3.1.5
site calibration	$s_{\mathrm{SC},i}$	A	$\mathrm{m\,s^{-1}}$	
method	$u_{\mathrm{M},i}$	B	$\mathrm{m\,s^{-1}}$	
Sensitivity factor for				
air temperature	$c_{\mathrm{T},i}$	-	$\mathrm{kW\,K^{-1}}$	Eq. (5.18)
air pressure	$c_{\mathrm{B},i}$	-	$\mathrm{kW\,Pa^{-1}}$	Eq. (5.19)
relative humidity	$c_{\mathrm{RH},i}$	-	kW	Eq. (5.20)
wind speed	$c_{\mathrm{V},i}$	-	$\mathrm{kW/(m\,s^{-1})}$	Eq. (5.21)

standards is based on a number of assumptions that have little physical or scientific background.

5.3.1.1 Standard uncertainties on electric power

The category A standard uncertainty $s_{\mathrm{P},i}$ in electric power is a statistical uncertainty component characterising the observed scatter of the normalised power $P_{\mathrm{n}} = P_{10\,\mathrm{min}}$ (for pitch-regulated turbines) in wind speed bin i. It is computed as:

$$s_{\mathrm{P},i} = \frac{\sigma_{\mathrm{P},i}}{\sqrt{N_i}} = \frac{1}{\sqrt{N_i}} \sqrt{\frac{\sum_{j=1}^{N_i} \left(P_i - P_{\mathrm{n},i,j}\right)^2}{N_i - 1}} \,, \tag{5.8}$$

where P_i and N_i are respectively the mean normalised power and number of periods in bin i.The category B standard uncertainty $u_{\mathrm{P},i}$ in electric power is a combined uncertainty related to the sensors used to measure $P_{10\,\mathrm{min}}$ and expressed as follows:

$$u_{\mathrm{P},i}^2 = u_{\mathrm{P,CT},i}^2 + u_{\mathrm{P,VT},i}^2 + u_{\mathrm{P,PT},i}^2 + u_{\mathrm{dP},i}^2 \,, \tag{5.9}$$

where the uncertainty components are detailed in Table 5.2.

Table 5.2: Components of combined category B uncertainty $u_{\mathrm{P},i}$ on electric power in bin i. The value used in the mathematical expression of the uncertainty and the comments are specific to the measurement systems used in the NKE campaign.

Source	Symbol	Expression	Comment
current transformer	$u_{\mathrm{P,CT},i}$	$\frac{0.002}{\sqrt{3}} P_i$	Class 0.2S, 0.2 % at 20 % load.
voltage transformer	$u_{\mathrm{P,VT},i}$	0	No voltage transformer was used.
power transducer	$u_{\mathrm{P,PT},i}$	$\frac{0.005 \cdot (3000-(-500))}{\sqrt{3}}$	Class 0.5, range: −500 to 3000 kW.
data acquisition	$u_{\mathrm{dP},i}$	$0.001 \cdot 3500$	Default IEC value, 0.1 % of electric power range.

5.3.1.2 Standard uncertainty on temperature

The category B standard uncertainty $u_{\mathrm{T},i}$ in air temperature is a combined uncertainty related to the sensor used to measure $T_{10\,\mathrm{min}}$ and expressed as follows:

$$u^2_{\mathrm{T},i} = u^2_{\mathrm{T,cal},i} + u^2_{\mathrm{T,shield},i} + u^2_{\mathrm{T,mnt},i} + u^2_{\mathrm{dT},i} \ , \tag{5.10}$$

where the uncertainty components are detailed in Table 5.3. All the sub-components are independent of measurements. For the NKE temperature sensor (Vaisala HMP155), we compute: $u_{\mathrm{T},i} = 1.53\,\mathrm{K}$. The prevailing uncertainty source is the radiation shielding.

Table 5.3: Components of combined category B uncertainty $u_{\mathrm{T},i}$ on air temperature in bin i. The value used in the mathematical expression of the uncertainty and the comments are specific to the measurement systems used in the NKE campaign.

Source	Symbol	Expression	Comment
calibration	$u_{\mathrm{T,cal},i}$	0.0275 K	From certificate.
radiation shielding	$u_{\mathrm{T,shield},i}$	1.5 K	Default IEC value.
mounting	$u_{\mathrm{T,mnt},i}$	0.25 K	Default IEC value.
data acquisition	$u_{\mathrm{dT},i}$	$0.001 \cdot (60 - (-80))$	Default IEC value, 0.1 % of temperature range.

5.3.1.3 Standard uncertainty on pressure

The category B standard uncertainty $u_{\mathrm{B},i}$ in air pressure is a combined uncertainty related to the sensor used to measure $T_{10\,\mathrm{min}}$ and expressed as follows:

$$u^2_{\mathrm{B},i} = u^2_{\mathrm{B,cal},i} + u^2_{\mathrm{B,mnt},i} + u^2_{\mathrm{dB},i} \ , \tag{5.11}$$

where the uncertainty components are detailed in Table 5.4. All the sub-components are independent of measurements.

Table 5.4: Components of combined category B uncertainty $u_{\mathrm{B},i}$ on air pressure at hub height in bin i. The value used in the mathematical expression of the uncertainty and the comments are specific to the measurement systems used in the NKE campaign.

Source	Symbol	Expression	Comment
calibration	$u_{\mathrm{B,cal},i}$	0.065 hPa	From certificate.
mounting	$u_{\mathrm{B,mnt},i}$	0.036 hPa	10 % of correction to hub height.
data acquisition	$u_{\mathrm{dB},i}$	$0.001 \cdot (1060 - 800)$ hPa	Default IEC value, 0.1 % of pressure range.

In NKE, the air pressure sensor was mounted at 77 m agl. The corrected air pressure B_{hub} at hub height $H_{\mathrm{hub}} = 80\,\mathrm{m}$ is according to the ISO:2355 standard equal to

$$B_{\mathrm{hub}} = B_{77} + B_0 \cdot \left[1 - \left(\frac{288 - 0.0065 \cdot 80}{288 - 0.0065 \cdot 77}\right)^{5.255}\right] \ , \tag{5.12}$$

and the correction is $B_{\mathrm{hub}} - B_{77} \approx 0.36\,\mathrm{hPa}$. For the NKE pressure sensor (Vaisala PTB110), we compute: $u_{\mathrm{B},i} = 0.27\,\mathrm{hPa}$. The prevailing uncertainty source is in the data acquisition.

5.3.1.4 Standard uncertainty on relative humidity

The category B standard uncertainty $u_{\mathrm{RH},i}$ in relative humidity is a combined uncertainty related to the sensor used to measure $RH_{10\,\mathrm{min}}$ and expressed as follows:

$$u^2_{\mathrm{RH},i} = u^2_{\mathrm{RH,cal},i} + u^2_{\mathrm{RH,mnt},i} + u^2_{\mathrm{dRH},i} \ , \tag{5.13}$$

where the uncertainty components are detailed in Table 5.5. All sub-components are independent of measurements.

Table 5.5: Components of combined category B uncertainty $u_{\mathrm{RH},i}$ on relative humidity in bin i. The value used in the mathematical expression of the uncertainty and the comments are specific to the measurement systems used in the NKE campaign.

Source	**Symbol**	**Expression**	**Comment**
calibration	$u_{\mathrm{RH,cal},i}$	0.01	From certificate.
mounting	$u_{\mathrm{RH,mnt},i}$	$0.001 \cdot RH_i$	Default IEC value.
data acquisition	$u_{\mathrm{dRH},i}$	$0.001 \cdot (1-0)$	Default IEC value, 0.1 % of full range.

Independently of the measured RH_i value, the mounting and data acquisition uncertainty sources can be neglected. The combined uncertainty $u_{\mathrm{RH},i}$ essentially equals to the calibration uncertainty.

5.3.1.5 Standard uncertainties on wind speed

The category B standard uncertainty $u_{\mathrm{V},i}$ on the wind speed is a combined uncertainty related to the sensor (hardware) used to measure $V_{10\,\mathrm{min}}$ and to the potential flow distortion due to the terrain. It is expressed as follows:

$$u_{\mathrm{V},i}^2 = u_{\mathrm{VHW},i}^2 + u_{\mathrm{VT},i}^2 \ , \tag{5.14}$$

Hereafter, the hardware uncertainty is expressed separately for the cases of the mast-mounted cup anemometer and of the two nacelle-mounted lidar systems (5B-Demo and ZDM). In addition, the values used for the flow distortion uncertainty $u_{\mathrm{VT},i}$ are specified.

Measured by the mast top-mounted cup anemometer

The component $u_{\mathrm{VHW},i}$ in Eq. (5.14) is replaced in this case by $u_{\mathrm{VS},i}$, which is expressed as follows:

$$u^2_{\mathrm{VS},i} = u^2_{\mathrm{VS,precal},i} + u^2_{\mathrm{VS,postcal},i} + u^2_{\mathrm{VS,class},i} + u^2_{\mathrm{VS,mnt},i} + u^2_{\mathrm{VS,lgt},i} + u^2_{\mathrm{dVS},i} \ , \tag{5.15}$$

where the uncertainty components are detailed in Table 5.6.

Table 5.6: Components of combined category B uncertainty $u_{\mathrm{VS},i}$ on wind speed in bin i measured by a mast-mounted sensor. The value used in the mathematical expression of the uncertainty and the comments are specific to the measurement systems used in the NKE campaign.

Source	**Symbol**	**Expression**	**Comment**
pre-calibration	$u_{\mathrm{VS,precal},i}$	$0.025 + \frac{0.01}{\sqrt{3}} V_i$	From certificate, and variability between wind tunnels.
post-calibration	$u_{\mathrm{VS,postcal},i}$	-	Discarded.
classification	$u_{\mathrm{VS,class},i}$	$\frac{1.3}{\sqrt{3}} (0.05 + 0.005 V_i)$	Class A1.3, WindSensor P2546A anemometer.
mounting	$u_{\mathrm{VS,mnt},i}$	$0.005 V_i$	Default IEC value for top-mounted anemometer.
lightning finial	$u_{\mathrm{VS,lgt},i}$	$0.001 V_i$	Default IEC value.
data acquisition	$u_{\mathrm{dVS},i}$	$0.001 \cdot (30 - 0)$	Default IEC value, 0.1 % of full range.

In this case (NKE), no site calibration was performed, the terrain is flat and the mast is distant by $2.5 D_{\mathrm{rot}}$ from the turbine under test. Thus $u_{\mathrm{VT},i} = 0.02 \cdot V_i$ (default IEC value, used in Eq. (5.14)).

Estimated by the nacelle lidar, using the 'wind' model

(see Sect. 4.1, Page 53)

The component $u_{\mathrm{VHW},i}$ in Eq. (5.14) is replaced in this case by $u_{\mathrm{VNL1},i}$, which is expressed as follows:

$$u^2_{\mathrm{VNL1},i} = u^2_{\mathrm{VNL1,mod},i} + u^2_{\mathrm{VNL1,mnt},i} + u^2_{\mathrm{dVNL1},i} \ , \tag{5.16}$$

where the uncertainty components are detailed in Table 5.7.

Table 5.7: Components of combined category B uncertainty $u_{\mathrm{VNL1},i}$ on wind speed in bin i estimated using nacelle lidar measurements and the 'wind' model.

Source	Symbol	Expression	Comment
model uncertainty and inadequacy	$u_{\mathrm{VNL1,mod},i}$	$\frac{1}{N_i}\sum_{j=1}^{N_i} u_{c,V_{\mathrm{H}},j}$	see Eq. (4.5)
mounting	$u_{\mathrm{VNL1,mnt},i}$	$0.001V_i$	0.1 % of measured speed
data acquisition	$u_{\mathrm{dVNL1},i}$	$0.001 \cdot (30-0)$	0.1 % of full range.

In this case (NKE), no site calibration was performed, the terrain is flat and the lidar measurements were taken at distances above $2D_{\mathrm{rot}}$ and less than $3D_{\mathrm{rot}}$ from the turbine under test. Thus $u_{\mathrm{VT},i} = 0.02 \cdot V_i$ (default IEC value).

Estimated by the nacelle lidar, using the 'combined wind-induction' model (see Sect. 4.2, Page 54)

The component $u_{\mathrm{VHW},i}$ in Eq. (5.14) is replaced in this case by $u_{\mathrm{VNL2},i}$, which is expressed as follows:

$$u^2_{\mathrm{VNL2},i} = u^2_{\mathrm{VNL2,mod},i} + u^2_{\mathrm{VNL2,mnt},i} + u^2_{\mathrm{dVNL2},i} \ , \tag{5.17}$$

where the uncertainty components are detailed in Table 5.8.

Table 5.8: Components of combined category B uncertainty $u_{\mathrm{VNL2},i}$ on wind speed in bin i estimated using nacelle lidar measurements and the 'combined wind-induction' model.

Source	Symbol	Expression	Comment
model uncertainty and inadequacy	$u_{\mathrm{VNL2,mod},i}$	$\frac{1}{N_i}\sum_{j=1}^{N_i} u_{c,V_\infty,j}$	see Eq. (4.8)
mounting	$u_{\mathrm{VNL2,mnt},i}$	$0.001V_i$	0.1 % of measured speed
data acquisition	$u_{\mathrm{dVNL2},i}$	$0.001 \cdot (30-0)$	0.1 % of full range.

In this case (NKE), no site calibration was performed, the terrain is flat and the lidar measurements were taken at distances less than $2D_{\mathrm{rot}}$. A 1 % uncertainty is proposed, and $u_{\mathrm{VT},i} = 0.01 \cdot V_i$. Note that there is no specification in the standards for this uncertainty component, as the method of using lidar measurements close to the rotor to estimate the free stream wind speed represents a strong deviation from the standards' requirements.

5.3.1.6 Sensitivity factors

According to the standards – for a pitch-regulated turbine – the expressions of the sensitivity factors present in the power curve uncertainty (see Eq. (5.7)) are given in bin i by:

$$c_{\mathrm{T},i} = -\frac{c_{\mathrm{V},i} V_i}{3\rho_i} \left(\frac{\rho_i}{T_i} + \frac{RH_i P_{\mathrm{w},i}}{T_i} \left[\frac{1}{R_0} - \frac{1}{R_\mathrm{w}} \right] \right) \tag{5.18}$$

$$c_{\mathrm{B},i} = \frac{c_{\mathrm{V},i} V_i}{3\rho_i T_i R_0} \tag{5.19}$$

$$c_{\mathrm{RH},i} = -\frac{c_{\mathrm{V},i} V_i}{3\rho_i T_i} \left(\frac{1}{R_0} - \frac{1}{R_\mathrm{w}} \right) P_{\mathrm{w},i} \tag{5.20}$$

$$c_{\mathrm{V},i} = \frac{1}{2} \left(\frac{P_{i+1} - P_i}{V_{i+1} - V_i} + \frac{P_i - P_{i-1}}{V_i - V_{i-1}} \right) \ , \tag{5.21}$$

where $P_{\mathrm{w},i} = 0.0000205 \cdot \exp(0.0631846 \cdot T_i)$ is the average water vapour pressure in bin i, etc.

5.3.2 Results

The power curve uncertainty results analysed hereafter are the category A power uncertainties, the category B uncertainties in the wind speed, and the combined power curve uncertainty. Once again, results obtained with the two nacelle lidars and two wind field reconstruction models are compared to the ones obtained with the mast top-mounted cup anemometer.

5.3.2.1 Category A power uncertainty

Fig. 5.6 displays the category A power uncertainty $s_{\mathrm{P},i}$ results (see Eq. (5.8)). Below rated wind speed, the uncertainty obtained using the two nacelle lidars are more than 30 % lower than that with the cup anemometer.

Furthermore, the combined wind-induction models using lidar measurements close to the turbine rotor (Fig. 5.6(b); Fig. 5.6(c)) appear to yield slightly lower category A power uncertainty than the case of the wind model and measurements at the mast distance (Fig. 5.6(a)).

Those results are consistent with the observations made on the scatter plots of the measured power curves (Fig. 5.1).

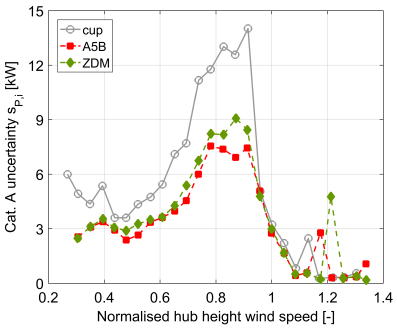

(a) Mast-based; 5B-Demo and ZDM using the 'wind' model.

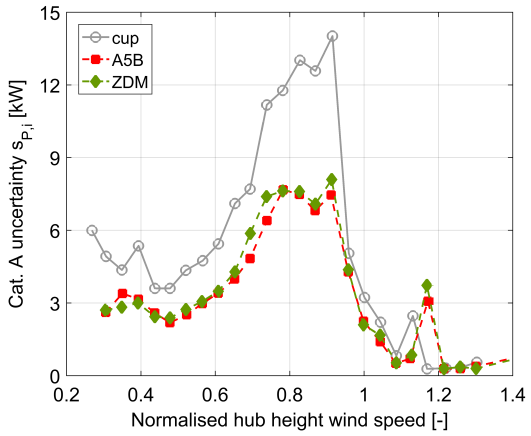

(b) Mast-based; 5B-Demo and ZDM, using the 'wind-induction' model and wind speed estimated at $2.5D_{\text{rot}}$.

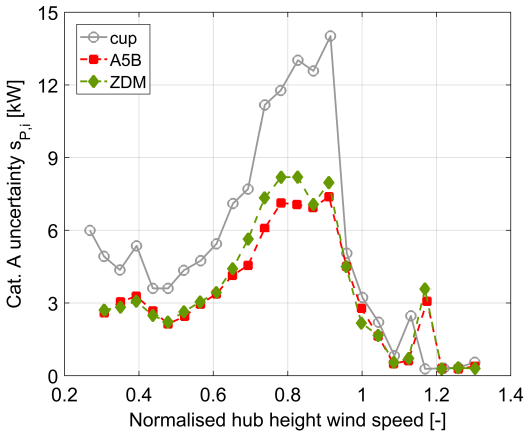

(c) Mast-based; 5B-Demo and ZDM, using the 'wind-induction' model and the V_∞ characteristic.

Figure 5.6: Category A power uncertainty as a function of bin-averaged normalised wind speed.

5.3.2.2 Wind speed uncertainty

In Fig. 5.7, the so-called 'hardware' wind speed uncertainty $u_{\text{VHW},i}$ (see Eq. (5.15), Eq. (5.16) and Eq. (5.17)) is shown as a function of the bin-averaged normalised speed.

The dashed lines represent the lidar model uncertainties, computed for each 10 min period by performing multivariate interpolation in the look-up tables of uncertainties. We recall that the look-up tables were obtained by using Monte Carlo simulations (Chapter 4) in order to propagate the wind field reconstruction models' inputs to the outputs – the wind field characteristics. The wind speed model uncertainty was shown to vary linearly (Fig. 4.8(a) and Fig. 4.11(a)) with

the wind speed due to the domination of the LOS velocity uncertainty by the reference cup anemometer wind speed uncertainty (see Fig. 14, Page 32).

The cup anemometer wind speed uncertainty (gray squares) also increases linearly with the wind speed. However, its magnitude is significantly higher due to a higher classification uncertainty – anemometer of class A1.3 during the NKE campaign vs. class A0.9 for the LOS velocity calibration in Høvsøre.

By adding the model inadequacy – the RMSE fitting residuals – to the uncertainty budget of the lidar model uncertainty, the bin-averaged lidar-based 'hardware' wind speed uncertainties are derived.

For the wind model case, the uncertainties are significantly higher than with the mast and rather independent of the wind speed. This suggests that the RMSE dominates at low wind speed, and is of lesser magnitude at high wind speed. We additionally note that the 'hardware' wind speed uncertainty is higher for ZDM than for 5B-Demo by approximately $0.04\,\mathrm{m\,s^{-1}}$, which is consistent with the RMSE results presented in Table 3.5.

For the combined wind-induction model cases, the magnitude of the RMSE is lower. The RMSE contributes to a lesser extent to $u_{\mathrm{VHW},i}$, and the hardware wind speed uncertainties are comparable to those obtained for the cup anemometer. At high wind speed, the uncertainty is even lower for 5B-Demo than for the cup. A linear increasing trend is observed in $u_{\mathrm{VHW},i}$.

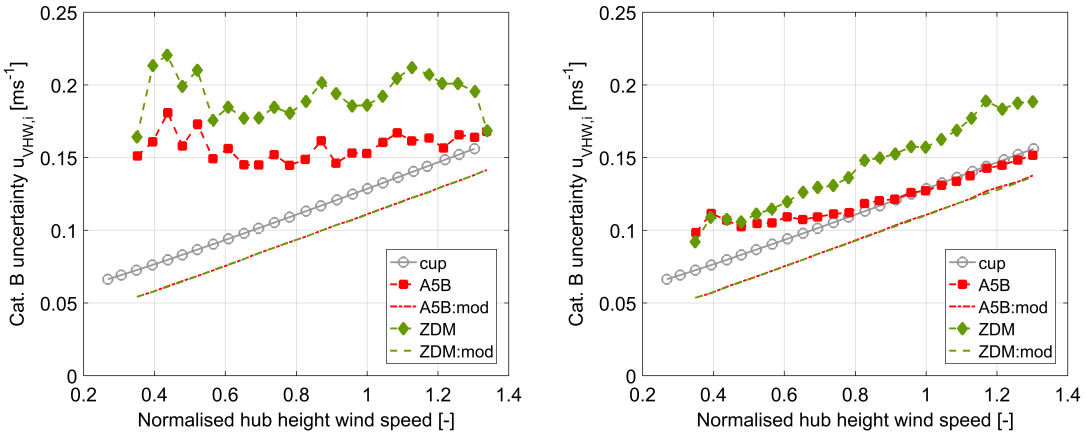

(a) Mast-based; 5B-Demo and ZDM using the 'wind' model.

(b) Mast-based; 5B-Demo and ZDM, using the 'wind-induction' model.

Figure 5.7: Category B wind speed uncertainty $u_{\mathrm{VHW},i}$ in hardware as a function of bin-averaged normalised wind speed.

Fig. 5.8 shows the combined wind speed uncertainty $u_{\mathrm{V},i}$ (see Eq. (5.14)) – accounting for the hardware and the flow distortion due to terrain – as a function of the bin-averaged normalised speed.

Using the wind model, the lidar-based $u_{\mathrm{V},i}$ is slightly higher than for the cup anemometer, due to a significant and equal contribution of the flow distortion terrain uncertainty (2 % of the wind speed) for all the three systems.

For the combined wind-induction model case, the lidar measurements were taken close to the rotor, at less than $1.3D_{\mathrm{rot}}$. It was therefore proposed to use a lower flow distortion uncertainty, set to 1 % of the wind speed. As a result, $u_{\mathrm{V},i}$ is significantly lower for the lidar cases than for the cup anemometer, as it can be observed in Fig. 5.8(b). Note that the reduction in the wind speed uncertainty is artificial as the flow distortion uncertainty value is chosen rather arbitrarily. This shows that the combined wind speed uncertainty values depend critically on the magnitude of the flow distortion component.

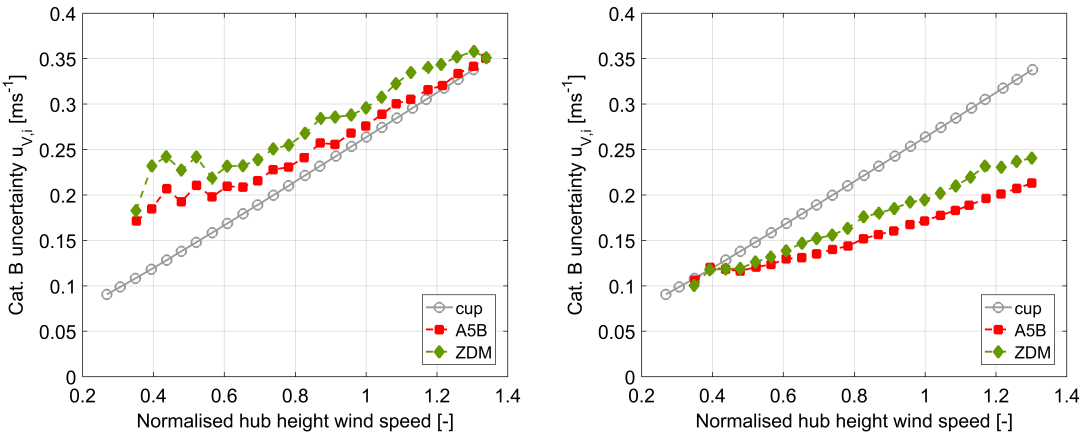

(a) Mast-based; 5B-Demo and ZDM using the 'wind' model.

(b) Mast-based; 5B-Demo and ZDM, using the 'wind-induction' model.

Figure 5.8: Combined wind speed uncertainty $u_{\mathrm{V},i}$ (category B) as a function of bin-averaged normalised wind speed.

5.3.2.3 Power curve combined uncertainty

Fig. 5.9 shows the combined power curve uncertainty $u_{c,\mathrm{P},i}$, which is the end-result of the uncertainty assessment process described in Section 5.3.1.

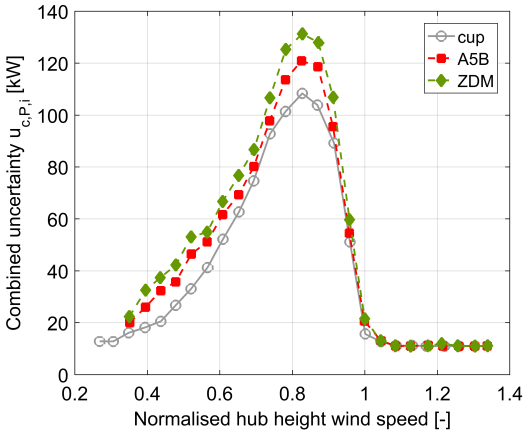

(a) Mast-based; 5B-Demo and ZDM using the 'wind' model.

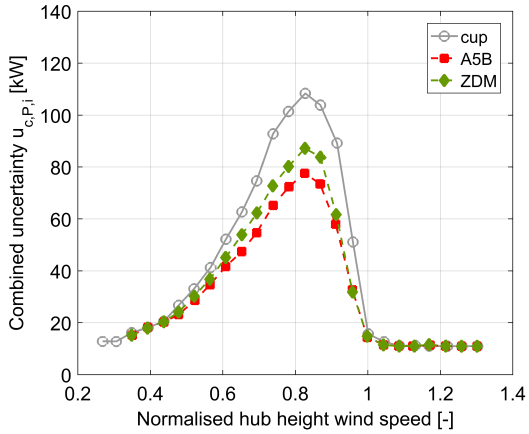

(b) Mast-based; 5B-Demo and ZDM, using the 'wind-induction' model and wind speed estimated at $2.5D_{\mathrm{rot}}$.

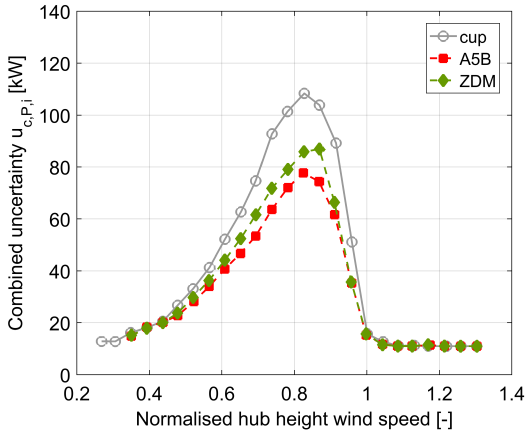

(c) Mast-based; 5B-Demo and ZDM, using the 'wind-induction' model and the V_∞ characteristic.

Figure 5.9: Combined power curve uncertainty $u_{c,\mathrm{P},i}$ as a function of bin-averaged normalised wind speed.

To understand the evolution of the power curve uncertainty as a function of speed, two elements must be considered. First, below rated wind speed the power curve uncertainty $u_{c,\mathrm{P},i}$ is extensively dominated ($> 90\,\%$) by the category B wind

speed uncertainty term $c_{V,i}u_{V,i}$. Then, since $u_{V,i}$ was shown to increase linearly with the wind speed, the evolution of the power curve uncertainty is strongly linked to the variation of the sensitivity coefficient $c_{V,i}$. In essence, $c_{V,i}$ is the slope of the tangent to the bin-averaged power curve. For the measured power curves of the NKE turbine (Fig. 5.4), the sensitivity coefficient $c_{V,i}$:

- is zero below cut-in wind speed;
- increases slowly for normalised speeds between 0.2 and 0.6;
- takes its maximum value approximately at a normalised speed of 0.8;
- decreases rapidly above a normalised speed of 0.9;
- is zero above rated wind speed, as the blades' pitch regulation ensures a constant nominal power output.

As a consequence, below rated wind speed, the power curve uncertainty evolution is intimately related to the sensitivity coefficient on the wind speed and to the wind speed uncertainty. The reduction of category A uncertainty in power with the nacelle lidars is negligible compared to the category B wind speed uncertainty. The power curve uncertainty increases regularly and reaches a maximum at a normalised speed of approximately 0.8, and drops rapidly after this maximum is reached.

Above rated wind speed, both the category A uncertainty in power and the sensitivity coefficient on the wind speed are small. The prevailing uncertainty component is the category B uncertainty in power (Table 5.2), which is constant since the power output has the same nominal value.

For the case where the lidar wind speed is estimated using the wind model (Fig. 5.9(a)), below rated speed, the power curve uncertainty is lower with the mast than with the lidars. The scatter reduction in the power curve is insufficient to compensate for the higher wind speed uncertainties due to the model inadequacy (RMSE fitting residuals).

For the combined wind-induction case, not only the category A uncertainty is lower than with the mast-mounted cup anemometer for both lidar systems, but the wind speed uncertainty is also lower than with the cup due to a lower contribution of the flow distortion uncertainty component.

The lidar short-range technique where the combined wind-induction model is applied to lidar measurements close to the rotor has demonstrated its ability to provide valid estimations of true free stream wind speed in Section 3.2. It also shows potential to reduce the power curve uncertainty.

5.4 Annual energy production

The AEP (Annual Energy Production) is defined as the energy that the turbine is expected to produce each year, on average. Therefore, it is a critical element to assess the financial viability of a wind farm project, or to perform asset management. The AEP is usually expressed in MW h or GW h. It results from the combination of the measured or extrapolated power curve with a wind speed frequency distribution.

During a power performance test, the AEP shall be derived using a site specific wind speed frequency distribution if available. Alternatively, the AEP can be estimated using a number of reference Rayleigh wind speed distributions, with average wind speeds V_{ave} from 4 to 11 m s^{-1} as suggested in IEC 61400-12-1, 2017.

Practically, the AEP is derived as follows:

$$AEP = N_{\text{h}} \sum_{i=1}^{N} \left[F\left(V_i\right) - F\left(V_{i-1}\right) \right] \left(\frac{P_{i-1} + P_i}{2} \right) \ , \tag{5.22}$$

where $N_{\text{h}} = 8760$ is the number of hours in a year, V_i and P_i are respectively the normalised wind speed and power in bin i, $F\left(V_i\right)$ is the cumulative probability of wind speed for bin i. For a Rayleigh distribution, $F\left(V_i\right)$ is given by

$$F\left(V_i\right) = 1 - exp\left(-\frac{\pi}{4} \left(\frac{V_i}{V_{\text{ave}}} \right)^2 \right) \ . \tag{5.23}$$

The AEP can be calculated either for the measured power curve, or for the extrapolated power curve, see details on the method in IEC 61400-12-1, 2017. The difference between both AEP calculations is small, unless a significant number of wind speed bins were not measured during the data collection campaign. Those missing bins are usually at high wind speeds, such that for a pitch-regulated turbine the power output can safely be assumed to take its nominal value, and the power curve uncertainty from the last valid bin may be used.

The AEP was calculated for the cup anemometer case and the six lidar cases (see Section 5.1.1). Fig. 5.10 displays the relative difference $\Delta\text{AEP}_{\text{rel}}$ between the extrapolated AEP for the nacelle lidar cases and the cup anemometer case – here used as the reference – as a function of the Rayleigh mean wind speed V_{ave}.

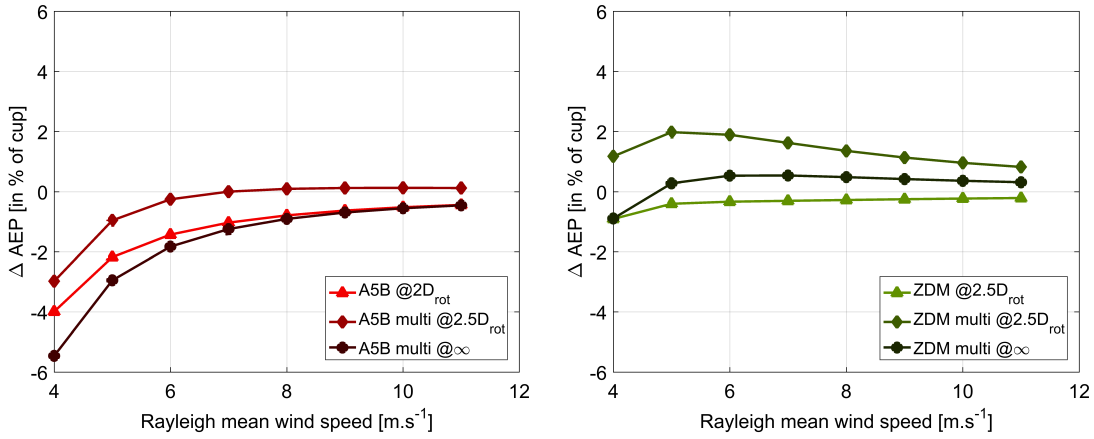

(a) For 5B-Demo. **(b)** For ZDM.

Figure 5.10: Relative difference in extrapolated annual energy production as a function of Rayleigh mean wind speed. For each lidar, the power curve was measured with three different methods to estimate the wind speed: 1) using the wind model; 2) using the combined wind-induction model and a speed estimated at $2.5D_{\text{rot}}$; 3) using the combined wind-induction model and the V_{∞} characteristic.

Using the combined wind-induction model, it is interesting to notice that the AEP is lower when the power curve is based on the free stream wind speed characteristic V_{∞} than with the wind speed estimated at $2.5D_{\text{rot}}$. This difference decreases with the mean wind speed, since at higher speeds the turbine will operate more frequently at low thrust coefficient conditions – where the speed difference between $2.5D_{\text{rot}}$ upstream and the true free stream is negligible.

For ZDM, the best agreement with the cup-derived AEP is obtained when using the wind model and lidar measurements at $2.5D_{\text{rot}}$. Contrary, for 5B-Demo the best agreement is obtained with the wind-induction model cases. These observations are directly related to: the overestimation of wind speed by 5B-Demo for the case using the wind model (lower AEP); the underestimation of wind speed by ZDM for the combined wind-induction case.

Irrespective of the wind field reconstruction cases, the lidar-based AEP is within 2 % of the cup-derived AEP for mean wind speeds above $6\,\text{m}\,\text{s}^{-1}$.

5.5 Discussions

In light of the methods and results presented in this chapter, several questions related to the use of nacelle lidars for power performance testing are discussed hereafter – such as the benefits from using profiling nacelle lidars, the need for complementary instrumentation, the reasons for the absence of 'lidar classification uncertainty', and the flow distortion wind speed uncertainty.

5.5.1 Profiling- vs. two-beam nacelle lidars

In Section 3.2, wind field reconstruction algorithms were developed. The developed wind models were designed specifically to be applicable to nacelle-based wind lidars. They not only provide hub height wind speed and direction, but also information on the shear profile. However, in this chapter, only the hub height wind speed was considered as input to the power curve measurement. A legitimate question arises: what then are the benefits of using profiling nacelle lidars in comparison to (simpler) two-beam systems?

First and foremost, the profiling capabilities of the two nacelle lidar systems that were used during the NKE campaign ensure that the wind speed reconstructed from the lidar measurements is estimated at the correct height, the hub height. In contrast, because of the variability of the nacelle motion (tilting and rolling) with the wind speed, two-beam nacelle-based lidars probe the wind at heights that can be erroneous by up to 2 %. This was demonstrated in Wagner et al., 2015. This erroneous sensing height is a source of measurement biases, that can hardly be modelled and corrected for. Wagner consequently added an extra component to the lidar wind speed uncertainty due to the measurement height – which can roughly be approximated to 0.5 % of the estimated wind speed. Moreover, the unavoidable sensing height error with two-beam nacelle lidars is outside the tolerance of the IEC 61400-12-1, 2017 standards, now required to be within 1 % of the hub height.

It should also be noted that the uncertainty results presented in Wagner et al., 2015 did not account for any model inadequacy, whereas this is the case in this chapter. In more complex situations than flat terrain or offshore, the validity of the flow homogeneity assumption made by two-beam nacelle lidars is certainly questionable.

This issue of effectively estimating the wind speed at the correct height is even more crucial in complex terrain (e.g. mountainous, hilly or forested). In combination with a topographic map of the area surrounding the turbine under test, profiling nacelle lidars could estimate the wind speed at the desired heights (agl.) irrespective of the yaw position of the turbine. This capability may shorten the duration of the power

performance tests in complex sites, by allowing the use of wider wind direction sectors.

The fundamental idea behind the REWS is to measure independently the wind speed at several heights across the rotor swept area (no shear profile assumed). The shear parameter estimated using either the wind or combined wind-induction model could be used to estimate an energy equivalent wind speed by integration of the shear profile over the rotor swept area (Eq. (5.2)), although this would represent a deviation from the REWS definition. Alternatively, mimicking the standards (Sect. E.11 in IEC 61400-12-1, 2017), another wind model where two different power law shear profiles – below and above hub height – may be useful.

Further work will be required in order to investigate such methods and assess in which conditions they would be valid – such as in flat terrain or offshore where unusual wind shear profiles are scarce.

Retrieving estimates of the REWS from profiling nacelle lidar is also feasible by using multiple pairs of beams at several heights and several distances upstream the rotor plane, including some close to the rotor plane. The wind model would then consist in assuming horizontal flow homogeneity at a given height and combining the measurements with e.g. the simple induction model (see Page 50). The ZDM reconstruction algorithms derive the REWS using such a method but only at a single measurement distance. Multi-beam pulsed lidar systems would certainly require to measure at a significantly larger number of ranges – the maximum for 5B-Demo was 10 – in order to estimate the REWS without assuming any shear profile.

5.5.2 Why the absence of lidar classification uncertainty?

In power performance standards (IEC 61400-12-1, 2017), for the case of ground-based profiling remote sensing devices (lidars or other types), it is stated that the classification uncertainty shall be included in the wind speed uncertainty assessment since the:

> "Sensitivity of the device due to varying conditions introduces uncertainty due to the fact that the meteorological conditions during the application of the remote sensor may deviate from the meteorological conditions present during the calibration test."

The philosophy behind this uncertainty component is similar to the classification uncertainty of cup or sonic anemometers, which measurements are known to be

sensitive to external variables. Indeed, ground-based profiling lidars are usually calibrated using a 'black-box' approach. The reconstruction of e.g. the wind speed at a given height is more likely to be sensitive to atmospheric conditions and to the terrain than if the 'white-box' methodology were used.

Investigations of the sensitivity of nacelle lidar V_{los} measurements to external variables (temperature, pressure, rain, turbulence, turbulence intensity, wind direction, etc) were carried out using extensive datasets of calibration data collected over several years at DTU's test site for large wind turbines, Høvsøre, Denmark (credit: Ginka Georgieva Yankova). The V_{los} measurement errors between the lidars and reference instruments (used to provide the pseudo LOS velocity, see Eq. 2, Page 18) showed no evidence of sensitivity to any of the studied variables.

Thus, adding an arbitrary classification uncertainty to the nacelle lidar wind speed estimates would be metrologically incorrect, leading to an unnecessary overestimation of the wind speed uncertainties. Consequently, no classification uncertainty was included in the combined wind speed uncertainties (see Section 5.3.1.5) that shall be used for power curve uncertainty assessment. Instead the model inadequacy was accounted for through V_{los} fitting residuals.

5.5.3 On the flow distortion uncertainty due to terrain

The power performance standards require for the wind speed uncertainty to include a component covering

> "the flow distortion of the wind speed between the measurement point and the wind turbine due to the local terrain."

In flat terrain, there is little probability for such a flow distortion to occur, except maybe in coastal areas where longitudinal gradients are frequently observed. Offshore, this uncertainty component is even less justified.

In Section 5.3.2.3, the contribution of the flow distortion uncertainty $u_{\text{VT},i}$ to the total wind speed uncertainty, and further to the combined power curve uncertainty, proved to be very significant. Therefore, studies on how to quantify the flow distortion uncertainty – if any – more accurately would improve the power curve uncertainty assessment procedures. With the technological advances in computational power, flow distortion uncertainties could primarily be quantified via detailed CFD simulations in order to assess plausible flow distortion issues at a given site. Note that this approach is different from the so-called 'numerical site calibration' as the purpose is not to apply corrections to the measurements but to quantify potential flow distortion phenomena.

Finally, since in the standards the magnitude of the flow distortion uncertainty is increasing with the distance between the measurement location and the turbine position, it was fair to propose a smaller value for the cases where lidar measurements close to the rotor were used and the combined wind-induction model was applied.

5.5.4 Instrumentation requirements for stand-alone nacelle lidars

To measure a turbine's power curve, the wind speed measurement must be complemented by measurements of several other atmospheric variables – namely the air temperature, air pressure and relative humidity – in order to normalise the wind speed by the air density.

For the power performance test of the NKE campaign, the nacelle lidar measurements were used to estimate the wind speed, and instruments mounted on met. mast provided measurements of air density. One of the great advantage of using nacelle-mounted lidars for power curve measurement is to obviate the need and cost of a mast. In the future, nacelle lidars will thus be measuring stand-alone, and requirements for complementary instrumentation have thus to be defined. An obvious suggestion is that the requirements for complementary measurements – of temperature, pressure, humidity and any other complementary variables that cannot be measured by a wind lidar – are based on the IEC 61400-12-2, 2013, the standards for power performance testing based on nacelle anemometry. These requirements are to measure air temperature within 10 m of hub height, and air pressure within a radius of 5 km from the turbine (at or corrected to hub height) – both sensors shall be placed such that the measurements are not affected by the turbine operation (blades, ventilation system, etc). The implications of these requirements on the power curve uncertainty are expected to be negligible since the values of uncertainty components related to measurements for calculating air density (T, B and RH, see Eq. (5.7)) are orders of magnitude lower than the wind speed (category B) and power (category A and B) uncertainties.

CHAPTER 6
Conclusions and future work

6.1 Conclusions

Forward-looking nacelle-mounted profiling lidars were shown to be suitable instruments providing reliable wind measurements for testing the power performance of wind turbines.

It was demonstrated that the field calibration of nacelle lidars can be performed using the so-called white-box methodology. The developed calibration procedures are generic as they can be applied to any existing or upcoming wind lidar system – continuous wave or pulsed, scanning or multi-beam, etc. Indeed, the most central part of the generic methodology is the calibration of the line-of-sight (LOS) velocity, which is the primary measurand in all Doppler wind lidar systems.

Lidar measurements, as for any measuring instrument, are uncertain. The calibration procedures shall include the assessment of measurement uncertainty. This was achieved for the LOS velocity measured by the nacelle lidars, but also for LOS positioning quantities such as inclination angles or opening angles between the (multiple) lidar beams.

The calibration procedures were applied to two different commercially developed nacelle lidar systems: the five-beam Demonstrator (5B-Demo) by *Avent Lidar Technology* and the ZephIR Dual-Mode (ZDM) by *Zephir Lidar*. The high quality of the calibration results demonstrated the validity of the procedures, the level of genericity of the methods and their repeatability. A limitation of calibrating wind lidars in-field is that the process is time-consuming, requiring a data collection campaign with a duration of possibly several months. Finally, the combined LOS velocity uncertainty was dominated by the wind speed uncertainty of the reference sensors, and other uncertainty sources are negligible in comparison. This conclusion emphasizes the need to reduce the uncertainty of the cup anemometer used as a reference, or to investigate the alternative of using other instruments than can provide calibrated wind speed reference measurements.

A wind lidar does not measure directly the wind speed or direction as a cup anemometer or a wind vane do, but instead primarily estimates the wind vector component along its line(s)-of-sight. Other information is necessary to convert LOS velocities taken at multiple measurement locations into useful wind field

characteristics such as speed, direction or shear.

The model-fitting wind field reconstruction technique was developed for this purpose. Essentially, the method fits a wind model to the lidar LOS velocities measured at several distances and heights by simulating the lidar measurements and solving an error minimisation problem. For each considered time-period, the wind model parameters are output, yielding estimates of wind field characteristics. The method is elegant as it clearly provides all the assumptions made in order to reconstruct wind characteristics from the lidar measurements. Two types of models were used – but many more can easily be defined for various wind energy applications (wake measurement, wind turbine control, resource assessment, etc).

The first developed wind model accounts for shear through a power law profile. It uses nacelle lidar measurements at a single range and multiple heights in order to estimate the hub height wind speed, relative direction (yaw misalignment) and shear exponent.

The second model combines the previous wind model with a simple induction model based on the actuator disk and vortex-sheet theory. Using the combined wind-induction model and lidar LOS velocity measurement at several distances close to the turbine rotor – approximately between 0.5 and 1.5 rotor diameters – one can estimate the free stream wind speed ('V infinity'), the relative wind direction, the shear exponent and the axial induction factor.

A full-scale 7-month measurement campaign in flat terrain provided the experimental data allowing to test the validity of the wind characteristics estimated with the model-fitting approach. The wind characteristics were compared to reference measurements taken by classic mast-mounted instrumentation (IEC-compliant setup). In particular, the lidar-estimated hub height wind speed was shown to be within 0.7 % of the wind speed measured by the top-mounted cup anemometer. Other wind characteristics – such as yaw misalignment, shear exponent and induction factor – were also compared to reference quantities. Using the estimated induction factor and free stream wind speed, it is for instance possible to estimate the thrust coefficient curve of a wind turbine solely using nacelle-mounted lidars.

The model-fitting approach and the developed wind or combined wind-induction models are rather complex in comparison to the simple analytical method commonly used by two-beam nacelle lidars. The uncertainty of the model-fitted wind characteristics can be assessed by employing numerical error propagation techniques. For this purpose, Monte Carlo simulations were performed for both lidar systems and both reconstruction models. The implemented Monte Carlo methods propagate the uncertainty of the model inputs – LOS velocities and positioning quantities – to its outputs, the wind characteristics. In this way, it was possible to quantify the model uncertainties of all wind characteristics (speed, direction, shear, induction factor) and the inter-dependence between the uncertainties (correlation). Moreover, the

fitting residuals were combined with the model uncertainties in order to account for the potential (plausible) inadequacy of the model.

The experimental data of the full-scale campaign was used to measure the power curve of the turbine on which the two lidars were mounted. The procedures relied as much as possible on the international turbine power performance testing standards, the IEC 61400-12-1, 2017.

The use of the lidar-based wind speed estimates obtained with both models was investigated, and the power curve was also measured with the mast top-mounted cup anemometer. The power curves measured by the three systems – 5B-Demo, ZDM and the cup – proved to be in excellent agreement. Further, the power curve uncertainties and the annual energy production were derived. For a mean Rayleigh speed of $8\,\mathrm{m\,s^{-1}}$, the lidar-derived annual energy production values were within 1 % of the one obtained with the cup anemometer.

The possibility of estimating the (true) free stream wind speed from nacelle lidar short-range measurements represents a paradigm shift in the ways that power performance tests could be routinely conducted in the near-future. For decades, power performance measurements have been performed by using a meteorological mast placed at a distance from the turbine between 2 to 4 rotor diameters; the measured wind speed was then considered as a sufficient approximation of the free stream wind speed. For modern turbines this approximation may not be good enough any more. And, due to their large size, other issues such as signal decorrelation between electrical power and wind speed arise at such large distances.

Moreover, the combined wind-induction model and lidar short-range measurement technique gives hope for estimating the free stream wind speed in situations where it cannot be approximated with mast measurements – such as in complex terrain, or in the middle of an offshore wind farm due to the presence of wakes.

For modern multi-megawatt turbines, nacelle-based lidars are cost-efficient since they obviate the need for deploying tall and expensive masts – especially offshore – and can provide wind measurements more representative of the wind driving the turbine than mast-based measurements. In the future, nacelle lidars are likely to replace meteorological masts for power performance testing.

6.2 Recommendations for future work: what's next?

Alongside this Ph.D. project, several ideas have sprung up. Each of these ideas has the potential for being a future research topic on its own. They are listed below:

1. The model-fitting approach for reconstructing wind field characteristics should be further developed for and applied to other types of lidars than the nacelle-based systems.
   For ground-based lidars performing vertical azimuth display scans, shear and veer models could easily be included into a wind model and applied to LOS velocity measurements at multiple ranges.
   Moreover, the model-fitting approach could also be used for long-range scanning lidar systems – independently of the trajectory (plan position indicator, range height indicator, complex- or custom- trajectories, etc). The wind models could also integrate models of large-scale wind fluctuations.

2. A lidar simulator for smart campaigns. The term of lidar simulator can be understood in several manners, at several levels of complexity. Basically, the lidar simulator is a numerical tool allowing to simulate lidar measurements according to a model flow field or given atmospheric conditions. The lidar simulator should be adaptable to any kind of existing or upcoming wind lidar system. Following the measurement chain described in Fig. 1.2, the numerical tool may be able to achieve some or all of the following items:

   - simulate the signals of backscatter light, depending e.g. on aerosols concentration;
   - generate the Doppler spectrum using Fast Fourier Transforms. Here, the FFT size may be adapted in order to test computational power requirements and the effect of this processing step on the lidar measurements;
   - estimate the LOS velocity – and maybe other parameters such as its variance within the Doppler spectrum;
   - retrieve wind field characteristics according to chosen wind models, e.g. using the model-fitting approach.

   The lidar simulator naturally relies on how realistic the virtual flow field and atmospheric conditions are. Such a simulator would however be extremely valuable to plan measurement campaigns. For example, for scanning lidar campaigns, the locations of the lidar systems and the measurement trajectory may be optimised and decided based on simple lidar simulations. 'Smart campaigns' would ensure higher quality and availability of the measurement data, and consequently have lower costs.

3. Optimisation of lidar design and trajectory. This idea consists of using a lidar simulator – e.g. in its simplest form, point-like LOS velocity estimation from steady-state CFD simulations – to test the optimal trajectory for a given application. Such an optimisation would be beneficial for lidar manufacturers to make design choices (number of beams, number of ranges, scanning speed or minimum accumulation time per beam, etc). Optimising the lidar trajectory will also be required in order to assist the end-user in configuring the lidar measurement distances. For instance, in the case of the combined wind-induction model developed to for nacelle lidar measurements close to the rotor, the optimisation will help defining guidelines and minimum requirements for the lidar configuration in order to reconstruct the most accurate wind field characteristics.

4. Developing wind field reconstruction models for wakes. The analysis of measurement campaign data for studying the wakes of wind turbines is too often performed from a qualitative perspective only. Quantitative information is, in my opinion, equally or more valuable. Simple wake models could be integrated in a wind field reconstruction model – such as the Jensen wake model (Jensen, 1983). In this way, wake parameters such as decay and expansion coefficients could be estimated. Other wake metrics – center, azimuthal radius, width, height, etc – may also be retrieved from backward-looking nacelle-based or scanning lidar measurements (Doubrawa et al., 2016).

5. Testing the lidar short-range wind field reconstruction technique using the combined wind-induction model shall be tested in sites where the terrain is complex. Such studies are planned within the *UniTTe* project, with two full-scale measurement campaigns in moderately complex sites.
   In addition, the sort-range nacelle lidar measurement technique may allow the power curve of wind turbine located inside a wind farm to be measured, for instance in an offshore array. Due to the presence of wakes, the simple induction model may however need significant adjustments.

APPENDIX A

The GUM applied to the wind and combined wind-induction models

In Section 4.7.1 and Section 4.7.2, the GUM was applied to the wind model accounting for shear through a power law (Eq. (4.5)) and to the combined wind-induction (Eq. (4.9)), denoted respectively f_1 and f_2. The expressions of the partial derivatives are given hereafter

Partial derivatives for the wind model (see Eq. (4.7))

In respect to the hub height wind speed V_{H}:

$$\frac{\partial f_1}{\partial V_{\mathrm{H}}} = \left(\frac{z_{\mathcal{H}} + H_{\mathrm{hub}}}{H_{\mathrm{hub}}}\right)^{\alpha_{\mathrm{exp}}}. \tag{A.1}$$

In respect to the relative wind direction (or yaw misaligment) θ_{r}:

$$\frac{\partial f_1}{\partial \theta_{\mathrm{r}}} = 0. \tag{A.2}$$

In respect to the shear exponent α_{exp}:

$$\frac{\partial f_1}{\partial \alpha_{\mathrm{exp}}} = V_{\mathrm{H}} \ln\left(\frac{z_{\mathcal{H}} + H_{\mathrm{hub}}}{H_{\mathrm{hub}}}\right) \left(\frac{z_{\mathcal{H}} + H_{\mathrm{hub}}}{H_{\mathrm{hub}}}\right)^{\alpha_{\mathrm{exp}}}. \tag{A.3}$$

Partial derivatives for the combined wind-induction model (see Eq. (4.10))

In respect to the hub height free stream wind speed V_∞:

$$\frac{\partial f_2}{\partial V_\infty} = \left(\frac{z_{\mathcal{H}} + H_{\mathrm{hub}}}{H_{\mathrm{hub}}}\right)^{\alpha_{\mathrm{exp}}} \sqrt{\cos^2\theta_{\mathrm{r}} \left(1 - a_{\mathrm{ind}}\left[1 + \frac{\xi}{\sqrt{1+\xi^2}}\right]\right)^2 + \sin^2\theta_{\mathrm{r}}}. \tag{A.4}$$

In respect to the relative wind direction (or yaw misalignment) θ_{r}:

$$\frac{\partial f_2}{\partial \theta_{\mathrm{r}}} = V_\infty \left(\frac{z_{\mathcal{H}} + H_{\mathrm{hub}}}{H_{\mathrm{hub}}}\right)^{\alpha_{\mathrm{exp}}} \times \frac{\cos\theta_{\mathrm{r}} \sin\theta_{\mathrm{r}} \left[1 - \left(1 - a_{\mathrm{ind}}\left[1 + \frac{\xi}{\sqrt{1+\xi^2}}\right]\right)^2\right]}{\sqrt{\cos^2\theta_{\mathrm{r}} \left(1 - a_{\mathrm{ind}}\left[1 + \frac{\xi}{\sqrt{1+\xi^2}}\right]\right)^2 + \sin^2\theta_{\mathrm{r}}}}. \quad \text{(A.5)}$$

In respect to the shear exponent α_{exp}:

$$\frac{\partial f_2}{\partial \alpha_{\mathrm{exp}}} = V_\infty \ln\left(\frac{z_{\mathcal{H}} + H_{\mathrm{hub}}}{H_{\mathrm{hub}}}\right) \left(\frac{z_{\mathcal{H}} + H_{\mathrm{hub}}}{H_{\mathrm{hub}}}\right)^{\alpha_{\mathrm{exp}}} \times \sqrt{\cos^2\theta_{\mathrm{r}} \left(1 - a_{\mathrm{ind}}\left[1 + \frac{\xi}{\sqrt{1+\xi^2}}\right]\right)^2 + \sin^2\theta_{\mathrm{r}}}. \quad \text{(A.6)}$$

In respect to the induction factor a_{ind}:

$$\frac{\partial f_2}{\partial a_{\mathrm{ind}}} = V_\infty \cos^2\theta_{\mathrm{r}} \left(\frac{z_{\mathcal{H}} + H_{\mathrm{hub}}}{H_{\mathrm{hub}}}\right)^{\alpha_{\mathrm{exp}}} \times \frac{-\left[1 + \frac{\xi}{\sqrt{1+\xi^2}}\right]\left(1 - a_{\mathrm{ind}}\left[1 + \frac{\xi}{\sqrt{1+\xi^2}}\right]\right)}{\sqrt{\cos^2\theta_{\mathrm{r}} \left(1 - a_{\mathrm{ind}}\left[1 + \frac{\xi}{\sqrt{1+\xi^2}}\right]\right)^2 + \sin^2\theta_{\mathrm{r}}}} \quad \text{(A.7)}$$

Bibliography

Abbe, C. 1888. *Treatise on meteorological apparatus and methods*. 392 p., 36 plates. 392 p., 36 plates. Washington: [s.n.]

Angelou, N., et al. 2012. "Direct measurement of the spectral transfer function of a laser based anemometer". *Review of Scientific Instruments* 83 (3): 033111. doi:10.1063/1.3697728.

Angelou, N., et al. 2010. *Doppler lidar mounted on a wind turbine nacelle – UPWIND deliverable D6.7.1*. Danmarks Tekniske Universitet, Risø Nationallaboratoriet for Bæredygtig Energi. ISBN: 978-87-550-3868-4.

Antoniou, I., et al. 2007. "Remote sensing the wind using lidars and sodars". In *Conference proceedings (online)*. European Wind Energy Association (EWEA).

Beck, Hauke, and Martin Kühn. 2017. "Dynamic Data Filtering of Long-Range Doppler LiDAR Wind Speed Measurements". *Remote Sensing* 9, number 6 (): 561. doi:10.3390/rs9060561.

Bingöl, Ferhat, Jakob Mann, and Dimitri Foussekis. 2009. "Conically scanning lidar error in complex terrain". *Meteorologische Zeitschrift* (Stuttgart, Germany) 18, number 2 (): 189–195. doi:10.1127/0941-2948/2009/0368.

BIPM. 2014. *The International System of Units (SI), SI Brochure, [8th edition, 2006; updated in 2014]*. Technical report. Bureau International des Poids et Mesures.

Borraccino, Antoine, and Michael Courtney. 2016a. *Calibration report for Avent 5-beam Demonstrator lidar*. Technical report. Denmark: DTU Wind Energy.

— . 2016b. *Calibration report for ZephIR Dual Mode lidar (unit 351)*. Technical report. Denmark: DTU Wind Energy.

Borraccino, Antoine, Michael Courtney, and Rozenn Wagner. 2016. "Generic Methodology for Field Calibration of Nacelle-Based Wind Lidars". *Remote Sensing* 8 (11): 907. ISSN: 2072-4292. doi:10.3390/rs8110907.

Borraccino, A., et al. 2017. "Wind field reconstruction from nacelle-mounted lidar short-range measurements". *Wind Energy Science* 2 (1): 269–283. doi:10.5194/wes-2-269-2017.

Branlard, Emmanuel. 2017a. "The Blade Element Momentum (BEM) Method". Chapter 10 in *Wind Turbine Aerodynamics and Vorticity-Based Methods: Fundamentals and Recent Applications*, 181–211. Cham: Springer International Publishing. ISBN: 978-3-319-55164-7. doi:10.1007/978-3-319-55164-7_10.

— . 2017b. "Velocity Field Upstream of Aligned and Yawed Rotors: Wind Turbine and Wind Farm Induction Zone". Chapter 24 in *Wind Turbine Aerodynamics and Vorticity-Based Methods: Fundamentals and Recent Applications*, 321–332. Cham: Springer International Publishing. ISBN: 978-3-319-55164-7. doi:10.1007/978-3-319-55164-7_24.

Cariou, J.P., M. Valla, and G. Canat. 2007. "Fiber lasers: new effective sources for coherent lidars". In *Lidar Technologies, Techniques, and Measurements for Atmospheric Remote Sensing III*, 6750:675007-675007-12. doi:10.1117/12.741584.

Christensen, C J, and J B. Dragt. 1987. *Accuracy of Power Curve Measurements*. Risø National Laboratory. ISBN: 87-550-1307-4.

Cox, Maurice G, and Bernd R L Siebert. 2006. "The use of a Monte Carlo method for evaluating uncertainty and expanded uncertainty". *Metrologia* 43 (4): S178.

Doubrawa, Paula, et al. 2016. "Wind Turbine Wake Characterization from Temporally Disjunct 3-D Measurements". *Remote Sensing* 8 (11): 939. ISSN: 2072-4292. doi:10.3390/rs8110939.

Foti, Daniel, Xiaolei Yang, and Fotis Sotiropoulos. 2016. "Uncertainty quantification of infinite aligned wind farm performance using non-intrusive polynomial chaos and a distributed roughness model". *Wind Energy* 20, number 6 (): 945–958. doi:10.1002/we.2072.

Frehlich, R. 2013. "Scanning Doppler Lidar for Input into Short-Term Wind Power Forecasts". *Journal of Atmospheric and Oceanic Technology* 30, number 2 (): 230–244. doi:10.1175/jtech-d-11-00117.1.

Goldstein, Michael, Allan Seheult, and Ian Vernon. 2013. "Assessing Model Adequacy". In *Environmental Modelling*, 435–449. John Wiley & Sons, Ltd. ISBN: 9781118351475. doi:10.1002/9781118351475.ch26.

Hansen, Martin Otto Laver. 2008. *Aerodynamics of Wind Turbines: second edition*. 2nd edition. Earthscan Publications Ltd. ISBN: 978-1-84407-438-9.

Hardesty, R. M., and B. F. Weber. 1987. "Lidar Measurement of Turbulence Encountered by Horizontal-Axis Wind Turbines". *J. Atmos. Oceanic Technol.* 4, number 1 (): 191–203. doi:10.1175/1520-0426(1987)004<0191:lmoteb>2.0.co;2.

Harris, Michael, Graham Constant, and Carol Ward. 2001. "Continuous-wave bistatic laser Doppler wind sensor". *Appl. Opt.* 40, number 9 (): 1501–1506. doi:10.1364/AO.40.001501.

Huard, D., and A. Mailhot. 2006. "A Bayesian perspective on input uncertainty in model calibration: Application to hydrological model abc". *Water Resources Research* 42 (7). ISSN: 1944-7973. doi:10.1029/2005WR004661.

IEA. 1990. *Recommended practices for wind turbine testing and evaluation: 1 Power performance testing, Second edition*. Edited by International Energy Agency. DTI, London, UK.

IEC 61400-12. 1998. *IEC 61400-12 Wind turbine power performance testing*. International Electrotechnical Commission.

IEC 61400-12-1. 2005. *IEC61400-12-1 Power performance measurements of electricity producing wind turbines*. International Electrotechnical Commission.

— . 2017. *IEC61400-12-1 Power performance measurements of electricity producing wind turbines*. International Electrotechnical Commission.

IEC 61400-12-2. 2013. *IEC 61400-12-2 Ed. 1.0b. Power performance of electricity-producing wind turbines based on nacelle anemometry*. IEC.

JCGM. 2008a. *Evaluation of measurement data - Guide to the expression of uncertainty in measurement*. Technical report. JCGM.

— . 2008b. *Evaluation of measurement data - Propagation of distributions using Monde Carlo method*. Technical report. JCGM.

— . 2012. *International vocabulary of metrology - Basic and general concepts and associated terms (VIM)*. Technical report. JCGM.

Jensen, N.O. 1983. *A note on wind generator interaction*. Technical report. Risø National Laboratory.

Kaimal, J. C., and J. A. Businger. 1963. "A Continuous Wave Sonic Anemometer-Thermometer". *Journal of Applied Meteorology* 2 (1): 156–164. doi:10.1175/1520-0450(1963)002<0156:ACWSAT>2.0.CO;2.

Kaimal, J. C., and D..A. Haugen. 1977. "An Acoustic Doppler Sounder for Measuring Wind Profiles in the Lower Boundary Layer". *Journal of Applied Meteorology* 16 (12): 1298–1305. doi:10.1175/1520-0450(1977)016<1298:AADSFM>2.0.CO;2.

Kawabata, Hirokazu. 2016. "Wind inflow measurements for wind turbine control using a nine-beam nacelle lidar". In *IEA Wind Task 32 Workshop*.

Klaas, Tobias, Lukas Pauscher, and Doron Callies. 2015. "LiDAR-mast deviations in complex terrain and their simulation using CFD". *Meteorologische Zeitschrift* (Stuttgart, Germany) 24, number 6 (): 591–603. doi:10.1127/metz/2015/0637.

Lataniotis, Christos, Stefano Marelli, and Bruno Sudret. 2015a. *UQLab user manual - the INPUT module*. doi:10.13140/RG.2.1.3909.8080.

— . 2015b. *UQLab user manual - The MODEL module*. doi:10.13140/RG.2.1.2205.8721.

Lawrence, T. R., et al. 1972. "A Laser Velocimeter for Remote Wind Sensing". *Rev. Sci. Instrum.* 43 (3): 512–518. doi:10.1063/1.1685674.

Lebrun, Régis, and Anne Dutfoy. 2009. "A generalization of the Nataf transformation to distributions with elliptical copula". *Probabilistic Engineering Mechanics* 24 (2): 172–178. ISSN: 0266-8920. doi:http://dx.doi.org/10.1016/j.probengmech.2008.05.001.

Lhermitte, R. M. 1962. "Note on Wind Variability with Doppler Radar". *J. Atmos. Sci.* 19, number 4 (): 343–346. doi:10.1175/1520-0469(1962)019<0343:nowvwd>2.0.co;2.

Madsen, Helge Aa., et al. 2010. "Validation and modification of the Blade Element Momentum theory based on comparisons with actuator disc simulations". *Wind Energy* 13, number 4 (): 373–389. doi:10.1002/we.359.

Magee, E. P., T. J. Kane, and R. G. Frehlich. 1998. "Bistatic coherent laser radar performance. [Wind remote sensing]". In *Geoscience and Remote Sensing Symposium Proceedings, 1998. IGARSS '98. 1998 IEEE International*, volume 5, 2433–2435 vol.5. doi:10.1109/IGARSS.1998.702237.

Marelli, Stefano, and Bruno Sudret. 2014. "UQLab: A Framework for Uncertainty Quantification in Matlab". In *Vulnerability, Uncertainty, and Risk*. American Society of Civil Engineers (ASCE). doi:10.1061/9780784413609.257.

Metropolis, N. 1987. "The beginning of the Monte Carlo Method". *Los Alamos Science, Special Issue*, number 15.

Metropolis, Nicholas, and S. Ulam. 1949. "The Monte Carlo Method". *Journal of the American Statistical Association* 44, number 247 (): 335–341. doi:10.1080/01621459.1949.10483310.

Meyer Forsting, Alexander Raul, Niels Troldborg, and Mac Gaunaa. 2016. "The flow upstream of a row of aligned wind turbine rotors and its effect on power production". *Wind Energy*: n/a–n/a. ISSN: 1099-1824. doi:10.1002/we.1991.

Nygaard, Nicolai Gayle, and Sidse Damgaard Hansen. 2016. "Wake effects between two neighbouring wind farms". *Journal of Physics: Conference Series* 753 (): 032020. doi:10.1088/1742-6596/753/3/032020.

Pedersen, T. F., G. Demurtas, and F. Zahle. 2014. "Calibration of a spinner anemometer for yaw misalignment measurements". *Wind Energy* 18, number 11 (): 1933–1952. doi:10.1002/we.1798.

Peña, Alfredo, et al. 2009. "Offshore wind profiling using light detection and ranging measurements". *Wind Energy* 12 (2): 105–124. ISSN: 1099-1824. doi:10.1002/we.283.

Reggiani, M. G., and F. E. Marchetti. 1975. "On Assessing Model Adequacy". *IEEE Transactions on Systems, Man, and Cybernetics* SMC-5, number 3 (): 322–330. ISSN: 0018-9472. doi:10.1109/TSMC.1975.5408407.

Réthoré, Pierre-Elouan. 2006. "Thrust and wake of a wind turbine: Relationship and measurements" [**inlang**eng]. Master's thesis, Technical University of Denmark.

Rosenblatt, Murray. 1952. "Remarks on a Multivariate Transformation". *Ann. Math. Statist.* 23, number 3 (): 470–472. doi:10.1214/aoms/1177729394.

Sareen, Agrim, Chinmay A. Sapre, and Michael S. Selig. 2014. "Effects of leading edge erosion on wind turbine blade performance". *Wind Energy* 17 (10): 1531–1542. ISSN: 1099-1824. doi:10.1002/we.1649.

Schotland, R M. 1955. "The measurement of wind velocity by sonic means". *Journal of Meteorology* 12 (4): 386–390. doi:10.1175/1520-0469(1955)012<0386:TMOWVB>2.0.CO;2.

Smith, David A., et al. 2006. "Wind lidar evaluation at the Danish wind test site in Høvsøre". *Wind Energy* 9 (1-2): 87–93. ISSN: 1099-1824. doi:10.1002/we.193.

Sudret, Bruno. 2008. "Global sensitivity analysis using polynomial chaos expansions". *Reliability Engineering & System Safety* 93, number 7 (): 964–979. doi:10.1016/j.ress.2007.04.002.

Troldborg, N., and A. Meyer Forsting. 2016. "Simulations of wind turbine induction in uniform inflow". Submitted to Wind Energy (UNPUBLISHED).

Vasiljevic, Nikola, et al. 2016. "Long-Range WindScanner System". *Remote Sensing* 8, number 12 (): 896. doi:10.3390/rs8110896.

Vignaroli, Andrea, and Carsten Weber Kock. 2016. *UniTTe MC2 Nørrekær Enge Measurement System & Calibration report*. Denmark: DTU Wind Energy.

Wagenaar, J.W., et al. 2016. *Wind Iris nacelle LiDAR calibration at ECN test site*. Technical report ECN-E–16-053. ECN.

Wagner, Rozenn, et al. 2011. "Accounting for the speed shear in wind turbine power performance measurement". *Wind Energy* 14 (8): 993–1004. ISSN: 1095-4244. doi:10.1002/we.509.

Wagner, Rozenn, et al. 2015. "Uncertainty of power curve measurement with a two-beam nacelle-mounted lidar". *Wind Energy*: n/a–n/a. ISSN: 1099-1824. doi:10.1002/we.1897.

Wagner, R., et al. 2014. "Power curve measurement with a nacelle mounted lidar". *Wind Energy* 17 (9): 1441–1453. ISSN: 1099-1824. doi:10.1002/we.1643.

Waldo, F. 1893. *Modern Meteorology*. Walter Scott Ltd.

Yu, Shaocai, et al. 2006. "New unbiased symmetric metrics for evaluation of air quality models". *Atmospheric Science Letters* 7 (1): 26–34. ISSN: 1530-261X. doi:10.1002/asl.125.